INFLUENCE OF MOLECULAR STRUCTURE ON RHEOLOGICAL AND PROCESSING BEHAVIOUR OF MOLTEN POLYMERS

by

IGOR B. KAZATCHKOV

Master of Applied Science, University of British Columbia, 1994
Diploma of Chemical Engineer, Mendeleyev University of Chemical Technology, 1989

A THESIS SUBMITTED IN PARTIAL FULFILMENT OF THE
REQUIREMENTS FOR THE DEGREE OF

DOCTOR OF PHILOSOPHY

in

the Faculty of Graduate Studies
Department of Chemical Engineering

We accept this thesis as conforming to the required standard

THE UNIVERSITY OF BRITISH COLUMBIA
December 1998

In presenting this thesis in partial fulfilment of the requirements for an advanced degree at the University of British Columbia, I agree that the Library shall make it freely available for reference and study. I further agree that permission for extensive copying of this thesis for scholarly purposes may be granted by the head of my department or by his or her representatives. It is understood that copying or publication of this thesis for financial gain shall not be allowed without my written permission.

Department of Chemical Engineering

The University of British Columbia
Vancouver, Canada

Date 22 Dec 1998

DE-6 (2/88)

ABSTRACT

The primary focus of this work was to study the effect of molecular characteristics of polymers on their rheological and processing behaviour. In particular, the melt fracture and wall slip phenomena have been extensively studied using various rheological tools and techniques. In order to study the effects of the two key molecular characteristics, the weight average molecular weight and the molecular weight distribution, two series of polyethylene resins have been specially selected. A new method of interpretation of the large-amplitude oscillatory shear (LAOS) data has been proposed. It provides an easier and more convenient way for the data analysis suitable for use as a non-linear viscoelastic polymer characterisation technique. In addition, this method has been shown to offer an alternative way for determination of the damping function. Furthermore, a criterion for melt fracture performance has been developed and it was found to be related to a characteristic relaxation time of polymers.

Additional experiments have been carried out with two metallocene polyethylene resins, which exhibited unusually long start-up transients during their capillary extrusion. This phenomenon has been investigated in detail and the results are explained in terms of a qualitative molecular model based on the two mechanisms of slip, namely flow-induced chain detachment and disentanglement.

A multimode dynamic slip model has also been developed and a procedure for the determination of its parameters is proposed. The model has been found to provide better predictions compared to a static and a single-mode slip models for the flow of molten polymers in transient experiments under slip conditions.

Finally, a flow visualisation apparatus has been developed using a quartz capillary and interrupted laser beam. It allowed the measurement of the velocity profiles at high temperatures and shear stresses. Using this apparatus, the effect of processing aids on the flow profile and melt fracture behaviour of molten polypropylene has been studied.

TABLE OF CONTENTS

LIST OF TABLES

LIST OF FIGURES

ACKNOWLEDGEMENTS

I wish to thank the following persons and organisations without whom my thesis could not have been in its present form:

My supervisor Dr. Savvas G. Hatzikiriakos, for his skilful guidance, support and encouragement during the course of this work;

Dr. Shiv K. Goyal and Mr. Nick Bohnet (NOVA Chemicals, Calgary, AB, Canada), for providing polymers with specified characteristics, financial support and assistance with experimental work (as well as behavioural lessons to facilitate my integration into a corporate structure) during my contract term at their research centre;

Natural Sciences and Engineering Research Council of Canada and E. I. DuPont de Nemours & Co. (Wilmington, DE, USA) for providing the financial support;

Dow Benelux B. V. (Netherlands), for providing samples of metallocene resins;

Dr. Eugene E. Rosenbaum, for help in designing and carrying out the visualisation experiments. Valuable insights during our weekly discussions over Friday night drinks are also greatly appreciated;

Mr. Divya Chopra, for his enthusiastic interest in my LAOS data analysis and for bombarding me with thousands of questions about it.

1. INTRODUCTION

The increasing role of synthetic polymers as materials of construction has prompted the study of their rheological and processing properties. It is known that the rate of production in such processes as extrusion, film blowing and moulding is limited by the onset of flow instabilities. These result in deterioration of the surface appearance of extrudates and eventually lead to commercially unacceptable products. For example, when the rate of extrusion is low, the extrudate is smooth and glossy. As the extrusion rate increases, the surface starts losing its glossiness and at higher rates small amplitude periodic distortions appear (surface or "sharkskin" melt fracture). At even higher rates not only is the surface rough, but the entire extrudate shape changes. It may become wavy with regular patterns, which may grow irregular (gross melt fracture) at some higher extrusion rate depending on the material and its molecular characteristics. Figure 1-1 illustrates these phenomena: the samples of extruded polypropylene

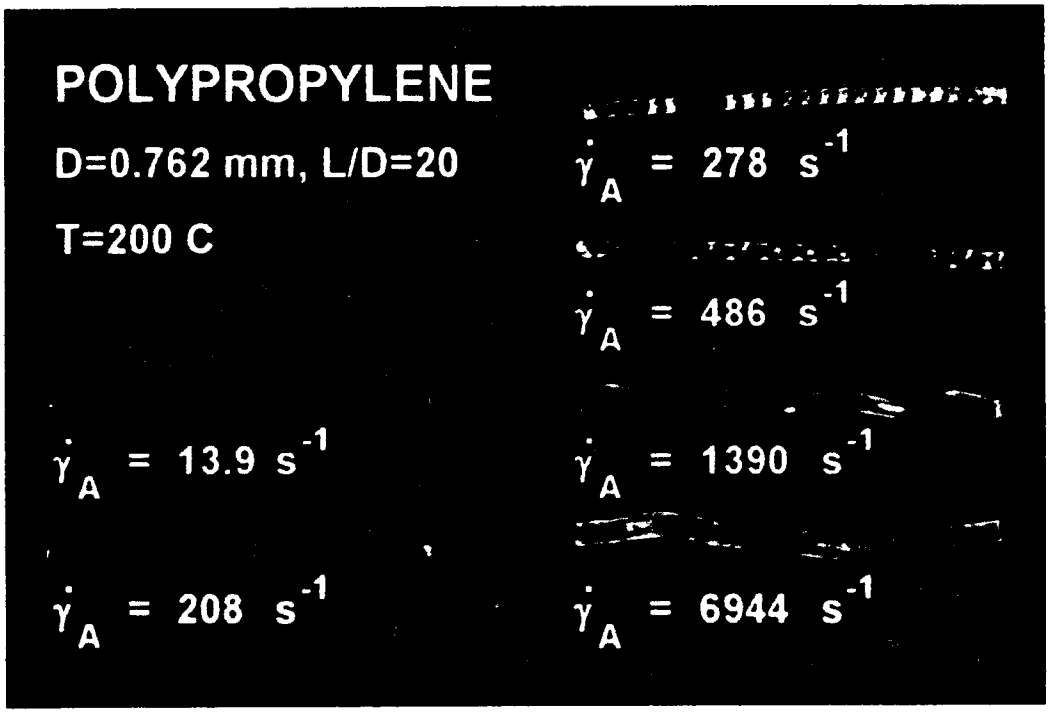

Figure 1-1. Extrudate samples obtained in extrusion of polypropylene through a die having a diameter of 0.762 mm and a length-to-diameter ratio of 20 at 200 °C.

are smooth at shear rates below 208 s^{-1}. Above that rate, the extrudates exhibit regular helix patterns and become grossly distorted at about 7000 s^{-1}. Another phenomenon inherent to polymer melt extrusion, can also be noted in Figure 1-1: extrudate swell almost doubles as the shear rate is increased from 13.9 to 7000 s^{-1}.

Melt fracture has been the subject of many investigations over the past decades. Numerous experimental, theoretical and computational studies have been reported, aimed at determining the origin and nature of flow instabilities in polymer melts and solutions. Some workers attributed the onset of melt fracture to pressure fluctuations resulting from the flow irregularities in the entrance region of the capillary due to the contraction flow [Weill, 1980; Bergem, 1976], while others related it to slip at the wall [Kraynik and Schowalter, 1981; Kalika and Denn, 1987]. Many terms have been used in the literature to describe this phenomenon: "melt fracture", "sharkskin", "waviness", "ripple", "bamboo effect", "sausage link", etc. For polyethylene, the distinction is usually made between surface melt fracture (or "sharkskin"), when the distortions are relatively small and affect only a thin layer on the surface, and gross melt fracture, with the extrudate appearance ranging from helical screw thread to severe irregular distortions. If the shear rate is increased further, some materials (e.g. linear polyethylene, tetrafluoroethylene-hexafluoropropylene copolymer) exhibit a second stable flow regime in which the extrudate is again smooth [Tordella, 1969]. Polymers such as branched polyethylene, polypropylene and polystyrene do not appear to have a second stable regime.

The interaction between a fluid and a solid interface in shear flow is of fundamental importance in many areas of technology, including polymer processing. It has long been recognised that polymer melts may violate the classical no-slip boundary condition of Newtonian fluid mechanics at solid surfaces under certain conditions [Vinogradov *et al.*, 1972; Ramamurthy,

1986; Kalika and Denn, 1987; Hatzikiriakos and Dealy, 1991]. For example, in the flow of linear polymers through cylindrical dies, the flow curve (shear stress versus apparent shear rate) has been found to depend on the diameter of the die once the wall shear stress rises above a critical value. This is consistent with the assumption of slip. If it is assumed that slip occurs at the interface, the data can be superposed once slip effects are accounted for. Mooney (1931) was the first to derive explicit relations for the slip velocity that can be used to calculate the slip velocity as a function of wall shear stress. Since then, many workers have dealt with it, but a comprehensive understanding of the mechanism causing the phenomenon is still lacking.

The subject of modelling polymer processing operations is one of the most difficult ones, since polymer melts defy the laws of Newtonian fluid mechanics and behave in unusual ways. A variety of viscoelastic constitutive equations exist [Bird *et al.*, 1987; Larson, 1988] and numerical solutions are needed (except for trivial cases) for predictions of the flow field. However, to simulate such processes realistically, it is necessary to have slip velocity models, which can adequately describe both the steady-state and dynamic nature of the slip phenomenon.

The purpose of this work is to investigate the melt fracture of a number of polymer melts, primarily polyethylenes, in order to identify the critical parameters for the onset of such instabilities. This will be approached by conducting a thorough rheological characterisation of a number of commercial linear low-density polyethylene (LLDPE) resins. Several rheological and processing properties such as linear dynamic moduli, capillary and sliding plate flow curves and their dependence on the test geometry, non-linear relaxation behaviour, and conditions for the onset of melt fracture and wall slip, will be determined. An attempt will be made to link these phenomena and properties to the molecular characteristics of the polymer, such as average molecular weight and molecular weight distribution. In addition to conventional LLDPEs, metallocene polyethylenes and a polyisobutylene will be studied to provide additional insights

into the origins of the phenomena. Finally, visual observation of the flow patterns developed at the entrance of the capillary and velocity profile measurements will be performed using a quartz capillary in conjunction with a laser-speckle technique. The determination of such flow patterns is expected to provide additional insights into the origins of melt fracture instabilities.

2. LITERATURE REVIEW

Rheological characterisation of polymer melts involves several types of experiments: capillary rheometer experiments, in which a molten polymer is forced through a channel of known diameter and length; linear dynamic viscoelastic experiments using a cone-and-plate or a parallel plate configuration; and sliding plate rheometer experiments producing various types of non-linear strain deformations. In this chapter, the basic flow equations in these types of experiments are presented. In addition, the melt fracture and wall slip phenomena are described and previous knowledge about these phenomena are reviewed.

2.1 Chemical structure of polyethylene and its applications

The vast majority of the experiments described in this work were performed using linear low-density polyethylene (LLDPE). This polymer results from the polymerisation of ethylene, $CH_2=CH_2$, and has the following structure:

$$\left(-CH_2-CH_2-\right)_n$$

where n is the polymerisation index.

The typical melting temperature of commercial PE resins is about 130 °C; however, there are exceptions, as shown in Chapter 6. Its glass transition temperature is about –125 °C. LLDPEs are predominantly semicrystalline materials at room temperature, exhibiting amorphous and crystalline structures.

LLDPE has numerous applications, ranging from films and extrusion coatings to various household items such as food containers. Two important advantages of polyethylene are its inertness to water and micro-organisms and its low cost, around $0.50 per kilogram.

2.2 Viscometric flows

Simple shear flow is generated by the rectilinear motion of one flat plate relative to another, where the two plates are parallel and the gap between them is constant with time. Steady simple shear is a simple shear flow that has been carried out at a constant shear rate for a sufficient length of time for the stresses in the material to attain steady-state values.

Steady simple shear is a uniform deformation, i.e., each fluid element undergoes exactly the same deformation, and the stresses are independent of position in space. There are also non-uniform flows for which the three material functions, viscosity and the two normal stress difference coefficients, govern the behaviour of the fluid. Such deformations are called "viscometric flows." While different fluid elements in the flow field may be subject to different shear rates, the shear rate experienced by any particular fluid element is constant with time. The three types of viscometric flows that were used in this work, viz., steady tube flow, steady slit flow, and steady simple shear flow, are discussed below.

2.2.1 Flow in a circular channel

Capillary flow is an example of a partially controllable flow. In this flow, the polymer melt flows from a large reservoir into a capillary of small diameter. Far from the capillary entrance where the flow is fully developed, the streamlines are parallel to the channel axis, but the velocity profile depends on the rheological nature of the fluid. Unless a specific constitutive equation is known to be valid for the fluid, as in the case of a Newtonian fluid or a power-law fluid, special computational techniques are required to calculate the shear stress, shear rate and viscosity.

For the steady flow of an incompressible fluid in a tube of radius R, driven by a pressure gradient dP/dz, Cauchy equation (momentum balance) on a cylindrical element of the fluid gives [Dealy and Wissbrun, 1990]:

$$0 = -\frac{dP}{dz} + \frac{1}{r}\frac{\partial}{\partial r}\left(\frac{1}{r}\sigma_{rz}\right) \qquad \text{eq. 2-1}$$

By integrating and assuming $P=P(z)$, and that stress is finite at the centerline,

$$\sigma_{rz}(r) = \frac{r}{2}\left(\frac{dP}{dz}\right) \qquad \text{eq. 2-2}$$

When the flow is fully-developed over length L, the absolute value of the shear stress at the wall σ_w is:

$$\sigma_w \equiv -\sigma_{rz}\big|_{r=R} = \frac{-\Delta P \cdot R}{2L} \qquad \text{eq. 2-3}$$

where ΔP is the pressure drop over the length of tube.

For a Newtonian fluid, the shear stress is proportional to the shear rate:

$$\sigma = \eta\dot{\gamma} \qquad \text{eq. 2-4}$$

and the viscosity, η, does not change with $\dot{\gamma}$. Combining eq. 2-1 with eq. 2-4, using $\dot{\gamma} = du/dr$ and assuming that the velocity at the wall is zero, the velocity profile can be obtained as:

$$u(r) = \frac{2Q}{\pi R^2}\left[1 - \left(\frac{r}{R}\right)^2\right] \qquad \text{eq. 2-5}$$

where Q is the volumetric flow rate. The velocity distribution is parabolic and the shear rate at the wall is given by:

$$\dot{\gamma}_w \equiv \left.\frac{du}{dr}\right|_{r=R} = \frac{4Q}{\pi R^3} \qquad \text{eq. 2-6}$$

For non-Newtonian fluids, if a specific constitutive equation is assumed, one can derive equations analogous to those valid for Newtonian fluids. For example, if shear stress depends on shear rate according to the power law relationship

$$\sigma = K\dot{\gamma}^n \qquad \text{eq. 2-7}$$

where K is the consistency index and n is the power-law exponent, it can be shown that the wall shear rate is [Dealy and Wissbrun, 1990]:

$$\dot{\gamma}_w = \frac{3n+1}{4n}\left(\frac{4Q}{\pi R^3}\right) \qquad \text{eq. 2-8}$$

and the velocity profile is given by:

$$u(r) = \frac{3n+1}{n+1}\frac{Q}{\pi R^2}\left[1-\left(\frac{r}{R}\right)^{\frac{1}{n}+1}\right] \qquad \text{eq. 2-9}$$

The bracketed quantity in eq. 2-8, which is equal to the wall shear rate in the case of a Newtonian fluid, no longer has this significance when the fluid is non-Newtonian. It is, however, referred to as the "apparent shear rate", $\dot{\gamma}_A$.

Using eq. 2-6, eq. 2-7 and eq. 2-8, it can be shown that the wall shear rate, σ_w, is:

$$\sigma_w = K\left(\frac{3n+1}{4n}\right)^n\left(\frac{4Q}{\pi R^3}\right)^n = K\left(\frac{3n+1}{4n}\right)^n\dot{\gamma}_A^n \qquad \text{eq. 2-10}$$

Therefore, a plot of $\log(\sigma_w)$ versus $\log(\dot{\gamma}_A)$ will be a straight line for a power-law fluid, and the constants K and n can be determined from the slope and the intercept. However, even if there is no constitutive equation relating the shear stress to the shear rate, a special technique can be used to determine the true wall shear rate and the viscosity for any non-Newtonian fluid. This technique requires pressure drop data for several different flow rates. It can be shown that

these data should fall on a single curve when a plot of $\log(\sigma_w)$ versus $\log(\dot{\gamma}_A)$ is made. The shear rate at the wall is given by

$$\dot{\gamma}_w = \frac{3+\mathbf{b}}{4}\left(\frac{4Q}{\pi R^3}\right) = \frac{3+\mathbf{b}}{4}\dot{\gamma}_A \qquad \text{eq. 2-11}$$

where **b** is the Rabinowitsch correction given by

$$\mathbf{b} = \frac{d(\log\dot{\gamma}_A)}{d(\log\sigma_w)} \qquad \text{eq. 2-12}$$

This correction term is a measure of the deviation of a polymeric fluid from Newtonian behaviour. It equals unity for a Newtonian fluid and $1/n$ for a power-law fluid.

In a capillary rheometer, there is a large pressure drop associated with the flow in the entrance region. This must be taken into account, if the reservoir pressure is the quantity measured to determine the wall shear stress. Moreover, it has been proposed that the excess pressure drop at the entrance to a capillary is itself a useful quantity that can be used to characterise polymers. There also appears to be a small residual pressure at the exit of the capillary. Wall pressures measured at various axial locations in a reservoir and capillary have been reported by Han (1978) for molten polymers. A typical result is shown in Figure 2-1. The total pressure drop for flow from the reservoir, through the capillary and out to the ambient pressure can be thought to consist of three components:

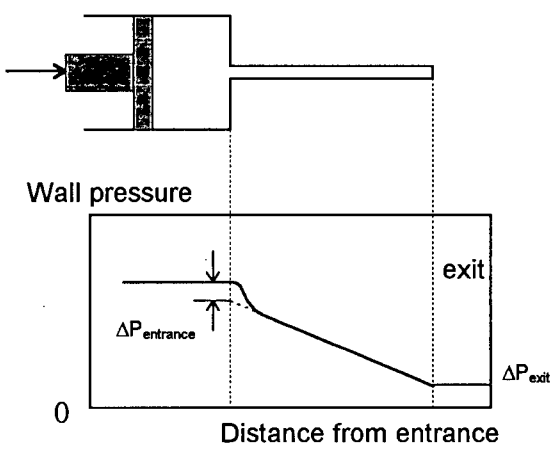

Figure 2-1. Pressure distribution in a reservoir and capillary.

$$\Delta P = \Delta P_{entrance} + \Delta P_{cap} + \Delta P_{exit} = \Delta P_{end} + \Delta P_{cap} \qquad \text{eq. 2-13}$$

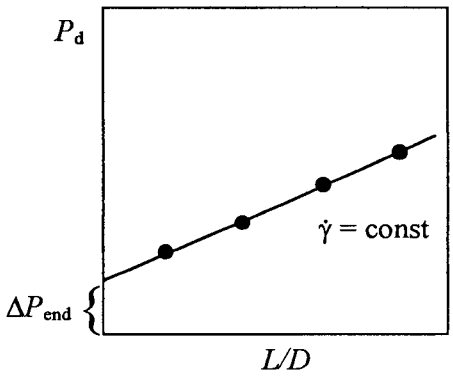

Figure 2-2. Bagley plot (schematic).

The end correction, ΔP_{end}, can be determined by using a technique outlined by Bagley (1931). He measured the driving pressure, P_d, for various values of the flow rate using a variety of capillaries having different lengths. For each value of $\dot{\gamma}_A$, the driving pressure is plotted versus L/D and a straight line is drawn through the points. Extrapolating the lines corresponding to various values of $\dot{\gamma}_A$ to L/D=0, an end correction is obtained, which is often called "Bagley correction" (Figure 2-2). Thus, the true wall shear stress which is obtained over most of the length of the capillary (except in the entrance) can be calculated as follows:

$$\sigma_w = (P_d - \Delta P_{end}) \,/\, (4L/D) \qquad \text{eq. 2-14}$$

In general, one should expect some curvature of the Bagley plot for long capillaries, which may indicate dependence of viscosity on pressure [Laun, 1987], pressure-dependent slip at the wall [Hatzikiriakos and Dealy, 1992a] or viscous heating [Rosenbaum *et al.*, 1997]. The accuracy of the capillary rheometer data is typically between 5 and 10%.

2.2.2 Flow in a rectangular channel

When a fluid flows through a rectangular channel in which the width, W, is much larger than the thickness, H, the edges make a negligible contribution to the pressure drop and this geometry can effectively be used for rheological measurements. The basic equations and entrance correction procedures are similar to those for capillary flow, but the difference in geometry has certain experimental advantages: flush-mounted wall pressure transducers can

obviate the need for end corrections; the two-dimensional flow field facilitates observation of the flow.

For the steady flow of an incompressible fluid in such a channel, the absolute value of the shear stress at the wall, σ_w, is given by [Dealy and Wissbrun, 1990]:

$$\sigma_w = -\Delta P \cdot H / 2L \qquad \text{eq. 2-15}$$

where ΔP is the pressure drop over a length of channel, L.

The apparent shear rate in a slit, which is the true wall shear rate for a Newtonian fluid is given by:

$$\dot{\gamma}_A = \frac{6Q}{H^2 W} \qquad \text{eq. 2-16}$$

For non-Newtonian fluids the wall shear rate is given by:

$$\dot{\gamma}_w = \frac{2+b}{3}\left(\frac{6Q}{H^2 W}\right) \qquad \text{eq. 2-17}$$

where b is the Rabinowitsch correction given by

$$b = \frac{d(\log \dot{\gamma}_A)}{d(\log \sigma_w)} \qquad \text{eq. 2-18}$$

As in the case of circular channels, a plot of $\log(\sigma_w)$ versus $\log(\dot{\gamma}_A)$ reveals the behaviour of the fluid. If all the data fall on a straight line with a slope of one, then Newtonian behaviour is obtained. If they fall on a straight line but the slope is not equal to one, then power-law behaviour is exhibited, with $n = 1/b$. Curvature indicates general non-Newtonian behaviour.

For a power-law fluid the wall shear stress is as follows:

$$\sigma_w = K\left(\frac{2n+1}{3n}\right)^n \dot{\gamma}_A^n \qquad \text{eq. 2-19}$$

The procedure for determination of the end effects is analogous to the one used for circular channels.

2.2.3 Flow in a sliding plate rheometer

The laboratory procedure that most closely approximates simple shear is to place a thin layer of fluid between two flat plates, clamp one of the plates in place, and translate the second plate at a constant velocity, as shown in Figure 2-3. Under no-slip conditions the actual shear rate, $\dot{\gamma}$, is equal to the nominal shear rate, $\dot{\gamma}_n$. The wall shear stress can be determined by measuring the force required to drive the motion of the moving plate and dividing it by the wetted area of the plates. When slip is present, the true shear rate is less than the nominal shear rate, as illustrated in Figure 2-4.

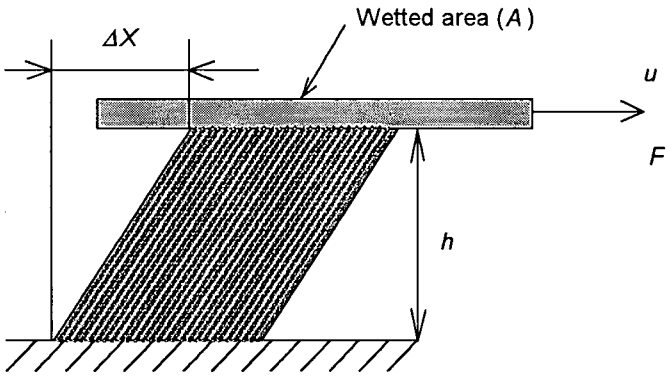

Displacement:	ΔX
Strain:	$\gamma = \Delta X / h$
Nominal shear rate:	$\dot{\gamma}_n = u / h$
Stress:	$\sigma = F / A$

Figure 2-3. Simple shear and related equations.

The advantages of the sliding plate geometry over the other two geometries discussed above are that there are no effects of pressure on measurements, and that the edge effects can be eliminated by measuring the shear stress locally (using a flush-mounted shear stress transducer). The first normal stress difference, $N_1 \equiv \sigma_{11} - \sigma_{22}$, is positive for molten polymers, and the shearing deformation will result in a force tending to separate the plates. Consequently, some way must be found to maintain the gap without introducing a significant frictional force.

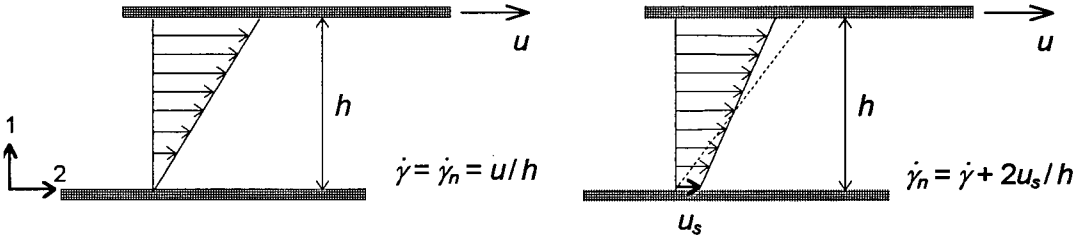

Figure 2-4. Velocity profiles in a sliding plate rheometer under no-slip (left) and slip conditions (right).

For this work a sliding plate rheometer with a flush-mounted shear stress transducer was used [Giacomin, 1987]. The basic features of the transducer are shown in Figure 2-5. An end plate is acted on by the shear stress generated by the fluid and transmits the resulting moment to the cantilever beam. To avoid melt penetration into the gap around the end plate, the deflection of the latter must be limited to very small levels. That is why a capacitance system was used, where a capacitor is formed

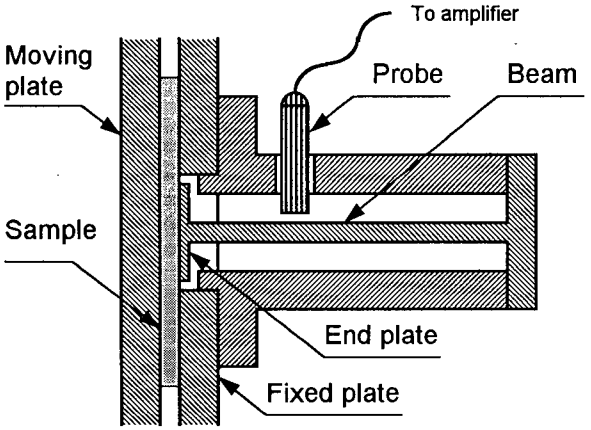

Figure 2-5. Schematic diagram of the shear stress transducer.

by the probe acting as one of the plates, and the beam as the second plate.

There are many advantages associated with the direct measurement of the shear stress:

- Uncontrolled flow at the edges of the sample does not affect the determination of the shear stress, allowing tests with large and rapid deformation to be carried out;
- Degradation occurring as a result of contact between the exposed edges of the sample and the environment does not affect the measurement;
- The exact size and shape of the sample need not be known, and this greatly simplifies sample loading;
- Tests can be carried out with only a few grams of sample;
- Bearing friction has no effect on the measured shear stress, as long as it does not introduce mechanical noise.

The accuracy of the sliding plate rheometer data is typically between 3 and 8%.

2.2.4 Parallel Plate Rheometer Measurements

Linear dynamic properties such as storage and loss moduli are measured at low deformations using rotational rheometers such as the cone-and-plate or parallel-plate rheometers (Figure 2-6). Two circular plates are mounted on a common axis of symmetry, and the sample is inserted in the space between them, having gap width h. The upper plate is rotated at a specified angular velocity $\omega(t)$ and the resulting torque, M, is measured (constant strain rheometers). Another mode of operation is to fix the torque and measure the displacement (constant-stress rheometers).

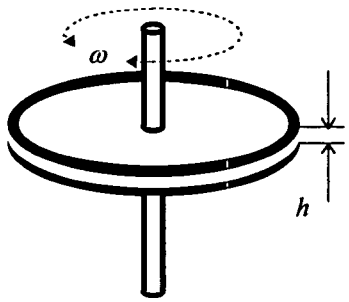

Figure 2-6. Parallel plate rheometer (schematic).

The most common type of experiment to determine the linear viscoelastic properties (the storage and loss moduli) of polymers is the small amplitude oscillatory shear test. In this experiment, a sample of material is subjected to a simple shear sinusoidal deformation such that the shear strain is a function of time given by:

$$\gamma(t) = \gamma_0 \sin(\omega t) \qquad \text{eq. 2-20}$$

where γ_0 is the strain amplitude and ω is the frequency. The stress is then measured as a function of time. If the amplitude does not exceed its small linear viscoelastic limit, it can be shown that the shear stress is sinusoidal in time and independent of strain:

$$\sigma(t) = \sigma_0 \sin(\omega t + \delta) \qquad \text{eq. 2-21}$$

where σ_0 is the stress amplitude and δ is a phase shift, or the mechanical loss angle. Using a trigonometric identity, one can rewrite eq. 2-21 in the following form:

$$\sigma(t) = \gamma_0 [G'(\omega)\sin(\omega t) + G''(\omega)\cos(\omega t)] \qquad \text{eq. 2-22}$$

where $G'(\omega)$ is the storage modulus and $G''(\omega)$ is the loss modulus. These two quantities can be calculated from the amplitude ratio, $G_d = \sigma_0/\gamma_0$, and the phase shift, δ, as follows:

$$G' = G_d \cos(\delta) \text{ and } G'' = G_d \sin(\delta) \qquad \text{eq. 2-23}$$

For a parallel plate rheometer, which was used in this work, the equations for calculating the storage and loss moduli in terms of the actual test variables are as follows:

$$G' = \frac{2M_0 h}{\pi R^4 \phi_0}\cos\delta \text{ and } G'' = \frac{2M_0 h}{\pi R^4 \phi_0}\sin\delta \qquad \text{eq. 2-24}$$

where M_0 is the torque amplitude, R is the plate radius, and ϕ_0 is the angular amplitude. The accuracy of the parallel plate rheometer data is typically between 1 and 3%.

Figure 2-7 schematically shows a typical plot of $G'(\omega)$ and $G''(\omega)$ for a polydisperse polymer. At low frequencies, the flow is dominated by the viscous component, and most of the energy is dissipated. As the frequency is decreased further, the $G'(\omega)$ and $G''(\omega)$ curves become straight lines. The storage modulus is proportional to ω^2, while the loss modulus is proportional to ω. In the region of higher frequencies less energy is lost, the elastic component becomes more significant, and $G'(\omega)$ is greater than $G''(\omega)$. The point where the moduli are equal is called the cross-over point, and $1/\omega_c$ is often used as a measure of a material's characteristic relaxation time.

In order to better understand the physical meaning of the storage and loss moduli, it is useful to examine two limiting cases: a Newtonian fluid, which is linear and purely viscous, and a Hookean solid, which is linear and purely elastic. In the case of a Newtonian fluid, G' is zero and G'' equals to $\eta\omega$, where η is the fluid viscosity. The mechanical loss angle is at its maximum, 90°. For a Hookean solid, G' equals to its shear modulus, G'' is zero, and the mechanical loss angle is zero.

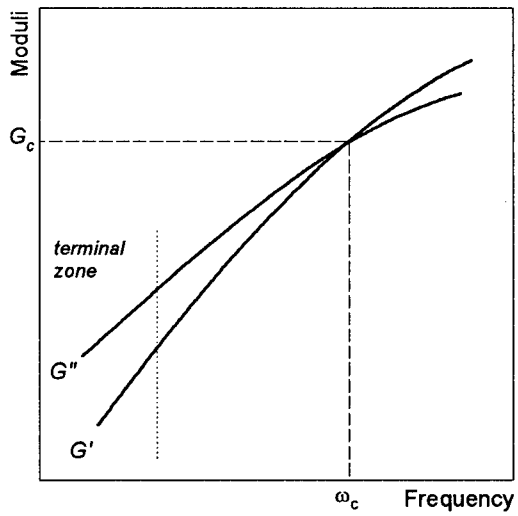

Figure 2-7. Key features of storage and loss moduli.

2.3 Melt fracture and Wall Slip

2.3.1 Melt Fracture

Melt extrusion is one of the most important processes for polymer conversion. When the wall shear stress exceeds a critical value, the polymer either ruptures or detaches from the wall [Vinogradov, 1977]. The term melt fracture was introduced by Tordella (1956) because of the audible tearing noises which accompanied the distortion of the extrudate. The appearance of a melt-fractured extrudate resembles that of a turbulent Newtonian fluid stream, which prompted Vinogradov and Ivanova (1968) to describe the same phenomenon as *elastic turbulence.* Figure 2-8 shows a typical apparent flow curve (wall shear stress versus apparent shear rate) for a linear polyethylene and representative appearances of extrudate distortions. Several different flow regimes can be identified. At low shear rates the extrudates are smooth and the behaviour of the melt resembles that of a Newtonian fluid (region 1) or can be approximated by a power law (region 2). At the first critical stress (σ_{c1} in Figure 2-8), which is typically of the order of 0.1 – 0.2 MPa, the extrudate surface exhibits a small-amplitude, high-frequency periodic distortion. This is generally known as surface melt fracture or *sharkskin.* As the name implies, sharkskin is a roughness that usually modulates the extrudate diameter by no more than 1% and consists of semiregular cracks or grooves that run mainly perpendicular to the flow [Piau *et al.*, 1990; Benbow and Lamb, 1963]. In general, increasing the shear rate further results in other types of distortions. Similar observations have been reported by many investigators, for different materials [Garvey *et al.*, 1942; Tordella, 1969; Ramamurthy, 1986; Kalika and Denn, 1987; Bergem, 1976; and Lin, 1985]. Surface melt fracture (region 3 in Figure 2-8) is accompanied by a change of slope of the apparent flow curve at increasing shear rates. This is mainly due to the effect of slip that causes a decrease in the wall shear stress. Piau and El Kissi (1994) using a photographic technique pointed out that in the case of highly entangled

polymers, the size and spacing of these cracks may be of the same order of magnitude as the diameter of the extrudate. They stated that in this case, it is impossible to define sharkskin as a small-amplitude, high-frequency roughness, and that this definition concerns only a secondary phenomenon, based on observations carried out well downstream of the outflow section and hence after relaxation of the stresses and cracks. Surface melt fracture often manifests itself as a change in the slope of the apparent flow curve [Ramamurthy, 1986] as discussed before.

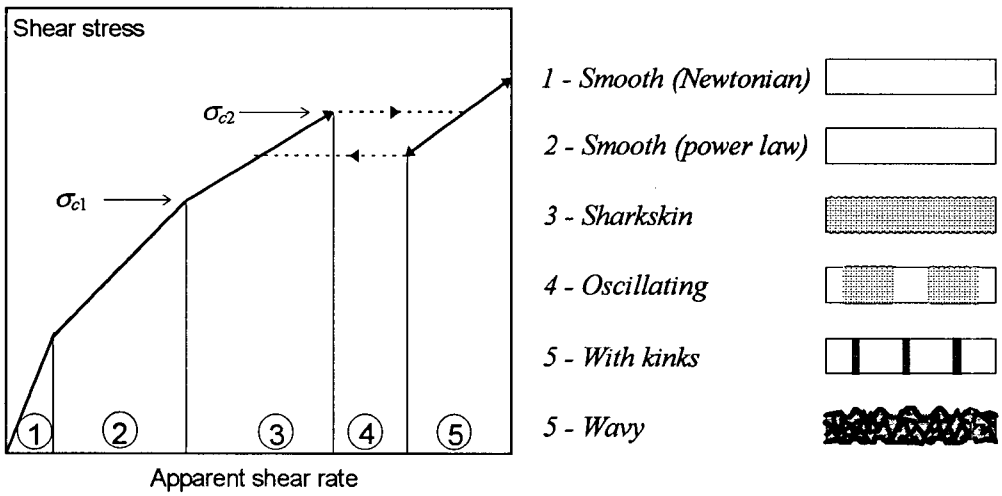

Figure 2-8. A typical apparent flow curve for a linear polyethylene and various forms of extrudate distortion.

For wall shear stresses greater than the second critical shear stress, σ_{c2}, and within a certain range of apparent shear rates, the flow becomes unstable (region 4 in Figure 2-8). Pressure oscillates between two extreme values and alternate smooth and distorted zones appear on the surface of extrudates. In this flow regime a hysteresis loop developes, as can be seen in Figure 2-8. Despite the scatter in the reported values of the second critical shear stress, it is generally accepted that gross melt fracture is a basic characteristic of polymer systems. The greater the molecular weight and the narrower its distribution, the greater the amplitude of the hysteresis

loop. This flow regime is known as *stick-slip*, oscillating melt fracture, or *spurt* flow. The average shear stress remains approximately constant in the stick-slip region. At very high shear rates (region 5 in Figure 2-8), the extrudate surface appears wavy or chaotic (*gross melt fracture*) depending on the type of the material.

Oscillations in pressure drop are not observed for all polymers. Pudjijanto and Denn (1994) as well as Waddon and Keller (1990) found a stable "island" in the stick-slip region of polyethylene, where pressure oscillations stopped, extrusion pressure significantly dropped, and the extrudate became reasonably smooth. This island exists only in a narrow temperature window and a small variation of temperature, e.g. of the order of 1 °C, can interchange oscillations with a stable response. If the shear rate is increased further, a second stable flow regime may be encountered in which the emerging extrudate is smooth again [Tordella, 1969]. This region is generally known as the superextrusion region.

While the origins of extrudate distortions are still in dispute, there is agreement that sharkskin and gross melt fracture are distinguished not only by the appearance of the extrudate, but also by the critical conditions for their onset and by the character of the accompanying flow inside the die. Gross melt fracture occurs when the wall shear stress reaches a critical condition that seems to depend only on the polymeric fluid and little or not at all on the characteristics of the die such as diameter, length, and the material of construction [Kalika and Denn, 1987; Piau *et al.*, 1990]. Sharkskin, on the other hand, does not occur for all polymers [Denn, 1990], and for those for which it does occur, the onset condition has been found to depend on the shape of the outlet region of the die [Piau *et al.*, 1990], the length of the die [Moynihan *et al.*, 1990] and in some cases on the material of construction of the die or the presence of lubricants or sticking agents at the die surface [Ramamurthy, 1986; Hatzikiriakos and Dealy, 1991, 1992b]. Finally, it is generally accepted that sharkskin originates at the die exit [Howells and Benbow, 1962], while

the flow within the die is unsteady only when gross melt fracture occurs [Benbow and Lamb, 1963].

2.3.2 Mechanisms of Melt Fracture

Several mechanisms of melt fracture have been proposed in literature, with the most important being the following:

- die entry effects;
- die exit effects;
- slip at the die wall.

It is commonly accepted that surface melt fracture (sharkskin) is developed at the die exit. The first theory about surface melt fracture (sharkskin) was proposed by Howells and Benbow (1962) and later by Cogswell (1977). They hypothesised that the polymer fractures due to high stretching rates and to high stresses as a result of the abrupt change (shear to free surface flow) in the boundary condition at the exit of the die. Bergem (1976) carried out capillary experiments for different polymers, using a tracer technique. He found that sharkskin arose from a tearing of the melt at the exit of the capillary. Piau *et al.* (1988) showed that cracks on the surface of extrudate always originate at the exit of the die. It should be noted that the existence of localised stresses at the die exit is confirmed by birefringence photographs [Vinogradov and Malkin, 1980]. Kurtz (1992) suggested that two critical conditions are required for sharkskin. First, a critical value of the wall shear stress must be exceeded and, second, the extrudate must be stretched for a sufficient period of time as it leaves the die. Moynihan *et al.* (1990) added to this conclusion that the melt should be first "pre-stressed" critically at the entry region of the die.

Ramamurthy (1986) suggested that the onset of sharkskin was accompanied by the occurrence of wall slip in the capillary. This suggestion is supported by a noticeable slope change in the flow curve at the onset of sharkskin [Kurtz, 1984], which can be interpreted as slip. However, Piau and El Kissi (1992) argued that slip in the die cannot explain the origin of the sharkskin. Hatzikiriakos (1994) carried out numerical simulations of the flow of high density and linear low density polyethylenes under slip conditions and showed that slip is not a necessary condition for the occurrence of the sharkskin phenomenon, although it may affect it. Instead, a critical extension rate at the capillary exit and a critical pre-stress of the polymer at the land region of the die provide the necessary conditions for its occurrence.

Wang *et al.* (1996) speculated that the slope change in the flow curve arises from a combination of interfacial slip and cohesive failure due to chain disentanglement initiated on the die wall in the exit region. Since the disentanglement state is unstable for the adsorbed chains, it is followed by a consequent re-entanglement, thus producing entanglement-disentanglement fluctuations that cause the sharkskin phenomenon. But perhaps the most significant finding made by Wang *et al.* (1996) is that the sharkskin dynamics is in good correlation with chain relaxation processes. They used capillaries of different diameter and measured the period of surface distortions. Regardless of the capillary geometry, the period of distortions was found to be directly proportional to a polymer characteristic relaxation time, which was determined as an inverse of the crossover frequency of the storage and loss moduli.

For the case of gross melt fracture, most authors agree in claiming that, above a certain extrusion rate, the flow upstream of the contraction becomes unstable. These instabilities occur in the form of sudden pulsations, which were confirmed by visualisation [Piau *et al.*, 1990] and birefringence measurements [Tordella, 1969]. They showed that such instabilities started along the upstream flow axis owing to the high elongation stresses that develop in this area. These

instabilities trigger the phenomenon of gross melt fracture, which is often seen in the form of a regular helix oscillating at the same frequency as that of the pulsations of the upstream elongational flow [Piau *et al.*, 1990].

2.3.3 Wall Slip

Ramamurthy (1986) concluded that the assumption of "no-slip" at the wall is not valid for polyethylene melts when the wall shear stress exceeds a critical value (σ_{c1} in Figure 2-8). He reported that the value for LLDPE was in the range of 0.1 – 0.14 MPa, independently of the molecular structure (molecular weight, its distribution, and branching), melt temperature and the capillary design. Deviations from the no-slip boundary condition have been observed by many other workers in the field [Vinogradov *et al.*, 1972; Kraynik and Schowalter, 1981; Lin, 1985; Cohen and Metzner, 1985; Müller-Mohnssen *et al.*, 1987; Hatzikiriakos and Dealy, 1991].

Using the Mooney technique (see Appendix A), Ramamurthy (1986) calculated the slip velocity as a function of wall shear stress. He suggested that the onset of slip occurs at a critical shear stress and is accompanied by both extrudate roughness and a change of slope in the flow curve. Kalika and Denn (1987) assumed a power-law model to describe the rheology of their LLDPE and calculated slip velocities from the deviation of the flow curve from the power-law. As a result of this assumption, they reported slip velocities that were significantly higher than those reported by Ramamurthy.

Kraynik and Schowalter (1981) used a flush-mounted hot-film probe to measure the heat transfer rate between the probe and the wall of a slit. They could distinguish between "stick" and "slip" modes of flow, because the rate of heat transfer from the melt to the probe was different in the two cases. Atwood and Schowalter (1989) also used a hot-film probe to

measure slip during flow of HDPE. They calibrated their sensor at a flow rate for which the no-slip boundary condition was valid. Melt slip velocities were then determined from the departure of the relationship between Nusselt and Peclet numbers for heat transfer from the behaviour expected for a no-slip boundary condition. It is noted that their method requires the solution of the 3-D energy equation. For $\sigma_w > \sigma_c$ their data were correlated as a linear relationship:

$$u_s = D\,(\sigma_w - \sigma_c) \qquad \text{eq. 2-25}$$

where D is a constant, and σ_w and σ_c are the wall shear stress and the critical shear stress, respectively.

More recent experiments using a series of high density polyethylenes proved that this relationship is not linear. Hatzikiriakos and Dealy (1991) have shown that above the critical shear stress of 0.09 MPa the slip velocity follows a power law:

$$u_s = a\sigma_w^m \qquad \text{eq. 2-26}$$

where the coefficient a is an increasing function of temperature, and the exponent m was found to be about 3.35 and independent of temperature.

Müller-Mohnssen *et al.* (1987) directly measured velocity profiles for polyacrylamide solutions using a laser-differential microanemometer and gold particles as tracers. They have found that the increase of the velocity from zero at the wall to the slip velocity u_s occurs within a fluid layer, the width of which is smaller than the spatial resolution of the method employed (0.15 μm). Migler *et al.* (1993) presented the first direct measurement of the flow velocity of a polymer melt within the first 100 nm from the solid wall. It was established that strong slip occurs at the interface for high enough shear rates.

Some other investigations of rheologically complex materials where the authors reported slip, include Mooney and Black (1952), Bagley *et al.* (1958), Tordella (1963), Bartos (1964), Blyler and Hart (1970), Worth *et al.* (1977), Chauffoureaux *et al.* (1979), Knappe and Krumböck (1986), Hatzikiriakos and Dealy (1991), Piau and El Kissi (1994), and Henson and Mackay (1995).

It should be emphasised that the term *slip* in the above discussions is interpreted in a continuum sense, i.e. the length scale over which changes in velocity can be observed is small with respect to the conduit dimensions but large with respect to macromolecular dimensions. True slip occurs when the polymer molecules have a finite velocity next to the solid wall, as opposed to apparent slip when there is a layer of material near the wall with a viscosity lower than the bulk viscosity due to the shear induced disentanglement. Experiments with polymer melts using very small gap spacings, in the order of a few microns [Shidara and Denn, 1993; Henson and Mackay, 1995], validate the true slip model.

2.3.4 Theory of Wall Slip

From the history of classical fluid dynamics one concludes that slip is neither a recent discovery nor a phenomenon confined to the rheology of complex fluids. Daniel Bernoulli, Coulomb, Poiseuille, Girard, Maxwell, and Stokes are among those who considered the possible effects of slip in Newtonian fluid dynamics. For example, the Navier slip law states that

$$\beta u_s = \mu \frac{\partial u}{\partial n}, \qquad \text{eq. 2-27}$$

where β is a constant, u_s is the slip velocity, μ is the fluid viscosity, u is the fluid velocity, and n is a unit vector normal to the wall directed into the fluid. The ratio μ / β can be considered as a "slip length," the distance from the wall into a non-slipping fluid to a position where $u = u_s$.

The physical interpretation of the above law (eq. 2-27) for a flat surface is that the slip velocity is proportional to shear rate at the wall, thus to the shear stress at the wall, σ_w (since from Newton's law of viscosity, $\sigma_w \propto \partial u/\partial n$). However, the existence of wall slip in Newtonian fluid mechanics has not received much attention because the no-slip assumption has led to predictions which agree very well with experimental observations.

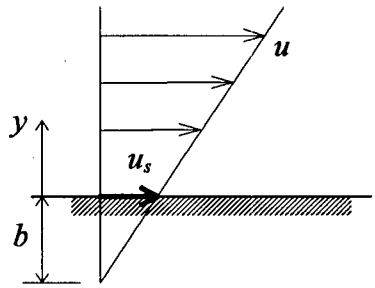

Figure 2-9. de Gennes' extrapolation length.

de Gennes (1979) developed an expression similar to that of Navier for the slip velocity of molten polymers. He extrapolated the velocity profile to zero and from a simple geometry (Figure 2-9) derived the following expression:

$$u_s = b\left.\frac{du}{dy}\right|_{y=0} = b\dot{\gamma}_w, \qquad \text{eq. 2-28}$$

where b is the extrapolation length, which is proportional to M_w^3 within the context of de Gennes' reptation theory [de Gennes, 1979] for the rheology of entangled molecules, and $du/dy|_{y=0}$ is the wall shear rate. For very viscous fluids of high molecular weight, b is large and the slip effects become significant. This theory applies to passive interfaces (no interaction between the fluid and the wall) and low shear rates. Experimental results show that slip is present for entangled polymer melts at these conditions [Burton *et al.*, 1983; White *et al.*, 1991; Migler *et al.*, 1993]. The theory of de Gennes was extended by Brochard and de Gennes (1992) for the case of adsorbing surfaces, where the slip effects are dramatically reduced and there appears to exist a critical stress for transition from weak to strong slip. This theoretical prediction was also confirmed experimentally by Migler *et al.* (1993, 1994).

In summary, all molten polymers slip no matter how small shear stresses they are subjected to, according to de Gennes' theory and experiments by Migler *et al.* (1993). However, these rates and stresses are very small to be of interest from an engineering point of view, as most polymer processing operations involve very high shear rates. It should be stressed that the methods generally used in engineering practice are not sensitive enough to detect the small effects discussed by de Gennes. For practical applications it is important to distinguish between the following three regimes (Figure 2-8): no slip for $\sigma_w < \sigma_{c1}$, weak slip for $\sigma_{c1} < \sigma_w < \sigma_{c2}$ and strong slip (plug flow) for $\sigma_w > \sigma_{c2}$. Accordingly, several models based on this point of view have been developed.

Based on the stick-slip assumption, Lau and Schowalter (1986) correlated the experimental data obtained by Vinogradov and Ivanova (1968) for a polyethylene/polypropylene blend at several temperatures. They have shown that, at a given temperature, the following power-law equation relating the wall slip velocity to the wall shear stress, is applicable:

$$u_s = c_1 \sigma_w^n \left[1 - c_2 \tanh\left(\frac{E - c_3 \sigma_w}{kT} \right) \right] \qquad \text{eq. 2-29}$$

where u_s is the slip velocity, σ_w is the wall shear stress, E is the activation energy associated with the detachment or the reattachment of a macromolecule from the wall, and c_1, c_2, c_3 and n are constants that depend on the nature of the melt.

Assuming that flow instabilities are associated with an adhesive failure between the melt and the die wall, Hill *et al.* (1990) have developed a framework based on the theory of elastomer adhesion. The theory permits a connection between the rate at which new interfacial area is created, i.e., during the peel test of the rubbery polymer under a constant applied force, and the critical stress and slip velocity of the molten polymer. The rheology of the bulk fluid was used

to represent the stored elastic energy. In addition, the pressure and temperature effects on the slip velocity are incorporated into their theory through the linear viscoelastic shift factor. The developed expression is as follows:

$$u_s = \frac{k}{a_T}\sigma_w^n \exp\left(-\beta\frac{4L}{D}\sigma_w\right) \qquad \text{eq. 2-30}$$

where k is proportional to the reciprocal of the surface work of adhesion, and to a length scale; a_T is the temperature-dependent viscoelastic shift factor; β is the pressure coefficient of viscosity; while L and D are the length and diameter of the capillary, respectively. Their prediction of the critical stress is rather good, as is the dependence of the critical stress on surface energy.

Stewart (1993) has formulated a theory of slip which combines features of the Hill's equation and kinetic adsorption/desorption analysis first proposed by Lau and Schowalter (1986). The major addition is a geometric-mean approximation for the work of adhesion to incorporate the surface tensions of the polymer and presumed coating layers explicitly. The agreement of the prediction of his theory with the data of both Kalika and Denn (1987) and Hatzikiriakos and Dealy (1991) is quite promising.

By adapting Eyring's theory of liquid viscosity for the special case of a polymer/wall interface, Hatzikiriakos (1993) has developed the following model which gives the slip velocity as a function of wall shear stress, temperature, pressure, work of adhesion and the molecular characteristics of a polymer:

$$u_s = \frac{2\alpha kT}{Nh} e^{-\frac{\Delta G_0}{RT}} \sinh\frac{\frac{\alpha}{\delta}\frac{\sigma_w\tilde{v}}{2} - \frac{fW_{adh}\tilde{v}}{\delta}}{RT} \qquad \text{eq. 2-31}$$

where α and δ are the projections of the radius of gyration of the molecule in the directions parallel and normal to the flow, N is the number of entanglements (= M_w / M_e), h is Planck's constant, G_0 is the free energy at equilibrium, $\tilde{v}$ is the molar volume, and f denotes some fraction of the work of adhesion W_{adh}. The model agrees well with the slip data for linear polyethylenes on steel surfaces and on steel surfaces treated with processing aids. Most importantly, it provides for a smooth transition from no-slip to slip flow at the critical stress.

Other slip velocity models have been reported by El Kissi and Piau (1989) and Leonov (1990). These and the above discussed slip models are "static", because they assume that the slip velocity is only a function of the instantaneous value of the wall shear stress. The observed instabilities in polymer extrusion, and the significant deviations of the stress response from sinusoidal shape in oscillatory shear flow, however, suggest that slip (and reattachment) occur via a relaxation process. In particular, hysteresis phenomena have been observed in dynamic experiments when elastomers slide over metal surfaces. Vinogradov *et al.* (1972) studied slip in melts and interpreted the results in terms of a "forced high elastic state" that facilitates slip at high shear stresses. The behaviour of melts at high rates of deformation thus may resemble that of elastomers, and a dynamic slip model might account for the hysteresis effects.

2.3.5 Slip in transient shear flows

Motivated to overcome the aforementioned limitation of the static models, Pearson and Petrie (1968) introduced a "memory slip model," which in differential form is:

$$u_s + \lambda_s \dot{u}_s = \phi(\sigma_w). \qquad \text{eq. 2-32}$$

The model assumes that the slip velocity is a functional of the history of the shear stress, with a slip relaxation time of λ_s.

Yoshimura and Prud'homme (1988) have presented an analysis of the slip effects on the dynamic response of oscillatory shear experiments. They have shown that even with a simple viscoelastic model (Kelvin-Voigt), the introduction of a dynamic slip model similar to eq. 2-32 results in non-linear, non-symmetric stress waveforms, resembling those they have observed in their experimental measurements [Yoshimura and Prud'homme, 1987].

Lim and Schowalter (1989) suggested that the transition from the slip to the stick condition in the oscillating flow region of the flow curve was gradual and showed characteristics of a relaxation process. They also reported that the relaxation time for this process was a decreasing function of shear rate. To incorporate such a relaxation process into a dynamic slip model that is also consistent with steady-state observations, Hatzikiriakos and Dealy (1991) proposed the following relationship:

$$u_s + \lambda_s \frac{du_s}{dt} = a\sigma_w^n \qquad \text{eq. 2-33}$$

where λ_s is a "slip relaxation time." They have studied the validity of this equation and estimated the parameter λ_s by observing slip in exponential shear experiments.

Adrian and Giacomin (1994) have studied molten polyurethane in large amplitude oscillatory shear (LAOS) under conditions outside the no-slip envelope. They found that the stress response was quasi-periodic and suggested that this can be explained by a slip boundary condition. Jeyaseelan and Giacomin (1994) have used a transient network theory to simulate the LAOS behaviour of a high-density polyethylene melt. They have shown that a steady slip model (eq. 2-33 with λ_s=0) cannot adequately describe the instabilities observed experimentally.

A stochastic dynamic slip model has been developed by Hatzikiriakos and Kalogerakis (1994), in which the slip phenomenon was considered as a stochastic process where the polymer

segments, modelled as Hookean springs, break off the wall due to the excessive tension imposed by the bulk fluid motion. This probabilistic, time-dependent model made it possible to calculate dynamic slip velocities which qualitatively agreed with the available experimental data. Hatzikiriakos (1995) has extended the model and developed a multimode interfacial constitutive equation, in order to obtain a better quantitative description of the slip dynamics. The polymer melt was considered as a network of different types of polymer segments, and the Hookean springs were allowed to have different relaxation times. It must be noted that these two network models, involving stochastic simulations, as well as the transient network model of Jeyaseelan and Giacomin (1994), are more complex and computationally demanding.

Graham (1995) related complicated non-periodic responses of polymer melts in LAOS experiments to the wall slip. The results of his theoretical and computational studies indicate that both fluid elasticity and a dynamic model for the wall slip are necessary for non-periodic dynamics to occur. The importance of dynamic slip in oscillatory shear suggests that these dynamics may play a major role in the stability and dynamics of other flows where slip and unsteadiness are important.

As an example of a transient shear experiment, Figure 2-10 illustrates the difference between static and dynamic slip models. A sliding plate rheometer was used to obtain the shear stress response as a function of time during the start-up of a steady-shear experiment. The experimental data points were obtained for Sclair 56B high-density polyethylene [Hatzikiriakos, 1991], and the dynamic slip model is based on eq. 2-33 coupled with Wagner's constitutive equation (see Appendix C) to describe the rheology of the melt. It can be seen that the no-slip assumption results in a large overshoot and an incorrect prediction of the steady-state value of the wall shear stress; the static model predicts the steady-state value, but the magnitude of the

overshoot is too small; finally, the dynamic model with a single relaxation time gives the correct steady-state stress and the overshoot, but fails to match the timing of the overshoot.

The above example shows that even for a simple experiment such as the start-up of steady shear, a single-mode slip model cannot simulate the experimental data quantitatively. This makes obvious the need for a multimode interfacial slip model which would be able to describe correctly the data from various rheological experiments. In addition, more experimental evidence on the dynamic behaviour of polymer melts is needed, i.e. other deformation histories such as exponential shear and large amplitude oscillatory shear.

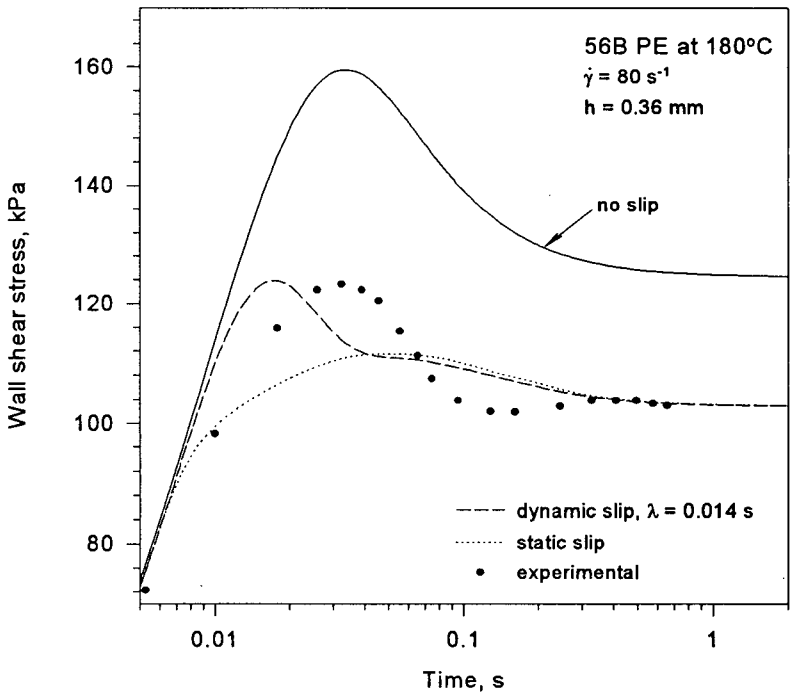

Figure 2-10. Comparison of experimental data for a high-density polyethylene and predictions of the Wagner model for different slip models (no-slip, static, dynamic).

2.4 Factors Affecting Polymer Flow

2.4.1 Pressure effects

The presence of large pressure gradients are typical in the processing of molten polymers. The compressibility of these materials in a molten state is quite high, and the effect of pressure on the viscosity cannot be neglected. It is known from experiments [Rauwendaal and Fernandez, 1985; Kalika and Denn, 1987] that the apparent flow curves do not superpose for capillaries of different L/D ratios. Instead, the apparent flow curves shift to higher values of the wall shear stress with increase of the L/D ratio and therefore, pressure. The pressure dependence of viscosity is typically represented by an exponential function (first order approximation) which for a given temperature can be written as

$$\eta = \eta^0 \exp(\alpha P) \qquad \text{eq. 2-34}$$

where η^0 is the viscosity at ambient pressure, α is the pressure coefficient of viscosity and P is the absolute pressure.

Because pressure increases the viscosity of polymers, it results in the formation of a "pre-stress zone" at the die entrance. It has been argued [Mounihan, 1990] that gross melt fracture occurs in the entrance region where a material attains its highest wall shear stress.

It has been proven that pressure has also an effect on the slip velocity. Hatzikiriakos and Dealy (1992a) studied the slip behaviour of several high density polyethylene blends at various pressures and temperatures. They have found that the slip velocity decreases with increase in pressure and this effect saturates at very high pressures. Therefore, as the pressure drops along the capillary, the slip velocity increases and the fluid accelerates near the exit of the capillary. This gives rise to a high extensional rate, which may be the primary cause of the surface melt fracture [Hatzikiriakos, 1994].

2.4.2 Temperature effects – time-temperature superposition

Rheological properties usually depend on temperature. This means that to obtain a complete picture of the behaviour, experiments must be carried out at several temperatures. It is often found that rheological data measured at several temperatures can be brought together on a single master curve by means of "time-temperature superposition." This greatly simplifies the description of the effect of temperature. Furthermore, it makes possible the display on a single curve of material behaviour covering a much broader range of time or frequency than can ever be measured at a single temperature. Materials whose behaviour can be displayed in this way are said to be "thermorheologically simple" [Dealy and Wissbrun, 1990].

It was found that data for different temperatures can often be superposed by introducing a shift factor, a_T, determined empirically. Thus, if one makes a plot of a rheological property versus time, a_T is obtained from the horizontal shift necessary to bring the data for any temperature T onto the same curve as data for temperature T_0. For example, flow curves (shear stress vs. shear rate) will be plotted as shear stress versus $\dot{\gamma}\, a_T$. Note that no shift factor is required for quantities containing no units of time. This implies that a plot of such a quantity versus another, both containing no units of time, will be temperature independent.

The shift factor is a function of temperature, and the WLF equation has been found useful [Ferry, 1980]:

$$\log(a_T) = \frac{-C_1^0(T - T_0)}{C_2^0 + (T - T_0)} \qquad \text{eq. 2-35}$$

where C_1^0 and C_2^0 are constants determined at T_0 for each material. This equation holds at temperatures very close to glass transition temperature, T_g. At temperatures at least 100 K above T_g, an empirical relationship, the Arrhenius equation, was found to be valid:

$$\log(a_T) = \frac{E_a}{R}\left(\frac{1}{T} - \frac{1}{T_{ref}}\right) \qquad \text{eq. 2-36}$$

where E_a is the flow activation energy, R is the gas constant, and T_{ref} is the reference temperature. Since polyethylenes are processed at temperatures much higher than T_g, this equation is often used by rheologists.

2.4.3 Viscous heating

In high speed processing operations, such as extrusion, viscous heating is inevitable. This is because of the high viscosity of the polymeric liquids that are subjected to large deformation gradients. Moreover, due to the low thermal conductivity of polymers, temperature increases are considerable and non-uniform. A reliable estimation of viscous heating effects and local temperatures is of particular interest in polymer flow problems because of their strong influence on the properties of polymers, such as viscosity and rate of chemical degradation.

Cox and Macosco (1974) observed large temperature rises in capillary extrusion of acrylonitrile butadiene styrene (ABS) which can be as high as 70 K for apparent shear rates of the order of 10^4 s^{-1}. Shidara and Denn (1993) have discussed the effect of viscous heating for a molten polystyrene in slit extrusion. To explain their results they assessed this effect to be significant. They also pointed out that a numerical solution of the full field in capillary/slit flow incorporating pressure and temperature effects is needed. One normally expects that the effect of viscous heating is less significant for high density polyethylene, and increases in significance

for linear low density polyethylene, polypropylene and polystyrene respectively. This can be determined by examining the values of the temperature-dependency coefficient of viscosity [Van Krevelen, 1991].

A review of approximate analytical solutions to the flow of power-law fluids in circular channels with viscous heating is given by Bird *et al.* (1987). These are series solutions that exist for certain values of the power-law constant (eq. 2-7) and constant values of thermophysical properties. In order to assess viscous heating effects, it is necessary to assume appropriate boundary conditions at the wall of the capillary. Two limiting cases are usually considered. In the isothermal case, the wall is assumed to be at a uniform temperature, and in the adiabatic case, it is assumed that there is no heat transfer at the wall. In the first case, the temperature profile asymptotically reaches a fully developed profile, while in the second case a continuous, infinite temperature rise is predicted for a infinitely long capillary. The real conditions in the extrusion of polymer melts are somewhere between these limiting cases. It is also important to note that, according to these solutions, the temperature rise is higher for longer capillaries and for those having a larger diameter. Thus, length and diameter of capillaries or length and height of slits are important parameters.

3. OBJECTIVES

The primary objective of this work is to study the origins of extrudate distortion in the extrusion of molten polymers. Due to the fact that melt fracture of many polymeric materials (e.g. linear low-density polyethylene) is accompanied by wall slip, special attention is to be placed on its study.

The objectives can be summarised as follows:

- Develop a method for analysing large-amplitude oscillatory shear data with the purpose of distinguishing various molecular relaxation processes. Prove its applicability using several polymeric systems.
- Determine the critical conditions for the onset of wall slip and melt fracture of linear low-density polyethylene as a function of key molecular characteristics, i.e. weight average molecular weight and molecular weight distribution. Identify possible correlations between these critical conditions and the rheological and processing properties of the selected materials. Finally, identify ways to improve the melt fracture performance of that group of resins.
- Study the rheology and processing of metallocene polyethylenes incorporating small amounts of long chain branching. Assess the effects of long chain branching on the rheological and processing behaviour of this type of polymer.
- Develop a dynamic slip velocity model by employing the notion of multiple relaxation times. Incorporate the improved slip model into one of the non-linear viscoelastic constitutive models and compare the predicted values with those observed experimentally in simple shear flows.

- Build an experimental apparatus and develop a method that allows visual observation the flow of molten polymers in a capillary at high shear stresses and temperatures. Determine velocity profiles in a transparent capillary by using laser-speckle photography. Furthermore, visualise the flow patterns developed at the entrance of the capillary for a virgin polymer and polymer incorporating processing aids. Identify mechanisms for elimination of melt fracture by observing the differences in the flow patterns in the case when processing aids are used.

3.1 How the thesis is organised

In this work, the melt fracture and wall slip phenomena were approached from several different perspectives. Chapter 4 presents a new way of analysing and interpreting experimental rheological data obtained using large-amplitude oscillatory shear (LAOS) experiments. The proposed LAOS data analysis method provides a closer examination of the complexity of the relaxation processes undergone by polymer melts subjected to large deformations. These relaxation processes, as shown in Chapter 5, play an important role in the melt fracture performance, and the LAOS analysis has a potential to become a useful tool in polymer rheological characterisation.

Chapter 5 studies the effects of molecular weight and its distribution on the rheological and processing behaviour of molten linear low-density polyethylenes. Two sets of specially chosen polyethylene resins made it possible to separate the effects of molecular weight from the effects of molecular weight distribution.

Chapter 6 examines an unusual interfacial phenomenon in the capillary extrusion of two metallocene polyethylene resins that incorporate small levels of long chain branching. Based on the previous reports found in literature and the findings of this work, a qualitative model for the mechanism of wall slip is presented.

In Chapter 7, a dynamic slip model is proposed in order to improve the predictions of a non-linear shear flow model. A non-linear viscoelastic constitutive model, namely Wagner's equation, was coupled with a multimode slip model and its predictions are compared with large-amplitude oscillatory data.

Finally, Chapter 8 describes flow visualisation experiments performed using a quartz capillary and laser-speckle technique. A number of photographs are included showing the flow patterns both in the capillary and near its entrance.

Some of the material included in the thesis has already been published.

Chapter 5:

Kazatchkov, I. B., Bohnet, N., Goyal, S.K., Hatzikiriakos, S.G., *Influence of molecular structure on the rheological and processing behaviour of polyethylene resins*. Paper accepted for publication in Polym. Eng. Sci. (1998).

Goyal, S. K., Kazatchkov, I. B., Bohnet, N., Hatzikiriakos, S. G., *Influence of Molecular Weight Distribution on the Rheological Behaviour of LLDPE Resins*: Soc. Plastics Eng'rs, ANTEC '97 Tech. Papers, **43**, Toronto, April 1997.

Chapter 6:

Hatzikiriakos, S. G., Kazatchkov, I. B., Vlassopoulos, D., *Interfacial Phenomena in the Capillary Extrusion of Single Site Catalyst Technology Polyethylenes*. J. Rheol., **41**, 1299-1316 (1997).

Chapter 7:

Kazatchkov, I. B., Hatzikiriakos, S. G., *Dynamic Interfacial Behaviour of a Linear Low Density Polyethylene*. Proceedings of the 12th International Congress of Rheology, pp. 29-30, Québec city, August 1996.

4. LARGE AMPLITUDE OSCILLATORY SHEAR IN POLYMER CHARACTERISATION

– EXECUTIVE SUMMARY –

■

Non-linear rheological experiments are not frequently used in industrial product characterisation

■

The proposed new method of interpreting data obtained from a sliding plate rheometer in large amplitude oscillatory shear has several advantages:

– Provides valuable non-linear data

– Easy set-up and data analysis

– Allows the determination of damping function, thereby providing an alternative method to the more difficult-to-run step-strain experiment

4.1 Introduction

Industrial polymer characterisation laboratories employ several types of rheological tests. The most common of these include capillary rheometer tests, linear viscoelastic dynamic tests using parallel plate and cone-and-plate rheometers and melt index tests. However apart from the absolute viscosity curve, none of them allow determination of non-linear rheological properties. For example, the capillary data can be used to determine the viscosity, although the data themselves suffer from end and pressure effects. Melt index data are very subjective and often confusing, while linear dynamic tests, as the name suggests, do not involve any non-linearity.

The advent of a sliding plate rheometer with a flush-mounted stress transducer [Giacomin, 1987] made it possible to accurately measure several steady-state and dynamic rheological polymer properties in the non-linear viscoelastic regime. This chapter deals with one such test, namely, the large amplitude oscillatory shear (LAOS) test. The method itself is not new. It has been mentioned many times in literature [Dealy and Wissbrun, 1990; Giacomin and Oakley, 1993; Graham, 1995]. Nevertheless, it has not been used extensively due to the lack of a systematic method of interpreting the data and due to the lack of convincing examples of its usefulness. The proposed procedure outlined below for analysing LAOS data aims to fill this gap.

4.2 Background

4.2.1 Linear Viscoelasticity and Small-Amplitude Oscillatory Shear

Linear viscoelasticity is the simplest type of viscoelastic behaviour. When the deformation and the rate of deformation imposed on a sample of material are sufficiently small (usually not exceeding 30–40% and 0.01 s^{-1}, respectively), the molecules are disturbed from their equilibrium

configuration and entanglement state to a negligible extent [Dealy and Wissbrun, 1990]. Under these conditions, all material properties of the viscoelastic fluid are independent of the imposed strain magnitude. For example, if a sample is suddenly deformed to a strain γ_0 (simple shear, see Figure 2-3) and the resulting shear stress is measured as a function of time, the stress is directly proportional to the strain, i.e.:

$$\sigma(t) = G(t)\gamma_0 \qquad \text{eq. 4-1}$$

where $G(t)$ is the shear relaxation modulus.

Small amplitude oscillatory shear is the type of experiment most widely used to determine the linear viscoelastic properties of polymeric fluids [Dealy and Wissbrun, 1990]. In this experiment, a flat sample of material is subjected to a simple shearing deformation, in which the shear strain changes in time according to the following relation:

$$\gamma(t) = \gamma_0 \sin(\omega t) \qquad \text{eq. 4-2}$$

where γ_0 is the strain amplitude and ω is the frequency.

For sufficiently small γ_0 and ω, within the linear viscoelastic regime, it turns out that the stress as a function of time can be written as:

$$\sigma(t) = \sigma_0 \sin(\omega t + \delta) \qquad \text{eq. 4-3}$$

where σ_0 is the stress amplitude, and δ is the phase shift of stress from strain. In terms of the storage (G') and loss (G'') moduli (see section 2.2.4 for their definitions), eq. 4-3 can be written as follows:

$$\sigma(t) = \gamma_0 [G'(\omega)\sin(\omega t) + G''(\omega)\cos(\omega t)] \qquad \text{eq. 4-4}$$

4.2.2 Non-linear Viscoelasticity and Large-Amplitude Oscillatory Shear

Large amplitude oscillatory shear is advantageous over other types of non-linear experiments such as step strain, start-up and creep in the sense that it does not require a sudden change in displacement, velocity or load. It is therefore well suited for sliding plate rheometers, or other types of rheometers involving mechanical parts with high mass inertia. Furthermore, it allows the independent variation of two test parameters, the deformation amplitude and the time scale (1/frequency), thus giving the experimenter more flexibility and control over the test conditions. This also generates a variety of deformations that subject the material to testing at various time scales.

In large amplitude oscillatory shear, a polymer sample is subjected to a sinusoidal deformation with an amplitude exceeding that used in linear viscoelasticity, i.e., the strain amplitude is typically above 40%. The strain is described by the same function as in the linear oscillatory test (eq. 4-2). However, the response of the material is no longer independent of the strain amplitude. Also, the resulting shear stress response is no longer sinusoidal but turns out to be a superposition of odd-numbered harmonics of the base frequency, i.e.:

$$\sigma(t) = \sum_{\substack{n=1 \\ n \text{ odd}}} \sigma_n \sin(n\omega t + \delta_n) \qquad \text{eq. 4-5}$$

where σ_n is the amplitude of the n-th harmonic, and δ_n is the phase shift (relative to the strain) of that harmonic. This complex shear stress response is due to non-linear viscoelastic properties of polymer melts. It is noted that wall slip can cause distortion of the shear stress response, and that in order to avoid this effect, the shear stress has to be less than the critical value for the onset of slip.

In terms of storage and loss moduli, eq. 4-5 can be written as

$$\sigma(t) = \gamma_0 \sum_{\substack{n=1 \\ n \text{ odd}}} [G'_n(\gamma_0, \omega)\sin(n\omega t) + G''_n(\gamma_0, \omega)\cos(n\omega t)] \qquad \text{eq. 4-6}$$

where G'_n and G''_n are respectively the storage and loss moduli of the n-th harmonic.

In order to better understand the physical significance of these higher harmonics, the following comparison is relevant. Human beings communicate to each other using voice and, by listening to the sound of a particular person's voice, they are able to recognise it and distinguish it from millions of other voices. It is all due to the fact that a human voice does not consist of a single frequency sound wave (otherwise it would sound like computer-generated voices in the 1960s science fiction thrillers), but of a whole array of different frequencies (also known as overtones), each having its own amplitude.

Applying this analogy to the LAOS experiments, one can say that the complex shear stress response of a particular polymer sample is its unique, characteristic "voice". By compiling the complex non-linear LAOS data as a function of strain amplitude and frequency, we can create a three-dimensional image of that "voice". However it remains to be seen how such 3-D "images" can be suitably used.

4.3 Experimental

4.3.1 Materials

Materials included linear low-density polyethylene, polyisobutylene (PIB) and a styrene-maleic anhydrite/polymethylmethacrylate (SMA/PMMA, 1:1) blend.

Two series of LLDPE resins, one having nearly constant M_w and different MWD, and the other series having nearly constant MWD and different M_w, were studied. Both series had

about the same degree of short chain branching. The molecular characteristics of the resins (measured at NOVA Chemicals) are summarised in Table 4-1 (Series 1) and Table 4-2 (Series 2). The values of the flow activation energy are also reported (see section 5.4.1 for details).

The PIB sample was supplied by Exxon Chemical Co. under the trade name Vistanex MML-80. It has a density of 0.92 g/cm^3, viscosity molecular weight (M_s) of 80,000 g/mol and viscosity-average molecular weight (M_v) of 1,000,000 g/mol.

Table 4-1. Table 1: Molecular Weight Characteristics of LLDPE Samples – Series 1

Sample	Weight Average Molecular Weight (M_w)	Polydispersity (PD)	Flow Activation Energy (E_a/R), K
Blend 1	111,100	3.3	3098
Blend 2	109,000	4.5	3528
Blend 3	104,900	6.6	3701
Blend 4	100,800	8.6	4079
Blend 5	98,700	9.6	4176
Blend 6	96,600	10.4	4240
Blend 7	94,600	11.3	4303
Blend 8	92,500	12.1	4350
Blend 9	90,400	12.7	4388

Table 4-2. Table 1: Molecular Weight Characteristics of LLDPE Samples – Series 2

Sample (Melt Index)	Weight Average Molecular Weight (M_w)	Polydispersity (PD)	Flow Activation Energy (E_a/R), K
MI = 0.76	110,000	3.9	1632
MI = 1.0	99,000	3.8	2477
MI = 2.1	87,000	3.8	2843
MI = 3.1	78,000	3.5	3060
MI = 5.6	66,000	3.9	3287
MI = 19.2	51,000	4.5	3507

The studied SMA/PMMA blend consisted of equal parts of styrene-maleic anhydrite and polymethylmethacrylate blended in a twin screw extruder at about 210 °C. SMA is a random copolymer of styrene and 32% by weight maleic anhydride. PMMA contained 10%

copolymerised ethyl acrylate, 0.75% lubricating agent and 0.25% each of thermal and UV stabilisers. The melt-blended samples were dehydrated in vacuum at 80 °C for several hours. The resulting blend showed no signs of degradation or phase separation after these procedures [Chopra *et al.*, 1997].

4.3.2 Sample Preparation, Series 1

Nine samples having similar average molecular weights and densities, but different polydispersities were prepared by melt blending two commercial LLDPE resins (butene copolymers) in different proportions. The original resins had an essentially constant weight average molecular weight of 100,000 ± 10% g/mol (melt flow index I_2 = 0.8 dg/min) and a density of 0.920 g/cm^3. Their polydispersities (M_w/M_n) were very different, namely 3.3 and 12.7, respectively. A Brabender twin screw extruder (Type 15-30-000-CTSE) equipped with counter-rotating mixing screws, a water cooling bath and a pelletiser was used for the blend preparations. The extrusion was conducted at a screw speed of 100 rpm and output rates of up to 3.5 kg/hr. The two original samples were also extruded through the same extruder to provide the virgin resins with a similar thermo-mechanical history as that of the blended samples. Figure Figure 4-1a shows the molecular weight distribution profiles for the resins belonging to Series 1 (constant M_w). As can be seen from the figure, these resins had quite different molecular weight distributions, but similar weight average molecular weights.

4.3.3 Sample Preparation, Series 2

Six different commercial pelletised polyethylene resins (butene copolymers) with weight average molecular weights ranging from 51,000 to 110,000 g/mol were selected for testing. They had

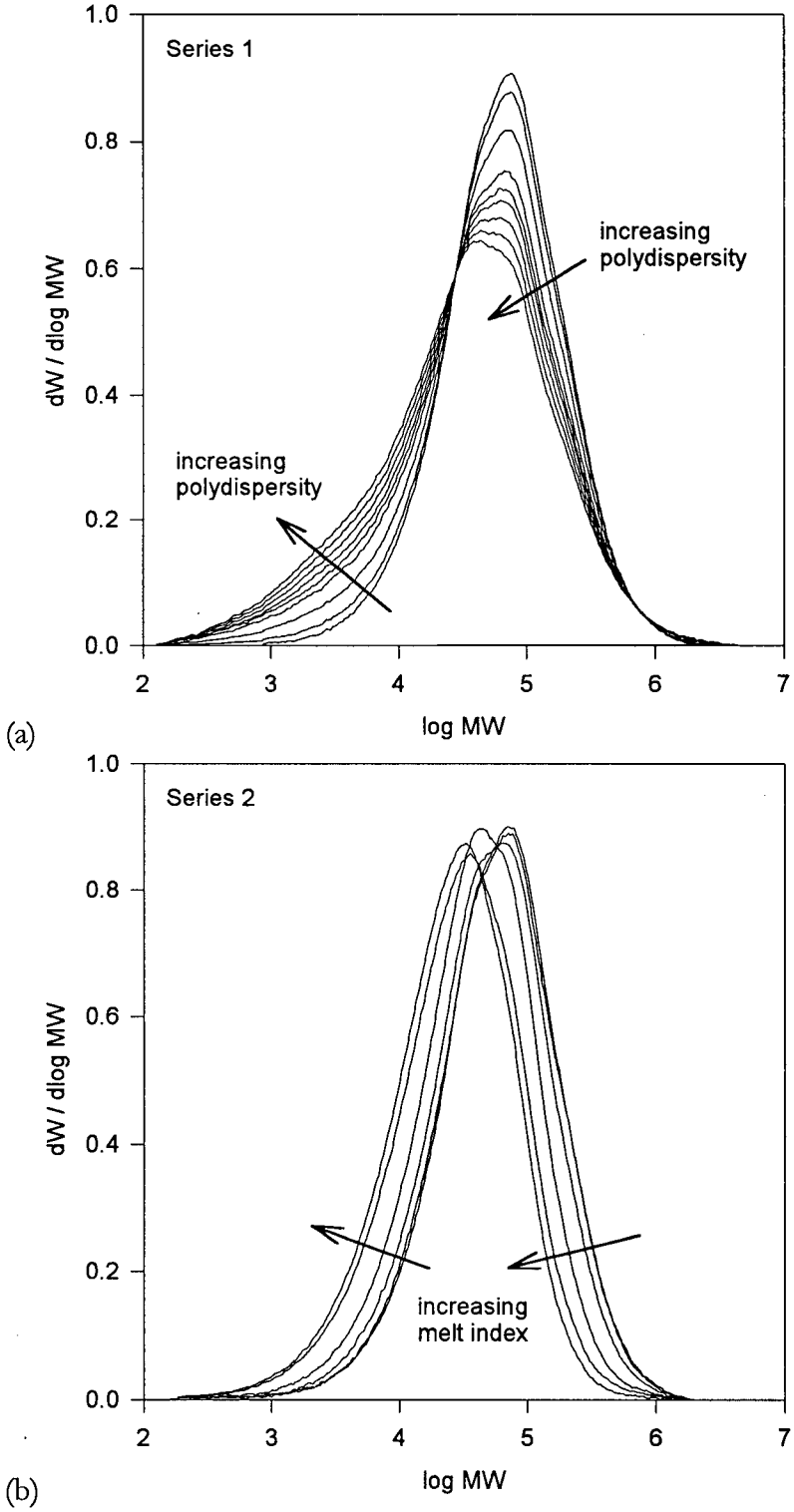

Figure 4-1. (a) Molecular weight distribution profiles for LLDPE samples in Series 1 (same molecular weight and varying polydispersity). (b) Molecular weight distribution profiles for LLDPE samples in Series 2 (same polydispersity and varying molecular weight).

nearly constant densities (0.925 ±0.005 g/cm^3) and polydispersities. Figure 4-1b plots the molecular weight distributions of the resins in this series. As can be seen, all resins had similar molecular weight distribution profiles (similar polydispersity), but shifted along the molecular weight axis.

4.3.4 Small-Amplitude Oscillatory Shear Tests

A Rheometrics System 4 parallel plate rheometer was used to measure the dynamic moduli of all polymers. Experiments were performed with a 0.8 mm gap between the plates at different temperatures in the range of 160 to 220 °C. Application of the time-temperature superposition principle resulted in G', G'' data over a wide range of frequencies.

4.3.5 Large-Amplitude Oscillatory Shear Tests

An Interlaken sliding plate rheometer with a 0.5 mm gap between the plates was used to perform the LAOS experiments. Each run consisted of a series of oscillations having the same strain amplitude and different frequency. Subsequent runs had the same frequencies, but a different strain amplitude. There were 3-minute pauses between them, to allow the polymer chains to relax. The ranges of strain amplitudes and frequencies, which would result in physically meaningful data were governed by the considerations summarised in Table 4-3.

In view of these constraints, the test conditions were typically limited to the following:

- Strain amplitude: 1 to 10;
- Frequency: 0.01 to 10 Hz (0.06 to 60 rad/s).

Table 4-3. Factors limiting the ranges of strain amplitudes and frequencies.

Lower limit on strain amplitude	Rheometer's noise-to-signal ratio Need to stay in the non-linear regime
Upper limit on strain amplitude	Sample break-up Stress transducer limit of 300 kPa
Lower limit on frequency	Sample degradation as the test time increased Accuracy of the hydraulic actuator motion
Upper limit on frequency	Sliding plate mass inertia

For each combination of amplitude and frequency, the rheometer was programmed to produce 7 cycles. The data collection started on the 3rd cycle and continued over 3 cycles, resulting in 60 data points (20 per cycle). This was done in order to accommodate the 20-point discrete Fourier transform method, described in detail below.

4.4 Raw Data

As an example of the raw data that are obtained directly from the sliding plate rheometer, Figure 4-2 illustrates the stress response obtained for the Blend 9 (Series 1) polyethylene. In the first two graphs (i.e., where the strain amplitude, γ_0, equals 1), the stress shows a pure sinusoidal response. This suggests that the response is within the linear viscoelastic regime. Increasing γ_0 to 5 and 20 results in distortions of the sine wave. This can be seen by the smoothed peaks and by their loss of symmetry (the left slope of the peaks is steeper than their right slope). However, it is quite difficult to determine the extent of deviation from linearity by looking at shear stress versus time plots.

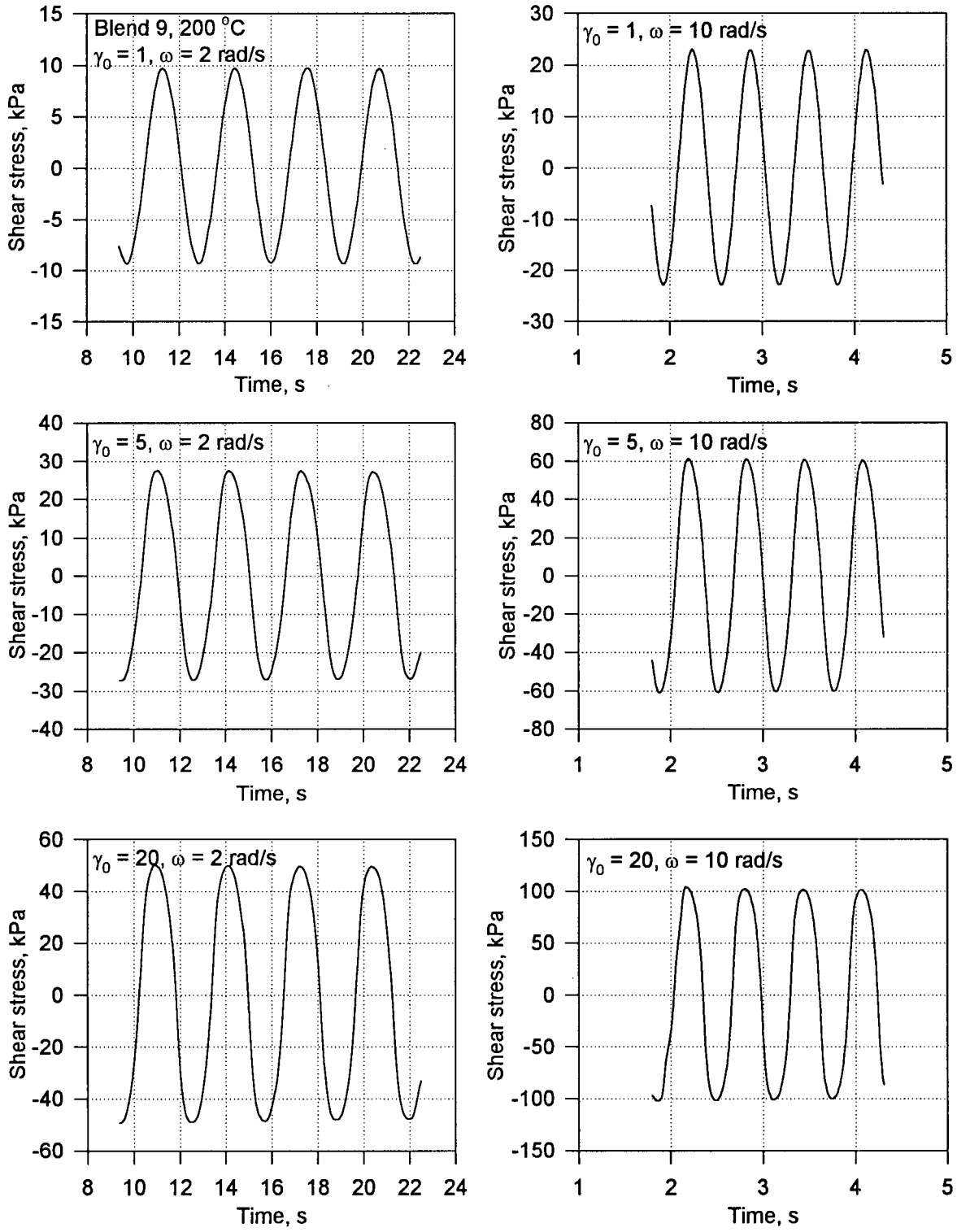

Figure 4-2. Raw LAOS data for Blend 9 at 200 °C obtained at strain amplitudes of 1, 5 and 20, and frequencies of 2 and 10 rad/s.

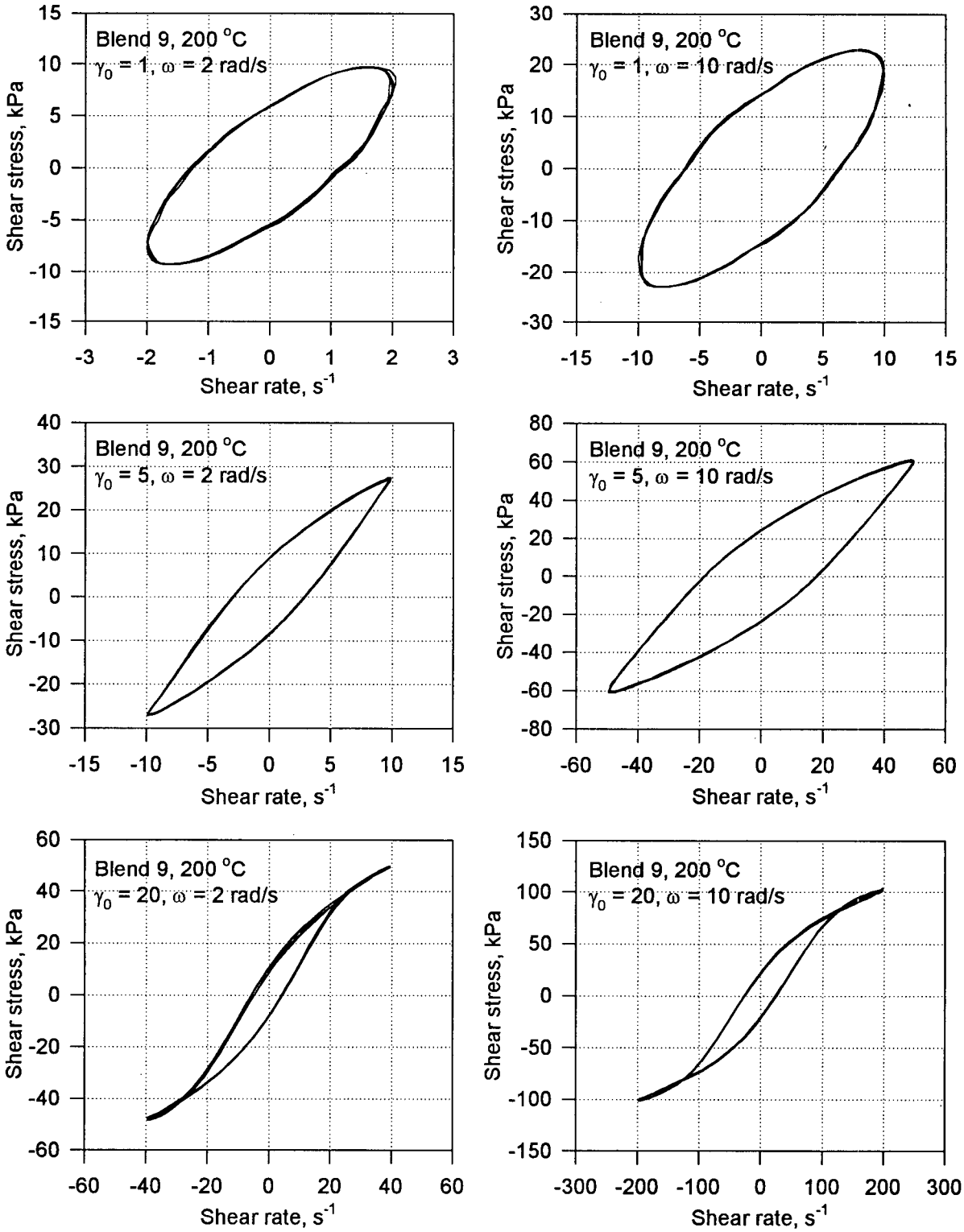

Figure 4-3. Lissajous diagrams for Blend 9 obtained at strain amplitudes of 1, 5 and 20, and frequencies of 2 and 10 rad/s.

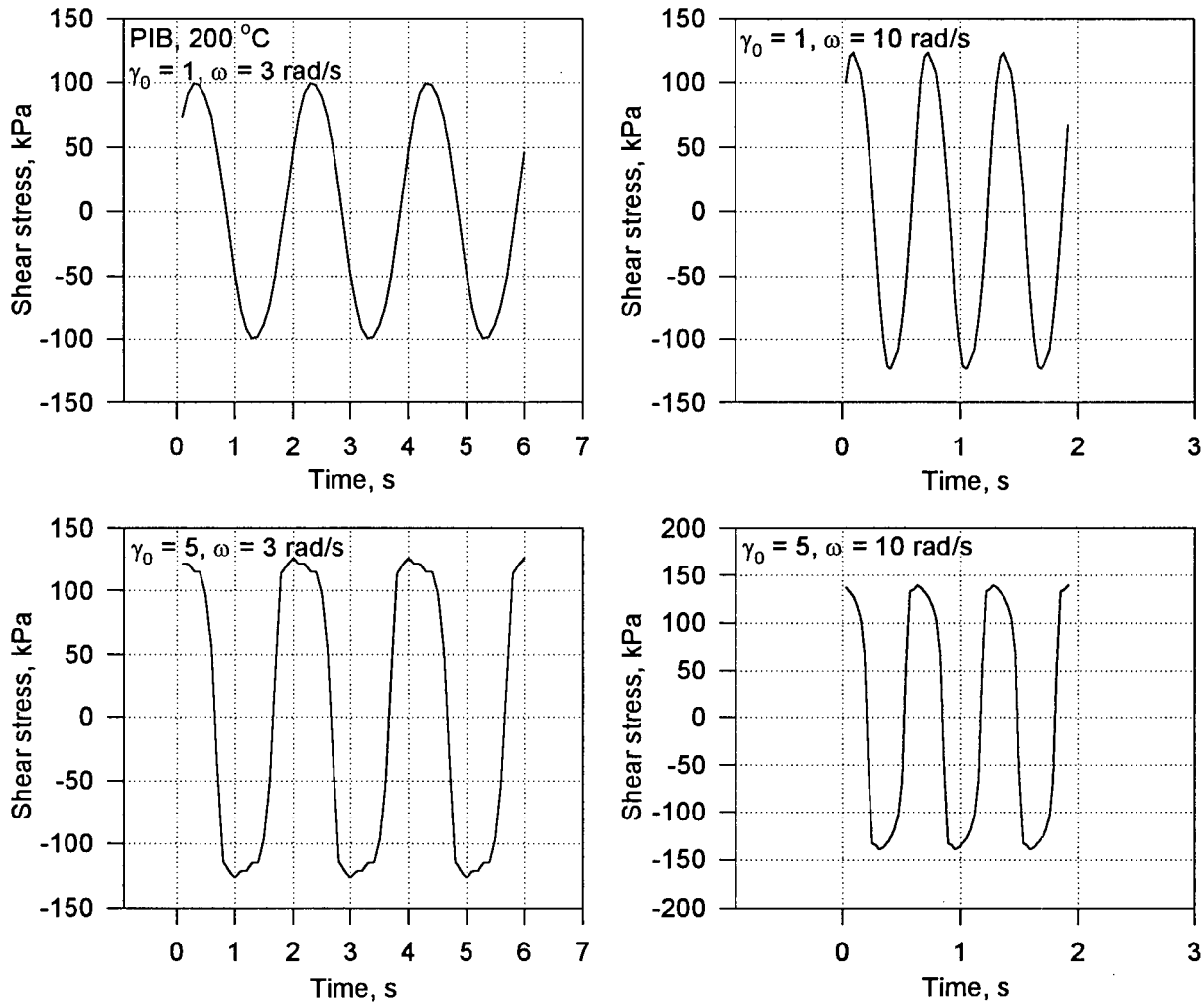

Figure 4-4. Raw LAOS data for polyisobutylene at 200 °C obtained at strain amplitudes of 1 and 5, and frequencies of 3 and 10 rad/s.

A better way to present the raw data is to plot shear stress versus shear rate (known as a Lissajous figure) [Tsang and Dealy, 1981]. The data of Figure 4-2 are replotted in Figure 4-3, this time as shear stress versus shear rate. By observing the shapes in Figure 4-3, one can easily identify the transition from a linear to a non-linear response. The two upper shapes are close to an ellipse, and therefore no higher harmonics are present. All of the other shapes significantly deviate from the ideal ellipse, becoming narrower with increasing strain amplitude.

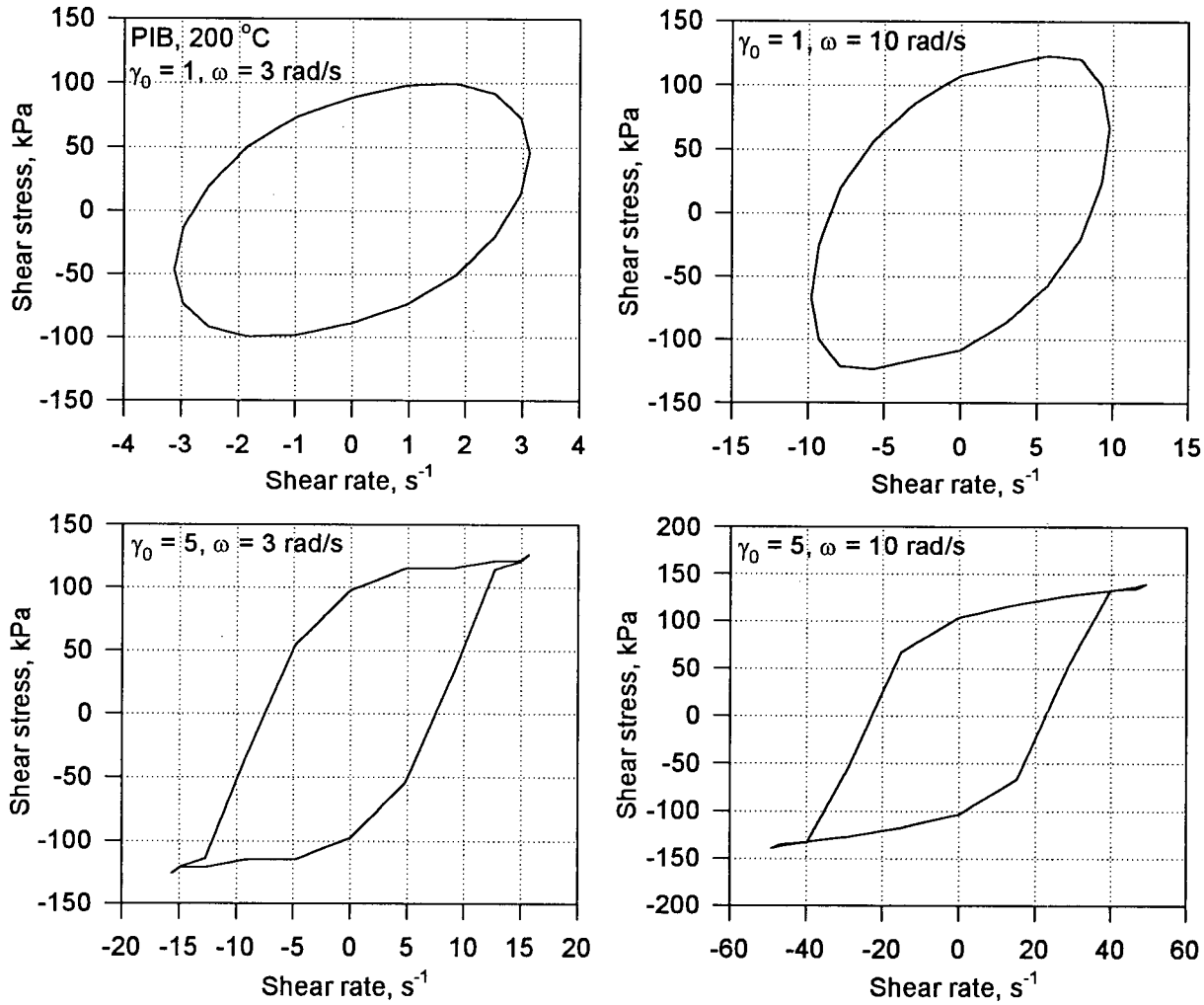

Figure 4-5. Lissajous diagrams for polyisobutylene at 200 °C obtained at strain amplitudes of 1 and 5, and frequencies of 3 and 10 rad/s.

Similar trends can be seen for polyisobutylene in Figure 4-4 (shear stress versus time) and Figure 4-5 (shear stress – shear rate loops). The shear stress responses at γ_0 =1 correspond to the linear viscoelastic regime, whereas at γ_0 = 5 the shapes are grossly distorted, suggesting non-linearity. More examples illustrating the differences between the polyethylene blends and polyisobutylene are given below (section 4.6.3).

The Lissajous figures are also not suitable for quantifying the deviation from linearity and are difficult to use for comparative purposes. There is a need for determining more relevant rheological values, based on LAOS data, by which different polymers could be identified and compared to each other. Obviously, it would be even more desirable if a structure–property relationship could be identified based on LAOS testing.

4.5 LAOS Data Analysis

The most straightforward approach to analysing LAOS data is to use Fourier transforms. The objective is to break the stress signal into its components to obtain: (1) the number of harmonics; (2) their amplitude and (3) their frequency.

For this purpose, a 20-point discrete Fourier transform (DFT) was employed. Since DFT and FFT methods yield practically identical results, DFT was chosen in order to simplify the procedure. The descriptions of both methods are given in numerous books on mathematical analysis (e.g. Ramirez, 1985). The DFT of time series $\sigma(n\Delta t)$ is given by

$$\sigma_d(k\Delta\omega) = \frac{1}{N}\sum_{n=0}^{N-1}\sigma(n\Delta t)\exp\frac{-i2\pi kn}{N} \qquad \text{eq. 4-7}$$

where N is the number of data points (20 in this case), $i = \sqrt{-1}$, $\Delta\omega = 2\pi/(N\Delta t)$, and k is the discrete frequency component index ranging from 0 to N–1.

The sought-after values of the stress response are:

$$\sigma_n = 2|\sigma_d(k\Delta\omega)|;\ n = \frac{k\Delta\omega}{\omega} \qquad \text{eq. 4-8}$$

and

$$\delta_n = \frac{\pi}{2} + \arctan\left[\frac{\mathrm{Im}(\sigma_d(k\Delta\omega))}{\mathrm{Re}(\sigma_d(k\Delta\omega))}\right];\ \text{for}\ \mathrm{Re}(\sigma_d(k\Delta\omega)) > 0 \qquad \text{eq. 4-9}$$

or $$\delta_n = \frac{3\pi}{2} + \arctan\left[\frac{\mathrm{Im}(\sigma_d(k\Delta\omega))}{\mathrm{Re}(\sigma_d(k\Delta\omega))}\right]; \text{ for } \mathrm{Re}(\sigma_d(k\Delta\omega)) < 0$$

These values can be expressed in terms of storage and loss moduli:

$$G_n'(\gamma_0,\omega) = \frac{\sigma_n}{\gamma_0}\cos(\delta_n) \qquad \text{eq. 4-10}$$

and $$G_n''(\gamma_0,\omega) = \frac{\sigma_n}{\gamma_0}\sin(\delta_n) \qquad \text{eq. 4-11}$$

Since only the first $N/2$ points of the Fourier transform are physically meaningful, a 20-point DFT allows the determination of 10 significant harmonics. This proved to be more than enough to accurately interpret the experimental data for the resins studied at the conditions chosen here. As shown later (section 4.6.2), only first three harmonics were found to be significant.

Another useful property that can be extracted from the LAOS data is the lost work per unit volume per cycle:

$$W_L = \pi\sigma_1\gamma_0\sin(\delta_1) \qquad \text{eq. 4-12}$$

which shows that all the lost work is due to the amplitude and phase angle of the first harmonic. This property characterises the energy dissipation per cycle per unit volume, and arises from the viscous (dissipational) part of the material viscoelastic behaviour [Dealy and Wissbrun, 1990].

4.6 Experimental Results and Discussion

4.6.1 Linear experiments

The linear storage and loss moduli of the Series 1 resins were determined at three different temperatures and the data were shifted using the time-temperature superposition principle at the reference temperature of 200 °C (see Figure 4-6). Only three of them are plotted for the sake of clarity. It can be seen that an increase in polydispersity increases the viscoelastic moduli at small frequencies while decreasing them at large frequencies. In other words, an increase in polydispersity renders the polymers more shear thinning (see also Figure 5-16) and elastic.

The moduli for the Series 2 resins at the same reference temperature are plotted in Figure 4-7. The following trend can be observed for the values of G' and G'': an increase in the weight average molecular weight results in higher values of both moduli, due to the expected increase of viscous and elastic properties of polymers at all time scales. A characteristic relaxation time can be defined as the inverse of the frequency, where the linear G' and G'' moduli cross. For LLDPE it is of the order of tens of milliseconds, as illustrated in Figure 4-8.

The G' and G'' curves of the polyisobutylene resin are shown in Figure 4-9. Two major differences from the data in Figure 4-8 are observed. Firstly, the cross-over frequency of the moduli is much lower than that of LLDPE, i.e. the characteristic relaxation time of PIB is higher, about 1.4 seconds, i.e. roughly two orders of magnitude higher. Secondly, the relative significance of G' and G'' changes drastically over the range of frequencies: at low frequency the loss modulus is much higher than the storage modulus. This suggests that this material behaves more like a viscous fluid when the rate of deformation is low. The opposite effect can be seen at high frequencies: storage modulus greatly prevails, suggesting a high degree of elasticity.

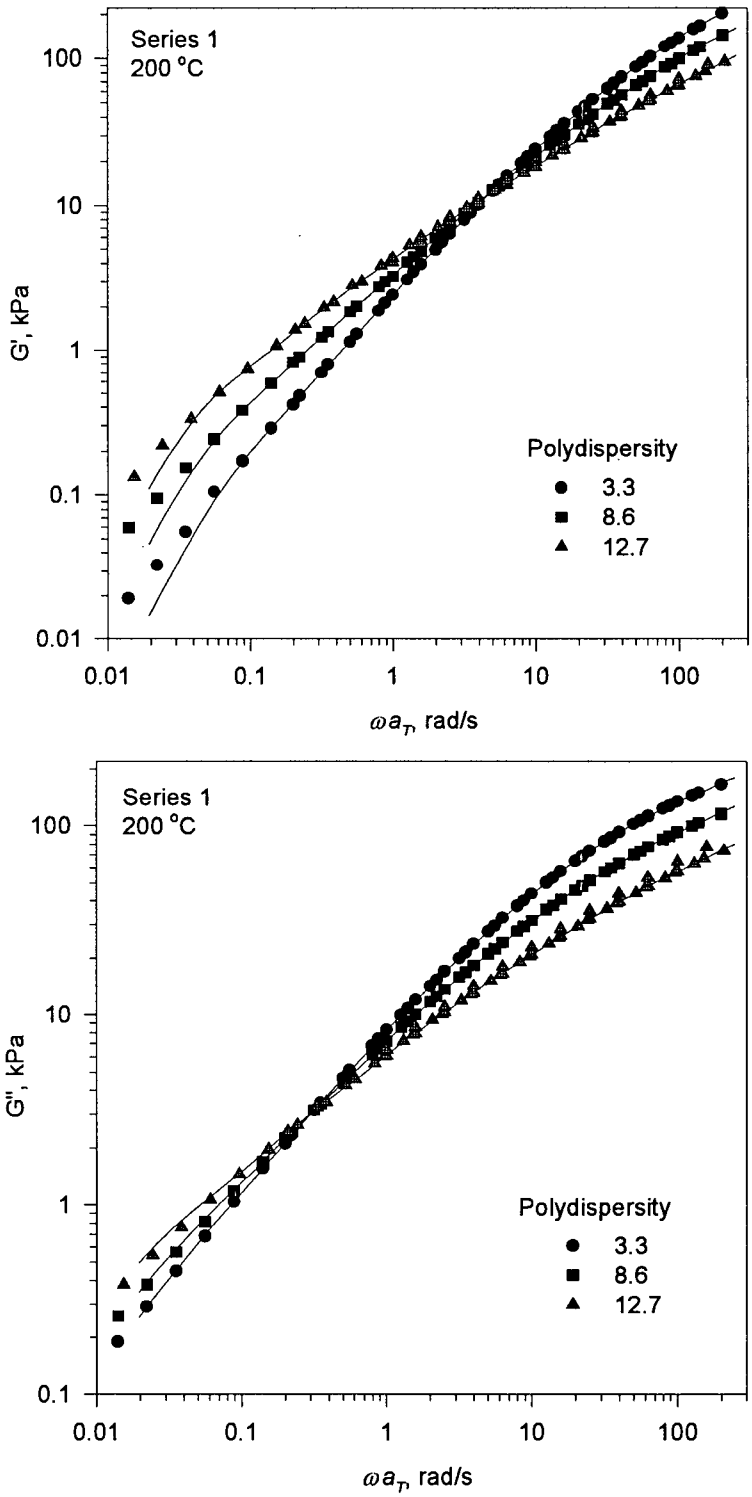

Figure 4-6. Linear viscoelastic moduli of selected resins in Series 1 at T_{ref}=200 °C.

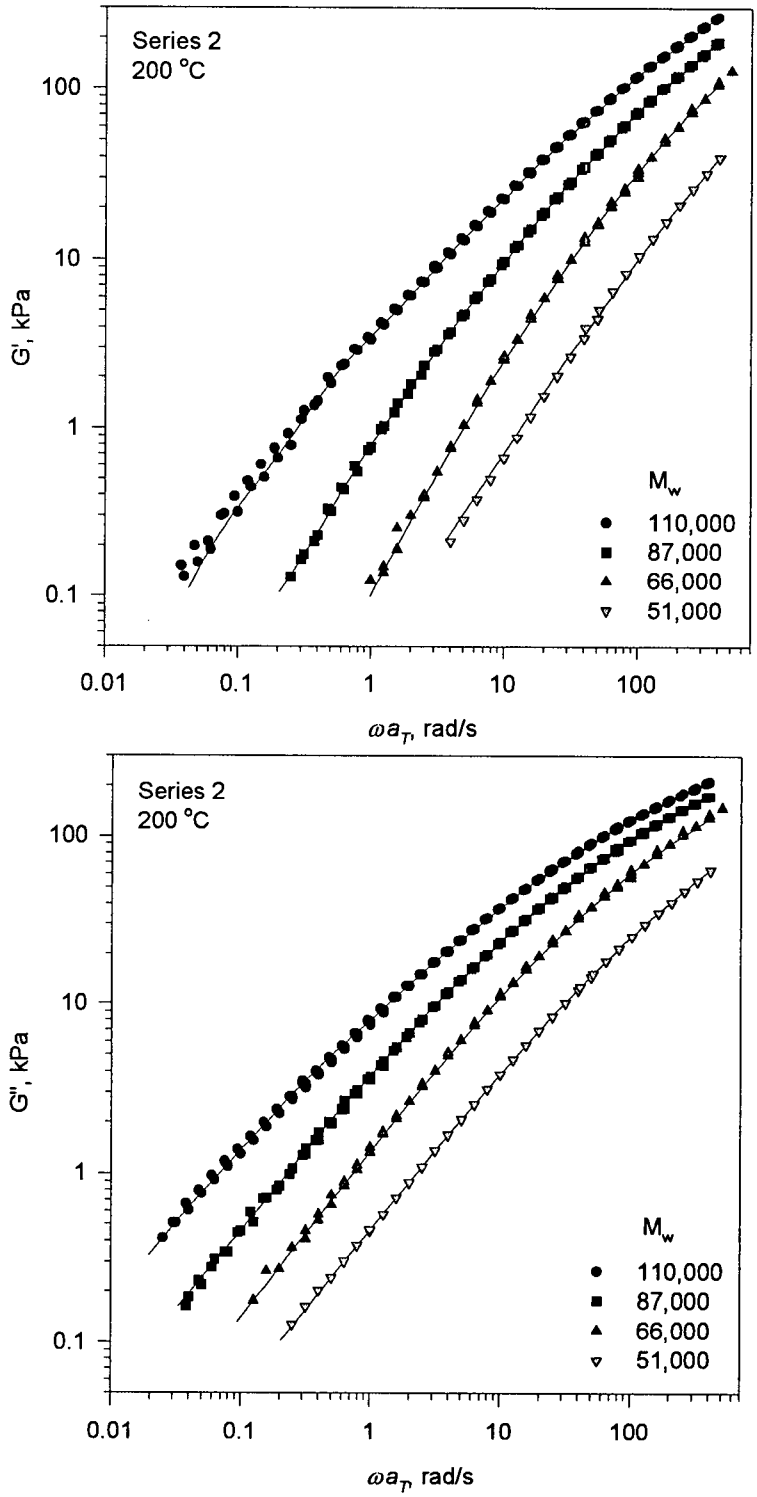

Figure 4-7. Linear viscoelastic moduli of selected resins in Series 2 at T_{ref}=200 °C.

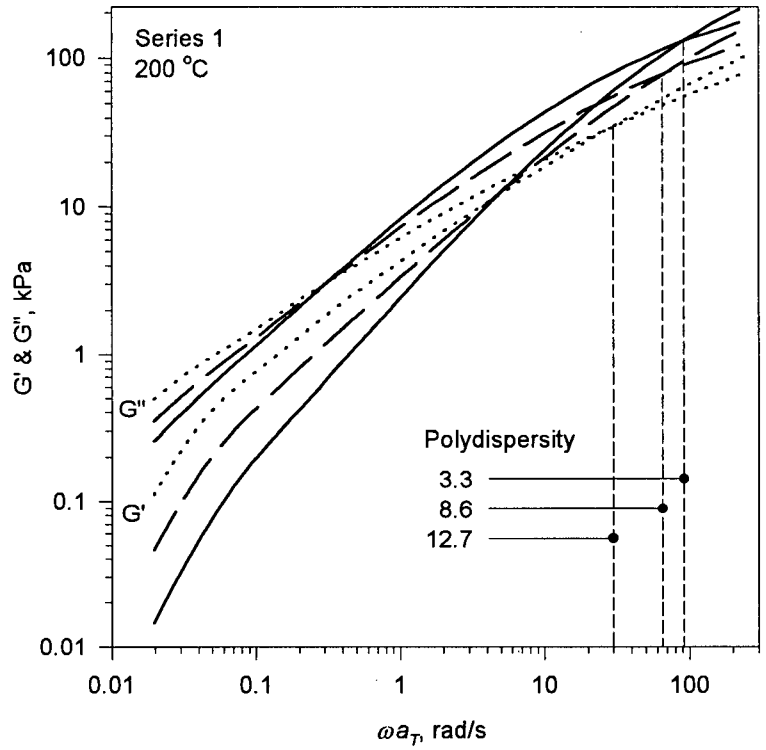

Figure 4-8. Linear viscoelastic moduli of selected resins in Series 1 at T_{ref}=200 °C showing the cross-over frequencies.

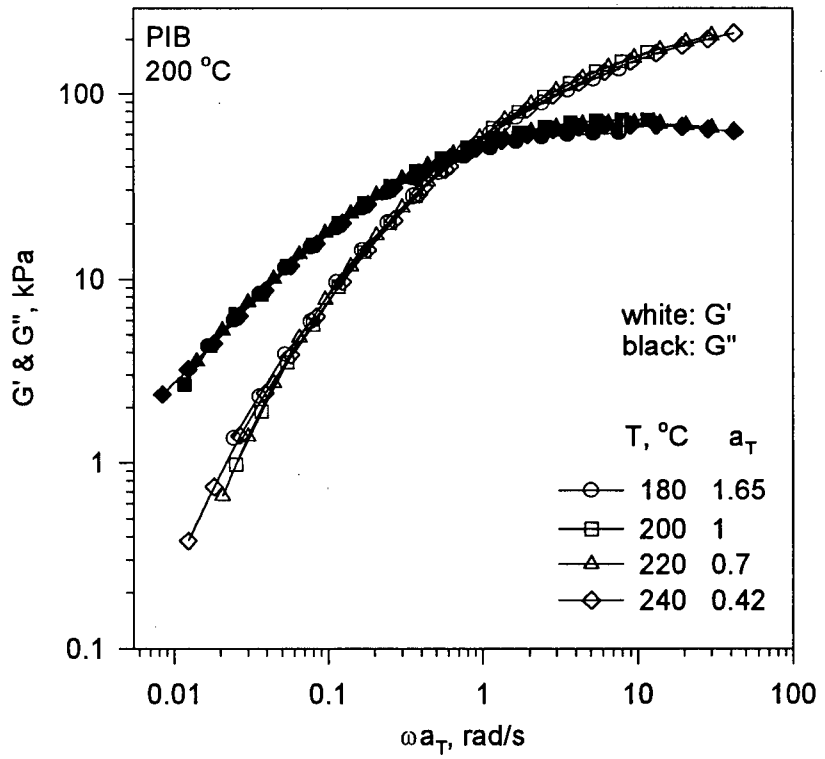

Figure 4-9. Linear viscoelastic moduli of polyisobytilene obtained at four different temperatures. Time-temperature superposition was applied with the reference temperature of 200 °C.

Finally, the linear dynamic moduli of the SMA/PMMA 1:1 blend are presented in Figure 4-10 for various temperatures. Note that the data have been shifted by applying the time-temperature superposition (TTS). SMA/PMMA blends are known to undergo shear-induced phase separation at certain temperatures, and one such blend was tested in the LAOS experiments of Chopra (1998). The *G'* and *G"* data points for temperatures below 215 °C approximately define a master curve. Above this temperature, the TTS fails due to phase separation. Further study of this phenomenon is beyond the scope of this work; it is noted however that understanding the effect of shear flows on the phase behaviour of polymer blends is important in materials processing applications. SMA/PMMA blends are superior compared to pure PMMA for uses in making car rear lamps, lenses of large diameter and street lamps [Chopra *et al.*, 1997].

4.6.2 LAOS: General Features

As was mentioned earlier, the non-linear complex moduli, G_n' and G_n'', are functions of two parameters, strain amplitude and frequency. Consequently, there are several ways to plot them:

- 2-D graph, as a function of frequency at a fixed value of amplitude;
- 2-D graph, as a function of amplitude at a fixed value of frequency;
- 3-D or contour graph, as a function of both frequency and strain amplitude.

In this study, the first and the third types of graphs were used. Figure 4-11 shows the first three odd harmonics for Blend 9 obtained at the strain amplitude of 4. Two more harmonics, the fifth and seventh, were measured but are not plotted because their magnitudes are comparable to experimental noise. Several observations can be made:

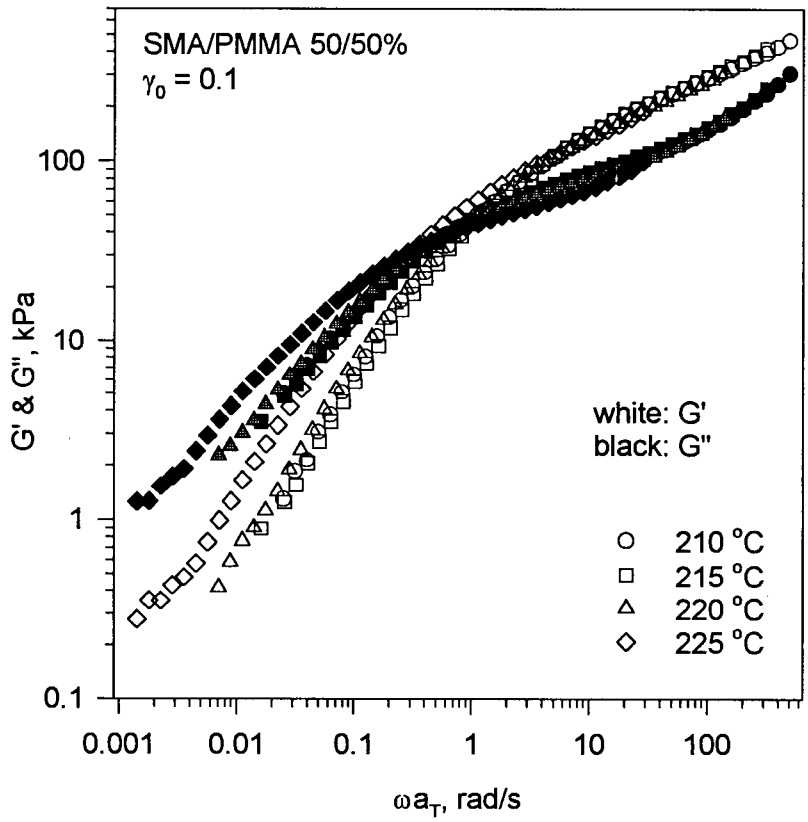

Figure 4-10. Linear viscoelastic moduli of a SMA/PMMA blend obtained at four different temperatures.

1. The data points for the first harmonic are below their corresponding linear data. This is to be expected, since the stress has been normalised with the strain amplitude. In other words, in the non-linear regime the stress is a function of amplitude. This effect is described in more detail in section 4.6.5.

2. As opposed to the first harmonic components and the linear viscoelastic moduli, higher harmonic components can be both negative and positive. Moreover, for a given resin, they can even change sign depending on the test parameters. Figure 4-12 demonstrates this. Increasing γ_0 to 10 changes the sign of the third harmonic of the loss modulus (G_3'') from positive to negative for the same sample. The physical significance of this sign change is that, at different

levels of deformation, different relaxation mechanisms are triggered, and this results in changes in the harmonic composition of the stress response.

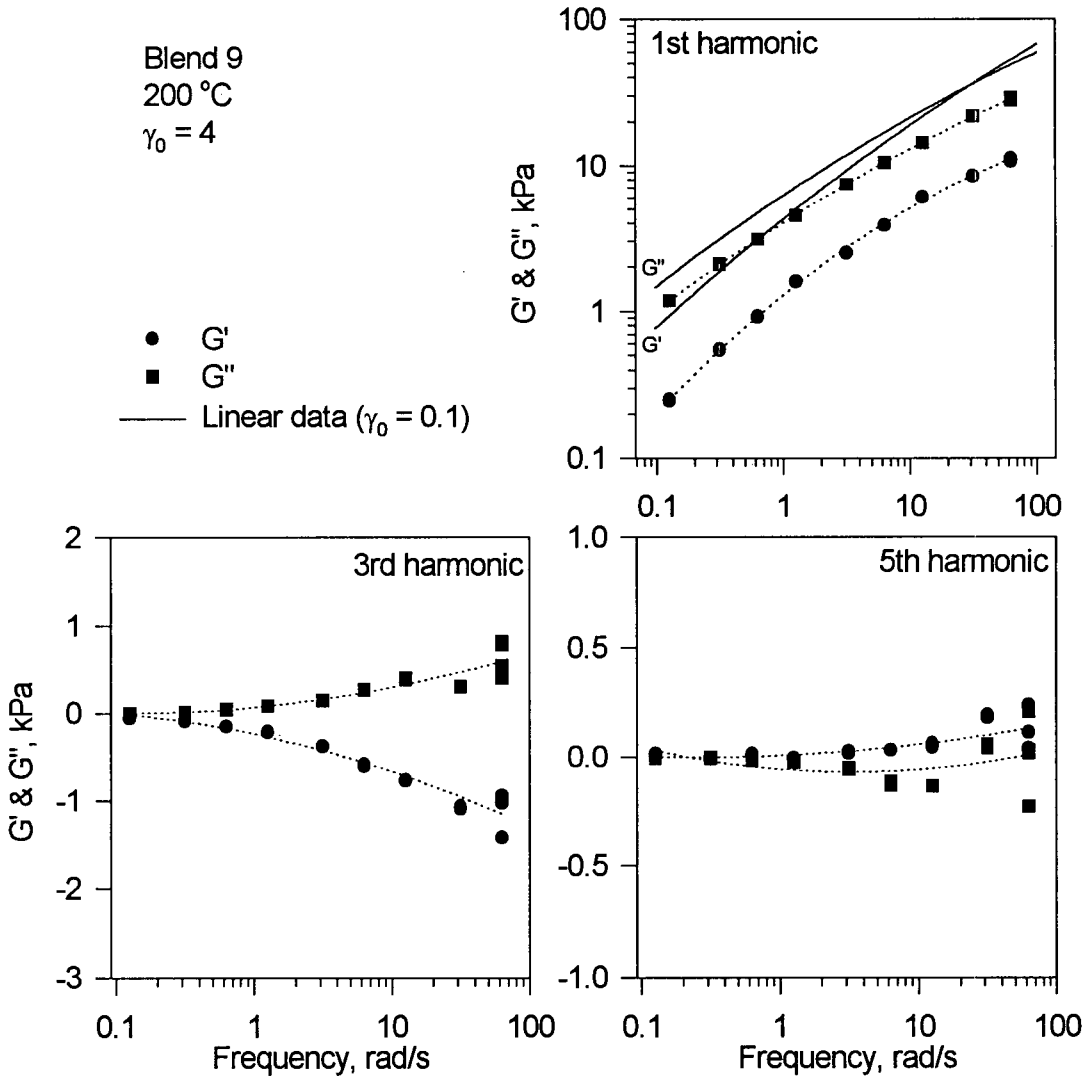

Figure 4-11. The 1st, 3rd and 5th harmonics of the non-linear complex moduli for Blend 9 obtained at a strain amplitude of 4.

3. At low frequencies the higher harmonics approach zero. This is due to the fact that when the rate of deformation is small, the material behaviour approaches the linear viscoelastic regime, where all higher harmonics are absent.

4. The higher the strain amplitude, the greater the significance of the higher harmonics and the greater the deviation from linear viscoelasticity. This means that the stress response becomes more complex, and different time scales play a role in the molecular relaxation.

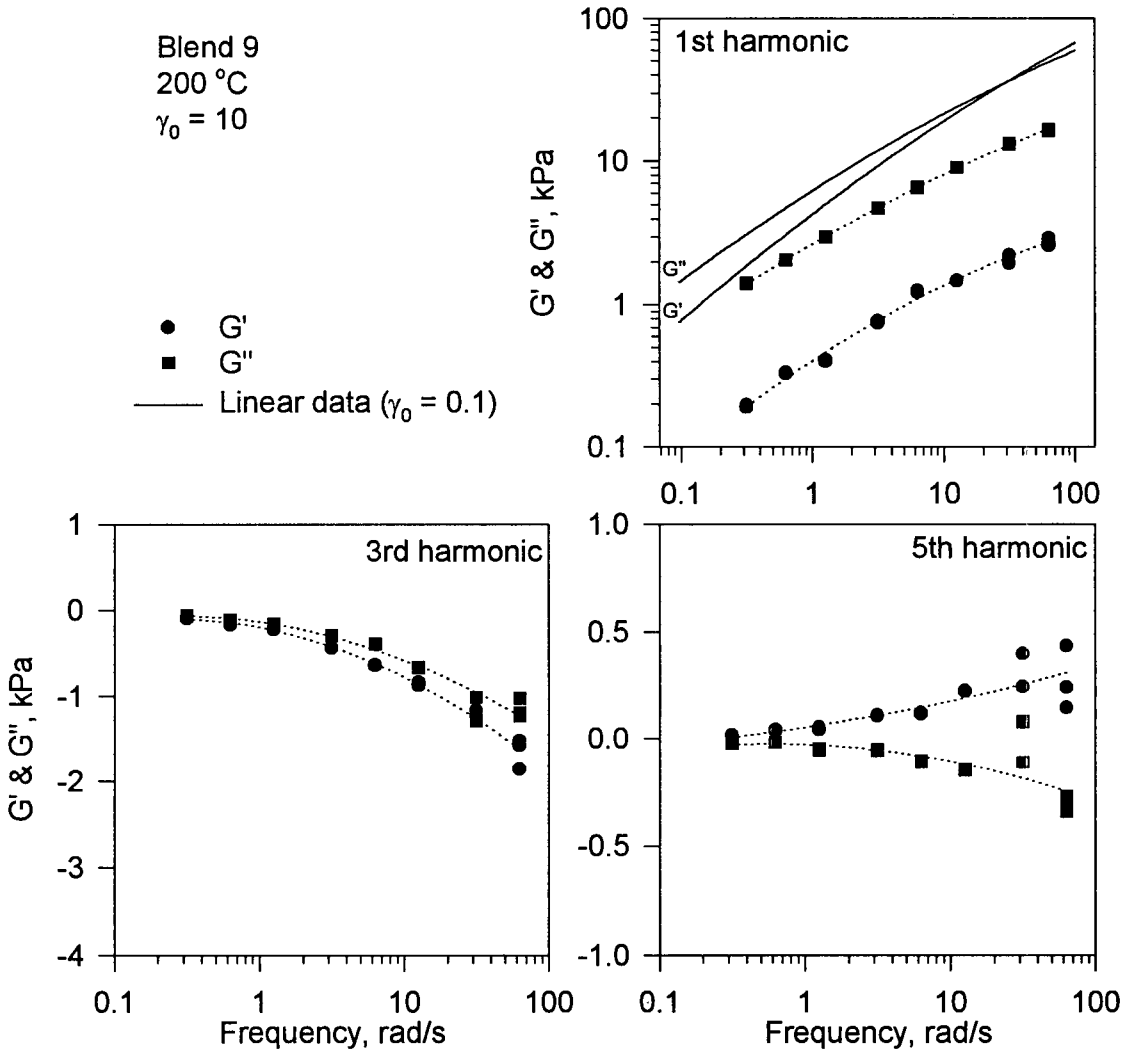

Figure 4-12. The 1st, 3rd and 5th harmonics of the non-linear complex moduli for Blend 9 obtained at a strain amplitude of 10.

4.6.3 LAOS: Effects of Molecular Structure

Let us now consider how changes in molecular structure affect the LAOS data. The Series 2 resins have approximately the same molecular weight distribution (PD ≈ 4), while their weight

average molecular weights differ significantly. Figure 4-13 shows the effect of M_w on the first and third harmonics of the Series 2 resins obtained at the strain amplitude of 10.

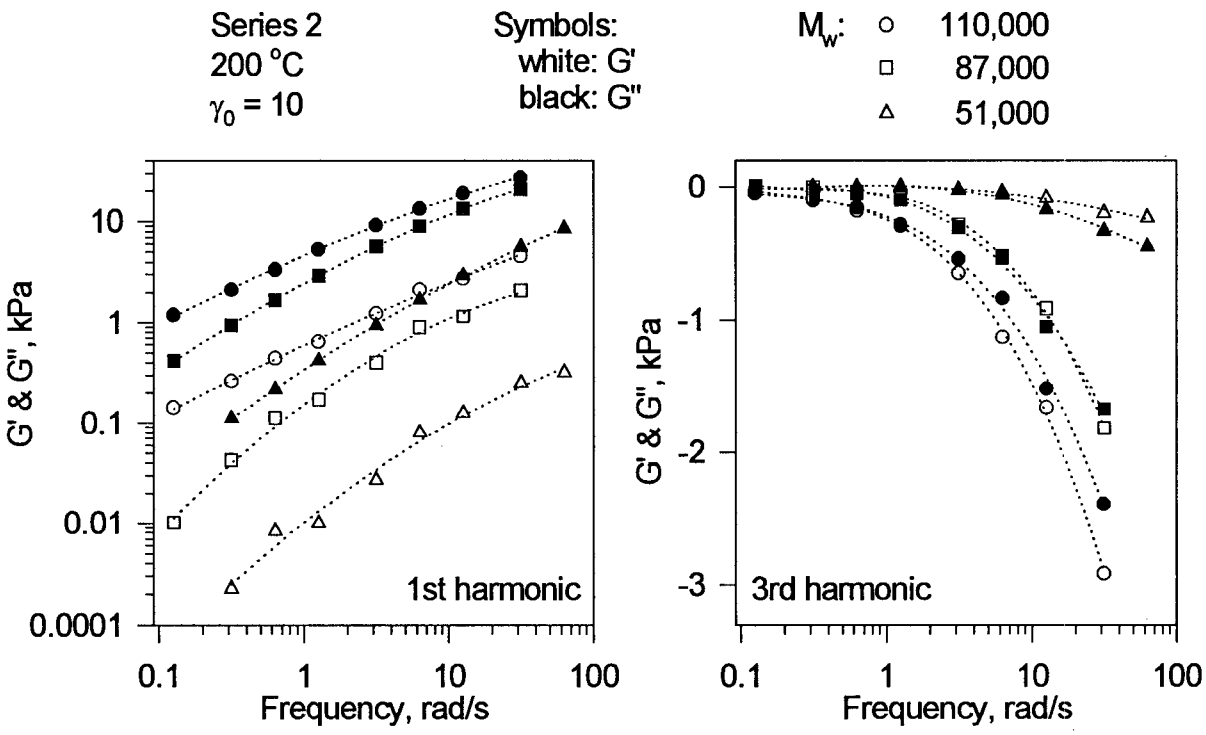

Figure 4-13. Effect of the average molecular weight on the 1st and 3rd harmonics of the non-linear complex moduli obtained for Series 2 resins at a strain amplitude of 10.

As the molecular weight decreases from 110,000 to 51,000 g/mol, the first harmonics of *G'* and *G"* decrease, following the same trend as their linear counterparts. Though the absolute magnitudes of the third harmonics decrease, a different behaviour can be observed: the relative positions of G_3' and G_3'' change depending on the resin. G_3' for the resin with M_w = 110,000 g/mol is less than G_3'' (white circles are below black ones), but for the resin with M_w = 51,000 g/mol, G_3' is greater than its G_3'' (white triangles are above black ones). For the resin having an intermediate M_w the third harmonics match over the entire frequency range.

It is noted that none of the rheological and processing properties obtained for the resins belonging to Series 2 (such as linear dynamic moduli, relaxation spectra, capillary flow curves, extrudate swell ratios and melt fracture performance, presented in Chapter 5) go through any kind of change of ordering with frequency or shear rate. Even though the observed changes in G_3' and G_3'' are not observed for all possible values of the strain amplitude, they may be attributed to the differences in the detailed molecular structure of these resins. Such differences may not be detected by GPC (gel permeation chromatography) in the determination of molecular weights and their distributions, or by FTIR (Fourier transform infrared spectrometry) and TREF (temperature rising elution fractionation) in the determination of low levels of long chain branching.

A different picture is observed for the changes in molecular weight distribution. In Figure 4-14 the Series 1 resins are compared in terms of their first and third harmonics. The data were obtained at a constant strain amplitude of 10 and over the same frequency range for each resin. The Series 1 resins have essentially the same weight average molecular weight (100,000 g/mol ±10%) and different MWD, ranging from PD=3.3 for Blend 1 to PD=12.7 for Blend 9.

It can be seen that the change in MWD did not result in a change of the relative order of the third harmonic, as was the case for the Series 2 resins with changing M_w (G_3' values are always lower than G_3''). The absolute magnitudes of the harmonics did change along the same trend as their corresponding viscosities: Blend 1 has the highest and Blend 9 has the lowest viscosity in that range of shear rates.

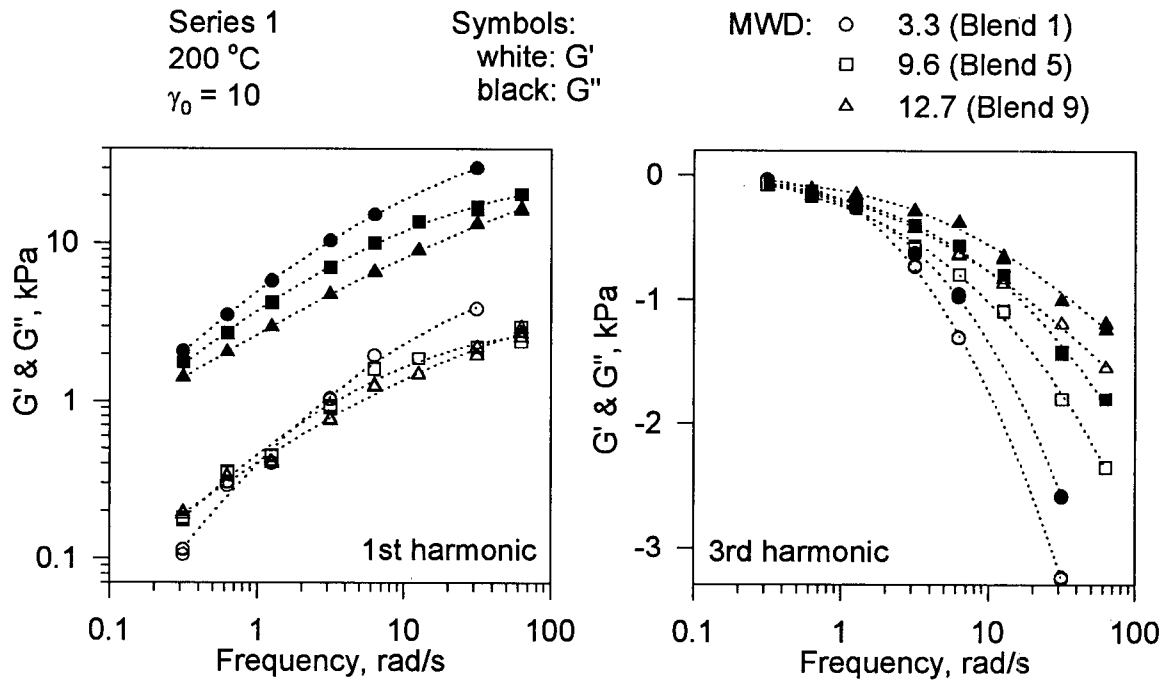

Figure 4-14. Effect of the molecular weight distribution on the 1st and 3rd harmonics of the non-linear complex moduli obtained for Series 1 resins at a strain amplitude of 10.

Blend 5, with PD=9.6, exhibited the best performance in terms of the critical shear rate at the onset of melt fracture (Figure 5-20a). It was established that there is a link between the melt fracture performance and the characteristic relaxation time (see Chapter 5). Since the LAOS data are affected by the molecular relaxation mechanisms, further harmonic analysis was carried out with the resins of Series 1.

The range of strain amplitudes was expanded to 25, and numerous data points were obtained for various combinations of frequency and amplitude. The results for the same three blends are summarised on contour plots in Figure 4-15. As the polydispersity increases, the domains monotonically flatten in a similar fashion for both G_3' and G_3''. No conclusion can be made based on these plots as to why Blend 5 exhibited the best melt fracture performance.

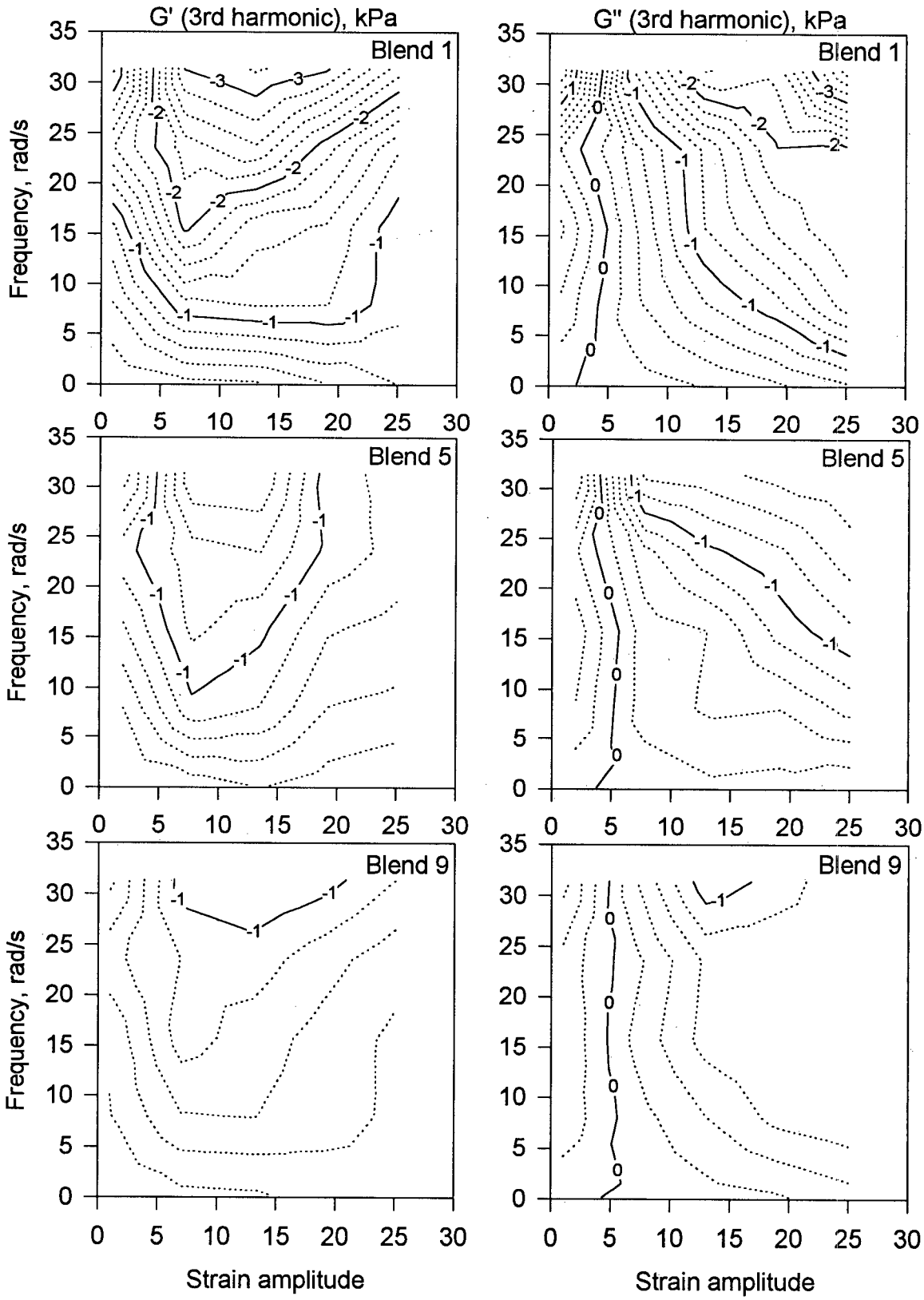

Figure 4-15. Contour plots comparing the 3rd harmonics of the non-linear complex moduli obtained for three resins of Series 1 at 200 °C as a function of strain amplitude and frequency.

All the above discussed examples involved polymer resins belonging to the same family, i.e. linear low-density polyethylenes. It would be interesting to compare their behaviour with that of other types, having a completely different molecular structure. For this purpose, a highly elastic material, polyisobutylene (PIB), was used in the LAOS experiments.

Figure 4-16 compares side by side the first harmonic of the storage and loss moduli for Blend 5 and PIB, and Figure 4-17 compares side by side the third harmonic for the same materials. In the first harmonic, one can see that PIB's moduli are much higher and the gradient of G_1' is greater. For example, at the point where $\gamma_0 = 3$ and $\omega = 10$ (marked with arrows in Figure 4-16):

Blend 5	PIB
$\frac{\partial G_1'}{\partial \gamma_0} = 1.5$ kPa	$\frac{\partial G_1'}{\partial \gamma_0} = 65$ kPa

In addition to higher gradients, more differences are found in the third harmonic (Figure 4-17):

1. Noticeable non-linearity for PIB is observed even at low values of the strain amplitude over the entire range of frequencies (the contours on the left side for PIB are non-zero, especially in G_3'').

2. Areas of non-linearity in G_3' for PIB spread much deeper into the region of lower frequencies.

For example, at $\gamma_0 = 3$ and $\omega = 10$ (marked as point "A"):

Blend 5	PIB
$G_3' = -0.4$ kPa	$G_3' = -8.6$ kPa
$G_3'' = 0.3$ kPa	$G_3'' = 4.6$ kPa

These findings confirm the high degree of elasticity inherent to polyisobutylene, and the use of the 3-D contour graphs allows to "visualise" the LAOS data for concise and clear presentation.

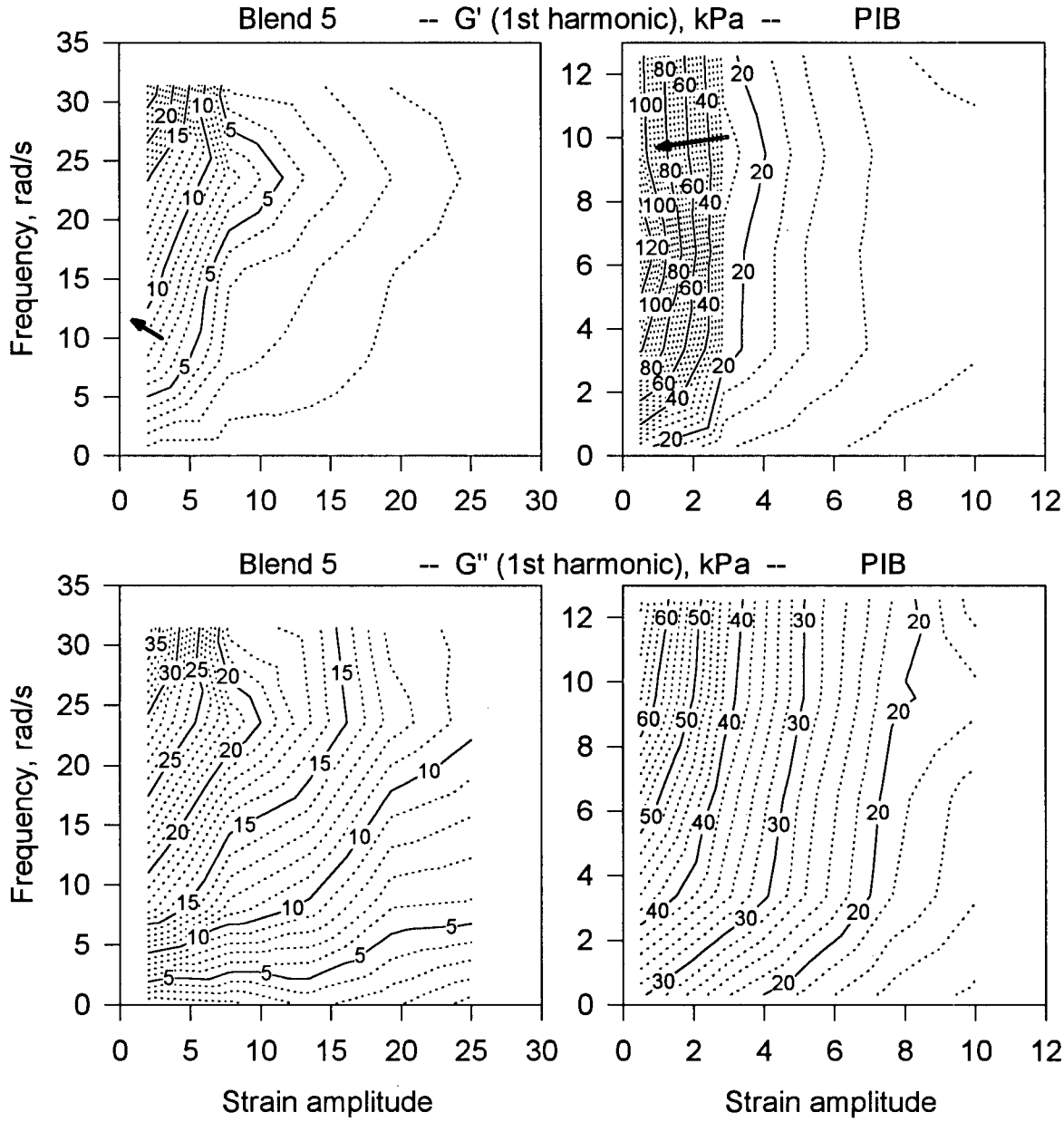

Figure 4-16. Comparison of the 1st harmonics of the non-linear complex moduli obtained for Blend 5 and polyisobytilene at 200 °C as a function of strain amplitude and frequency.

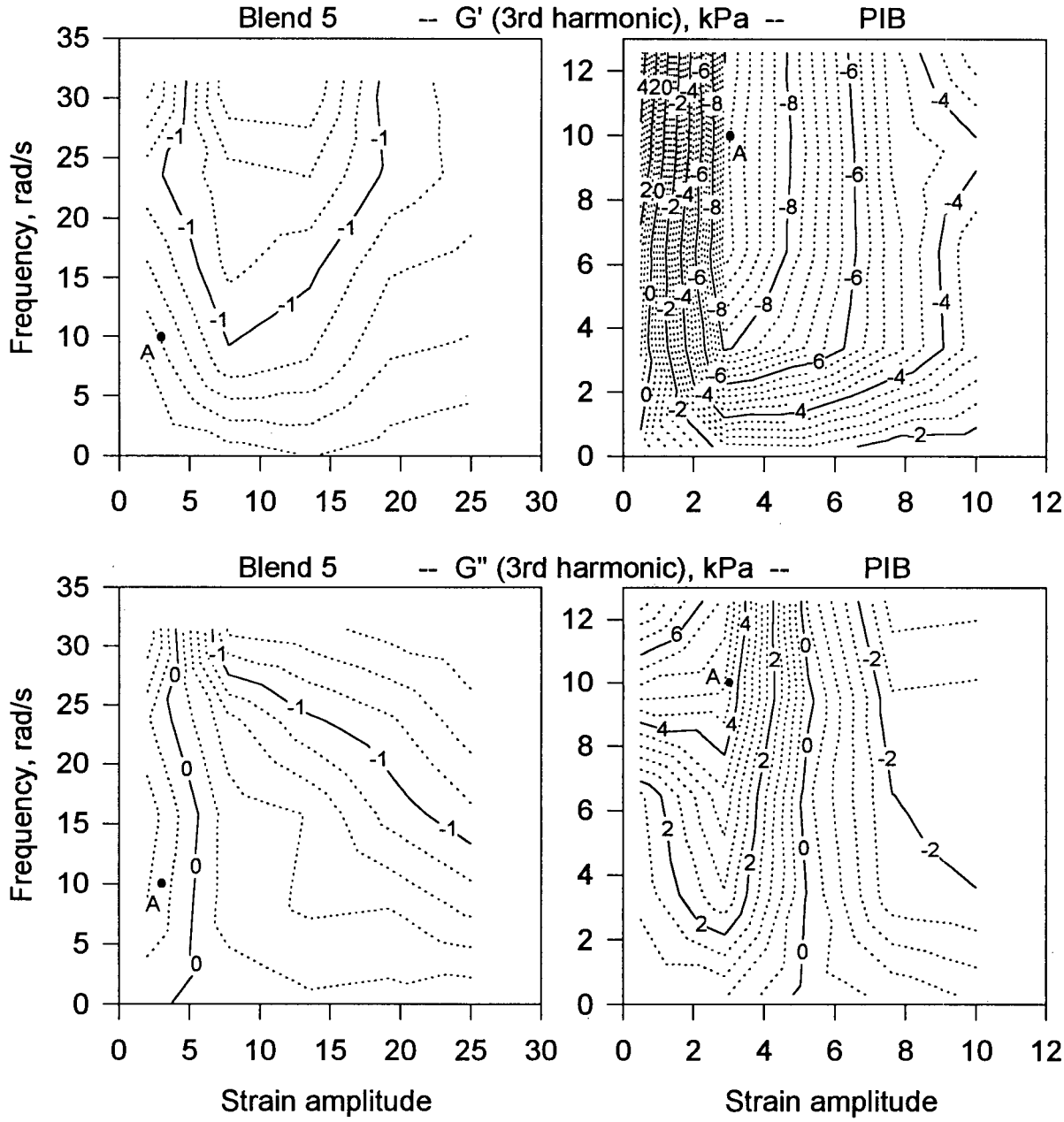

Figure 4-17. Comparison of the 3rd harmonics of the non-linear complex moduli obtained for Blend 5 and polyisobytilene at 200 °C as a function of strain amplitude and frequency.

4.6.4 LAOS: Effects of Sample Heterogeneity

Despite the fact that the LAOS data were not able to explain the performance maximum observed in the processing of the Series 1 resins (see Chapter 5), their usefulness can be

demonstrated by one more example. In Figure 4-18 the first and third harmonics are shown for a SMA/PMMA blend at a fixed strain amplitude of 10 and four different temperatures. Time-temperature superposition was applied to the first harmonic. It can be seen that before phase separation, the experimental data superpose well (210 and 215 °C, circles and squares). When phase separation takes place (220 and 225 °C, triangles and diamonds), the first harmonics shift slightly up at low frequencies and the third harmonics are significantly higher, especially G_3'. This picture differs from the one obtained in linear experiments (Figure 4-10). The difference in the measured values is much more pronounced compared to those obtained within the limit of linear viscoelasticity.

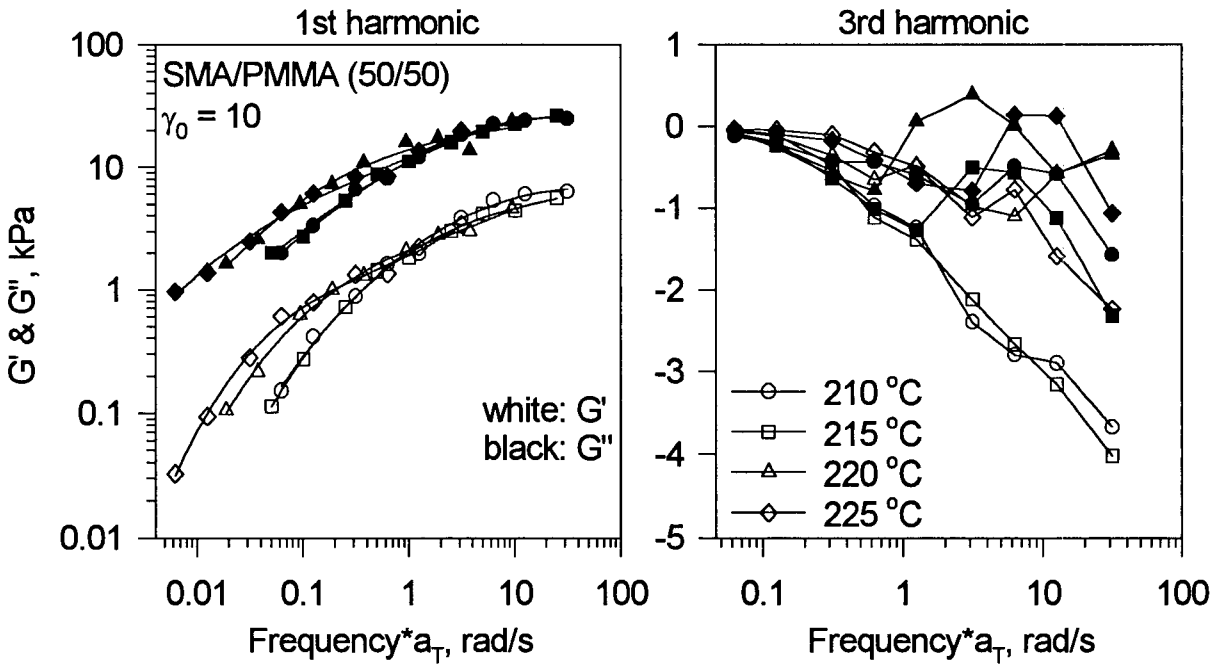

Figure 4-18. Changes in the non-linear complex moduli caused by phase separation of a SMA/PMMA blend.

4.6.5 Determination of Damping Function

The damping function is a non-linear experimental function, often used in the interpretation of experimental data and in the modelling of viscoelastic flows [Dealy and Wissbrun, 1990]. It is usually determined from a step-strain experiment. However, this method has certain disadvantages:

1. A perfect step strain is impossible to realise in practice, since no instrument is capable of instantaneous movement. There is always a finite rate of displacement, distorting the measured stress.
2. A sudden change of displacement required in the step experiment often results in a sample break-up.
3. For many polymers, the stress quickly drops to very small values, making it difficult to measure because of the transducer noise.

All the above-mentioned factors do not help the accuracy of the results, and the error in the damping function may reach 50%. The technique proposed below is based on the LAOS experiments and does not suffer from those drawbacks.

The basic idea of using the LAOS data to find the damping function is as follows. In the step-strain experiment, a sample is subjected to a sudden strain and after that the decaying stress is recorded as it approaches zero. During that process the elastic energy stored in the original configuration of polymer chains is allowed to dissipate. This implies that the relaxation behaviour is governed by the ability of those chains to store the elastic energy. The corresponding rheological property is the familiar storage modulus, G'. But G' is a linear property – and this is where the LAOS comes into play. Instead of G', the first harmonic of the complex storage modulus, G_1', will be used to obtain the necessary shift factors.

Figure 4-19 is a plot of first harmonic of the storage modulus for Blend 5 obtained at five different strain amplitudes over a broad range of frequencies. The linear G' is also plotted as a solid line. It can be seen that the higher the amplitude, the lower the corresponding values of G_1' and the greater the deviation from the linear storage modulus. The damping function is determined by calculating shift factors for each strain amplitude to superpose the non-linear data with the linear curve:

$$h(\gamma_0) = \frac{G_1'(\omega,\gamma_0)}{G'(\omega)} \qquad \text{eq. 4-13}$$

where $h(\gamma_0)$ is the damping function, $G_1'(\omega,\gamma_0)$ is the first harmonic of the storage modulus, and

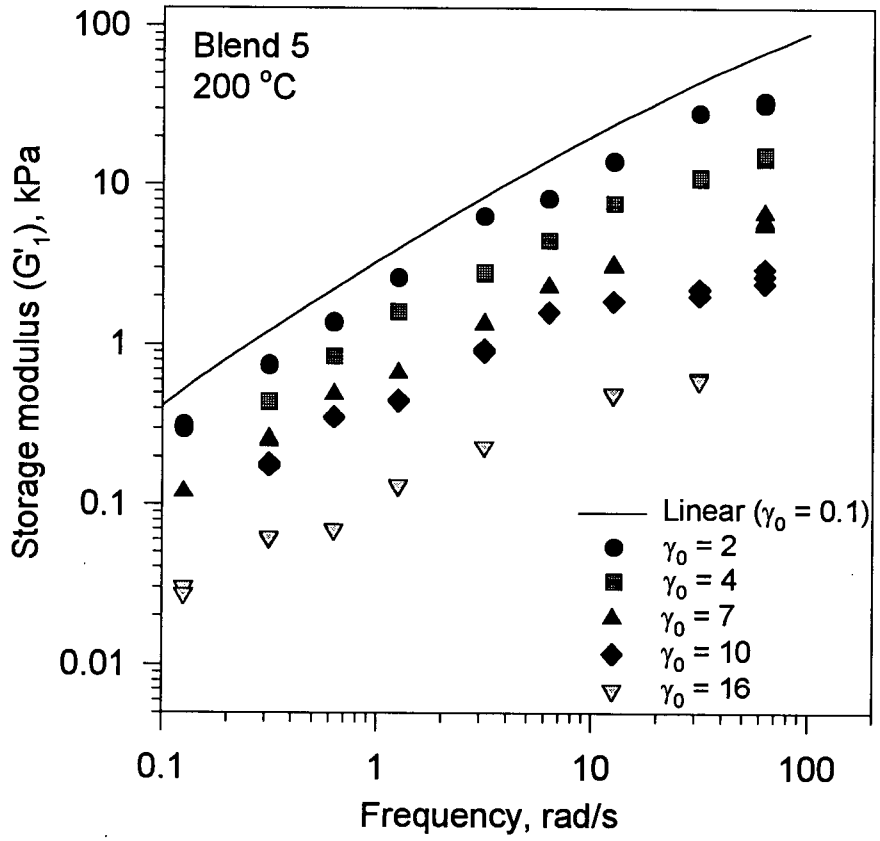

Figure 4-19. Effect of strain amplitude on the 1st harmonic of the storage modulus of Blend 5 at 200 °C taken at five different strain amplitudes.

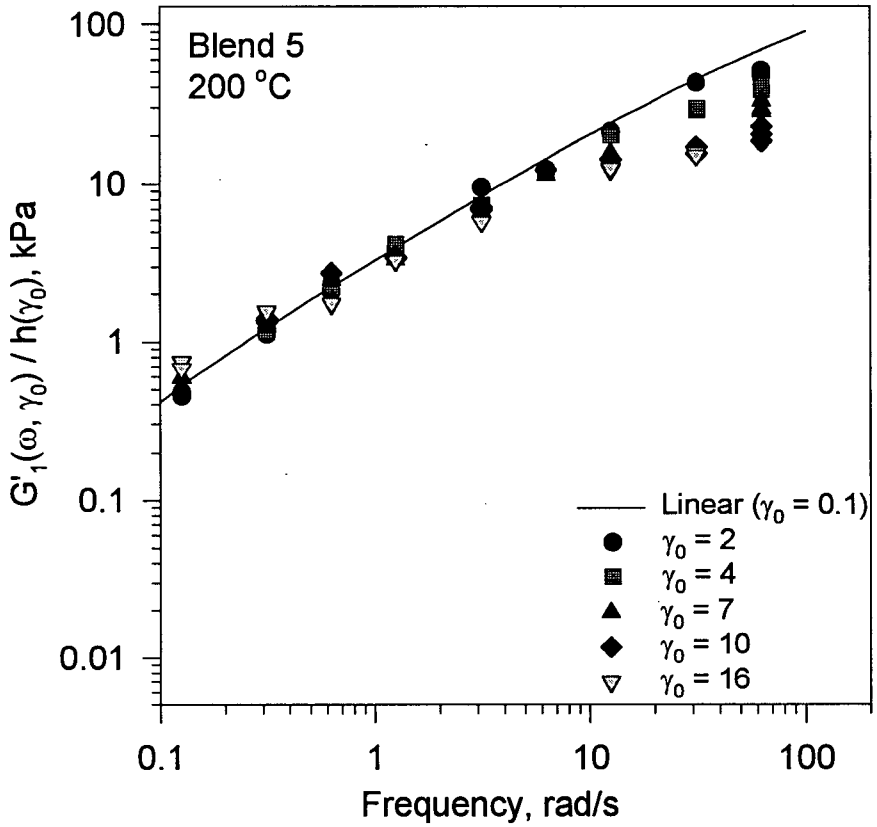

Figure 4-20. The superposed data of Figure 4-19.

$G'(\omega)$ is the linear storage modulus. The shift factors were found by trial and visual observation of the resulted graph, shown in Figure 4-20 for Blend 5.

This procedure was applied to the LAOS data for other resins from Series 1, and compared to data previously obtained from step-strain experiments. Considering the fact that the error of the step-strain data range from 20 to 40%, the values of the damping factors from the LAOS data are in good agreement with the step-strain data, thereby confirming the potential validity of the proposed technique (Figure 4-21). Error bars on some points reflect the scatter commonly observed in the data from step-strain experiments. It can be seen that there is a

good agreement between the step-strain data (white symbols) and the values calculated from the LAOS data (dark symbols).

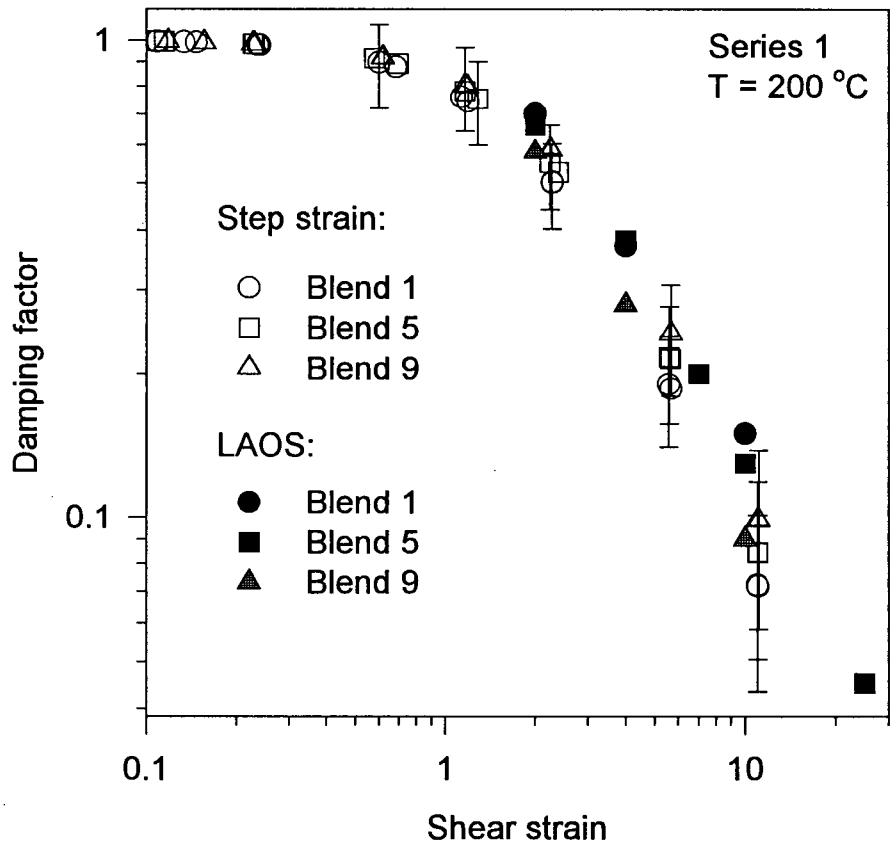

Figure 4-21. Damping functions of the blends of Series 1 resins determined from the step-strain and LAOS data.

4.6.6 Numerical Study

In order to rigorously prove the validity of the above proposed technique for the determination of the damping function, one must solve a non-linear constitutive equation for the case of oscillatory deformation. For example, the Wagner model (described in Appendix C) for the conditions of the LAOS test takes the following form:

$$\sigma(t) = \int_{-\infty}^{t} \frac{G_i}{\lambda_i} e^{-\frac{t-t'}{\lambda_i}} \frac{\gamma(t,t')}{1+\alpha\gamma^{\beta}(t,t')} dt' \qquad \text{eq. 4-14}$$

and $$\gamma(t,t') = \gamma_0(\sin(\omega t) - \sin(\omega t'))$$

The parameters and their determination are described in Chapter 7 for Dowlex 2049 (linear low-density polyethylene). The same range of strain amplitudes as shown in Figure 4-19 was used to solve eq. 4-14. A computer program was written in the C++ programming language, and 10-point Gauss quadrature was used for the integration. The shear stress response obtained as a result of the simulation was subjected to DFT analysis as described above in this chapter. Figure 4-22 shows the first harmonic of the storage modulus predicted for different shear strain amplitudes. The upper curve represents the model prediction for the linear case, and the damping function was determined using eq. 4-13. Figure 4-23 compares the damping function obtained using the Wagner model with the experimental data. The agreement between the two sets of data confirms the validity of the above proposed approach to determine the damping function from the LAOS data.

4.7 Conclusions

Large amplitude oscillatory shear experiments in combination with harmonic data analysis provide a valuable tool for studying non-linear rheological properties. The experiments were run using a sliding plate rheometer, capable of providing large deformations and accurate stress measurements that are free of end effects. It was demonstrated how the LAOS data can be analysed and presented. A few examples showing potential uses of the method, including the determination of the damping function, were also discussed.

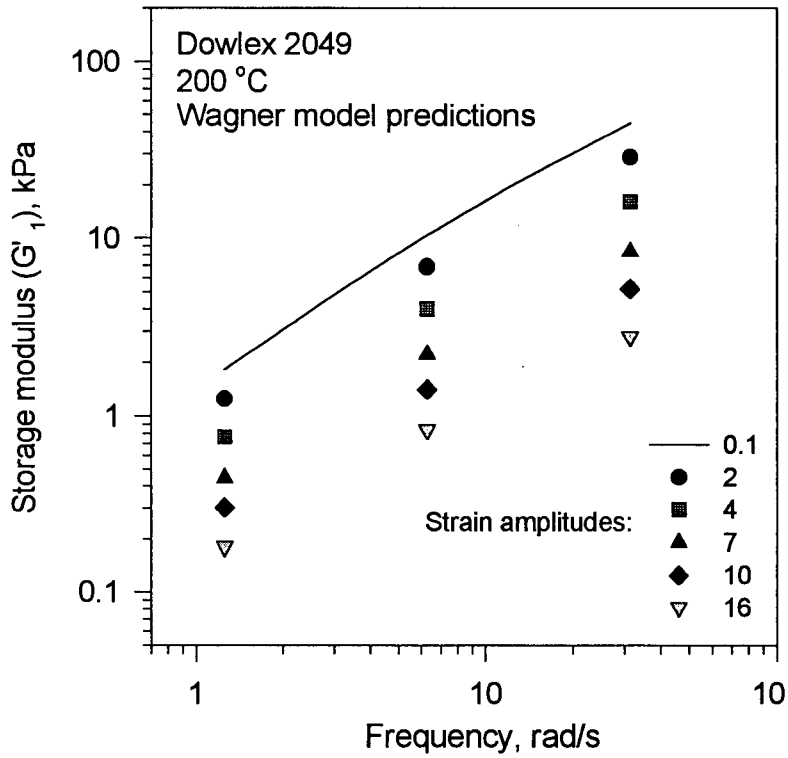

Figure 4-22. The Wagner model predictions for first harmonic of the storage modulus of Dowlex 2049 at 200 °C at different strain amplitudes.

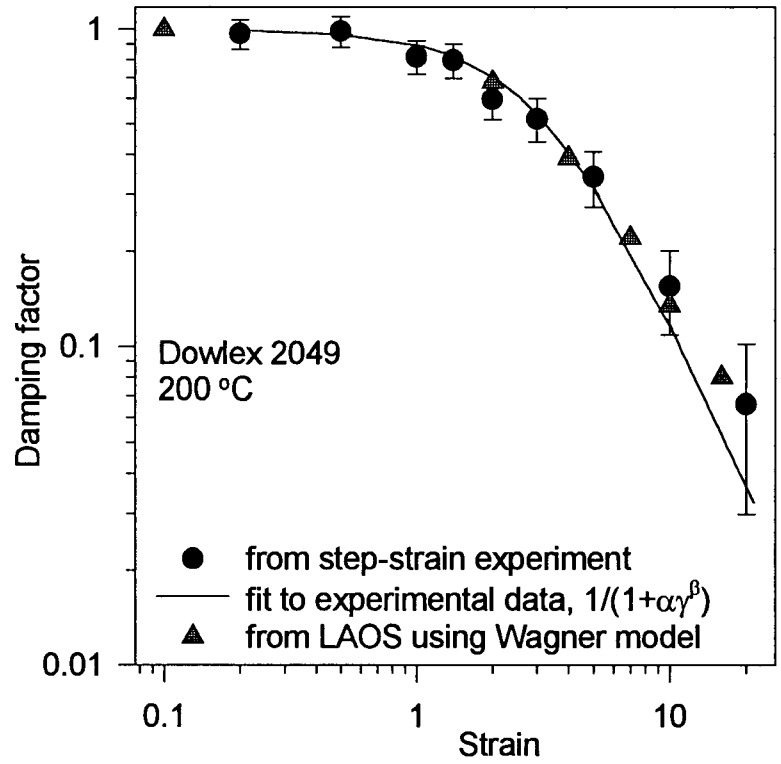

Figure 4-23. Damping function of Dowlex 2049 determined from step-strain experiments and from the Wagner model predictions.

A simplified version of the LAOS analysis, obtained at a fixed strain amplitude and plotted on a two-dimensional graph, could be useful in the industrial characterisation of polymers. The full version, when both strain amplitude and frequency are varied, provides a wealth of non-linear data and may be used for research purposes.

5. EFFECT OF MOLECULAR STRUCTURE OF POLYETHYLENE ON ITS RHEOLOGICAL AND PROCESSING BEHAVIOUR

– EXECUTIVE SUMMARY –

■

The effects of molecular weight and molecular weight distribution on rheological and processing behaviour were studied separately by using specially selected blends and resins

■

The melt fracture performance of a resin is linked to its characteristic relaxation time

5.1 Introduction

Linear low-density polyethylenes (LLDPE) are used in industry to manufacture films, pipes, sheets and profiles. The physical performance of products made with LLDPE resins depends on the molecular weight, molecular weight distribution, comonomer type and content, its distribution in the resin, and processing conditions. However, the processing characteristics of LLDPE resins are primarily influenced by the weight average molecular weight and the molecular weight distribution. A significant amount of research has been conducted in the past to study the effect of molecular weight and molecular weight distribution on the viscous and elastic behaviour of polyethylene resins [Han and Villamizar, 1978; Shroff and Mitsuzo, 1977; Bersted, 1976; Mendelson and Finger, 1975; Ishida *et al.*, 1971].

The weight average molecular weight (M_w) and the molecular weight distribution (MWD) affect the viscosity curve in different ways. Zero-shear viscosity in amorphous and linear polymers having molecular weight, M_w, above some critical value, has been found to be proportional to the 3.4-power of M_w. On the other hand, the variation of viscosity with shear rate is very dependent on MWD. A number of material functions that characterise the elastic behaviour of polymers including the steady-state compliance, first normal stress difference, extrudate swell, and capillary end correction, are extremely sensitive to MWD. For example, increase of the molecular weight, M_w, generally increases extrudate swell, but no simple relation between MWD and swell has been found because the effects of branching and MWD variation are difficult to separate [Dealy and Wissbrun, 1990].

A relevant way to evaluate the processability of polymers, particularly in extrusion applications, is to determine their melt fracture performance, i.e. to determine the critical shear stress and/or shear rate for the onset of the appearance of extrudate irregularities. Systematic information on

the influence of molecular weight distribution on the melt fracture performance of polyethylene resins is still very limited in the literature [Hatzikiriakos *et al.*, 1995; Goyal *et al.*, 1996]. Ramamurthy [1986] conducted an extensive study of the melt fracture phenomenon using a variety of polyethylene resins. He concluded that the surface melt fracture (loss of gloss, appearance of haziness and small amplitude periodic distortions) occurs at a critical shear stress between 0.1 and 0.14 MPa for all polyethylenes, regardless of molecular structure and temperature. However, the critical shear stress variation is much larger (0.1 – 0.5 MPa) across different families of polyethylene (including metallocene) resins. Furthermore, there is no general correlation reported in the literature between critical operating parameters and molecular characteristics of the resins. It also appears that the critical shear stress for the onset of melt fracture depends on a number of factors including temperature, geometric characteristics of dies (diameter and length-to-diameter ratio), metal of construction of the die, and thermal and processing history of the resin [Dealy and Wissbrun, 1990; Ramamurthy, 1986; Mounihan *et al.*, 1990; Pearson and Denn, 1997; Cogswell, 1977].

Recent observations suggest that there is a link between the tendency of a resin to exhibit melt fracture and a characteristic melt relaxation time. In other words, there seems to exist a correlation between the critical conditions for the onset of melt fracture and some characteristic relaxation time that can be defined in various ways. Sukhadia [1997] considered a characteristic time as the time scale parameter of the Carreau-Yasuda model. Wang *et al.* [1996] considered as a characteristic time the reciprocal of the crossover frequency of the two moduli (G' and G'') obtained from linear viscoelastic experiments. Finally, Wasserman [1997] used a characteristic relaxation time, defined as a measure of the breadth of the relaxation spectrum determined by analysing dynamic linear viscoelastic data. Wang *et al.* [1996] found that the sharkskin periodicity (time scale of small amplitude distortions) is directly proportional to the

relaxation time. In general, it has been found that the shorter the relaxation time, the better was the performance in terms of the onset of melt fracture [Sukhadia, 1997; Wang *et al.*, 1996].

The relationship between the key molecular characteristics and the processing performance of a polymer is quite complex and not fully understood. In an attempt to get one step closer to understanding the underlying mechanisms of that relationship, one must first determine the individual contribution of each molecular characteristic to the rheological behaviour of a given resin. Consequently, the purpose of the present study was to investigate the influence of two such characteristics, molecular weight and molecular weight distribution, on the rheological and processing behaviour of linear low-density polyethylene resins by changing both the M_w and its distribution.

5.2 Experimental

Materials included a series of linear low-density polyethylene resins (Series 1 and 2, see Chapter 4 for details on their molecular characteristics, GPC data and sample preparation procedures). To characterise the rheological and processing behaviour of the resins, the following experiments were performed. Linear dynamic oscillatory measurements were carried out for all resins at temperatures in the range of 160-220°C using: (a) a Rheometrics System IV equipped with 25 mm parallel plates and (b) an RDS-II spectrometer in the cone-and-plate geometry having a plate diameter of 25 mm and a cone angle of 0.1 rad. From the experiments the complex moduli, zero-shear viscosity, flow activation energy, relaxation spectra and crossover frequency were determined as functions of M_w and MWD.

An Interlaken sliding plate rheometer with a 0.5 mm gap was used to determine the absolute viscosities, which were also compared with Bagley- and Rabinowitch-corrected capillary data. A Kayeness capillary rheometer was used with dies having the same diameter and various length-to-diameter, L/D, ratios (10, 20 and 30). The pressure drop associated with changes in velocity profiles in the entrance and exit regions (end or Bagley correction) was calculated using the standard Bagley technique [Dealy and Wissbrun, 1990].

The processability of all polymers in terms of their melt fracture performance and ease of flow (apparent shear viscosities) were assessed by using a CEAST capillary rheometer at various apparent shear rates and a temperature of 200 °C. The melted polymer sample was extruded through a 1.0 mm (L/D = 20) tungsten carbide flat entry die. The extrudate swell measurements were also conducted for each sample at different shear rates. The measurements were performed on cooled samples and obviously do not represent the actual isothermal extrudate swell that is measured on-line as the polymer emerges from the die in the melt state [Dealy and Wissbrun, 1990]. The onset of melt fracture was also identified by means of visual inspection of the cooled extrudates.

5.3 RESULTS AND DISCUSSION

5.4 Rheological Testing

5.4.1 Linear viscoelasticity

The linear viscoelastic moduli of all polymers (representative data were plotted in Figure 4-6 and Figure 4-7) were used to determine their relaxation spectrum in terms of a discrete

spectrum of Maxwell relaxation times. Accordingly, the storage and loss moduli can be expressed in terms of the discrete Maxwellian spectrum as [Dealy and Wissbrun, 1990]:

$$G'(\omega) = \sum_i G_i \frac{(\omega\lambda_i)^2}{1+(\omega\lambda_i)^2} \text{ and } G''(\omega) = \sum_i G_i \frac{\omega\lambda_i}{1+(\omega\lambda_i)^2} \qquad \text{eq. 5-1}$$

To determine the pairs (G_i, λ_i) of eq. 5-1, a non-linear optimisation program (UBCFIT) was used [Rosenbaum and Hatzikiriakos, 1997]. The algorithm employed by the program results in the least number of (G_i, λ_i) parameters (so-called "parsimonious spectra") and was developed by Baumgartel and Winter [1989]. The spectra for the polymers in Series 1 (various polydispersities) and Series 2 (various molecular weights) are shown in Figure 5-1. Increase in polydispersity causes a higher degree of "shear-thinning" in the spectrum when G_i is plotted as a function of λ_i (see Figure 5-1a). On the other hand, increase in M_w shifts the spectrum to higher values of G_i, with the number of relaxation times needed to describe the data increasing as well (see Figure 5-1b). These observations are in agreement with previously reported results for the relaxation spectrum of other polymers [Winter *et al.*, 1993; Winter, 1997].

The calculated values of G' and G'' using the resulting spectrum and eq. 5-1 are plotted (solid lines) in Figure 4-6 and Figure 4-7 for Series 1 and 2, respectively. The overall agreement between experimental data and model predictions is good over the entire range of frequencies. The only apparent disagreement in Figure 4-6 occurs at low frequencies for the Series 1 resins and can be attributed to experimental error due to low transducer sensitivity.

The zero-shear viscosity of polyethylenes cannot be obtained directly from the experimental data without extrapolation, unless the rheometer has the capability of running at extremely small shear rates and one makes sure that degradation is not a problem. Two methods were

used to determine the zero-shear viscosity of all resins. First, it can be calculated from the determined relaxation spectrum as:

$$\eta_0 = \sum_i G_i \lambda_i \qquad \text{eq. 5-2}$$

The second method used was a fit of the complex viscosity data with the Carreau-Yasuda model:

$$\eta = \eta_0 \left[1 + (\lambda\dot{\gamma})^a\right]^{\frac{n-1}{a}} \qquad \text{eq. 5-3}$$

where η_0 is the zero-shear viscosity, λ is a characteristic relaxation time, and n and a are exponents. The zero-shear viscosities for both series of resins are shown in Figure 5-2 as functions of polydispersity and molecular weight, respectively. First, it can be seen from Figure 5-2a that the calculation using the spectra underestimates the zero-shear viscosities compared to the values from the Carreau-Yasuda model. For the Series 1 resins (all of high molecular weight), as polydispersity increases the zero-shear viscosity can only be approached at extremely low frequencies. Thus, by using spectra that were obtained over a limited range of frequency to calculate the zero-shear viscosity, a significant error is expected. However, it is clear from both methods that an increase in polydispersity increases the zero-shear viscosity significantly. For example, η_0 = 37.42 kPa·s for Blend 9 where M_w = 90,400 g/mol and PD = 12.7, while η_0 = 14.22 kPa·s for Blend 1 where M_w = 111,100 g/mol and PD = 3.3.

Figure 5-2b shows the effect of M_w on η_0. In this case it can be seen that both methods result in about the same values for the zero-shear viscosity. The reason for this agreement is that

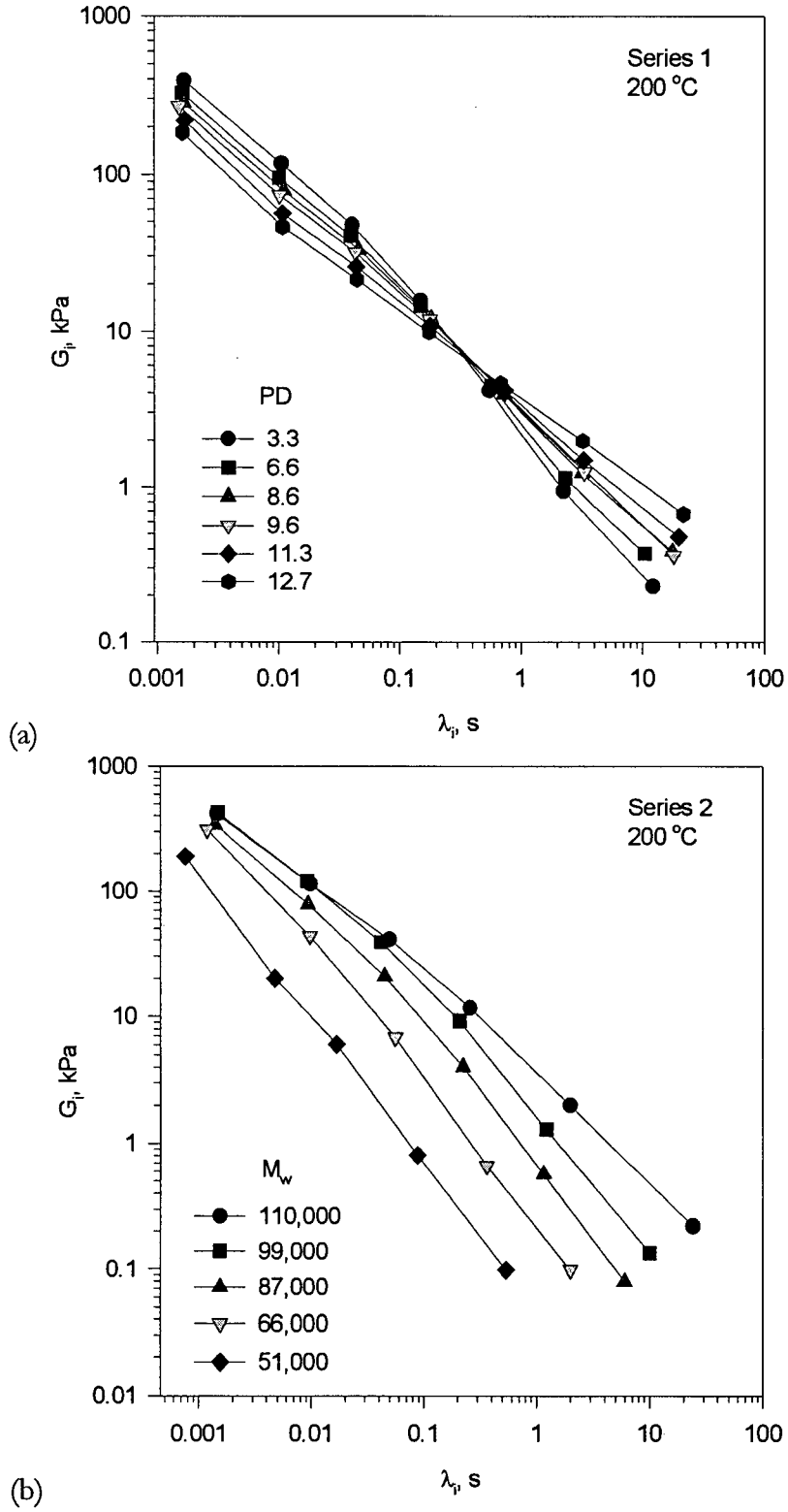

Figure 5-1. Relaxation time spectra showing effects of molecular characteristics of polyethylenes at 200°C, (a) varying polydispersity, (b) varying molecular weight.

polyethylenes in Series 2 are of narrow molecular weight distribution and some of them have a relatively small molecular weight. For such polymers, the zero-shear viscosity is obtained at frequencies much higher than those for polydisperse polymers of high molecular weight. It can also be seen from Figure 5-2b that η_0 is proportional to $M_w^{4.1}$. The effect of M_w on the zero-shear viscosity has been the subject of many theoretical and practical studies [Dealy and Wissbrun, 1990]. When η_0 was plotted as a function of M_w on a log-log scale, the value for the slope was reported to be about 3.4 for a number of linear polymers. In the present case the observed scaling is with the 4.1 power. This value may be considered reasonable taking into account that the value of 3.4 is valid only for linear polymers and it may be higher for slightly branched polymers with the exact value depending on the degree of branching.

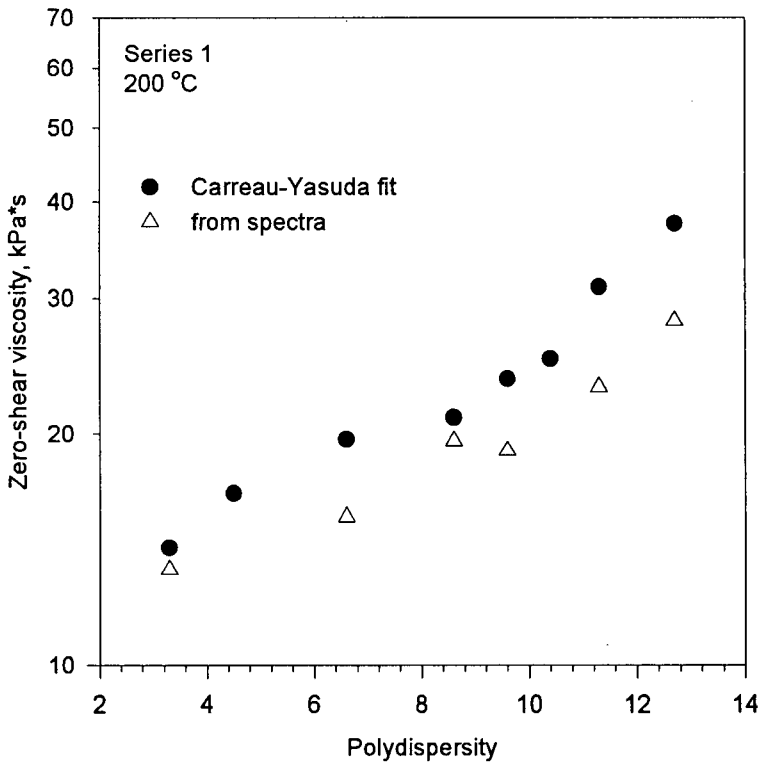

(a)

Figure 5-2. (a) The effect of polydispersity on the zero-shear viscosity.

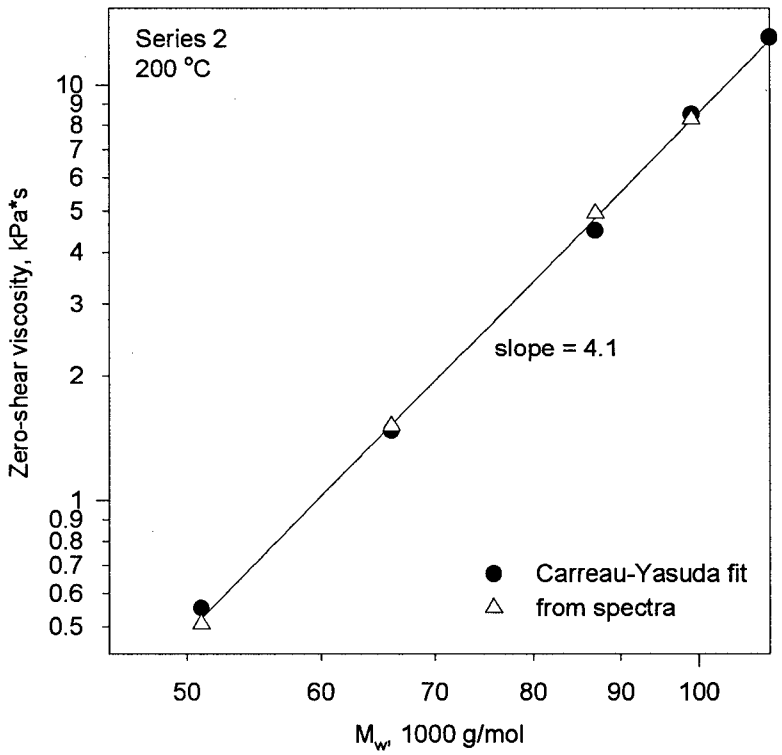

(b)

Figure 5-2. (b) The effect of molecular weight on the zero-shear viscosity.

The crossover frequency, where the storage (G') and loss (G'') moduli are equal, can serve as an indicator of the resin viscoelasticity. In other words, its inverse may represent a single characteristic relaxation time of a given resin [Tzoganakis, 1994]. Figure 5-3a shows the effect of polydispersity on the characteristic relaxation time defined by the crossover frequency. In general, increasing the polydispersity increases the characteristic time. Furthermore, there appears to exist a critical polydispersity (between 9 and 10) at which there is a sudden change in the slope. For polydispersities less than this critical value, the relaxation time depends weakly on polydispersity, with this dependence becoming stronger for highly polydisperse polyethylenes. As will be discussed later, this critical polydispersity is related to the optimum melt fracture performance for resins with a given molecular weight.

The molecular weight was found to have a strong effect on the resin relaxation time, as can be seen in Figure 5-3b. It can also be noted that the slope of relaxation time versus M_w on a double logarithmic curve approximately equals that of the zero-shear viscosity versus M_w curve, as expected [Bird *et al.*, 1987]. It was not possible to determine the relaxation time for the resin with the lowest M_w (51,000 g/mol), because the G' and G'' curves did not cross over within the accessible frequency range (0.01 to 500 rad/s).

Zeichner and Patel (1982) have noticed a correlation between the polydispersity of a linear resin and its crossover modulus ($G_c = G' = G''$). They have found that if a rheological polydispersity index defined as:

$$PI \equiv \frac{10^5}{G_c}, \text{ where } G_c \text{ is in Pascals} \qquad \text{eq. 5-4}$$

is plotted versus M_w/M_n on a double logarithmic plot, the data points fall on a straight line. Figure 5-4 plots the polydispersity index, *PI*, as a function of polydispersity. In our case, where a wider range of polydispersities is examined, there was no simple correlation between *PI* and polydispersity on a double logarithmic plot [Tzoganakis, 1994]. Instead, a change in slope is seen in Figure 5-4 at a critical polydispersity value about equal to that obtained from Figure 5-3a. As discussed later, this critical value of polydispersity corresponds to the optimum melt fracture performance for the resins in this series (see Figure 5-20a).

As it was mentioned before, the frequency sweep experiments were carried out at four different temperatures (160, 180, 200, and 220°C) in order to determine the temperature dependence of the viscoelastic properties of the resins. This can be done by applying the time-temperature superposition principle [Dealy and Wissbrun, 1990] to determine the shift factor, a_T. An Arrhenius equation, that is,

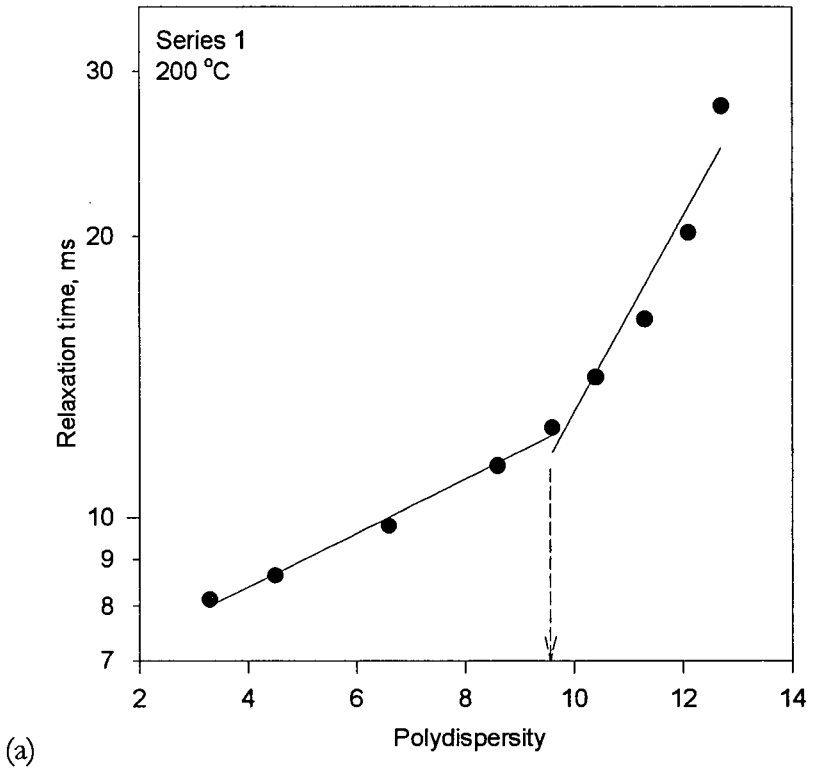

(a)

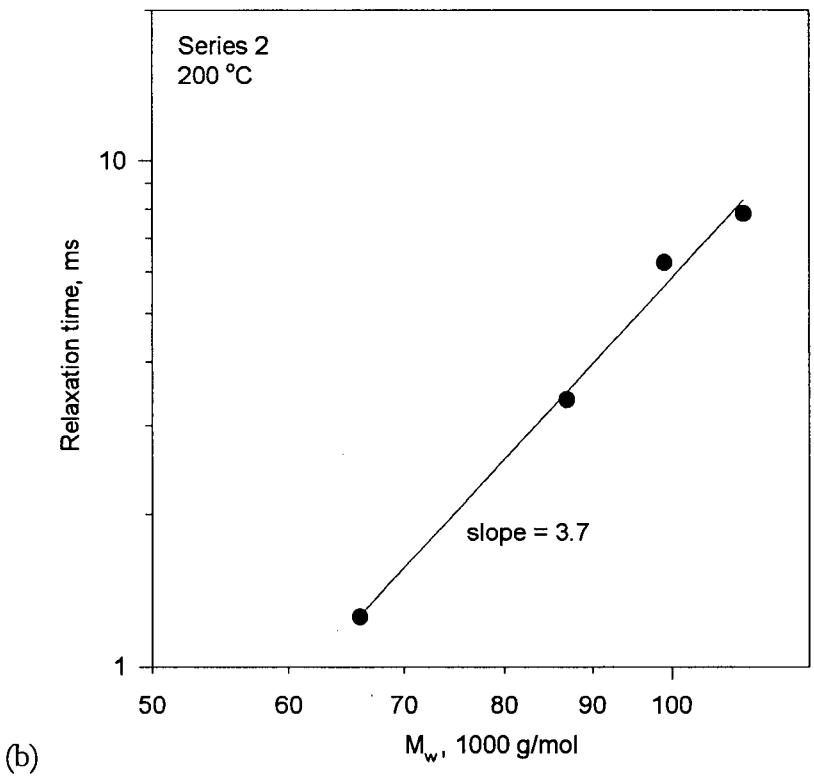

(b)

Figure 5-3. (a) The effect of polydispersity on relaxation time (inverse of crossover modulus). (b) The effect of molecular weight on relaxation time.

$$\alpha_T = \exp\left[\frac{E_a}{R}\left(\frac{1}{T} - \frac{1}{T_{ref}}\right)\right] \qquad \text{eq. 5-5}$$

where T_{ref} is the reference temperature (taken as 473 K here), was found to fit all the data well. The values of the calculated flow activation energy, E_a, are plotted in Figure 5-5 as a function of polydispersity and molecular weight, respectively. The flow activation energy for the tested resins in Series 1, increases with polydispersity. It is also known that the flow activation energy increases with increase of short/long chain branching and in general with the comonomer content [Mavridis and Shroff, 1992; Wang and Porter, 1995]. In our case, all polymers in Series 1 have the same comonomer type and content. The flow activation energy also decreases with increase of molecular weight (Figure 5-5b). The origins of these findings are not known,

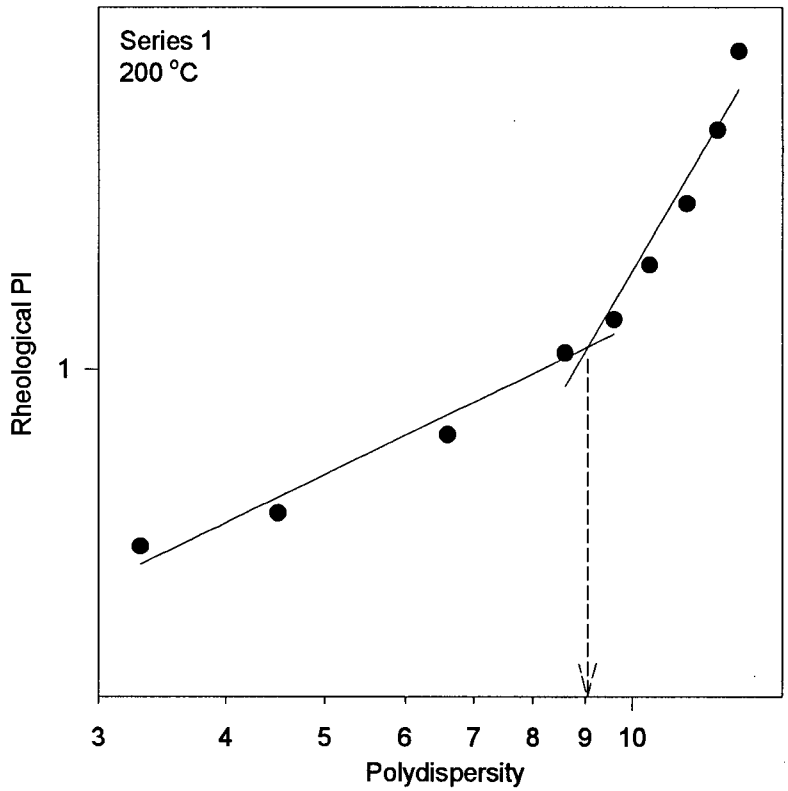

Figure 5-4. The rheological polydispersity index as a function of polydispersity.

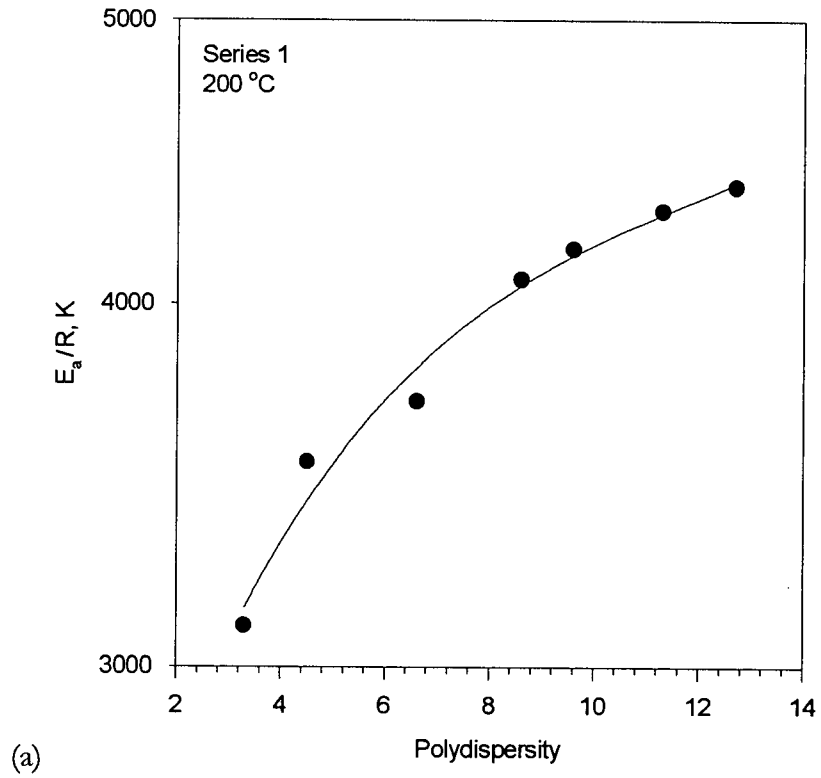

(a)

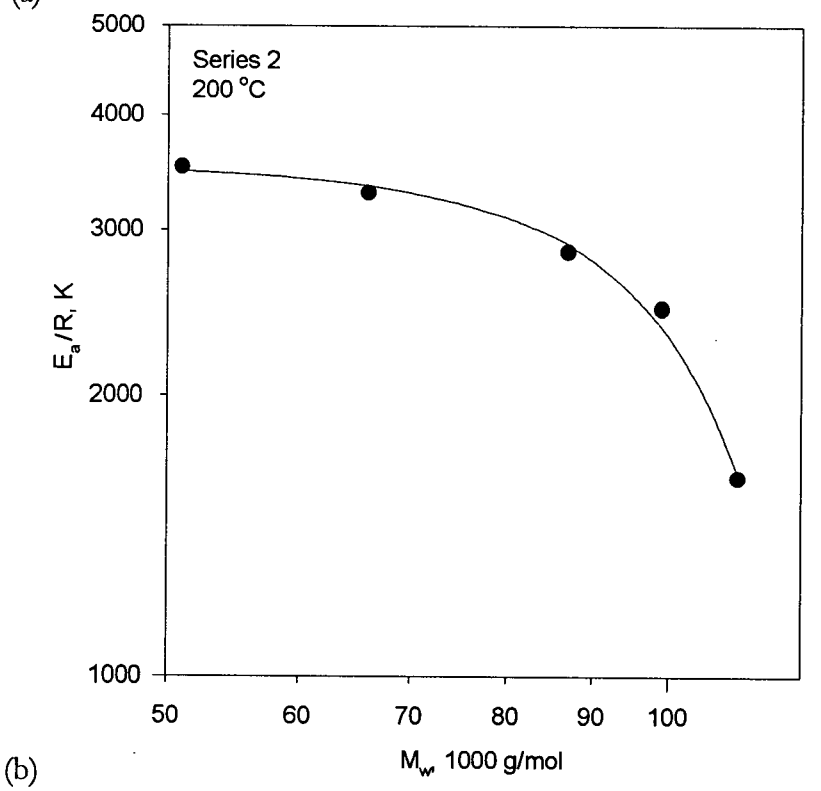

(b)

Figure 5-5. (a) The effect of polydispersity on the flow activation energy. (b) The effect of molecular weight on the flow activation energy.

although a reasonable explanation can be given in terms of the free volume concept. In other words, polydispersity increases free volume which renders rheological properties more sensitive to temperature changes, whereas M_w decreases the free volume due to much less mobile $-CH_3$ end groups. Finally, it is noted that the magnitudes of the flow activation energy for all polymers in this work are in agreement with those reported earlier for linear polyethylenes [Wang and Porter, 1995].

5.4.2 Start-up of Steady Shear

Start-up and cessation of steady shear are frequently used methods for studying non-linear viscoelasticity [Dealy and Wissbrun, 1990]. In the start-up test, a sample initially at rest is subjected to a steady shear rate, $\dot{\gamma}$, and the shear stress is monitored as a function of time. The relevant material function is the shear stress growth coefficient:

$$\eta^+(t,\dot{\gamma}) = \frac{\sigma(t)}{\dot{\gamma}} \qquad \text{eq. 5-6}$$

If the shear rate is small enough, the non-linear shear stress growth coefficient becomes equal to its linear counterpart:

$$\lim_{\dot{\gamma}\to 0}\left[\eta^+(t,\dot{\gamma})\right] = \eta^+(t) \qquad \text{eq. 5-7}$$

which can be expressed in terms of the parameters of the generalised Maxwell model as

$$\eta^+(t) = \sum_{i=1}^{N} G_i\lambda_i\left(1-e^{-t/\lambda_i}\right) \qquad \text{eq. 5-8}$$

Note that eq. 5-8 at large times reduces to eq. 5-2, i.e. η^+ becomes η_0.

The start-up test was performed with the resins in Series 1. Figure 5-6 depicts typical data obtained for Blend 1. The experimental curves were obtained for shear rates ranging from 0.5

to 200 s^{-1}. The linear shear stress growth coefficient was calculated using eq. 5-8. It can be seen that the lower the shear rate, the closer the curves approach the limiting linear behaviour. Typical start-up overshoots can also be noticed at high shear rates; they become smaller as the shear rate is decreased. Note that the waviness at low shear rates is due to experimental noise at low levels of shear stress.

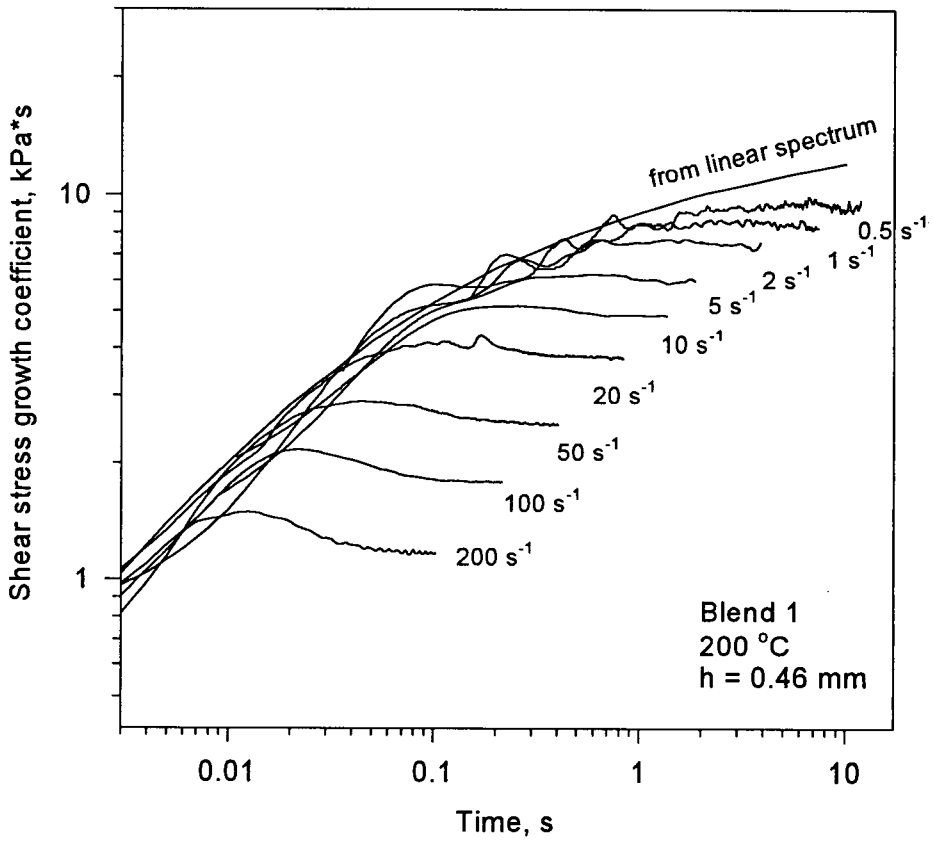

Figure 5-6. Start-up of steady shear curves for Blend 1 at 200 °C, obtained at different shear rates.

The shear stress growth coefficient is not the only material function which can be determined from start-up experiments. As will be described later in this chapter, the characteristic relaxation time of a polymer melt plays an important role in its melt fracture performance. Such a characteristic relaxation time can be defined as the ratio of the viscosity at some specified shear rate to the shear modulus. The required shear modulus can easily be obtained

from the start-up of steady shear data, specifically, from the slope of the rising segment of the start-up curves. Figure 5-7 illustrates that a typical start-up curve has a region where the stress rises almost linearly as a function of time (and consequently, shear strain). The shear modulus is then calculated from the slope according to the following equation:

$$G = \frac{d\sigma}{d\gamma} \qquad \text{eq. 5-9}$$

The shear moduli were determined for the Series 1 blends and are shown in Figure 5-8 for five selected blends as functions of shear rate. As can be seen, the shear modulus decreases with shear rate and with polydispersity. These values will be used later to develop the correlation for melt fracture performance.

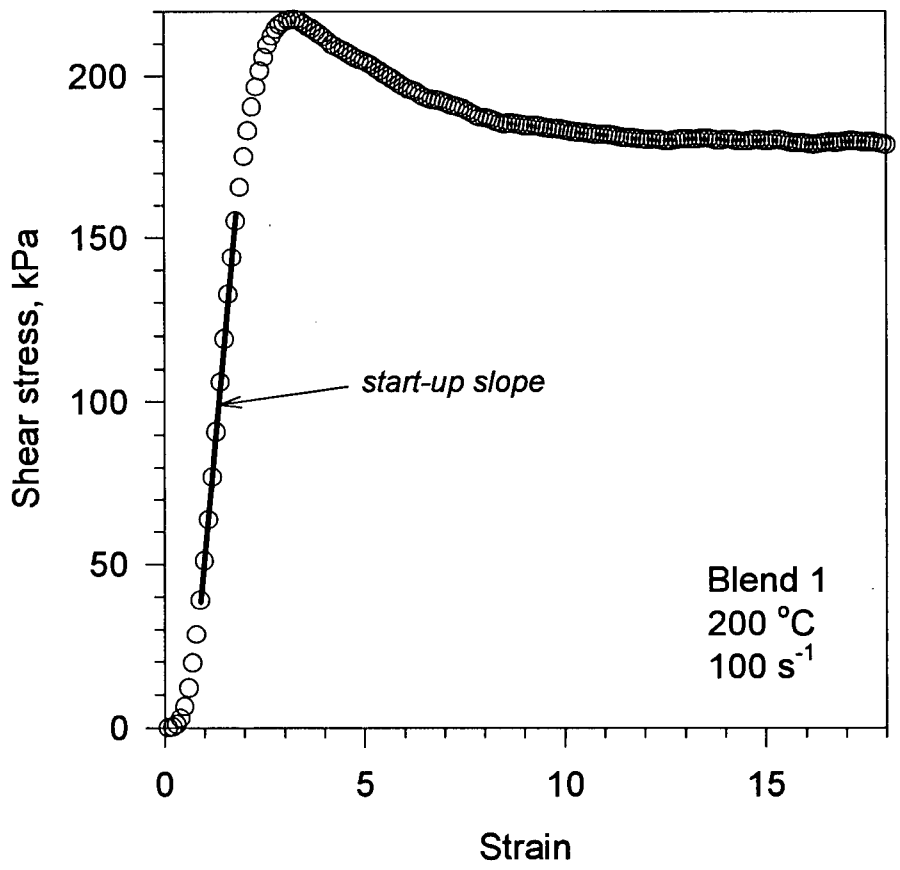

Figure 5-7. Determination of slope from the start-up test on the example of the data for Blend 1 at 100 s^{-1}.

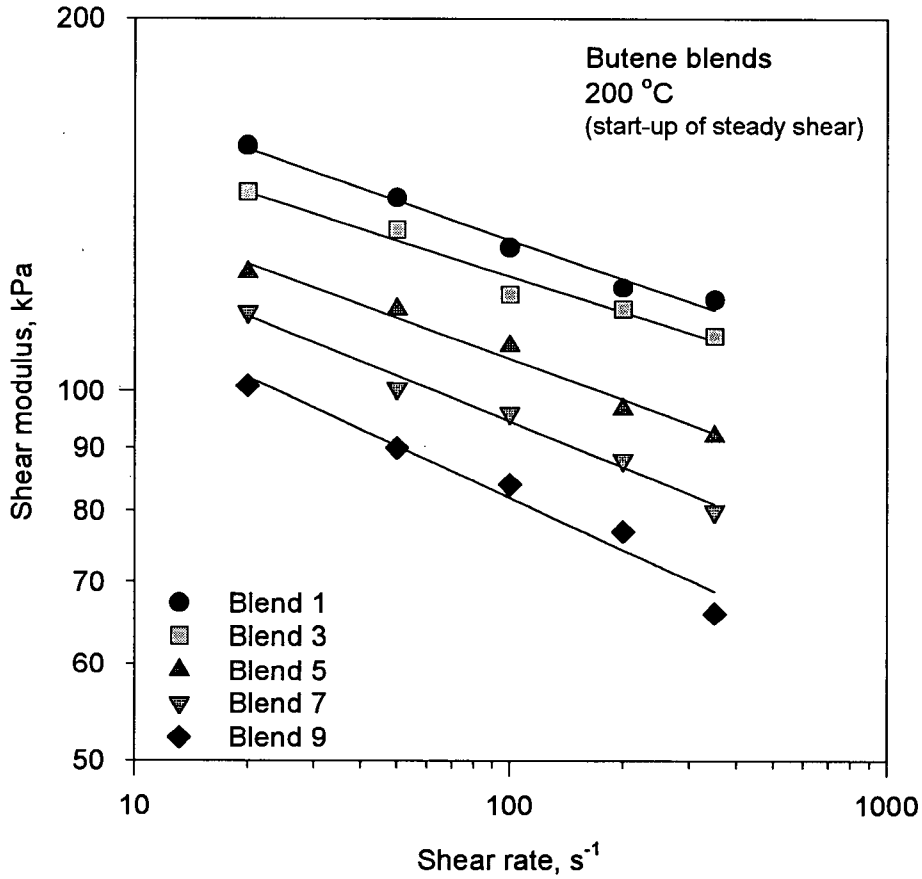

Figure 5-8. Shear moduli of the Series 1 blends determined from the start-up experiments.

5.4.3 Cessation of Steady Shear

In this test, a sample is subjected to steady shear at a shear rate $\dot{\gamma}$. Once the shear stress reaches a steady-state value, the motion is suddenly halted, and the stress is measured as a function of time. The relevant material function is the shear stress decay coefficient:

$$\eta^{-}(t,\dot{\gamma}) = \frac{\sigma(t)}{\dot{\gamma}} \qquad \text{eq. 5-10}$$

This test was performed with the Series 1 resins, and the results for selected resins at the shear rates of 1, 5 and 20 s^{-1} are plotted in Figure 5-9 to Figure 5-11. In order to make the comparison between resins easier, the shear stress decay coefficient, $\eta^{-}(t,\dot{\gamma})$, was normalised

with respect to steady-state viscosity at the corresponding shear rate, $\eta(\dot{\gamma})$. Therefore, all the curves of the shear stress decay coefficient start at the value of 1. Several observations can be made:

1. As the shear rate increases, the relaxation of the stress occurs more rapidly. This indicates that pre-shearing affects the relaxation process.
2. The rate of decay is higher for Blend 1 (having the lowest polydispersity value). This holds true for all shear rates used in the test. Stress relaxation is a measure of elasticity, and since Blend 9 is the most polydisperse, it is expected to be more elastic.
3. There is a saddle point in the relaxation curve at a time of about 0.2 second. It is more pronounced for Blend 1 at the lowest shear rate of 1 s^{-1} (Figure 5-9). An increase in polydispersity from 3.3 (Blend 1) to 12.7 (Blend 9) results in weakening of this feature. As the shear rate is increased to 5 s^{-1}, it loses intensity (Figure 5-10), and completely disappears at the shear rate of 20 s^{-1} (Figure 5-11).

It is interesting to note that the above mentioned relaxation feature at small shear rates is not observed for polyisobutylene (Figure 5-12). This indicates that the observed behaviour of the Series 1 resins is not an experimental flaw, but rather a manifestation of some relaxation mechanisms occurring on different time scales. A similar behaviour has been observed [Dealy and Wissbrun, 1990] for concentrated solutions of polystyrene having a high molecular weight and a narrow molecular weight distribution. These polystyrene solutions exhibited complex relaxation behaviour, with two inflexion points, similar to that of Blend 1 at 1 s^{-1}. This suggests the appearance of another relaxation process that did not manifest itself in the linear viscoelastic regime.

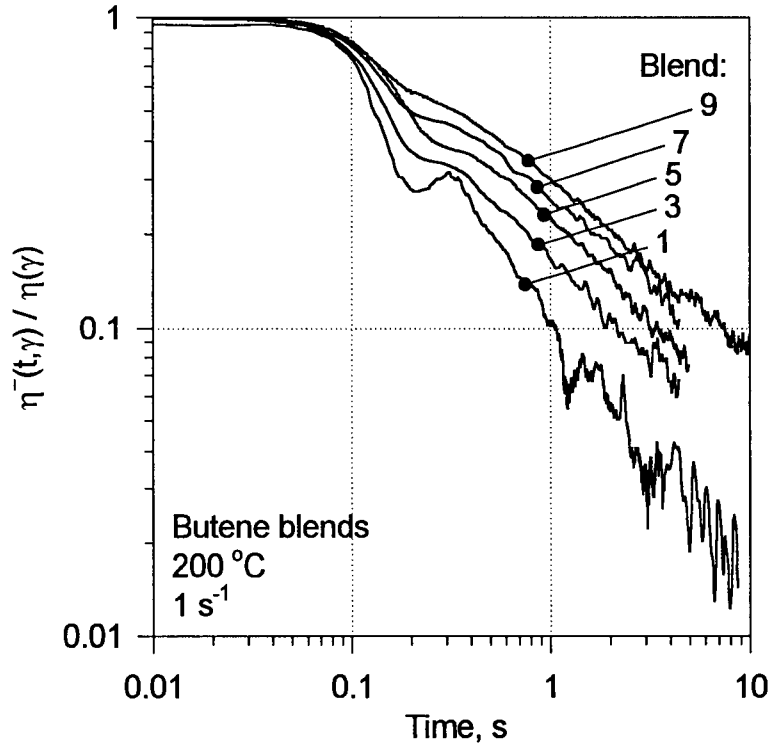

Figure 5-9. Normalised shear stress decay coefficient for the Series 1 resins measured after steady shear at 1 s^{-1} and 200 °C.

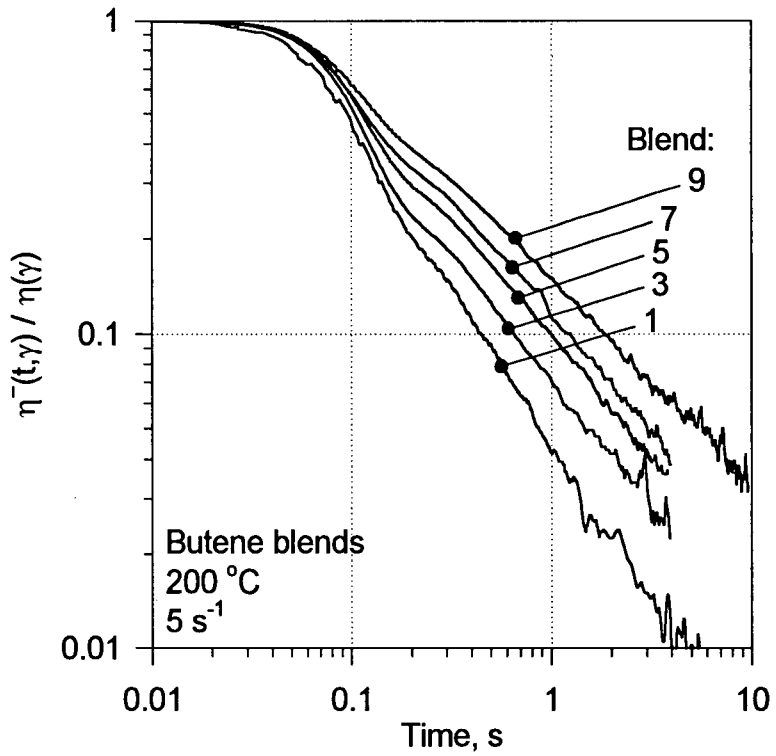

Figure 5-10. Normalised shear stress decay coefficient for the Series 1 resins measured after steady shear at 5 s^{-1} and 200 °C.

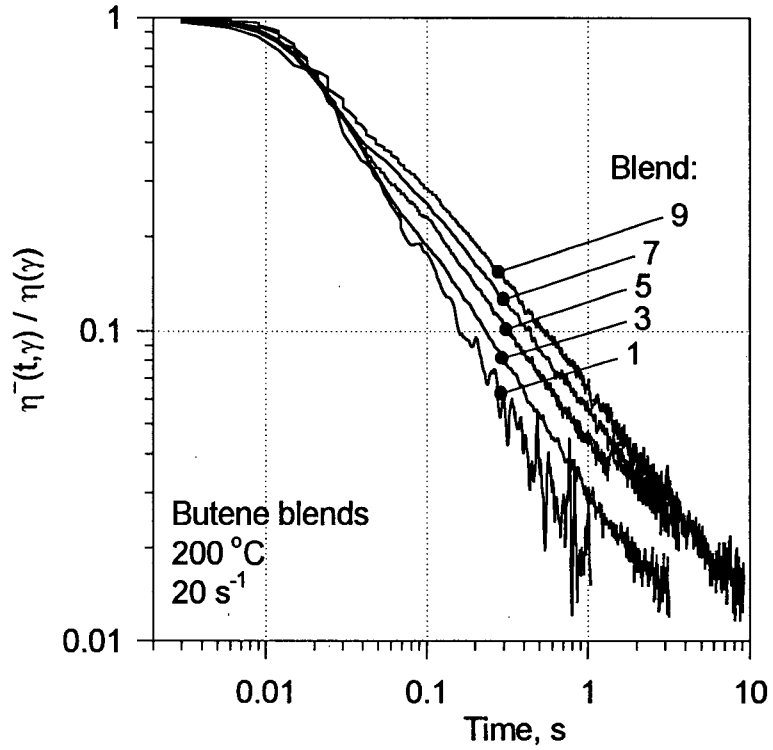

Figure 5-11. Normalised shear stress decay coefficient for the Series 1 resins measured after steady shear at 20 s^{-1} at 200 °C.

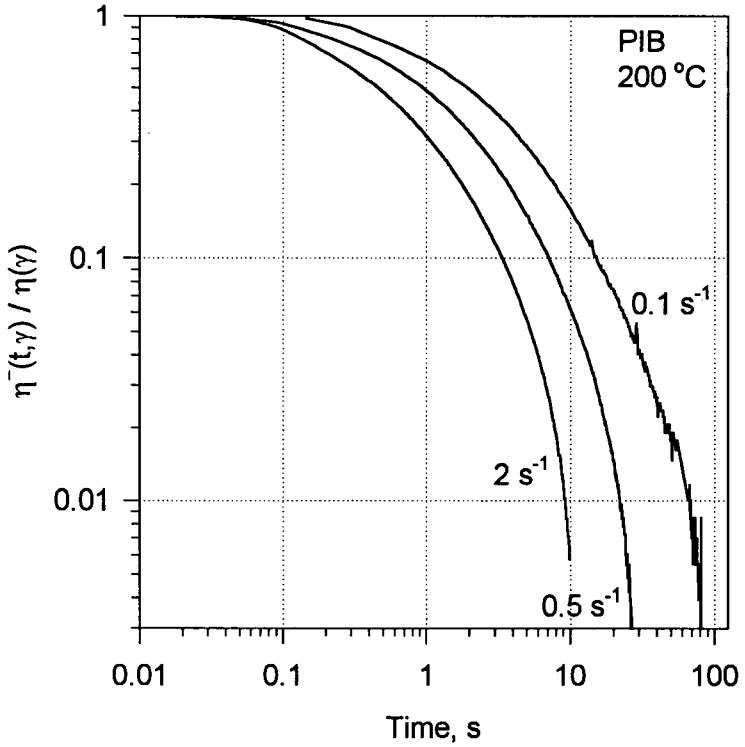

Figure 5-12. Normalised shear stress decay coefficient for polyisobutylene at 200 °C.

5.4.4 Exponential shear

Exponential shear is the type of deformation that is of special interest, since it generates a high degree of molecular stretching and thus a "strong" flow [Dealy and Wissbrun, 1990]. The strain changes according to the following relation:

$$\gamma(t) = A\left(e^{\alpha t} - 1\right) \qquad \text{eq. 5-11}$$

where A is the strain scale factor and α is the exponential rate constant. By differentiating, the shear rate is given by:

$$\dot{\gamma}(t) = \alpha A e^{\alpha t} \qquad \text{eq. 5-12}$$

The response quickly becomes non-linear since the shear rate increases exponentially. It is not possible to define a material function for this type of flow that would be independent of α. However, it has been suggested [Dealy and Wissbrun, 1990] that the exponential shear data be presented in the form of the exponential viscosity:

$$\eta^e(t, \alpha, A) = \frac{\sigma(t, \alpha, A)}{\dot{\gamma}(t)} \qquad \text{eq. 5-13}$$

An example of the shear stress response in this type of experiment is shown in Figure 5-13 for Blend 5. The data were obtained with a fixed strain scale factor of 0.1 and six different values of the exponential rate constant, α. The curves are characterised by a sharp increase in shear stress in the beginning, which slows down later due to molecular stretching, and a rapid drop in the melt exponential viscosity. Figure 5-14 illustrates this: the exponential viscosity is lower and drops faster at higher values of the exponential rate constant.

The exponential viscosities were determined for the Series 1 blends and are compared in Figure 5-15. It can be seen that at the lowest value of the exponential rate constant (α = 0.1, upper left graph) the exponential viscosities at first scale with the molecular weight distribution, i.e. at low γ, η^e for

Blend 9 is the highest and η^e for Blend 1 is the lowest. As γ increases, the difference in the exponential viscosities between the blends disappears. It can also be noted that, with an increase in the exponential rate constant, α, the exponential viscosity for Blend 9 becomes lower than that for Blend 1, while the values for the other two blends remain in between.

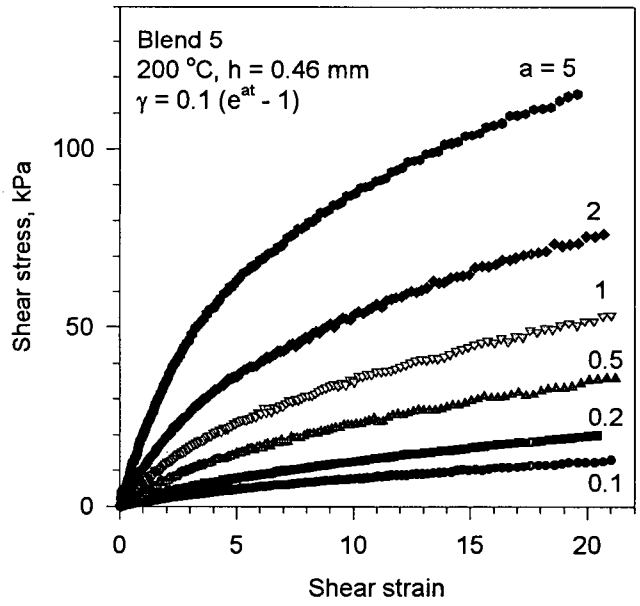

Figure 5-13. Shear stress response of Blend 5 in exponential shear experiments with different values of the exponential rate constant.

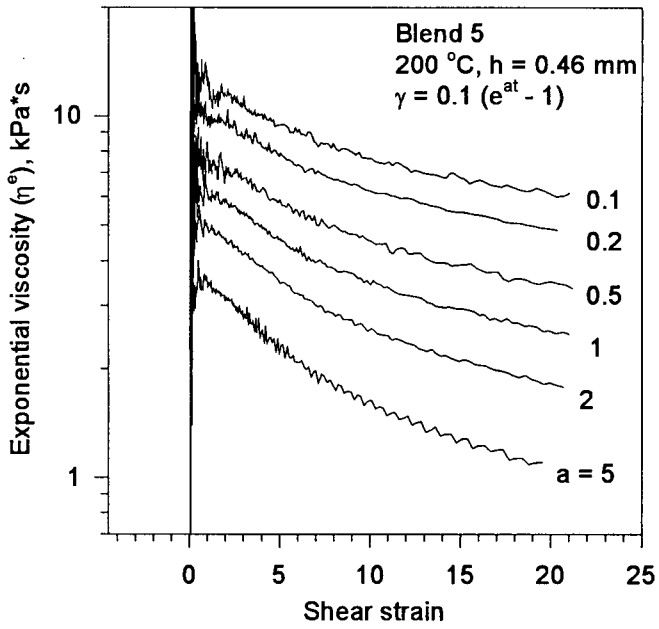

Figure 5-14. Exponential viscosity of Blend 5 at the same conditions as in Figure 5-13.

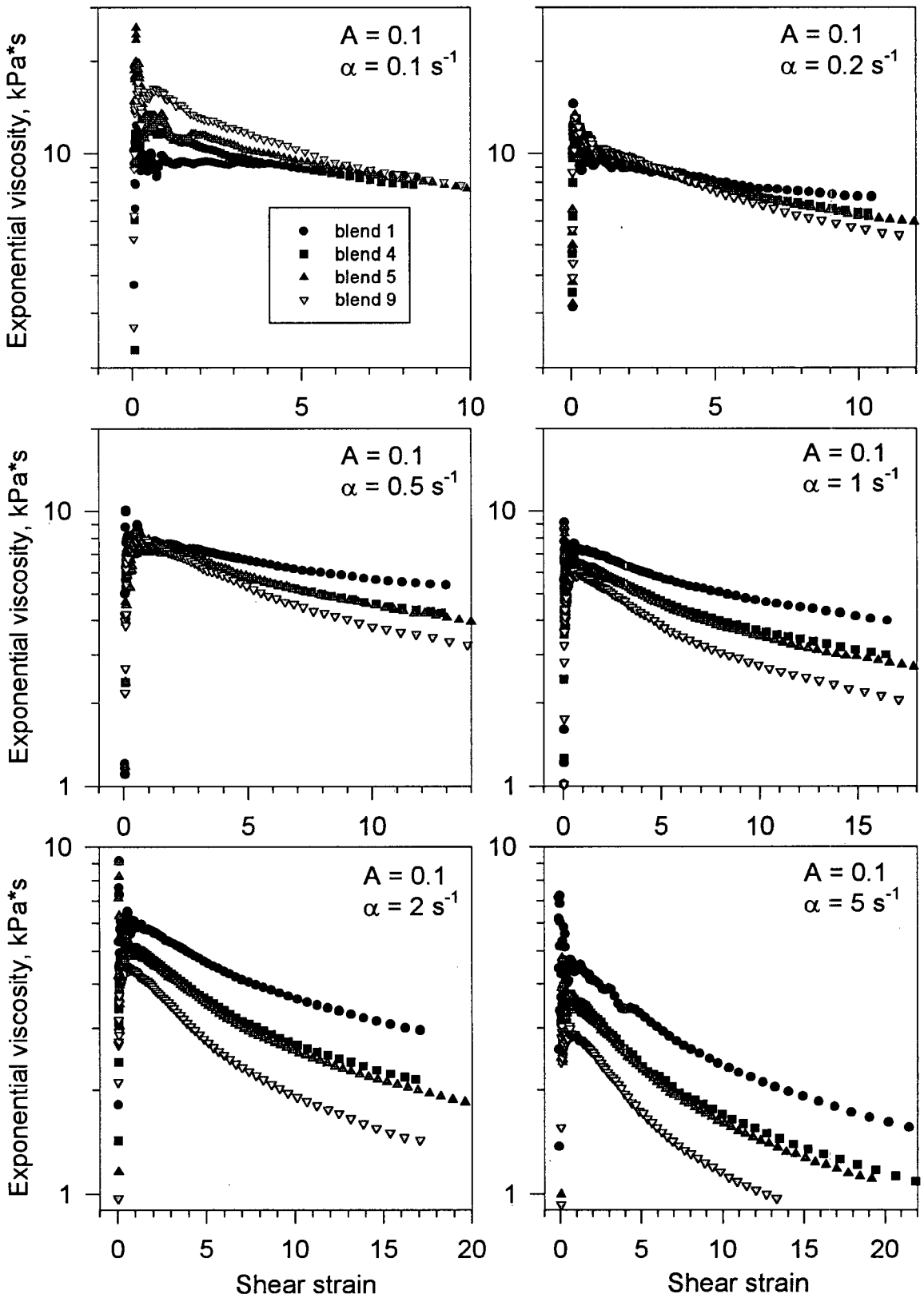

Figure 5-15. Comparison of exponential viscosities for Blends 1, 4, 5, 9 obtained at the same strain scale factor and six different exponential rate constants.

5.4.5 Viscosity

Figure 5-16a compares the complex viscosity (from dynamic parallel-plate experiments) with the absolute viscosity determined using the sliding plate rheometer for representative polymers of Series 1 (various polydispersities). It can be seen that overall a good agreement exists between the dynamic and absolute viscosities, thus validating the Cox–Merz rule [Dealy and Wissbrun, 1990] over the range of shear rates (or frequencies) of at least up to about 30 s^{-1}. It can also be seen that an increase in polydispersity increases the degree of shear thinning and the zero-shear viscosity of the polymers (as discussed before).

Figure 5-16b compares the complex viscosity (from dynamic parallel-plate experiments) with the absolute viscosity determined using the sliding plate and capillary rheometers for representative polymers of Series 2 (various molecular weights). There is again a very good agreement between all three sets of experimental data. It is noted that Bagley and Rabinowitsch corrections [Dealy and Wissbrun, 1990] were applied to the capillary data in order to transform apparent viscosities and apparent shear rates into true quantities.

Figure 5-17 plots the Bagley correction of representative polymers in Series 1 as a function of the wall shear stress. It is interesting to note that the values of the Bagley correction for Blend 9 (higher polydispersity) are higher than those for Blend 1, even though the viscosity of Blend 9 is lower at the corresponding shear rate value (see Figure 5-16a). However, it is known that the elastic properties of polyethylenes increase with polydispersity, and since the entrance pressure (Bagley correction) can serve as an indication of the level of extensional viscosity of resins [Cogswell, 1981], this observation (increase of Bagley correction with polydispersity) is in order.

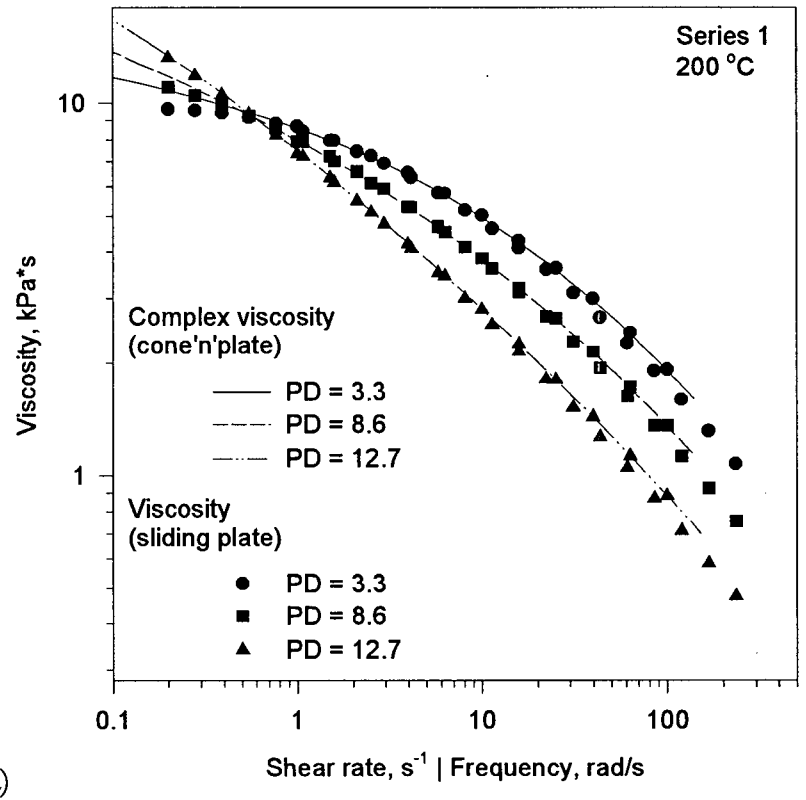

(a)

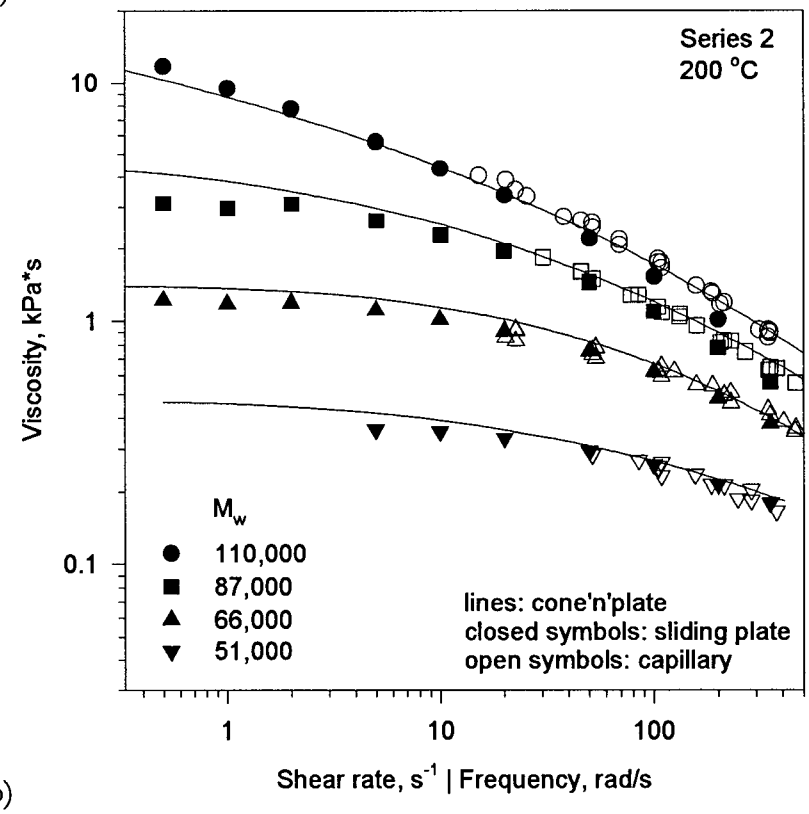

(b)

Figure 5-16. The viscosity of polymers in Series 1 and 2 at 200°C obtained using different instruments: (a) sliding plate rheometer and cone-and-plate rheometer, (b) capillary, sliding plate and cone-and-plate rheometers.

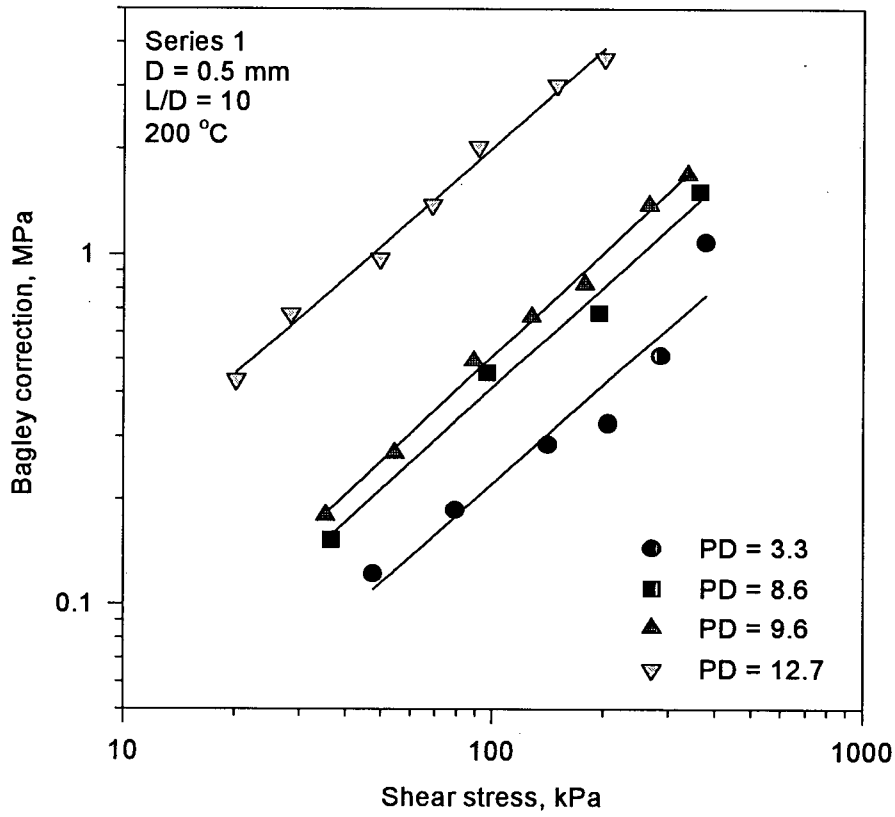

Figure 5-17. The effect of polydispersity on the Bagley correction at 200°C.

5.5 Processing Results

5.5.1 Critical Conditions for the Onset of Melt Fracture

As discussed above, a second capillary rheometer was also used to assess the processability of all resins in terms of ease of flow and melt fracture performance. Figure 5-18 depicts the apparent shear viscosities of polyethylenes in Series 1 and 2, respectively, as functions of the apparent shear rate. Filled symbols represent data points, where no visual defect (no surface or gross melt fracture) was observed on the surface of extrudates. On the other hand, open symbols correspond to experiments where surface defects were observed on the extrudates (surface/sharkskin or gross melt fracture).

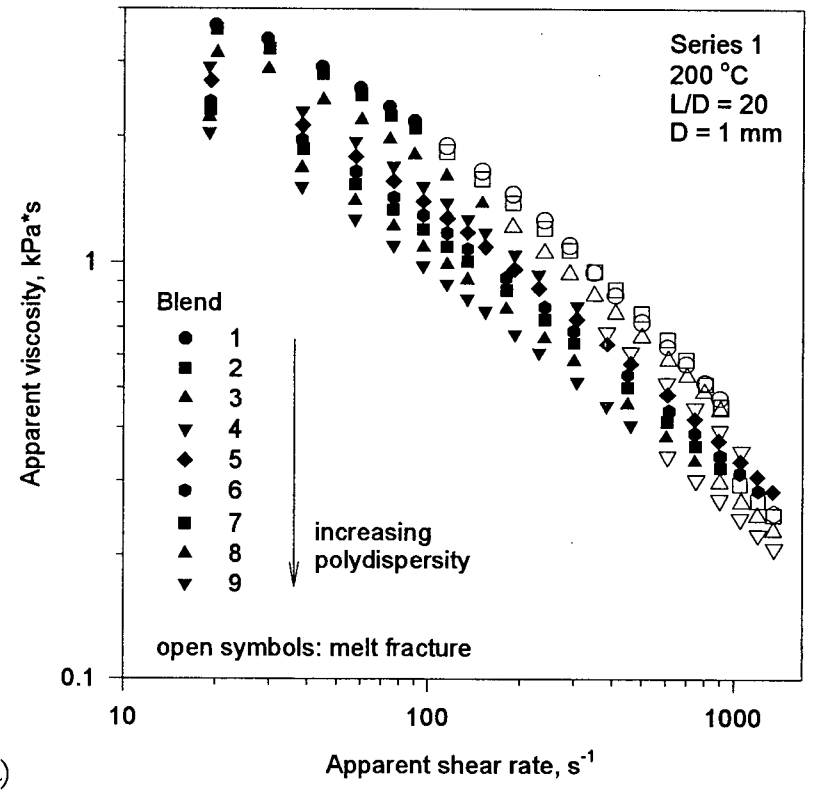

(a)

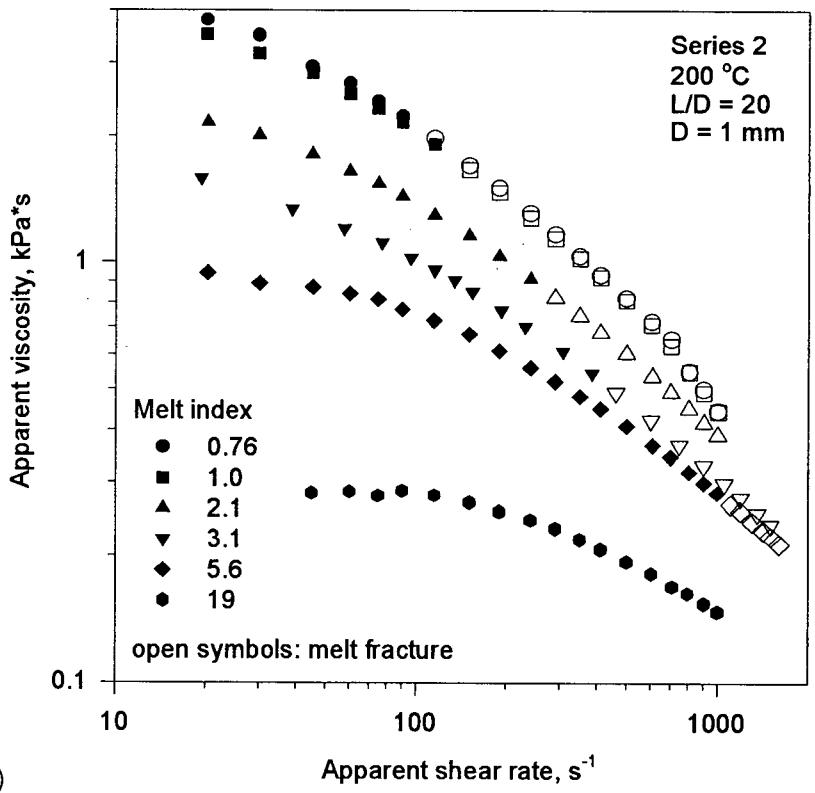

(b)

Figure 5-18. Effect of molecular characteristics on apparent viscosity profiles, (a) varying polydispersity, (b) varying molecular weight.

The influence of the molecular weight distribution on the extrudate swell ratio is illustrated in Figure 5-19a at several levels of shear rate. Again, the expected behaviour of an increase in extrudate swell with increase in polydispersity and shear rate can clearly be seen. Figure 5-19b illustrates the effect of molecular weight, M_w, on the extrudate swell of polyethylenes belonging to Series 2. As expected, an increase in M_w, and shear rate, increases the extrudate swell.

The influence of molecular characteristics (MWD and M_w) on the apparent shear rate for the onset of melt fracture is shown in Figure 5-20. As seen in Figure 5-20a, the apparent shear rate for the onset of melt fracture slowly increases as polydispersity is increased from 3.3 to 8.6. At this critical value (about the same with the critical value seen in Figure 5-3a and Figure 5-4), the shear rate for the onset of melt fracture increases dramatically between polydispersities of 8.6 and 9.6. A further broadening of the molecular weight distribution beyond the polydispersity of about 10 actually results in a reduction of the apparent shear rate for the onset of melt fracture. These results are quite surprising and, to our knowledge, have not been previously reported in the literature.

Furthermore, the type of melt fracture observed on the extrudates at its onset also appears to be influenced by the molecular weight distribution of polyethylene resins (see Figure 5-21). Below the polydispersity of 8.6, the capillary extrudates initially showed a sharkskin type (low amplitude, high frequency) of melt fracture (sample A). Above the polydispersity of 9.6, a wavy type (high amplitude, low frequency) melt fracture was observed (sample B), even though all the resins employed in this study were LLDPE resins having similar densities. It appears that the sharkskin type of melt fracture can essentially be eliminated, if the polydispersity of a resin

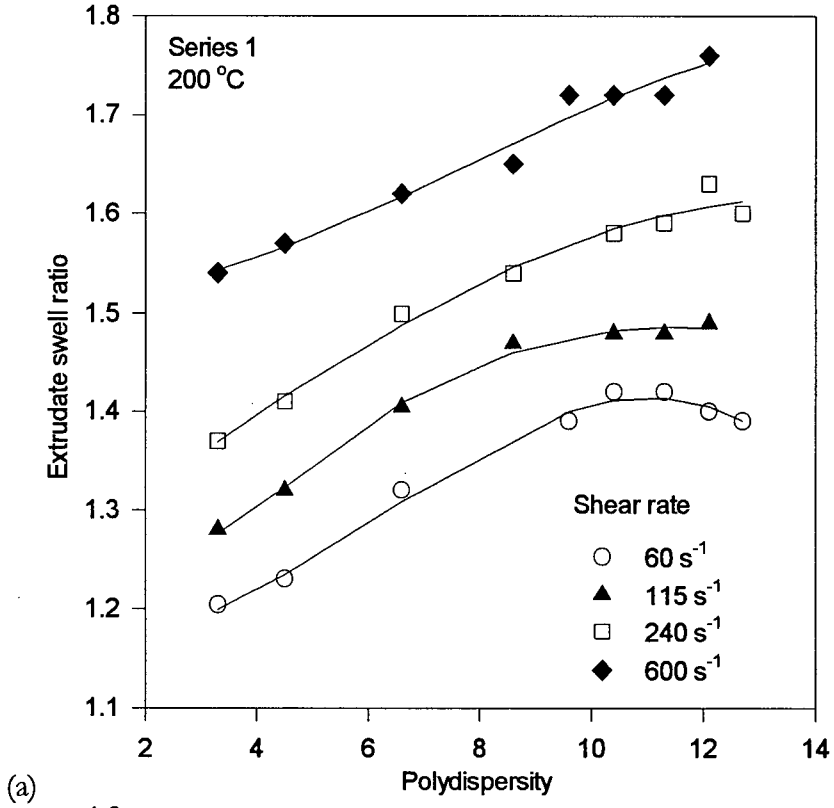

(a)

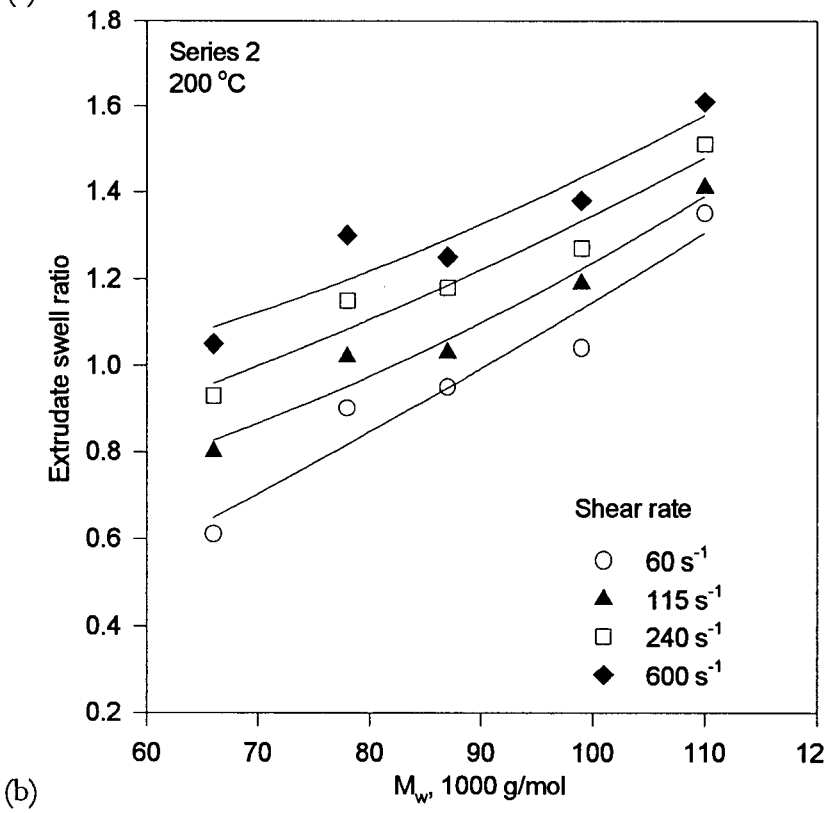

(b)

Figure 5-19. (a) The effect of polydispersity on the extrudate swell ratio at 200°C. (b) The effect of molecular weight on the extrudate swell ratio at 200°C.

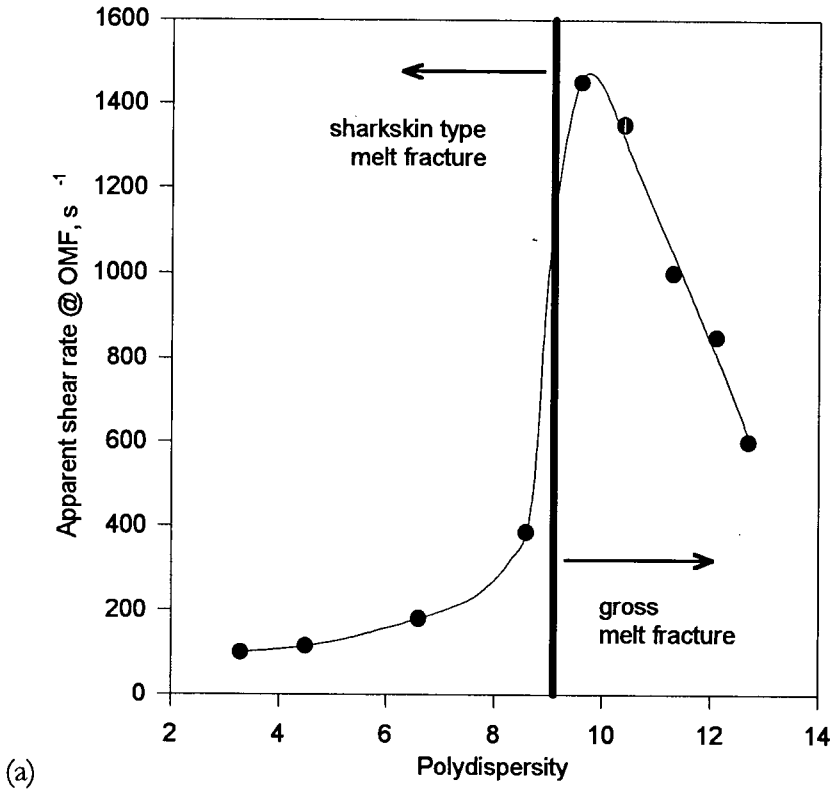

(a)

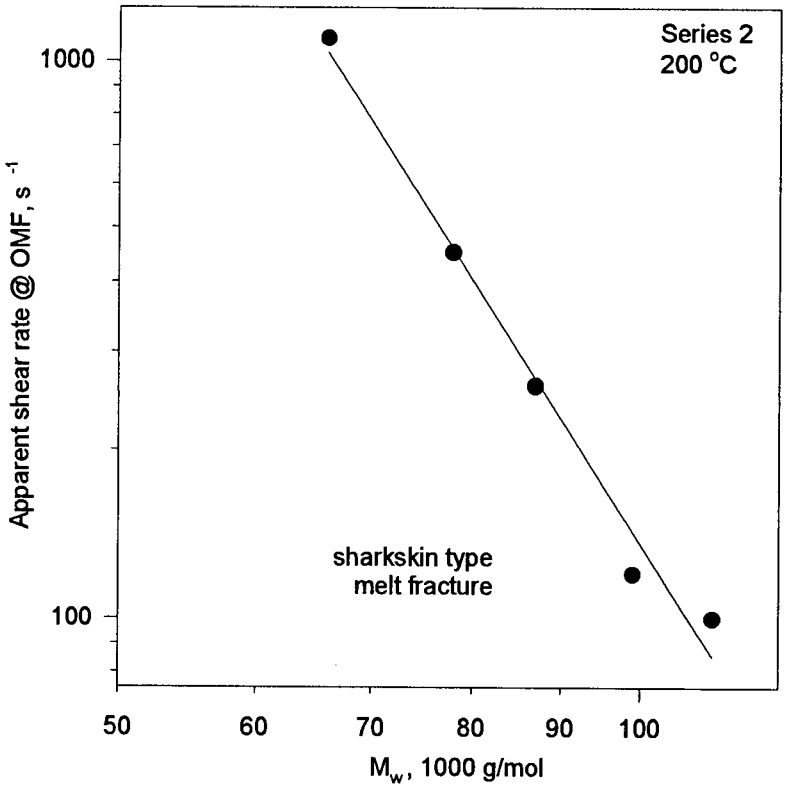

(b)

Figure 5-20. (a) The effect of polydispersity on the critical apparent shear rate for the onset of melt fracture. (b) The effect of molecular weight on critical apparent shear rate for the onset of melt fracture.

is increased above a value of about 10. On the other hand, increasing the polydispersity above 10, gross melt fracture starts appearing at smaller apparent shear rates. Thus, the optimum performance is obtained at a polydispersity between 8.6 and 9.6.

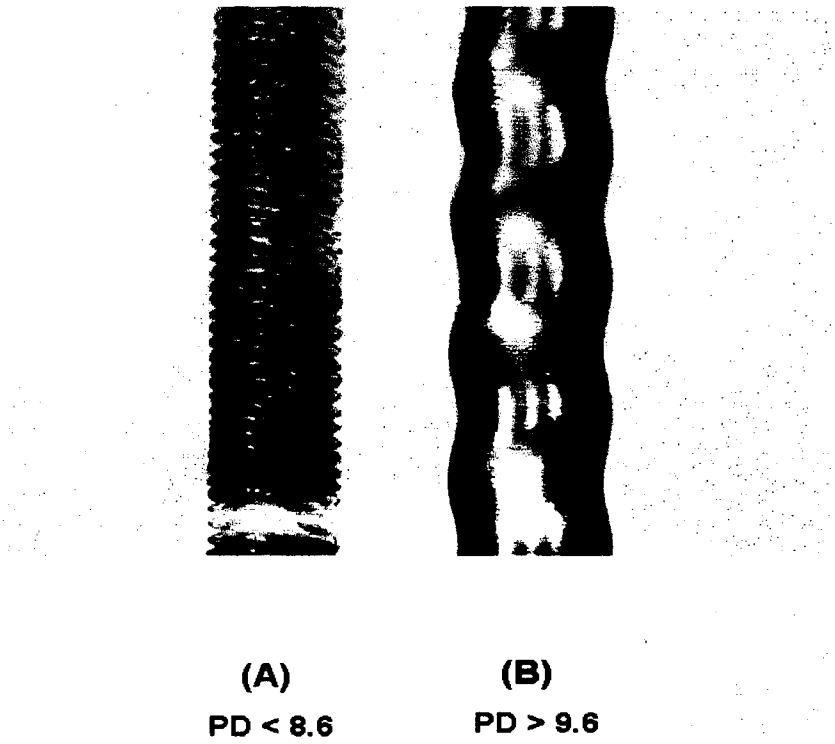

Figure 5-20. Typical fractured extrudate appearances of polymers in Series 1.

Figure 5-20b illustrates the effect of M_w on the critical apparent shear rate for the onset of melt fracture. As expected, the critical rate decreases with an increase of M_w (Figure 5-20b). In fact, a power-law dependence was found (critical rate $\propto M_w^{-5}$). The type of melt fracture at its onset was always sharkskin, in agreement with the results plotted in Figure 5-20a, since the Series 2 polyethylenes have polydispersities much smaller than 10. Melt fracture was not observed for the polymer having the lowest average molecular weight (M_w = 51,000; MI = 19.2). It is noted that Figure 5-20 plots the critical apparent shear rate for the onset of melt fracture and not the shear stress. However, the same picture is obtained when critical shear stress is plotted as a

function of M_w and polydispersity. This means that the critical shear stress at the onset of melt fracture is also strongly influenced by the molecular weight distribution of LLDPE resins.

5.5.2 A Criterion/Correlation for the Onset of Melt Fracture

It is important to note that although the melt fracture performance of the sample with polydispersity of 9.6 was the best (Figure 5-20a) among polymers in Series 1, none of the other rheological properties have shown a maximum at this critical value of polydispersity. This suggests that the polymer properties governing the melt fracture performance of LLDPE resins are still to be identified. Furthermore, as discussed before, a characteristic relaxation time may be a relevant quantity to formulate a criterion/correlation for the onset of melt fracture [Wang *et al.*, 1996; Wasserman, 1997]. Based on these studies, a hypothesis may be formulated that the melt fracture behaviour of a polymer is affected by a balance between its viscous (viscosity) and elastic properties (recoverable shear). This hypothesis was tested by calculating characteristic relaxation times for all polymers at the onset of melt fracture. Such an apparent characteristic relaxation time, λ, can be defined [Cogswell, 1981] as the ratio of polymer viscosity, η, and shear modulus, G, that is:

$$\lambda = \eta / G \qquad \text{eq. 5-14}$$

The shear modulus can be estimated through the measurement of extrudate swell at the onset of melt fracture, such that $G = \tau / \gamma_\infty$; τ is the shear stress, γ_∞ is the recoverable shear strain at the die wall. The values of γ_∞ for different polymer samples were calculated [Cogswell, 1981] from the following equation:

$$B_L^2 = \frac{2}{3}\gamma_\infty \left[\left(1 + \frac{1}{\gamma_\infty^2} \right)^{\frac{2}{3}} - \frac{1}{\gamma_\infty^3} \right] \qquad \text{eq. 5-15}$$

where B_L is the extrudate swell ratio.

The above described technique was used to calculate the relaxation times for all polymers in Series 1 at various shear rates. As Figure 5-22 shows, the relaxation time decreases with inceasing the shear rate and lowering polydispersity. However, the difference becomes insignificant after a certain level of polydispersity (Blend 5 to 9).

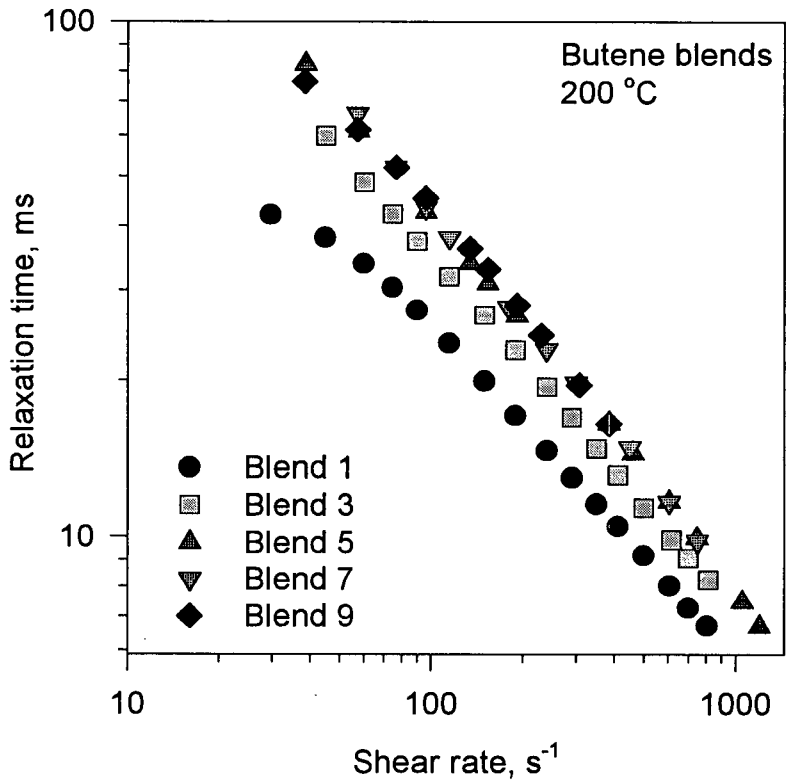

Figure 5-22. Relaxation time determined from extrudate swell data for the Series 1 blends at 200 °C.

Figure 5-23 plots the apparent shear rate for the onset of melt fracture versus relaxation time for Series 1 and 2. It is seen that the shear rate at the onset of melt fracture decreases with an increase in relaxation time for both series of resins. A noticeable disagreement between the data

for the two series may be attributed to minor differences in the molecular structure, e.g. degree of short chain branching and detailed branch configuration, as well as differences in the percentage of high molecular weight fractions. These data indicate that a proper balance between polymer melt viscosity and elasticity (shear modulus) is needed to improve the melt fracture performance. An increase in polydispersity (or a decrease in average molecular weight) reduces the apparent melt viscosity of a resin. At the same time, an increase in polydispersity (or average molecular weight) decreases the value of the shear modulus as manifested by an increase in extrudate swell (Figure 5-19). Therefore, the best melt fracture performance is achieved when a proper balance between the polymer melt viscosity and shear modulus is realised, thus minimising the apparent relaxation time (eq. 5-14).

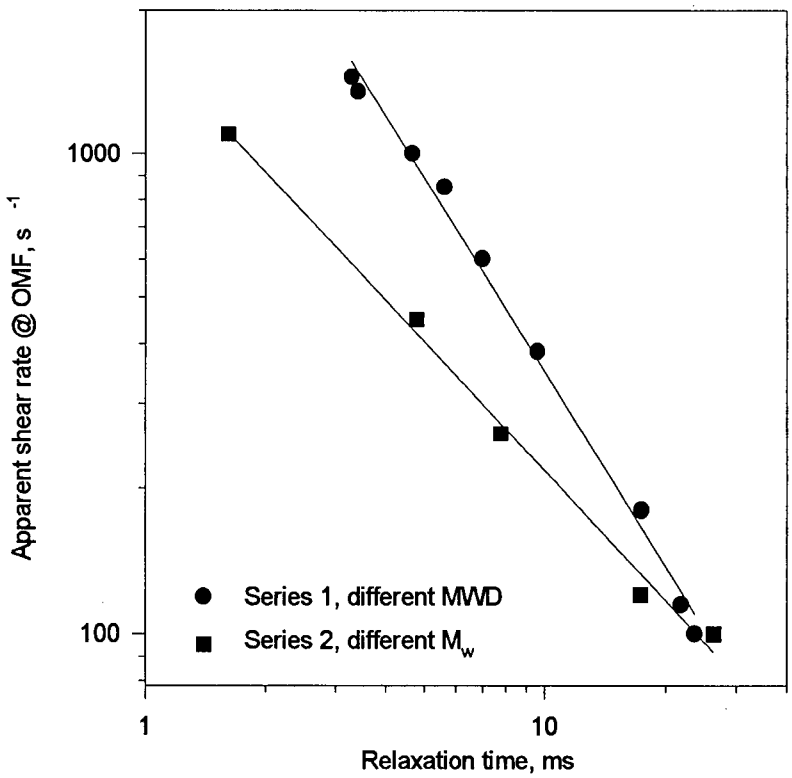

Figure 5-23. A correlation of melt fracture: the relationship between the critical apparent shear rate for the onset of melt fracture with the relaxation time defined by eq. 5-14.

It is noted that the shear modulus was calculated using extrudate swell data from capillary experiments. As was discussed earlier, start-up of steady shear can also be used for this purpose (section 5.4.2). However, one must distinguish between these two methods. In the case of the start-up experiments, a sliding plate rheometer was used, and the polymer melt was subjected to simple shear. Hence, the obtained shear modulus was a characteristic of the melt in simple shear kinematics. In the case of capillary experiments, the determined shear modulus characterises the material in radial expansion after shearing.

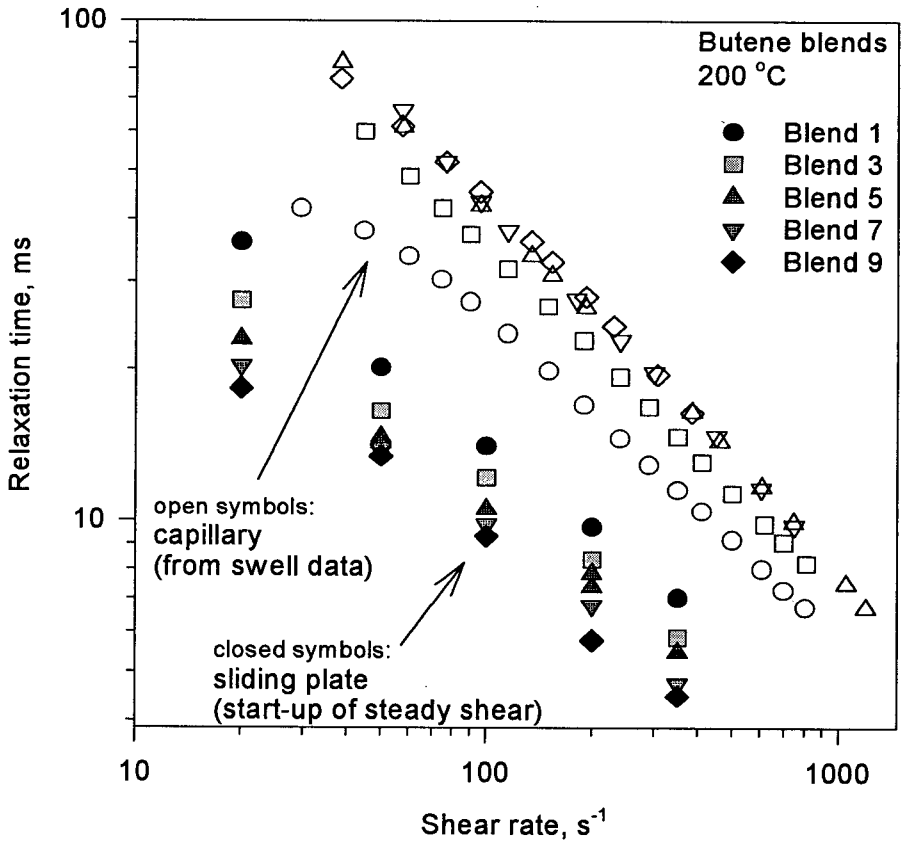

Figure 5-24. Comparison of relaxation times for the Series 1 blends at 200 °C determined using two different methods: extrudate swell data from capillary rheometer, and start-up experiments using sliding plate rheometer.

The comparison of the two methods in terms of relaxation time is shown in Figure 5-24. It can be seen that the data differ not only in their magnitude, but also in their ordering with respect

to the blend number (and hence polydispersity). Since the melt fracture performance is determined in capillary extrusion experiments, determination of the shear modulus from the extrudate swell data is more preferred.

5.6 Conclusions

Several experimental techniques were employed to study the rheological and processing behaviour of two series of polyethylene resins in order to examine independently the effects of molecular weight and polydispersity. In particular, the linear viscoelastic properties, the flow curves, the extrudate swell ratio, and the critical conditions at which visual defects appear on the surface of extrudates were determined.

The present study shows that increase of polydispersity increases the zero-shear viscosity, the flow energy of activation, the degree of shear thinning, and the extrudate swell. On the other hand, the shear rate and the shear stress at the onset of melt fracture were increased as the polydispersity increased from 3.3 to about 9. However, a further increase in polydispersity actually deteriorated the melt fracture performance. Thus, for a given molecular weight, a critical polydispersity value exists that results in an optimum processing performance. This critical polydispersity value was also obtained from correlations between rheological properties with polydispersity. Specifically, the relationships between: (a) the inverse of the crossover frequency (determined from linear viscoelasticity) and polydispersity, and (b) the rheological polydispersity index with polydispersity, have shown sudden change of slopes at the critical value of polydispersity on double logarithmic plots. An increase in weight average molecular weight of a resin increases its apparent melt viscosity and extrudate swell, but decreases its shear rate and shear stress for the onset of melt fracture.

Finally, the results were interpreted in terms of an apparent characteristic relaxation time defined as the ratio of the viscosity to the shear modulus at the critical points. A criterion was identified in this study that the optimum melt fracture performance is characterised by a minimisation of the apparent characteristic relaxation time. Furthermore, the criterion indicates that a proper balance between polymer melt viscosity and elasticity is required to optimise the melt fracture performance of linear low-density polyethylenes.

6. INTERFACIAL PHENOMENA IN CAPILLARY EXTRUSION OF METALLOCENE POLYETHYLENES

– EXECUTIVE SUMMARY –

■

Metallocene polyethylenes with a small amount of long chain branching are thermorheologically complex. They exhibit wall slip at shear stresses as low as 0.05 MPa depending on their structure

■

Long transients were observed in capillary extrusion due to specific interactions between calcium stearate and long chain branching

■

A qualitative molecular mechanism for wall slip is proposed based on chain desorption and disentanglement and the work of adhesion

6.1 Introduction

A major recent technical advancement in the polyolefins industry is the development of homogeneous metallocene catalysts for polymerisation reactions. This class of catalysts produces polymers with narrow molecular weight and comonomer distributions, which, combined with controlled amounts of long chain branching, it is claimed to lead to both excellent processability and superior mechanical properties (Knight and Lai, 1992; Swogger *et al.*, 1995).

In spite of their claimed excellent processability, these polymers exhibit many idiosyncrasies not previously observed for other conventional polyethylenes (high density and linear low density) as will be shown below. It is believed that these are due to their narrow molecular weight distribution in combination with their controlled long chain branching. In particular, it has been reported in the past that molecular weight distribution has a significant effect on the critical shear stress for the onset of slip. A decrease in the molecular weight distribution results in a decrease of the critical shear stress for the onset of slip and that for the onset of melt fracture (Blyler and Hart, 1970). Thus, the polymers studied in this chapter, due to their narrow molecular weight distribution, are expected to exhibit enhanced flow instabilities and this in a sense will facilitate our study of phenomena such as wall slip and melt fracture.

A common indirect method to determine the slip velocity of polymers as a function of wall shear stress is to use the Mooney technique in capillary rheometry. This method has been used extensively in the past to assess slip phenomena of polyethylenes (Lupton and Regester, 1965; Blyler and Hart, 1970, Ramamuthy, 1986; and Hatzikiriakos and Dealy; 1992a). The extensive use of capillary rheometry to study the slip behaviour of polymers is mainly due to experimental difficulties encountered in using a direct optical method (Galt and Maxwell, 1964;

Migler et. al, 1993; Archer *et al.*, 1995) or other direct techniques utilising flush-mounted probes (Lim and Schowalter, 1989). In general, whenever a pressure-controlled capillary rheometer is used, the flow curves of polyethylenes are found to be independent of capillary diameter and this leads to the conclusion of the absence of slip in the sharkskin region (Pearson, 1985; Wang *et al.*, 1996). On the other hand, use of a piston-speed controlled rheometer leads to determination of a diameter dependence of the flow curves, which in turn allows the use of the Mooney technique for the determination of slip velocity. It is our belief that it is safer to use the latter mode of capillary operation since it can be observed directly whether or not has steady state been approached. On the other hand, in a pressure controlled rheometer the observation is only indirect i.e., by weighting extrudates at constant time intervals, and thus the experimental errors can be quite large. The transients associated with both modes of operation can be very long and these have been well-documented in the literature (Schreiber, 1960; Hatzikiriakos and Dealy, 1994; Dealy, 1995).

In this study, we show that a diameter dependence of the flow curves of the studied polyethylenes is indeed obtained at relatively small values of apparent shear rate, where the experimental results are quite reproducible. For these polymers the spurt effect (oscillating melt fracture) is never observed, and slip starts at very small values of wall shear stress. Then, it gradually increases at higher wall shear stresses to approach values close to those corresponding to plug-flow.

The main objective of this work is to carry out a structure-property relationship study of these metallocene polyethylenes and furthermore to compare their behaviour with that of conventional polyethylenes. To accomplish this, we first have to understand the bulk and interfacial (phenomena taking place at the polymer-wall interface which may possibly affect

rheological measurements) rheology of this new class of polyethylenes; and secondly to link these interfacial phenomena to a processing performance by means of capillary rheometry.

6.2 Experimental

Two ethylene/octene copolymers (linear low density polyethylenes) produced by Dow using the constrained geometry single site catalyst system, were studied. Both resins have a polydispersity of about two as reported by the manufacturer. Resin A contains a higher amount of octene comonomer (about three times more than resin B), which results in a lower density for the resin (870 kg/m^3). However, it is resin B that has more long branches (i.e. branches that contain more than six carbon atoms), about four times as many as resin A. The molecular weight of resin A is about 100,000 g/mol. Resin B contains less octene comonomer and has a higher density than resin A (902 kg/m^3). The molecular weight of resin B is about 80,000 g/mol.

Additional experiments were also performed with a conventional linear low density polyethylene (Dowlex 2049) having comparable molecular characteristics with the above polymers (molecular weight of 119,600 g/mol and polydispersity of 3.82) in order to point out basic differences in the rheology and processing of metallocene polyethylenes. Table 6-1 summarises all the properties of the polymers studied including the power-law parameters determined from their viscosity material function.

All capillary experiments were carried out at a constant temperature of 150 °C using an Instron constant-speed piston-driven capillary rheometer. Each data point was taken from at least two measurements, in order to check reproducibility. Circular dies of three different diameters (D =

0.508, 0.762, 1.27 mm) and five different length-to-diameter ratios (L/D = 0, 10, 20, 40, 70) were used. The dies are made of tungsten carbide and have a 90° entrance cone.

Table 6-1. Molecular characteristics and viscosity power-law parameters of the polymers studied.

Polymer	M_w	M_w/M_n	ρ kg/m^3	Melting point (°C)	K at 150 °C MPa·s^n	n at 150 °C	E/R K	Branches per 1000 carbons
Resin A	100,000	2	870	57	0.0151	0.92	4822	0.026
Resin B	80,000	2	902	104	0.0150	0.88	5385	0.113
Dowlex 2049	119,600	3.82	926	126	0.0203	0.67	3628	0

The experiments in the constant stress rheometer (Rheometrics Scientific SR-200) were carried out at several temperatures above the melting point, T_m. The time-temperature superposition principle was used in order to determine the linear viscoelastic properties of these polymers over a wide range of time scales. The creep behaviour of all materials was also assessed by this rheometer in order to classify them in terms of elasticity.

Time stability tests for all materials were carried out over periods of time of about 24 hours in order to determine their stability at long exposure times at high temperatures under an inert N_2 environment. These tests first included complete dynamic frequency sweeps at regular time intervals over a period of about twenty-four hours. The experiments were carried out at several temperatures in the range 130 – 200 °C. At the end of the cycle (24 hours), we repeated a frequency sweep at the first temperature (start of the cycle) and compared it with the original. We observed virtually no change. Secondly, time sweep experiments at fixed frequencies (1 and 5 rad/s) again at several temperatures (130 – 200 °C) were also performed as additional time stability tests over long periods of time. It was found from these tests that the dynamic moduli, G' and G'', remained constant within ±3%.

To detect safely the temperature range over which the polymers are in the melt state, differential scanning calorimetry (Rheometrics Scientific, model PL-DSC) was used for all resins. Multiple runs of untested and tested samples practically gave similar results. The measurements were carried out with a heating rate of 20 °C/min. Representative results are plotted in Figure 6-1. It can be seen that resin A has a very low melting point compared to the others and that the melting range is quite broad compared to those of resin B and Dowlex 2049. Using these findings, rheological measurements are reported only over temperatures beyond those covered by the peaks in the DSC analysis.

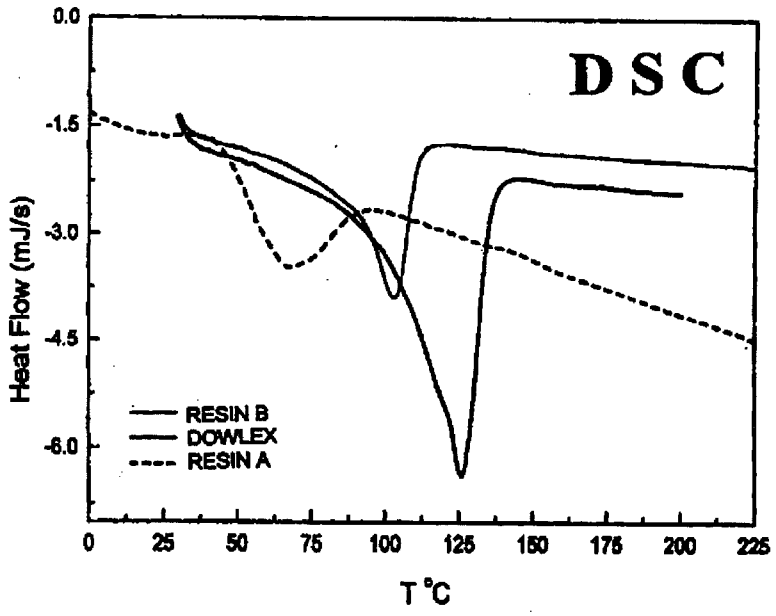

Figure 6-1. Differential scanning calorimetry for all resins studied in this work.

Finally, it has to be pointed out that resins A and B do not have any fluoropolymer processing aids in their composition according to the manufacturer. Additives include only small amounts of antioxidants and calcium stearate which are standard additives for stabilising the structure of polyolefins. To confirm these, additional testing was performed to detect levels of fluoropolymer as well as excessive amounts of calcium stearate in the resins by using bomb

calorimetry and FTIR respectively. Both tests were negative. There is no fluoropolymer in the resins (25 ppm is the sensitivity of the method used) and the level of calcium stearate is less than about 1000 ppm (sensitivity level of the method). Conventional polyethylenes usually contain stearates in the range of 1000 – 2000 ppm. It is noted that the stearates are used to scavenge acidic catalyst residues. It is not surprising that metallocene resins have a very low amount of calcium stearate (less than 1000 ppm), since the amount of catalyst used for the production is very small compared to those used in the Ziegler-Natta technology.

6.3 Linear Viscoelastic Measurements

6.3.1 Frequency Sweeps

Figure 6-2 and Figure 6-3 depict the master curves (T_{ref} = 200 °C) of the storage and loss moduli respectively of resin A and resin B by applying the time-temperature superposition (TTS) technique on dynamic frequency sweep data obtained at a wide range of temperatures from 90 to 210 °C. It can be seen from these figures that the superposition of the data is very good for G' with the exception of the data corresponding to the temperature of 90 °C (Figure 6-2a) which falls exactly at the end of the peak in the DSC results (Figure 6-1). This set of data was only included to emphasise that at 90 °C the polymer might not be quite in the melt state. For resin A (Figure 6-2a) the accessible temperature window spans over 110 °C (from 90 to 200 °C) and as a result the obtained superposed data is expanded over seven decades of frequency. For resin B, having a higher melting point, the range of accessible temperatures was smaller, from 130 to 210 °C (Figure 6-2b).

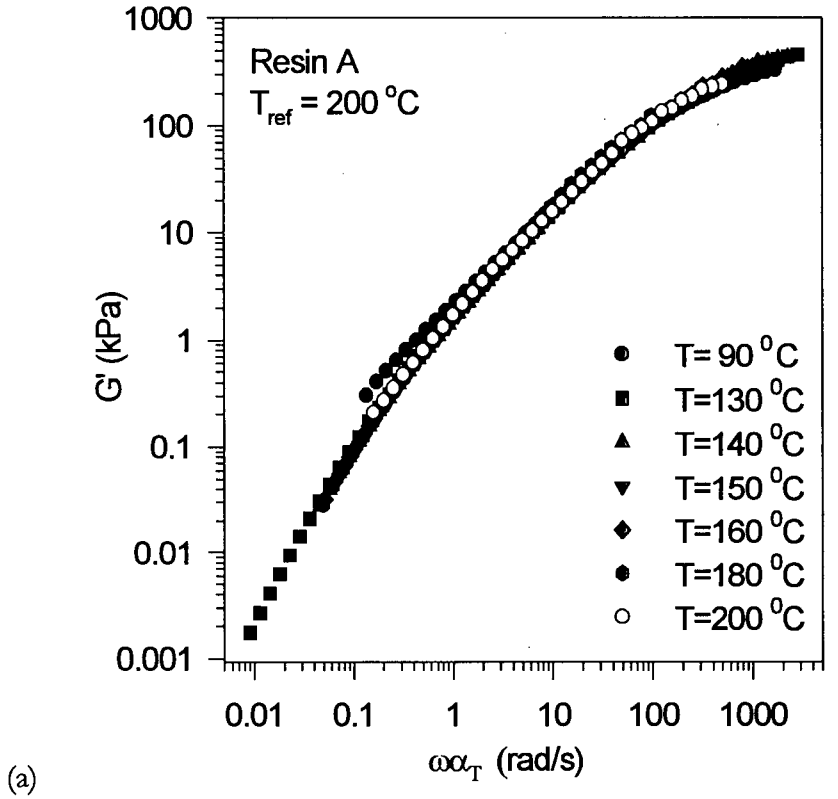

(a)

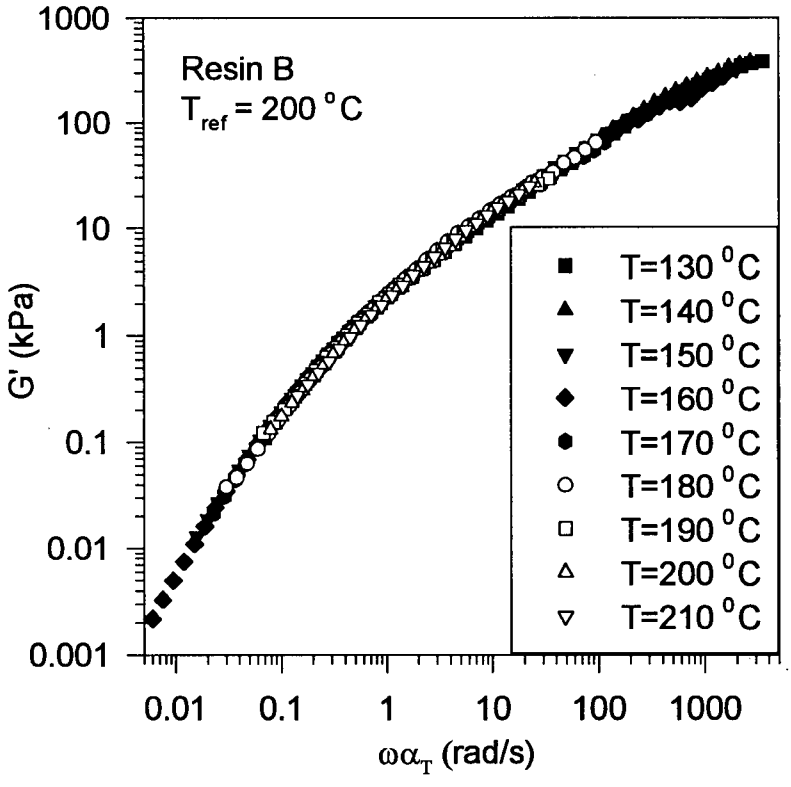

(b)

Figure 6-2. Master curve of storage modulus, G', for resin A (a) and resin B (b) at a reference temperature of 200 °C.

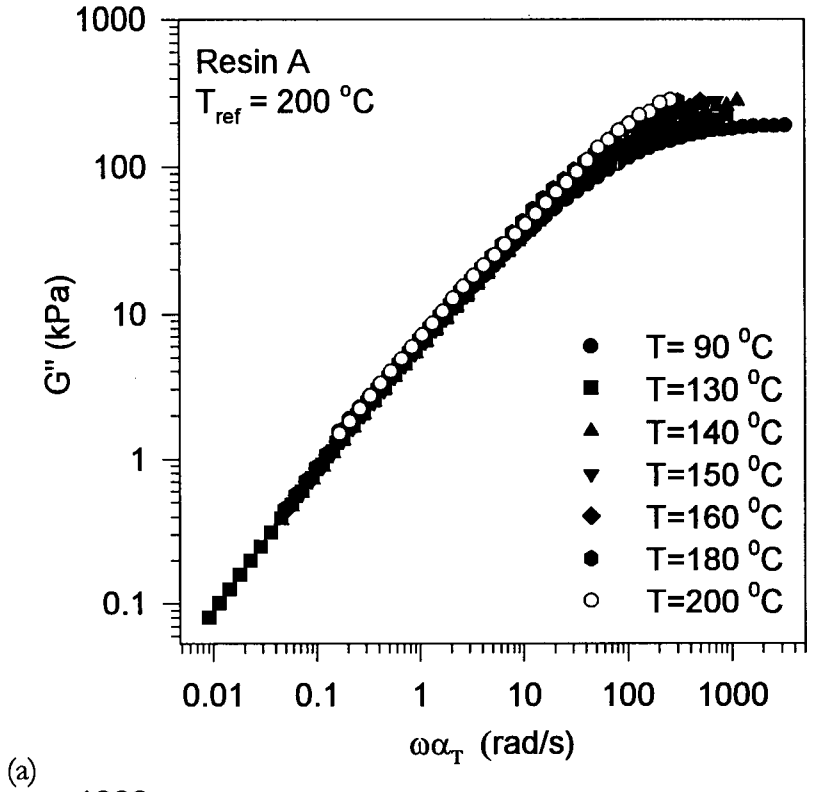

(a)

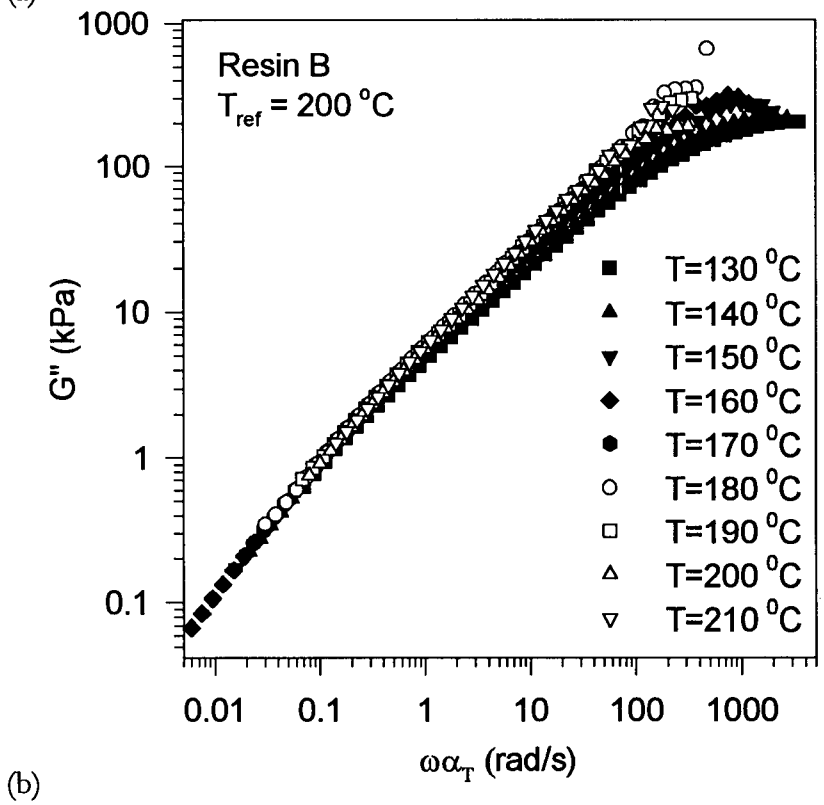

(b)

Figure 6-3. Master curves of loss modulus, G'', for resin A (a) and resin B (b) at T_{ref}=200 °C. The time-temperature superposition principle fails at high frequencies, suggesting presence of long branches.

The applicability of the time-temperature superposition for G'' breaks down over the range of temperatures used. Note that the same shift factors have been used in Figure 6-2a and Figure 6-3a for resin A and in Figure 6-2b and Figure 6-3b for resin B. It can also be seen from Figure 6-3 that this breakdown is more pronounced in the higher frequency regime and the level of G'' in this regime scales with temperature. In particular, the deviation of the data from a "master" curve (defined by data corresponding to only very high temperatures) increases with decrease of temperature. This is believed to be due to the presence of a small degree of long chain branching, which gives rise to this thermorheological complexity (Carella *et al.*, 1986). Thermorheological complexity similar to the one observed in this work has been obtained for poly-n-dodecyl methacrylate (Kurath *et al.*, 1959), polytrifluorochloroethylene (Tobolsky and McLoughlin, 1955) and cellulose tributyrate-dimethyl phthalate (Landel and Ferry, 1955). In these cases, the failure was attributed to the increase of crystallisation of the ester side groups with decrease of temperature. However, given the DSC results and the fact that metallocene polyethylenes have a small degree of crystallinity compared to conventional ones, the explanation of the TTS failure based on crystallisability and a hypothesis of retained order even at temperatures well above the melting point, is clearly inadequate.

It is worthwhile to note that in applying the TTS principle only a horizontal shift was applied. An applicable vertical shift is equal to $T_{ref}\rho(T_{ref})/T\rho(T)$, where $\rho(T_{ref})$ is the density of melt at T_{ref} and $\rho(T)$ is the density at T. The density changes very little over a range of 100 °C, typically 3-5%. This was also reported by Porter (1995). Thus, the highest value for the vertical shift can be obtained as the ratio of absolute temperatures. Applying such vertical shifts to the data plotted in Figure 6-2a, does not change the final conclusion that resin A is a thermorheologically complex fluid. Mavridis and Shroff (1992) have applied vertical shifts to produce master G' and G'' curves for low-density polyethylenes and pointed out that no careful

application of a vertical shift may lead to the conclusion of thermorheological complexity; however, this is not the case in the present study. It is noted that the TTS failure is more pronounced for resin B compared to resin A. This might be due to the higher degree of long-chain branching present in resin B.

A thorough discussion as to the origins of thermorheological complexity in semicrystalline materials was offered earlier by Ferry (1980) and more recently by Plazek (1996). According to Plazek (1996), successful time-temperature superposition of viscoelastic curves requires that all of the molecular mechanisms involved in a particular deformation have the same temperature dependence. This, however, is not the case if side groups (i.e. branches of the main backbone) are present. It was hypothesised that branches show weaker temperature dependence than the backbones. Another explanation offered was that the TTS failure is due to a changing entanglement concentration with a change in temperature.

Figure 6-4 plots the master curves of the dynamic moduli of Dowlex 2049. Although data for temperatures close to the melting point of this polymer have been used to apply the TTS (150 °C compared to its melting point of 127 °C), the data seems to superpose very well. This is in clear contrast with the behaviour exhibited by resins A and B. Therefore, the failure of the time-temperature superposition observed in the linear viscoelasticity of metallocene resins A and B may reasonably be attributed to the presence of long chain branching.

Figure 6-5 plots the shift factors for the available data for all of the resins studied. The time-temperature superposition was applied using a reference temperature of 200 °C. An Arrhenius equation was found to represent the data quite well, that is,

$$a_T = \exp\left[\frac{E}{R}\left(\frac{1}{T} - \frac{1}{T_{ref}}\right)\right] \qquad \text{eq. 6-1}$$

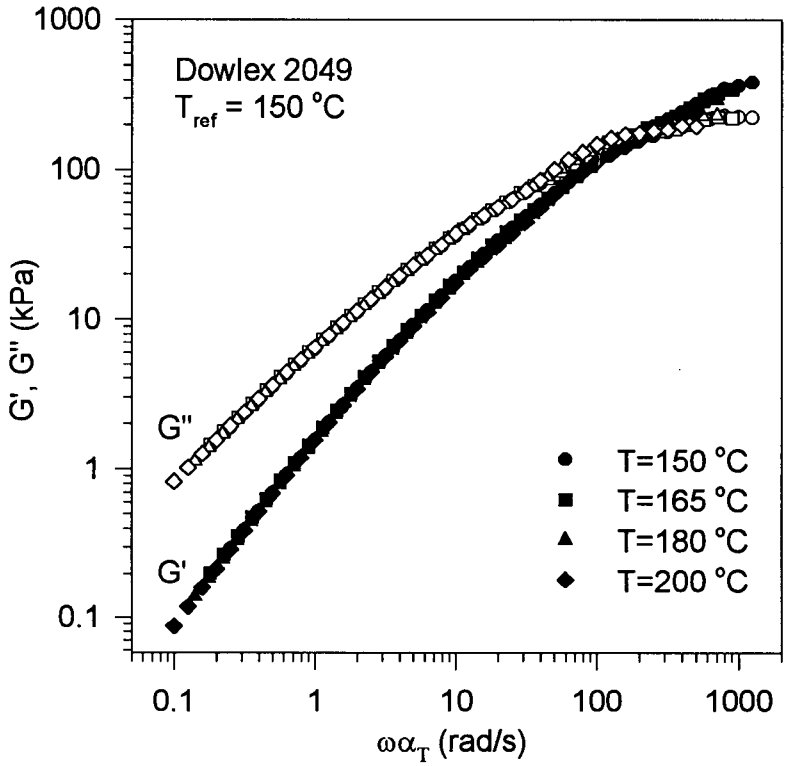

Figure 6-4. Master curves of storage and loss moduli, G', and G'', for Dowlex 2049.

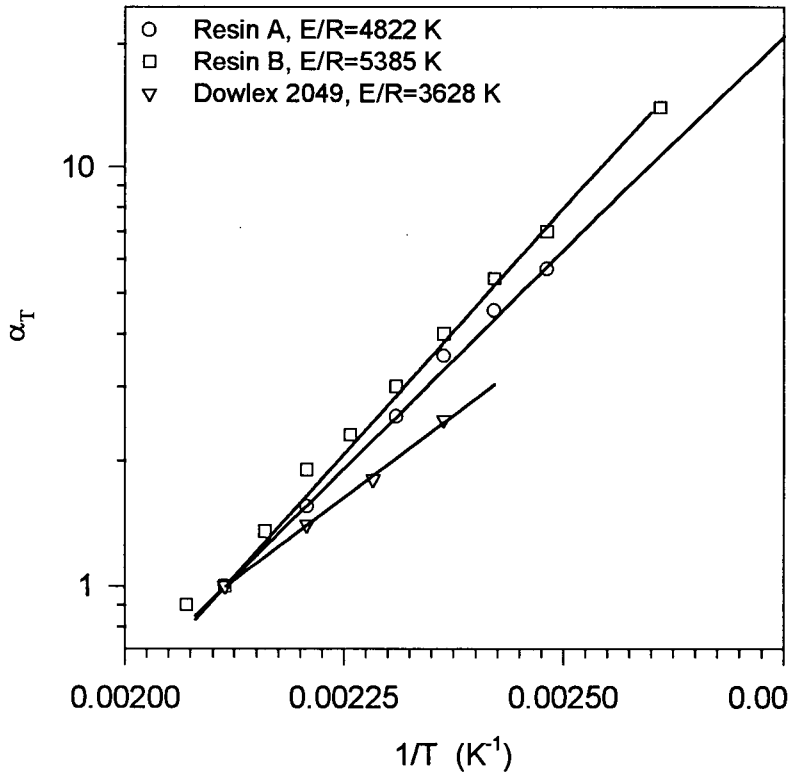

Figure 6-5. Shift factors for all resins calculated by applying the time-temperature superposition on data obtained by dynamic frequency sweep experiments at various temperatures.

where E is the flow activation energy, R is the gas constant and T_{ref} = 473 K. It can be seen from Figure 6-5 that the flow activation energy for all resins scales with the number of long chain branches. The flow activation energy for Dowlex 2049 was found to be as low as E/R = 3628 K, which is the due to the absence of long chain branching (Table 6-1).

Wang and Porter (1995) have compiled the flow activation energy of many polymers and they have correlated it with molecular structure based on the free volume concept. For linear polyethylenes (similar to Dowlex 2049 studied here), they have reported values of E/R in the range of 3,000–4,100 K. However, for long-chain branched polyethylenes they have reported a value for E/R of about 9,000 K which is about three times higher than that reported for linear polyethylenes. Thus, long chain branching in general increases the sensitivity of the rheological properties of polymers to temperature and this depends on the length, concentration and distribution of branches (Mavridis and Shroff, 1992). Our data for the flow activation energy conform with the reported values by Wang and Porter (1995) and Mavridis and Shroff (1992). Finally, Graessley (1982), Laun (1987) and Mavridis and Shroff (1992) have also reported that long chain branching has a significant effect on the flow activation energy of low density polyethylenes.

6.3.2 Creep Recovery

Creep and creep recovery tests (using a Rheometrics Scientific SR-200 rheometer) were also performed for all resins to classify them in terms of elasticity. In a creep test, a sample is subjected to a constant shear stress, and the shear strain is then monitored as a function of time. After steady state has been achieved, the shear stress is suddenly removed. The material

will recoil in a direction opposite to that of the original applied force, and the final amount of recoil, γ_r, is recorded.

It is known that creep recovery increases with polydispersity and long chain branching (Ferry, 1980; Dealy and Wissbrun, 1990). That is, for a given molecular weight, higher polydispersity and the presence of more long chain branches render the material more elastic. Table 6-2 summarises some representative results on the recoil of the three resins at fixed values of the wall shear stress.

Table 6-2. Recoil of the three resins at representative values of shear stress (150 °C)

Polymer	Shear stress, Pa	Recoil (γ_r)
Resin A	50	1.54
	5	0.36
Resin B	50	2.57
	5	0.31
Dowlex 2049	50	4.53
	500	15.6

First, it can be seen that Dowlex 2049 is the most elastic resin among all resins studied. Dowlex 2049 has a higher molecular weight but most importantly is a relatively polydisperse polymer, while resins A and B have smaller molecular weights with a few long chain branches incorporated in their structure. The two competing effects of polydispersity and long chain branching on elasticity balance out in such a way that render Dowlex 2049 to be the more elastic resin. Among the two remaining resins, the recoil of resin B is much higher than that of resin A. This is due to the presence of more long-chain branches in resin B in spite of its lower molecular weight. The effect of long chain branching can also be seen from the values of the zero-shear viscosities of the two resins (A and B). Resin B has a M_w 20% less than that of resin

A, however, it has a zero-shear viscosity of $4 \cdot 10^4$ Pa·s (at 150 °C) compared to 3×10^4 Pa·s of resin A.

6.4 Capillary Experiments

6.4.1 Transient Capillary Experiments

In a transient capillary experiment, depending on polymer compressibility, the amount of polymer in the barrel, the geometric characteristics of the capillary die (D and L/D) and operating conditions, the time required to obtain steady-state pressure drop along the die can often be very long. In particular, this is the case for very compressible polymers at small apparent shear rates and when a capillary of small diameter and large L/D ratio is used. A mathematical model to predict this behaviour has previously been developed by Hatzikiriakos and Dealy (1994).

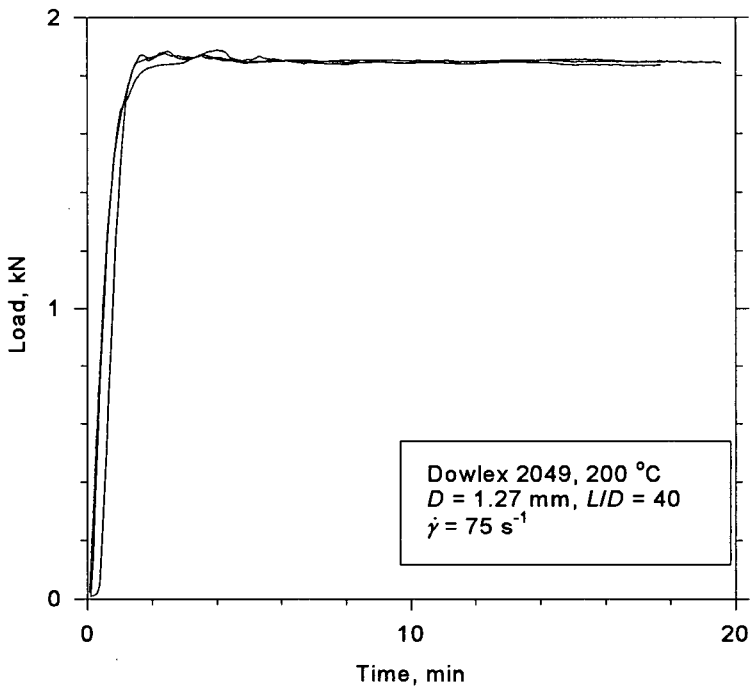

Figure 6-6. A typical pressure start-up transient in the capillary extrusion of Dowlex 2049.

Figure 6-6 illustrates a transient capillary experiment for Dowlex 2049, whose processability was also studied before (Hatzikiriakos *et al.*, 1995). It can be seen that the load (pressure force) increases gradually until it reaches its steady state value. A small drop in the load over the duration of the experiment can be associated with a small pressure drop within the barrel. The reproducibility of the experiment was excellent (superposition of three experiments). This behaviour has consistently been obtained for a number of different apparent shear rates and for other conventional polymers, such as polypropylenes.

For the metallocene polymers studied in this work, the behaviour was surprisingly unusual. Figure 6-7 illustrates a series of experiments for resin A numbered as 1 to 7. In all these experimental runs, we have used the same capillary die and same apparent shear rate (piston speed) as those used in the experiments plotted in Figure 6-6 for the Dowlex 2049. In addition, each run corresponds to extrusion of a full load of polymer in the barrel. We started the first run with a clean die. We placed the capillary die in an oven at 450–500 °C for about ½ to 1 hour, in order to degrade all the polymer left on its inside surface from the previous experiment.

As can be seen in Figure 6-7 during the first run, the load initially increases, goes through a maximum, and then gradually decreases. It was not possible to obtain a steady state during run #1, although all the polymer in the barrel was extruded. A steady-state value was finally obtained only after fully reloading the barrel with the polymer three times (see run #3). Also it is interesting to note that the maxima in experiments 1 to 3 gradually decrease and that the maximum pressure in the second experiment is at the point where the previous one ended. Such behaviour has been observed previously in the capillary extrusion of linear low density polyethylenes when a small amount of Teflon is included as processing aid (Hatzikiriakos *et al.*, 1995) and in the capillary extrusion of tetrafluoro-ethylene/hexafluoropropylene when a small

amount of polyethylene was included as processing aid (Rosenbaum *et al.*, 1995). The gradual decrease of the load in these experiments was associated with the gradual coverage of the wall with the processing aid and the gradual increase of slippage of the polymer over this layer. However, in the present case there is no fluoropolymer additive, which can readily explain the results as discussed. The only additive which may give rise to such effects is calcium stearate, which is possibly present at concentrations definitely less than 1000 ppm (see section 6.2). However, given that Dowlex 2049 includes calcium stearate at possibly higher concentrations and that no time dependent effects were observed during the extrusion of this resin, it is difficult to draw a clear conclusion. Further investigation and in-situ surface analysis at different stages of the extrusion process are needed in order to fully understand the phenomena. It is also worthwhile mentioning that the above experiments were subsequently reproduced by another capillary rheometer at a different site.

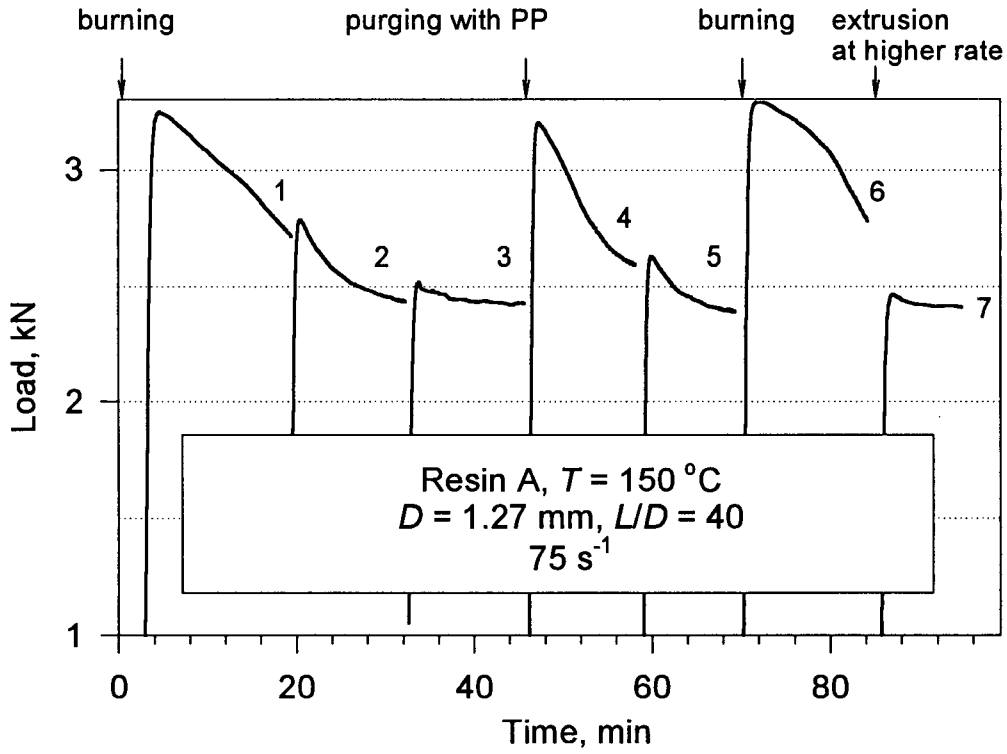

Figure 6-7. The effect of polymer/die surface interaction on the pressure response in the capillary extrusion of resin A.

The possibility of a gradual polymer degradation (structural change) should be excluded for two reasons: firstly, time stability tests at various frequencies and strains in a constant stress rheometer over a period of about ten hours resulted in practically identical results as discussed above. Secondly, if some kind of a structural change was taking place, then the pressure response in the second run would have been identical to that in the first one.

Before run #4 (also plotted in Figure 6-7) was conducted, the capillary die was purged by extruding two full loads of polypropylene at 200 °C, in order to see if we can recover the same interfacial conditions as those in the first experiment. It can be seen that indeed about the same response was obtained and the overall responses of runs #4 and #5 resemble those of runs #1 and #2 respectively. Subsequently, the die was placed in an oven to clean it as described above. Run # 6 was carried out. As can be seen from Figure 6-7, the same response as in runs #1 and #4 was obtained. Finally, to speed up the overall experiment in order to obtain the steady-state faster, a full load of polymer was extruded at a higher apparent shear rate between run #6 and #7. The obtained transient load response of run #7 resembles that of run #3.

Another series of transient experiments was performed with resin B. The same capillary die and the same operating conditions (as those specified for the experiments plotted in Figure 6-6 and Figure 6-7) were used for all the runs plotted in Figure 6-8, but this time for resin B. As in the previous experiment with resin A, each run corresponds to the capillary extrusion of a full load of polymer in the barrel. Starting with a clean die, several barrels were extruded on the same day. It can be seen that for this polymer (higher level of long branches than in resin A) five full loads of polymer were extruded in order to approximately reach a steady-state value (indicated by a dashed line).

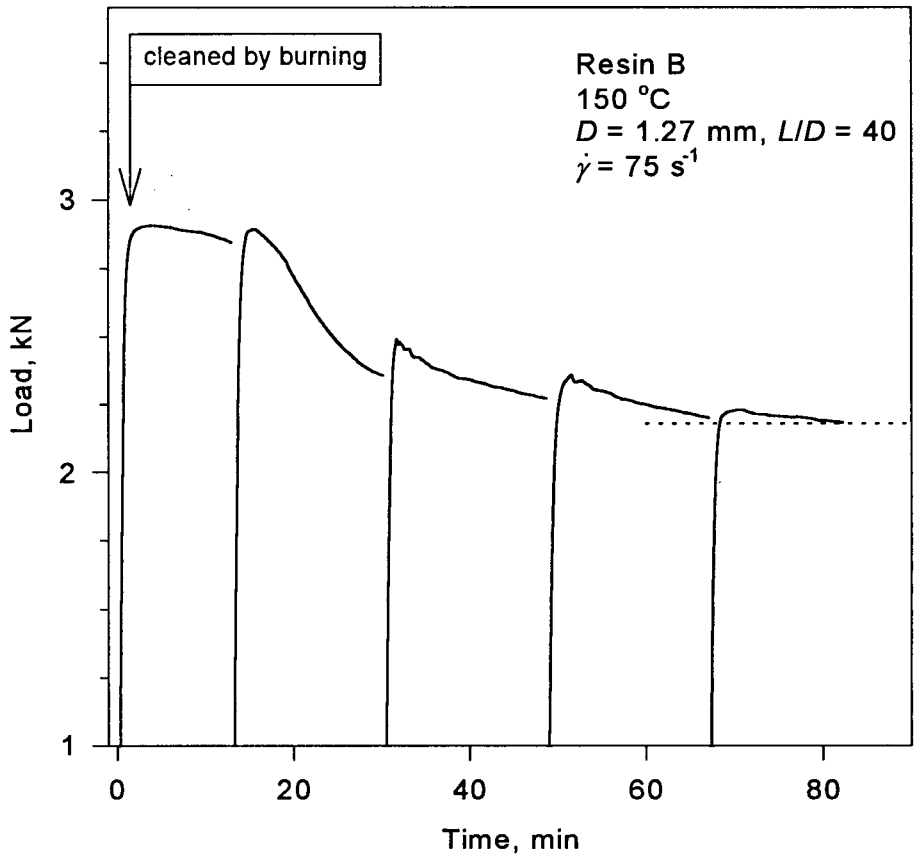

Figure 6-8. The effect of polymer/die surface interaction on the pressure response in the capillary extrusion of resin B.

The results presented in this section suggest that there is a long induction time for all of the physicochemical changes (interaction of polymer and/or polymer additives with the wall and gradual increase of wall slip) to take place at the interface. It is also important to note that when the load goes through its maximum, the extrudate is rough (sharkskin surface roughness). As the load decreases, the degree of roughness gradually decreases and eventually at low values of load, the extrudate appears smooth and glossy. It is also worth noting that the compressibility of both resins A and B (measured in a separate experiment by blanking off the reservoir and slowly compressing the polymer) is about 30% higher than that of Dowlex 2049. Although such a variation in the compressibility may result in long transients, it cannot explain the

extremely long responses presented in Figure 6-7 and Figure 6-8, i.e. the existence of maxima in the transients. The results presented so far clearly suggest that in order to control the processing behaviour of these polymers, we need to understand their bulk rheological behaviour as well as their interfacial behaviour when in contact with solid boundaries. One way to do this is to perform capillary experiments and analyse the interfacial behaviour of polymers by means of Mooney's technique.

6.4.2 Flow Curves and Melt Fracture

Figure 6-9 plots the Bagley correction as a function of wall shear stress for the two resins studied at 150 °C. These were determined by using orifice dies of various diameters as well as from extrapolation of Bagley lines at zero L/D ratios, i.e. plots of pressure versus L/D ratio. It can be seen that the Bagley correction is about the same for both resins over the range of shear stresses attained in this work.

Once the Bagley correction is known, the apparent flow curves can be determined. Two of these are plotted in Figure 6-10 for resins A and B, for a capillary die having an L/D ratio of 20 and a diameter of 0.762 mm. The wall shear stress, σ_w, is defined as, $\sigma_w = (P - P_{en})/4(L/D)$ where P is the total pressure and P_{en} is the ends pressure (plotted in Figure 6-9), and the apparent shear rate as, $\dot{\gamma}_A = 4Q/\pi D^3$, where Q is the volumetric flow rate and D is the capillary diameter. It is noted that a sharp change in the slope of both flow curves exists (around 0.3 MPa) which coincides with the appearance of extrudate defects for both resins. The critical shear stress for the onset of extrudate defects was found to be about 0.29 MPa for resin A and 0.33 MPa for resin B. The corresponding value for Dowlex 2049 is about 0.35 MPa

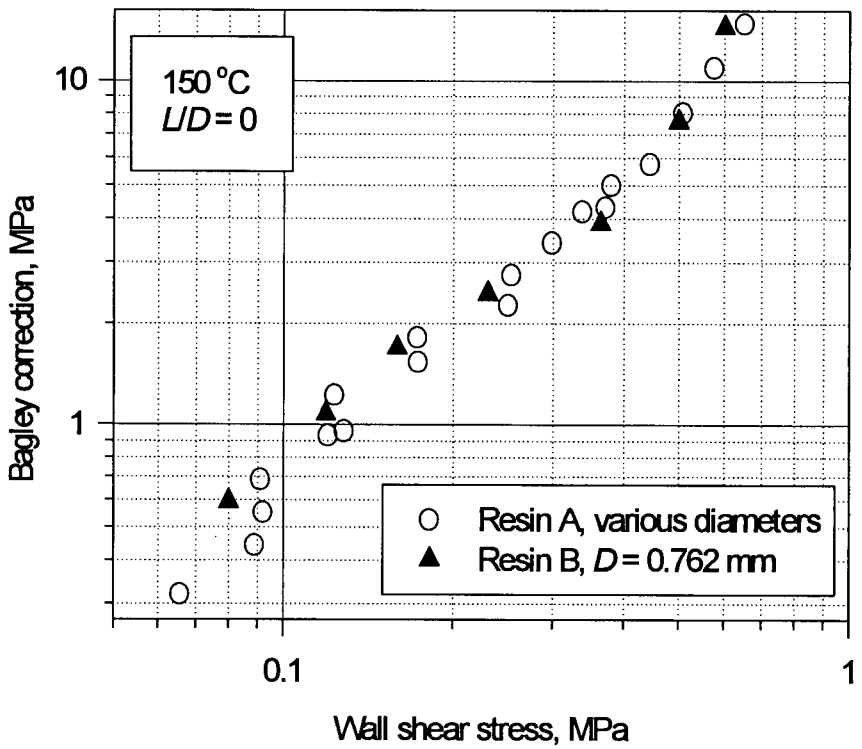

Figure 6-9. Bagley corrections for resins A and B determined by using orifice dies having various diameters at 150 °C.

(gross melt fracture) although small amplitude periodic distortions (sharkskin) start appearing at smaller values of the wall shear stress (beyond about 0.25 MPa). It is noted that sharkskin melt fracture for resins A and B appears only during the transient experiments when the load goes through its maximum and progressively disappears as the load decreases. This implies that the sharkskin region is very short for these resins and occurs over a limited range of apparent shear rate just before oscillating melt fracture commences.

Beyond these critical stresses, pressure oscillations (oscillating melt fracture accompanied by the appearance of alternate smooth and grossly fractured zones on the surface of extrudates) were obtained for resin A, but not for resin B. The flow curve for the latter was steady for all

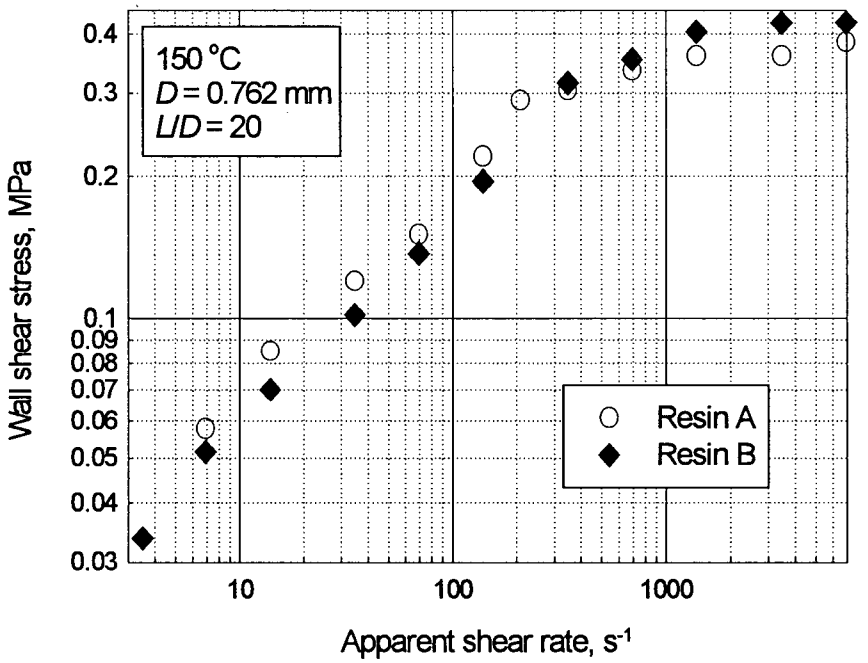

Figure 6-10. Apparent flow curves for resins A and B obtained by using a capillary die having D=0.762 mm and L/D=0 at 150 °C.

apparent shear rates. The magnitude of the pressure oscillations obtained during the capillary extrusion of resin A is so small that if an error bar was plotted to indicate the maximum and minimum values of pressure, this would collapse within the size of the symbols appearing in Figure 6-10.

These results are in clear contrast with previously reported results on the capillary extrusion of conventional linear polyethylenes (LLDPE, HDPE). During the extrusion of these polymers pressure oscillations clearly appear and the magnitude of these oscillations has been found to scale with $M_w^{3.4}$, particularly for the case of HDPE (Drda and Wang, 1995; Wang *et al.*, 1996). Metallocene polyethylenes do not appear to undergo spurt phenomena in a catastrophic sense (discontinuous flow curves connected through a hysteresis loop), rather their flow curves appear to be continuous. Their flow curves resemble those obtained for high molecular weight low density polyethylenes, which have randomly distributed long chain branching. For such

polymers, the flow curves are continuous, although sharkskin and consequently gross melt fracture are obtained at high enough wall shear stresses (Blyler and Hart, 1970; Hatzikiriakos, 1991). Thus, based on the present results, we may conclude that even a relatively small amount of long chain branching is sufficient to suppress the spurt phenomenon, i.e., flow curve discontinuities. This will be discussed further when we will propose a molecular mechanism for the slip of polyolefins later in this chapter.

6.4.3 Wall Slip

To study the onset of wall slip for molten polymers, the flow curves using capillary dies having a constant L/D ratio and a different diameter should be determined. According to the Mooney technique,

$$\dot{\gamma}_A = \dot{\gamma}_{A,s} + \frac{8u_s}{D} \qquad \text{eq. 6-2}$$

where $\dot{\gamma}_A$ is the apparent shear rate defined above, $\dot{\gamma}_{A,s}$ is the apparent shear rate corrected for the effect of slip (assumed to be solely a function of the wall shear stress), and u_s is the slip velocity at the wall shear stress defined by $\dot{\gamma}_{A,s}$. According to eq. 6-2, under slip conditions, the flow curve of a molten polymer becomes a function of capillary diameter.

Figure 6-11 plots the flow curves for resin A for three capillary dies having L/D = 40 and three different diameters. It can be seen that these flow curves diverge at a shear stress of about 0.05 MPa, which is taken to be the critical shear stress for the onset of slip. In addition, the type of

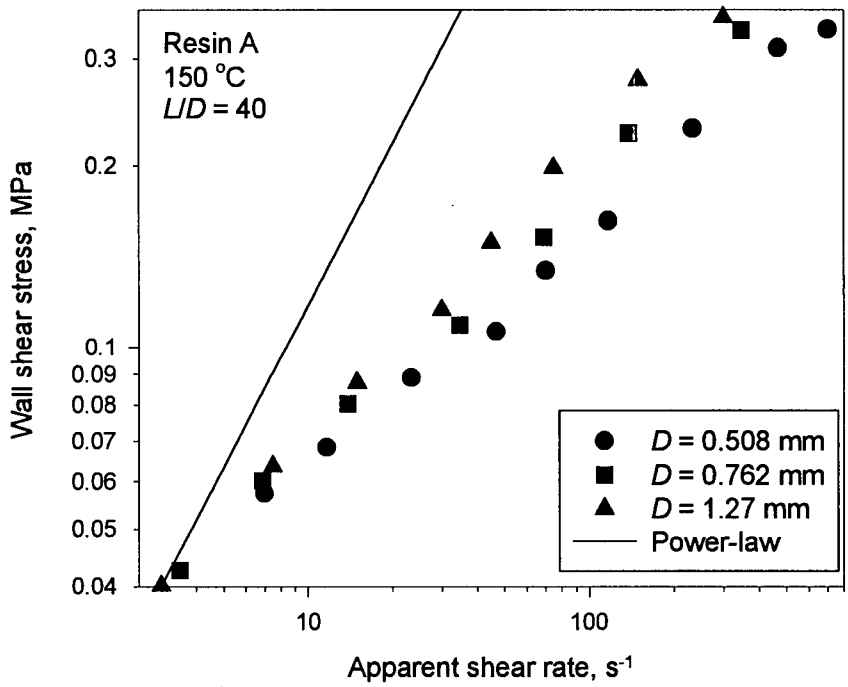

Figure 6-11. The effect of die diameter on the apparent flow curve of resin A. Diameter dependence of the flow curve indicates the presence of slip.

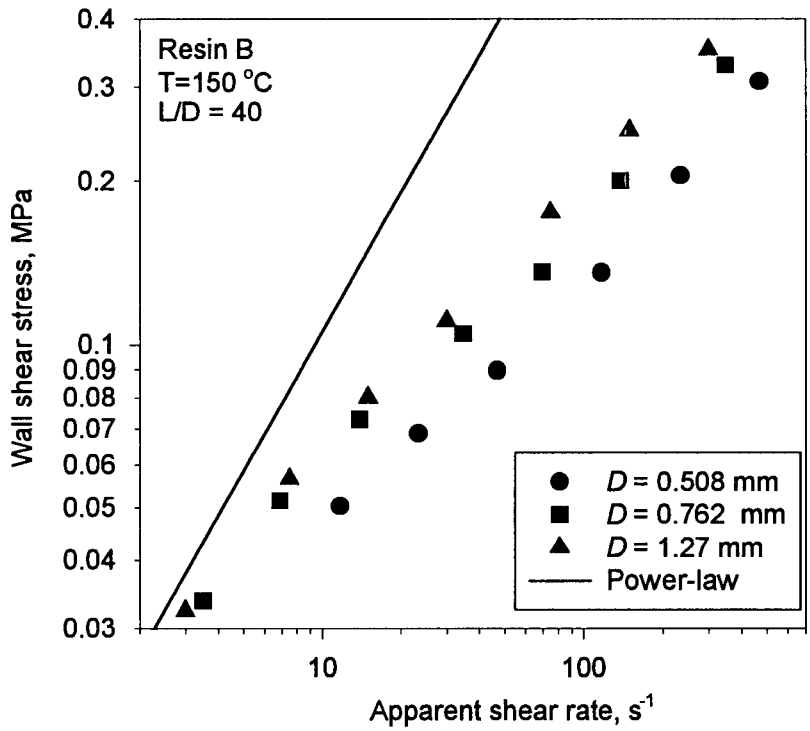

Figure 6-12. The effect of die diameter on the apparent flow curve of resin B.

diameter dependence obtained in Figure 6-11 is consistent with eq. 6-2 and the assumption of wall slip. A similar behaviour can be seen in Figure 6-12 for resin B. It is noted that the divergence of the flow curve occurs at relatively small values of apparent shear rate (10–200 s^{-1}) where capillary rheometry is quite accurate. Thus, the detected divergence is beyond of any expected level of experimental error.

Given the flow curve divergence beyond a critical shear stress (Figure 6-11), one may use the Mooney technique to assess the slip behaviour of resin A. Figure 6-13 is a Mooney plot for resin A. This is a plot of apparent shear rate, $\dot{\gamma}_A$, as a function of the inverse of capillary diameter ($1/D$) at various levels of the wall shear stress. It can be seen that extrapolation of the fitted straight lines (whose slopes are equal to $8u_s/D$) in the Mooney plot indicate that the apparent shear rate corrected for the effect of slip (actual deformation rate imposed on the melt) is very small. This implies that almost a plug flow is obtained at high enough apparent shear rates. Figure 6-14 is the corresponding Mooney plot for resin B.

The occurrence of plug flow can be seen more clearly in Figure 6-15, where the slip velocities calculated from the divergence of all flow curves from a power-law behaviour using the following equation (Kalika and Denn, 1987),

$$\frac{8u_s}{D} = \dot{\gamma}_A - \frac{4n}{3n+1}\left(\frac{\sigma_w}{K}\right)^{1/n} \qquad \text{eq. 6-3}$$

and the Mooney technique (from the slopes of lines in Figure 6-13) are plotted as functions of the wall shear stress.

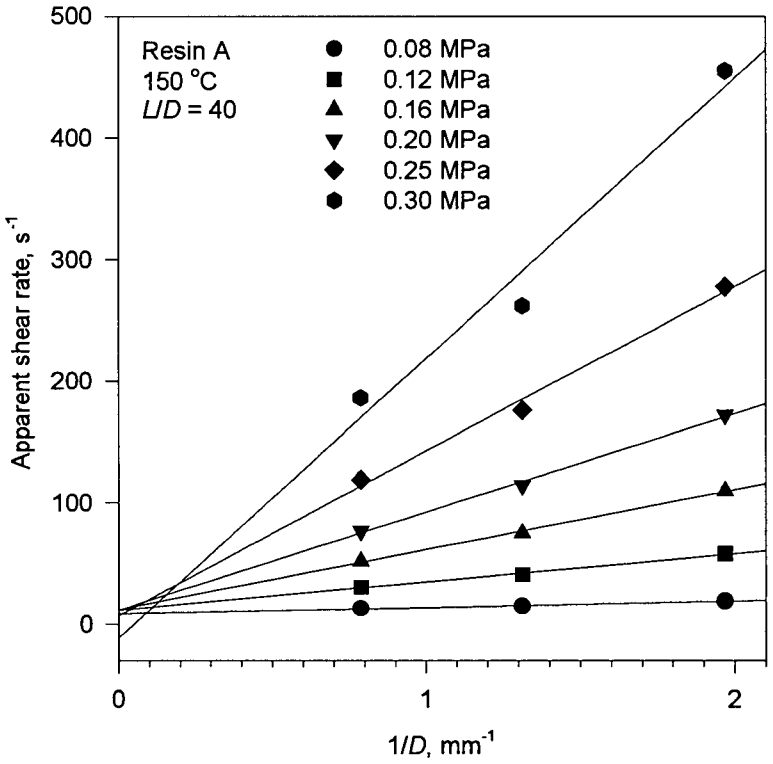

Figure 6-13. Mooney plot using the data of Figure 6-11 to estimate the slip velocity of resin A as a function of the wall shear stress.

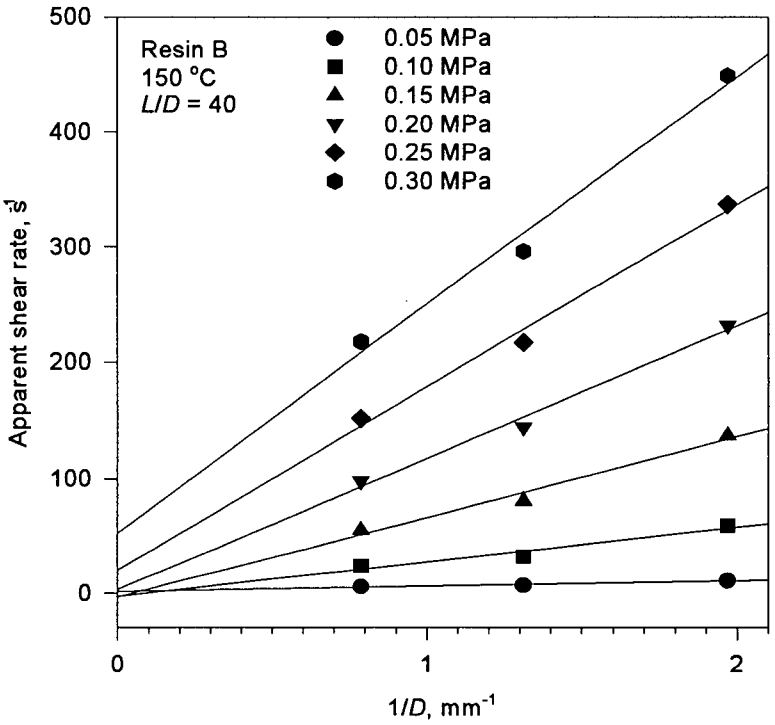

Figure 6-14. Mooney plot using the data of Figure 6-12 to estimate the slip velocity of resin B as a function of the wall shear stress.

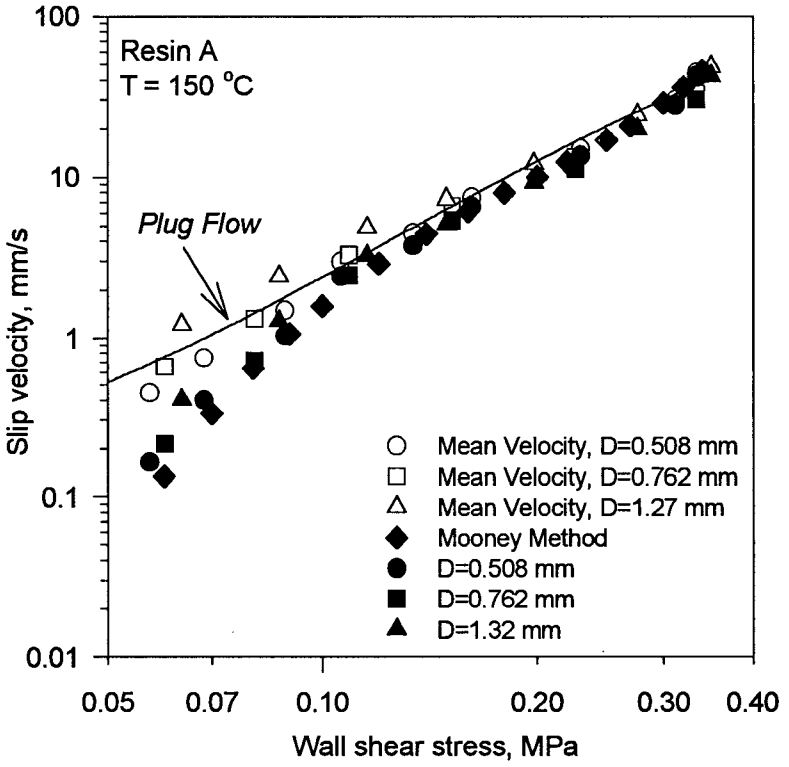

Figure 6-15. The slip velocity of resin A as a function of the wall shear stress determined by the Mooney technique and by the deviation of the apparent flow curves from an estimated no-slip one.

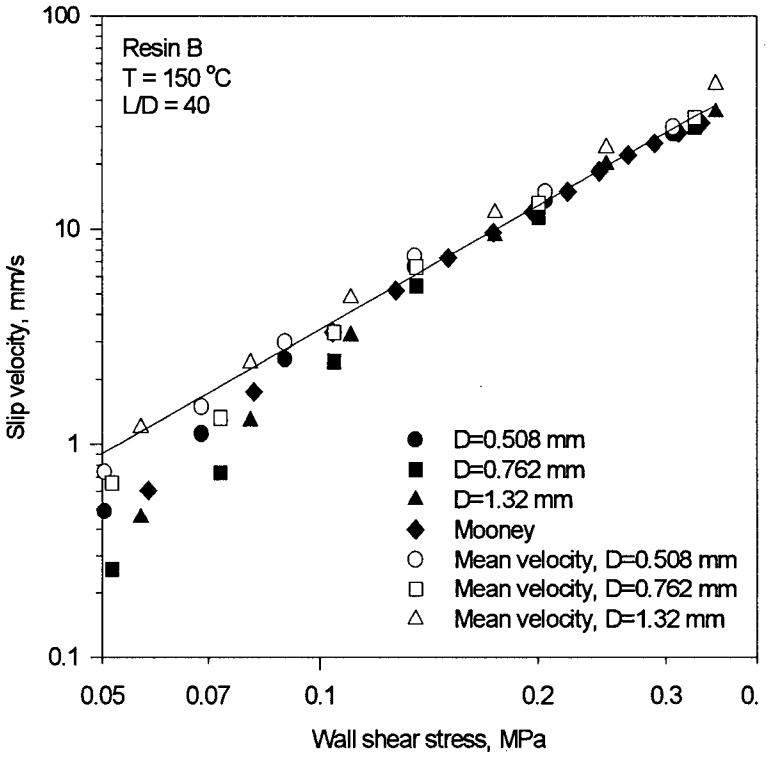

Figure 6-16. The slip velocity of resin B as a function of the wall shear stress determined by the Mooney technique and by the deviation of the apparent flow curves from an estimated no-slip one.

The parameters of the power-law model (plotted as a continuous solid line in Figure 6-11, $\sigma_w = K[(4n/(3n+1))\dot{\gamma}_A]^n$, with $K = 0.0151$ MPa·s^n, and $n = 0.92$) were determined by trial and error so that the slip velocities calculated from the divergence of all flow curves result in a single relationship (slip velocity independent of capillary diameter). First, a good agreement is obtained between the slip velocities calculated from the two methods (the Mooney technique by means of eq. 6-2 and the method by means of eq. 6-3). It can also be seen that the slip behaviour of resin A is not far from a plug flow for wall shear stresses greater than about 0.1 MPa. For example, there is little difference between the slip velocities determined by using the Mooney's technique and those determined by making the assumption of a plug flow (the mean flow velocity was calculated as $u_s = D\dot{\gamma}_A/8$, assuming that the apparent shear rate corrected for the effect of slip is zero). Thus, it can be seen that the slip behaviour of this polymer is very close to plug flow particularly at higher values of the wall shear stress.

The same analysis for slip was also performed for resin B and the results were found to be similar to those found for resin A (see Figure 6-14, the Mooney plot, and Figure 6-16, the slip velocity as a function of shear stress). Specifically, it was found that the flow curves again start diverging at wall shear stresses as low as 0.05 MPa, which implies the occurrence of wall slip. The calculated slip velocities from the Mooney technique were in agreement with those determined from eq. 6-3 using the power-law parameters of $K = 0.0150$ MPa·s^n and $n = 0.88$. Thus, resin B is slightly more shear thinning than resin A, possibly due to its higher degree of long chain branching as discussed previously.

Figure 6-17 compares the slip behaviour of all resins (A, B and Dowlex 2049). The data for Dowlex 2049 were reported by Hatzikiriakos *et al.* (1995) at 200 °C. These data were reduced to 150 °C by using the shift factor determined by applying the TTS technique (see Figure 6-4) in

order to make the comparison fair. It can be seen that the slip velocities of resins A and B are comparable, with those of resin B being consistently slightly higher.

Also plotted in Figure 6-17 are the slip velocities of Dowlex 2049 for both parts of its flow curve. These are separated by the onset of pressure oscillations and the transition from a weak slip to a strong one (plug-like flow) is indicated by the arrow. Note that strong pressure oscillations (spurt phenomenon) are obtained for Dowlex 2049. The oscillations are very weak for resin A, while no oscillations are obtained for resin B. At high enough shear rates all slip velocities define a single line (plug flow). In this flow regime, the bulk rheology of the polymer plays a minor role and the flow is primarily governed by the individual monomer-wall friction. Thus, in summary, our observations for the slip velocity of polyethylenes are as follows:

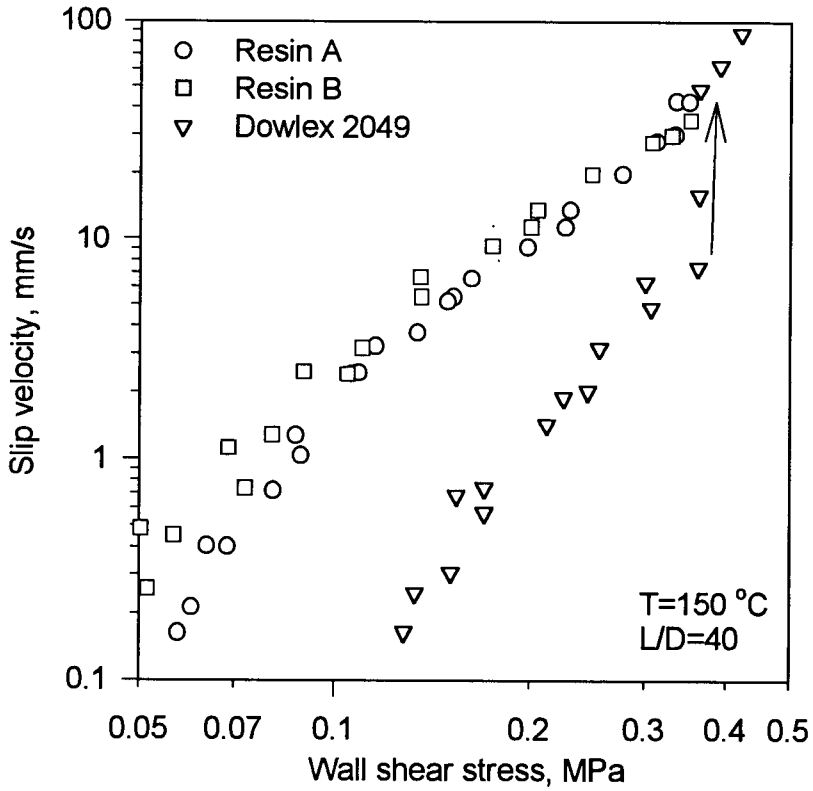

Figure 6-17. A comparison of the slip behaviour of all resins studied (resins A, B and Dowlex 2049) for capillary dies having L/D=40 and various diameters at 150 °C.

1. Linear polymers like Dowlex 2049 (no long branches) undergo pressure oscillations in capillary flow for apparent shear rates falling within a certain range. This also marks a transition from weak slip to strong slip.

2. With the addition of long branches, these pressure oscillations decrease in magnitude and this makes the transition from weak to strong slip less abrupt (resin A).

3. When the level of long chain branching exceeds a certain value, flow oscillations disappear and the transition from weak to strong slip (plug flow) occurs gradually (resin B).

4. At high enough shear rates, where essentially only plug flow exists, the slip velocity of polymers becomes independent of molecular structure and their flow is essentially governed by friction between the individual monomer and the wall. At these high rates and due to the relatively small rates of deformation in the bulk, most of the energy is dissipated at the polymer/wall interface. As a result, there should be a local increase of temperature. Such an observation remains to be seen experimentally in the future by means of a suitable probe.

The question which remains to be answered at this point is why long chain branching suppresses pressure oscillations and why in their presence the transition from a weak slip to a strong one occurs gradually. To answer these questions, a simple qualitative molecular mechanism for the wall slip of molten polyethylenes is proposed below.

6.5 A Qualitative Molecular Mechanism for the Wall Slip of Polyethylenes

Polymer molecules of high enough molecular weight (above the entanglement molecular weight) have the ability to entangle with each other and in this way they form a physical network. Considering a polymer next to a solid wall, it is reasonable to assume that there exists

a monolayer (Figure 6-18), where polymer molecules are attached to the wall through several sites along their backbone. These molecules are connected with the bulk of the material through entanglements with other molecules. Under flow, the polymer molecules in the bulk are stretched and these in turn, apply forces to the molecules at the interface through the entanglements. When these forces overcome a critical value some of the chains will be detached from the interface and as a result a weak slip boundary condition is obtained (Brochard and de Gennes, 1992). When the shear rate is increased further at the point where sudden disentanglement occurs (Wang *et al.*, 1996), strong slip (plug flow) is obtained (Figure 6-18). At this critical rate, the slip velocity of polymers is much less than the mean velocity (plug flow) and as a result pressure oscillations are sustained (continuous alternation between weak and strong slip). Figure 2-8 is a schematic showing a typical flow curve including the different flow regimes. In region 3, partial slip occurs due to the direct detachment of some of the chains from the interface. In region 4 (beyond a second critical shear stress) the flow becomes unstable, the pressure drop oscillates between two extreme values, and alternate smooth and distorted zones appear on the surface of the extrudate. This instability (stick-slip, oscillating melt fracture) is mainly due to a transition from a weak slip (chain detachment) to a strong one as a result of sudden disentanglement of the polymer chains attached to the wall from the rest of the chains in the bulk.

This flow instability (stick-slip) was also studied by using a sliding plate rheometer described previously. A polyisobutylene resin was used whose rheology was reported in previous sections (4.6.3 and 5.4.3). This resin was chosen because of its high viscosity (onset of instabilities

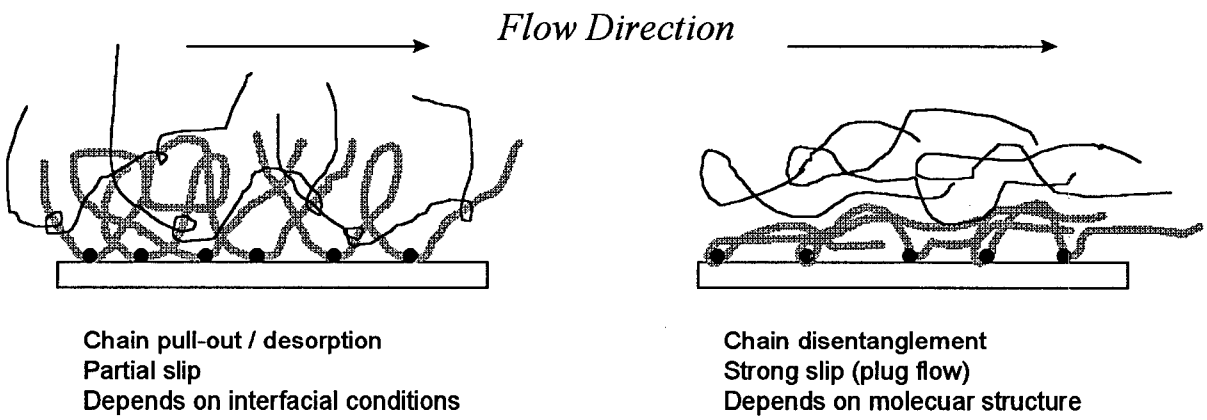

Figure 6-18. Schematic showing two different flow regimes: partial slip (left) and plug flow (right).

occurs at small shear rates) and elasticity (longer time scales are convenient for observation). Steady-shear experiments were performed using this material in order to determine the flow curve and its possible gap dependence. The gap dependence was not obtained, as shown in Figure 6-19. However, a sharp change in the slope of the flow curve around 100 kPa can be seen instead. At these high shear rates, stress oscillations were also observed (Figure 6-20). It can be seen that at small rates (0.2, 0.5 s^{-1}) the shear stress assumes a steady-state value. However, at higher rates (8, 35 s^{-1}) it can clearly be seen that the shear stress may oscillate. This is similar to the pressure oscillations observed in a capillary rheometer and it is attributed to a sudden disentanglement mechanism.

Evidence for this stick-slip transition was also found on the plates of the rheometer after the end of the experiment, when the plates were opened. As illustrated in the photo (the area of interest is circled in Figure 6-21), horizontal marks (lines) perpendicular to the direction of flow are left on the steel plate surface as the polymer sticked and slipped alternately. All these experimental findings suggest that flow instabilities, similar to oscillating melt fracture in capillary extrusion, occur in the sliding plate rheometer.

Numerous tests were carried out to quantify the phenomenon. The period of the shear stress oscillations was measured and plotted as a function of shear rate and shear stress (Figure 6-22). It can be concluded from these results that firstly, the onset of slip occurs at a certain value of shear stress but not shear rate (see also the plateau in Figure 6-19). Secondly, the existence of the marks left by the polymer on the interface and the occurrence of the stress oscillations suggests that the polymer slips over stainless steel in a periodic fashion. Whether or not this slip takes place exactly at the polymer–wall interface or over a monolayer of adsorbed polymer chains, is not known. Similar behaviour was also observed in experiments with polyethylene; however the oscillations occurred on a much smaller scale and were difficult to measure. This can be explained by the fact that the characteristic relaxation time of the polyethylene used is 10 to 20 times smaller than that of polyisobutylene (as was determined in section 4.6.1).

Returning to Figure 6-18, we can summarise now and provide additional experimental evidence as to what happens at the polymer–wall interface in the two slip regions. In the region of partial slip (region 3 in Figure 2-8) some of the polymer chains (thick lines in Figure 6-18) are attached (adsorbed) to the wall. These are entangled with other chains (thin lines in Figure 6-18) of the bulk material. Under flow conditions, some of the chains are detached from the wall and this leads to partial slip. As was hypothesised earlier by Hatzikiriakos (1991), this process depends on the interfacial conditions (e.g., presence of fluoropolymer coatings to reduce polymer adsorption, surface roughness, and material of construction of the die). Recent experimental findings by Anastasiadis and Hatzikiriakos (1998) support this hypothesis of an adhesive nature of slip in this flow regime (region 3 in Figure 2-8). Using a sessile drop method of determining the contact angles of polymer drops at various interfaces, they have calculated the work of

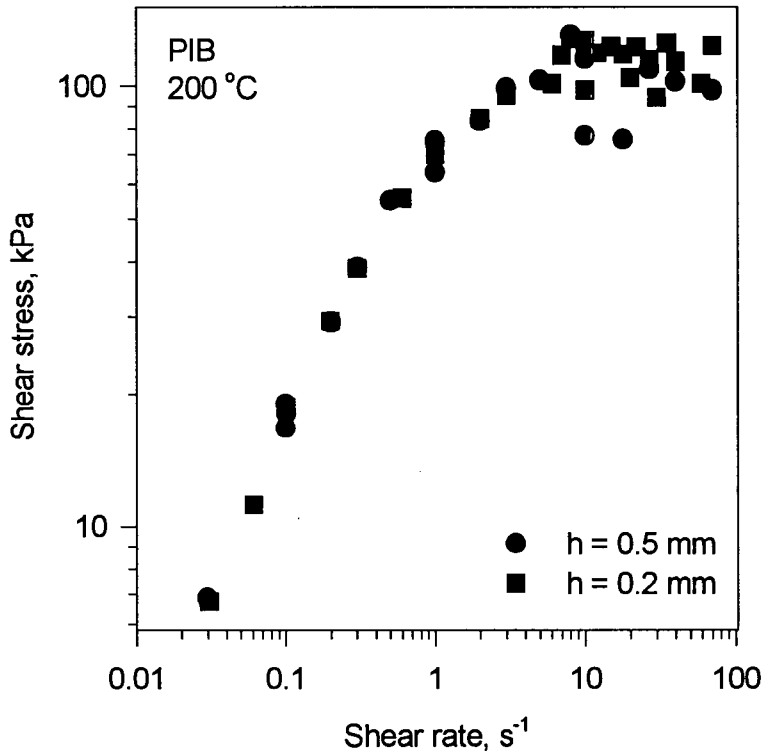

Figure 6-19. Flow curves of polyisobutylene determined at 200 °C using a sliding plate rheometer with two different gap spacings.

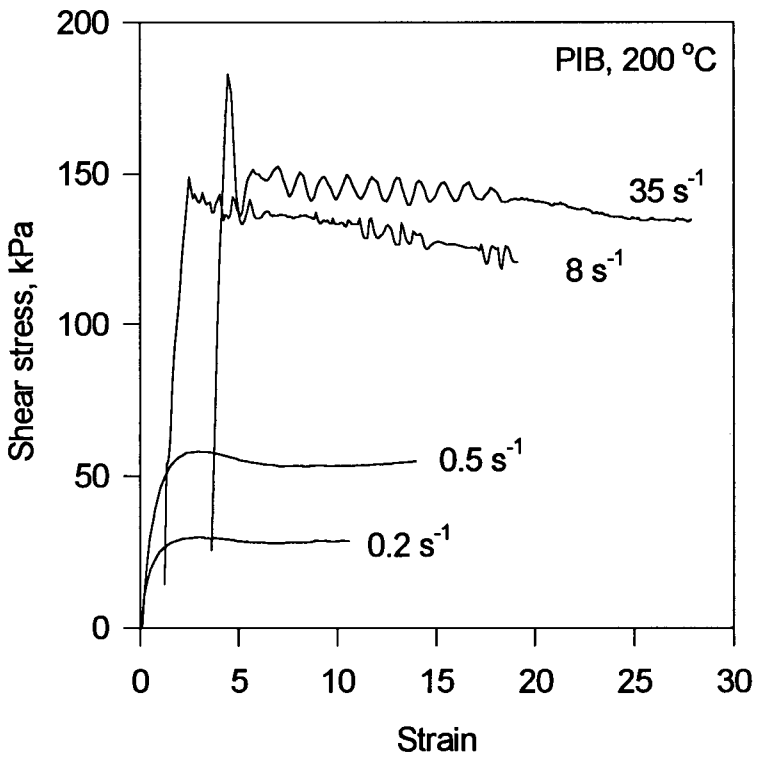

Figure 6-20. Stress oscillations obtained for polyisobutylene in a sliding plate rheometer with a 0.5 mm gap.

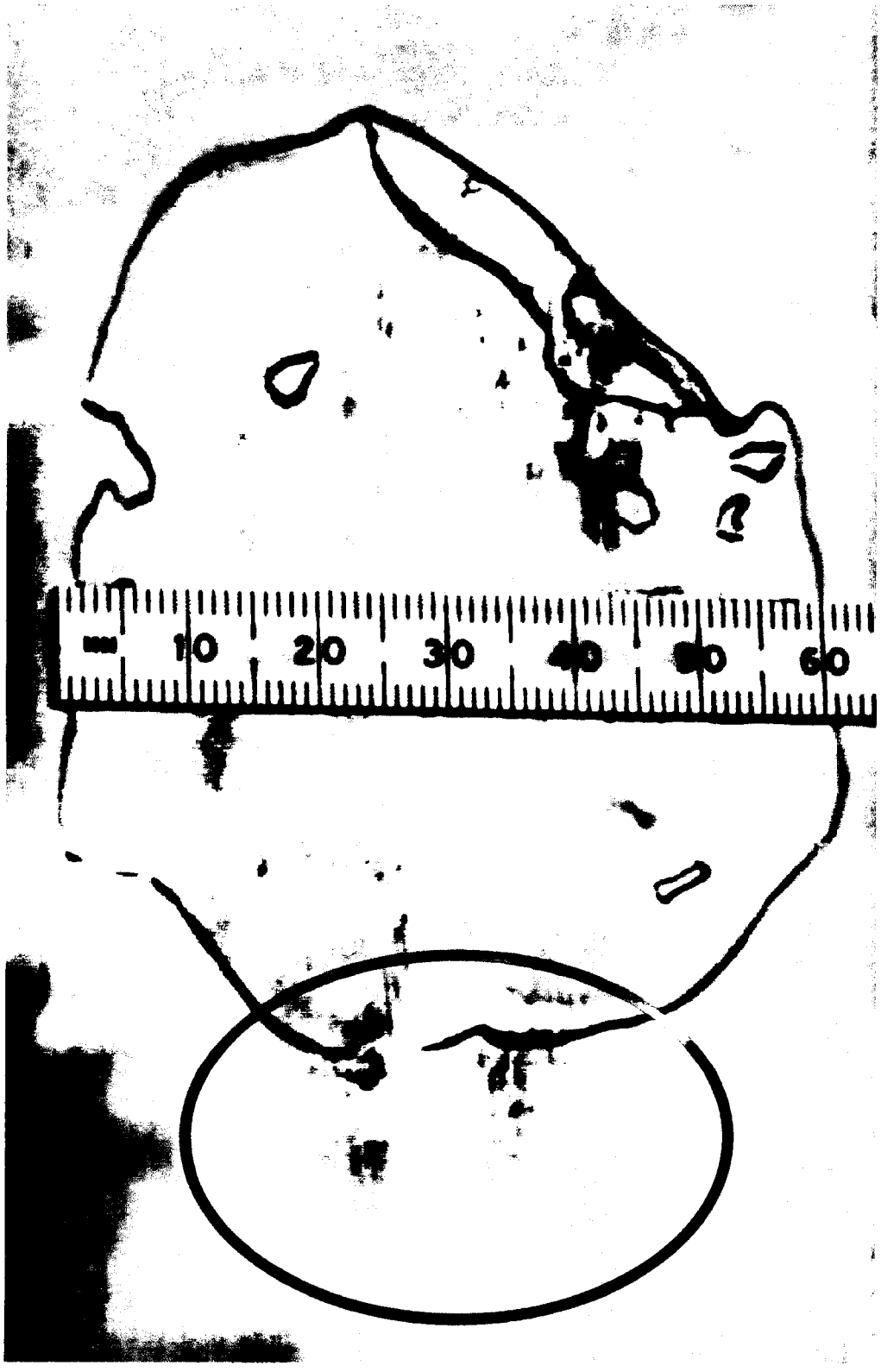

Figure 6-21. Photograph of a polyisobutylene sample attached to one of the plates of a sliding plate rheometer, obtained after a test in which stress oscillations were observed. The shear rate was 50 s^{-1}, the gap was 0.5 mm, distance between lines is about 1.3 mm, and the period of oscillations is 0.05 s.

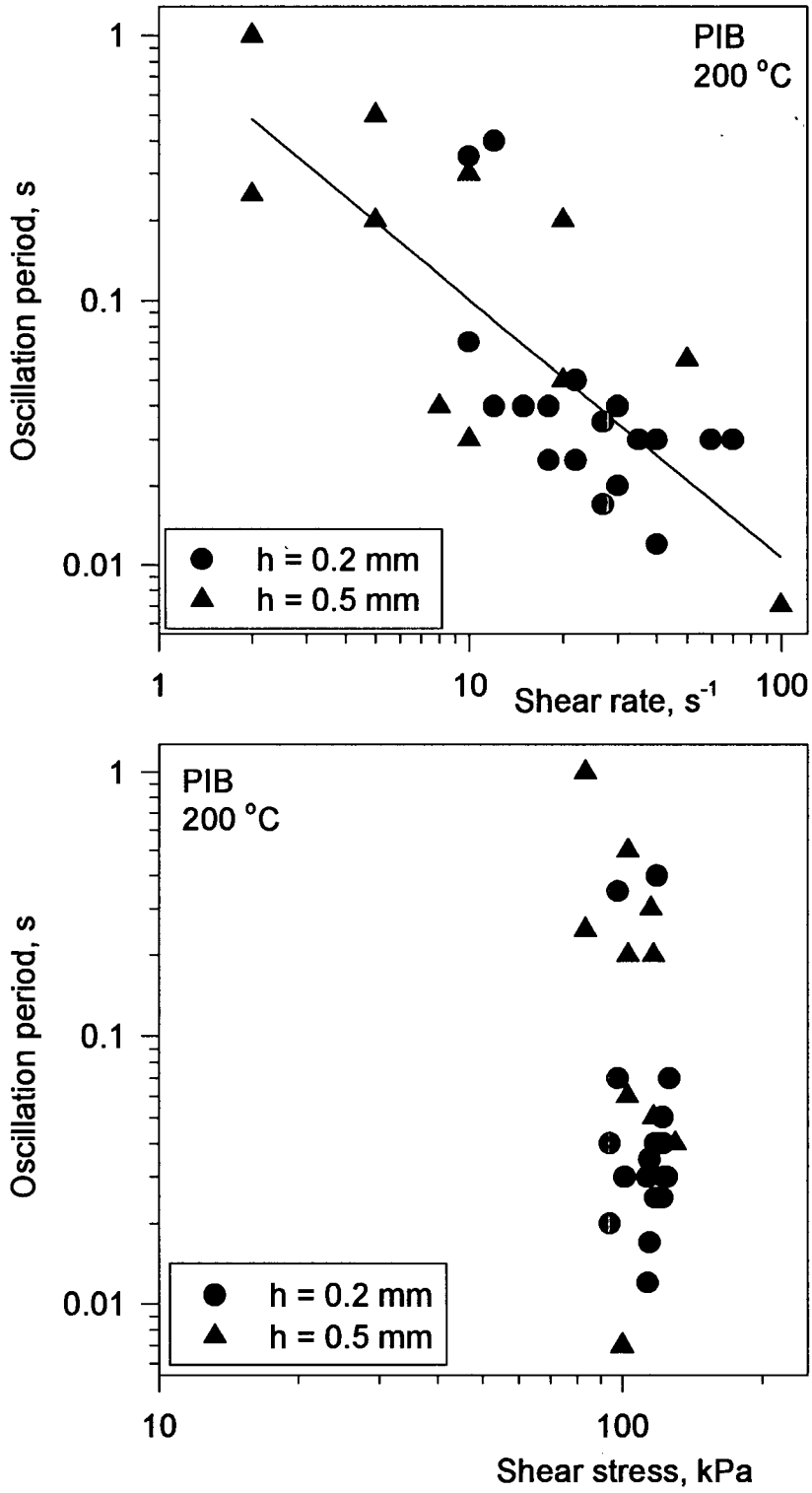

Figure 6-22. Dependence of the oscillation period of polyisobutylene on the shear rate (top) and on the shear stress (bottom).

adhesion of a number of polyethylene resins on clean and fluoropolymer-coated steel substrates. They have found that the critical shear stress for the onset of slip scales linearly with the work of adhesion (Figure 6-23). Note that the best linear regression does not go through the origin, but intercepts the work of adhesion axis at a finite value, indicating that some value of adhesive strength must be overcome for slip to occur.

The linear dependence of the critical shear stress for the onset of slip on the work of adhesion seen in Figure 6-23 is consistent with the proposed molecular theories of partial slip. Hill and co-workers (1990) and Hatzikiriakos (1993) have independently derived expressions suggesting this linearity:

$$\sigma_c = \frac{2fW_{adh}}{d} \qquad \text{eq. 6-4}$$

where fW_{adh} is a fraction of the work of adhesion that must be overcome by the stored elastic energy of adsorbed polymer chains for slip to occur, and d is the length over which a polymer chain jumps and is comparable to the radius of gyration of the chain.

Therefore, since the onset of slip apparently depends on the interfacial energetics, it suggests that the flow-induced chain detachment/desorption mechanism proposed in this section may account for the observed partial wall slip phenomenon in region 3 of Figure 2-8.

Additional experimental observations supporting the hypothesis that partial wall slip occurs due to failure at the polymer–wall interface, i.e. the mechanism of slip is adhesive failure, are summarised below. First, the material of construction of the die has been proven to affect surface melt fracture in this region [Ramamurthy, 1986], as well as to influence the slip

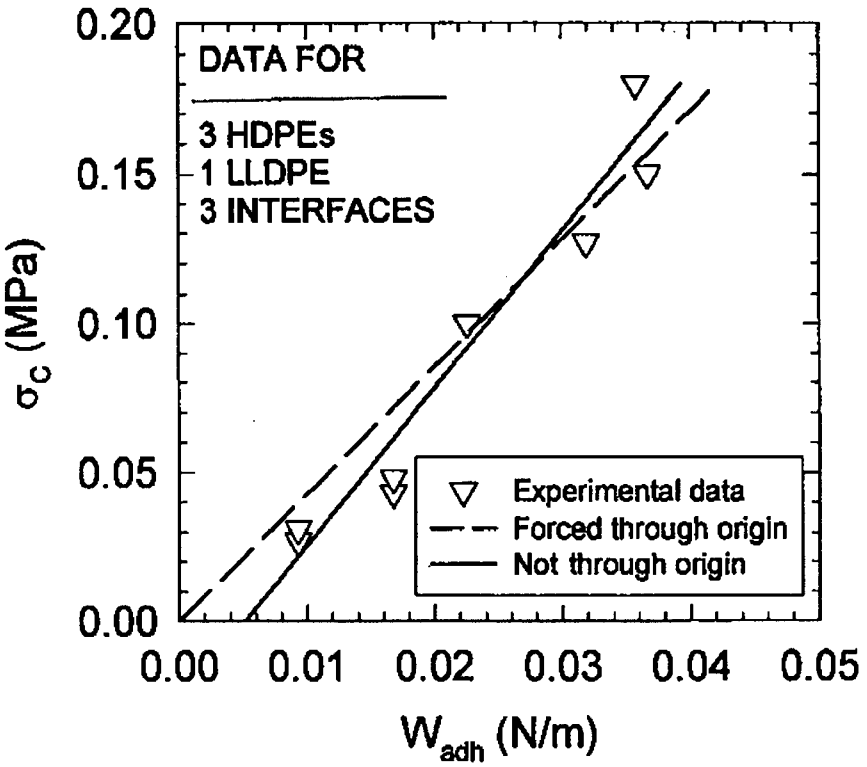

Figure 6-23. Correlation between the critical shear stress for the onset of slip and the work of adhesion. Data obtained by Anastasiadis and Hatzikiriakos (1998) for three different HDPEs, one linear LDPE, and three different interfaces (clean steel, Viton and Teflon coated steel).

behaviour of polymers [Person and Denn, 1997]. The presence of a thin layer of a fluoropolymer at the interface has a strong effect on the surface melt fracture and wall slip [Athey *et al.*, 1986; Rudin *et al.*, 1985; Hatzikiriakos and Dealy, 1991]. These findings suggest that there is a link between the conditions at the polymer–wall interfaces and the observed interfacial phenomena. Various die wall materials have different surface energies, and therefore interact differently with the molecules of molten polymers. The presence of oxides and other impurities on the surface of metals can dramatically change their surface energy [Fowkes, 1964].

At the second critical shear stress (region 4 in Figure 2-8), the polymer molecules at the interface (thick lines in Figure 6-18) are disentangled from the rest (thin lines in Figure 6-18) and as a result the polymer slips freely and essentially plug flow is obtained. Consequently, the

polymer chains relax and entangle again and the procedure is repeated in a continuous fashion. This process (unstable flow) mainly depends on the molecular characteristics of the polymer (mainly to the number of entanglements).

The magnitude of the oscillations as well as the rate of transition from weak to strong slip will strongly depend on the molecular weight of the polymers and both these should scale with the reptation time [Doi and Edwards, 1986; de Gennes, 1979]. Figure 6-24 compares the dependence of the slip extrapolation length (see section 2.3.4 for definition) on molecular weight, obtained at the point of transition. The experimental data were reported previously by Hatzikiriakos and Dealy (1992) and Wang and Drda (1996). The agreement between the data obtained by the two different research groups is very good, and the points essentially form a straight line on a logarithmic plot with a slope of about 3.4. This is in agreement with de Gennes' reptation theory [de Gennes, 1979] for the rheology of entangled molecules. It states that the slip length is proportional to M_w^3.

Based on these two molecular slip mechanisms, the slip behaviour of branched polymers can now be explained (see Figure 6-25). Firstly, the number of entanglements experienced by a branched polymer is much higher (due to the presence of branches) and secondly, the relaxation times for destroying these entanglements are much longer compared to those in the case of linear molecules. Note that the latter (relaxation times) are associated with the reptation time of the individual arms (Bick and McLeish, 1996). In this respect, the molecules at the interface feel much stronger forces and for longer periods of time. This in turn leads to an increased amount of chain detachment from the interface, which increases the partial slip of

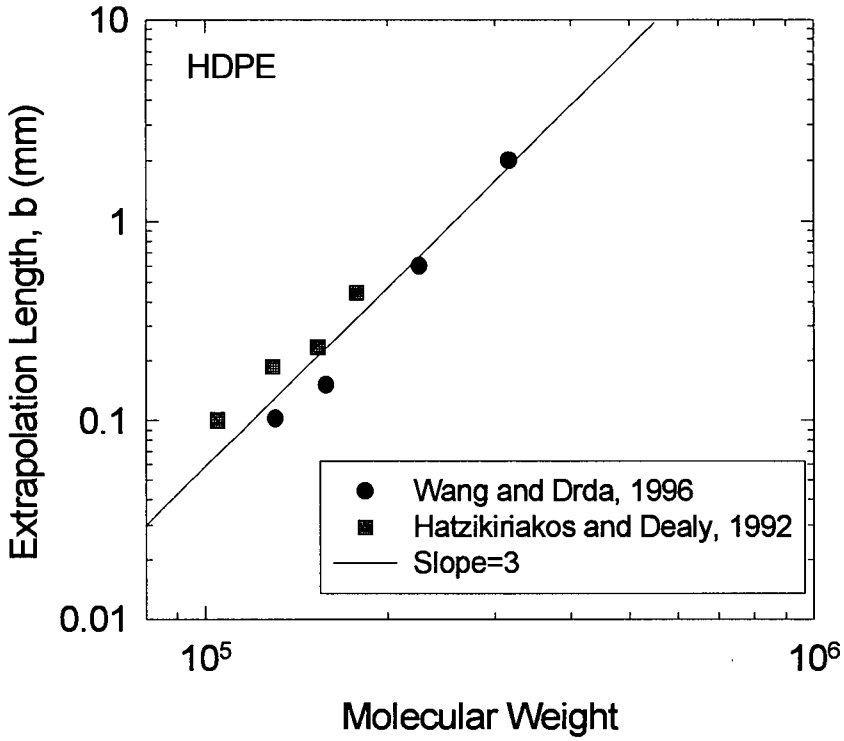

Figure 6-24. The slip extrapolation length (determined at the point of transition to strong slip) as a function of the weight average molecular weight.

branched polymers compared to that of linear ones. When the second critical shear stress for the onset of sudden disentanglement is approached, two possibilities exist. If the slip velocity of polymer is less than the mean velocity, small pressure oscillations take place (as was observed for resin A). If the slip velocity is about equal to the mean velocity (plug flow), then no pressure oscillations are obtained (resin B).

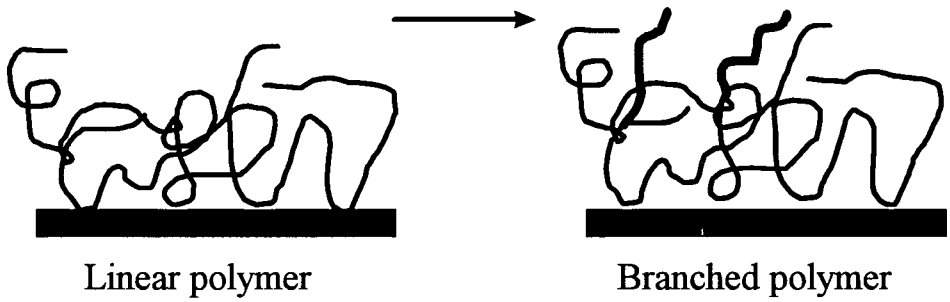

Figure 6-25. Schematic comparing linear (left) and branched (right) polymers.

Thus, following from the above tentative interpretation of the slip phenomenon in the flow of polyethylenes, one may visualise this phenomenon as a competition between chain detachment from the wall and sudden disentanglement (onset of unstable flow). If the rate of chain detachment is reduced (linear polymers), sudden disentanglement sets off pressure oscillations (unstable flow). If initially an increased rate of chain detachment is obtained and the flow becomes almost plug-like, sudden disentanglement cannot occur and as a result the unstable flow (spurt effect) is suppressed. Table 6-3 summarises the above described mechanisms and their relation to the molecular structure of the polymeric chains.

Table 6-3. Effect of molecular structure on the flow of polymers.

Molecular Structure	Response to Flow	Oscillations	Wall Slip
Low M_w, Linear chains (few entanglements)	Small molecules are difficult to pull out	Small or none	Weak
High M_w, Linear chains (more entanglements)	Large molecules are easier to pull out	Large, due to sudden disentanglement	Strong, intermittent
Branched (many entanglements)	Approaches plug flow before the critical stress for sudden disentanglement	Suppressed by bulk flow of disentangled chains	Strong, continuous

6.6 Conclusions

The rheology and processability of two metallocene polyethylenes was studied by using both a parallel plate and a capillary rheometers. Their rheological and processing characteristics were also compared to those of a conventional linear low density polyethylene (Dowlex 2049). In constant stress rheology, dynamic frequency sweep experiments over a wide range of temperatures has indicated that the two metallocene polyethylenes are thermorheologically

complex fluids compared to Dowlex 2049, where application of the time-temperature superposition technique reduces the dynamic data to a single master curve. This failure was attributed to the presence of long branches in the metallocene polyethylene resins.

In capillary rheometry, it was found that several physicochemical changes possibly take place at the polymer/wall interface during extrusion. Long pressure transients are obtained and multiple polymer loads should be extruded in order to obtain steady state operation. To our knowledge, this has never been observed in the capillary extrusion of conventional polyethylene resins. Diameter dependence of the flow curves and subsequent use of the Mooney technique resulted in slip velocities which were very close to those calculated under the assumption of plug flow. This latter observation is somewhat inconsistent with previous findings in the capillary extrusion of other polyethylenes, i.e. the slip velocity of Dowlex 2049 at the same conditions was found to be much lower than those of the metallocene resins. This was explained in terms of a qualitative molecular mechanism in which direct chain detachment from the interface and sudden disentanglement of the bulk of the polymers from the chains attached to the solid boundary were hypothesised. Branched polymers favour direct chain detachment and as a result slip more. However, at high enough shear rates where all polyethylenes exhibit almost plug-like flow behaviour, the flow is governed by monomer–wall friction (independent of molecular structure) rather than bulk rheology.

7. DYNAMIC MULTI-MODE SLIP MODEL

– EXECUTIVE SUMMARY –

■

Static and single-mode dynamic slip models cannot adequately describe the experimentally observed data for transient shear flows

■

A new model involving multiple slip relaxation times provides an improvement in predicting the stress response in steady and large-amplitude oscillatory shear

7.1 Introduction

Unlike Newtonian fluids, polymer melts slip over metal surfaces when the wall shear stress exceeds a critical value [Ramamurthy, 1986; Kalika and Denn, 1987; Hatzikiriakos and Dealy, 1991]. To determine and understand the "true" rheological behaviour of these materials at high shear rates, their interfacial behaviour under both steady-state and dynamic conditions should be understood. This could be extremely useful in evaluating the relative capabilities of molecular or continuum theory in predicting the rheological behaviour of molten polymers. In the previous chapters, the steady-state slip behaviour of linear polymers was studied and discussed in detail. Here, these concepts are extended to take into account the relaxation behaviour of slip in dynamic situations.

Most of the previously reported slip velocity models are "static" models, where the slip velocity depends on the instantaneous value of the wall shear stress. However, the experimental observations have suggested that the slip velocity may depend on the past states of the local wall shear and normal stresses [Hatzikiriakos and Dealy, 1991]. This is similar to the concept of the viscoelastic fluid memory, where the local state of stress depends on the past deformation history to which the fluid particles were subjected.

Although an integral constitutive equation coupled with a "static" slip velocity model can explain the steady-state results for linear low density polyethylenes in simple shear, it completely fails to describe their dynamic behaviour, i.e. stress growth during start-up of steady shear. The purpose of this work is to develop a multimode slip model which would overcome some of the limitations of static and single-mode dynamic models and would offer predictions that are more consistent with experimental results.

7.2 Background

7.2.1 Static Slip Model Predictions

There are numerous static slip models found in literature (see section 2.3.4 for an overview). They range from a very simple power-law model (Hatzikiriakos and Dealy (1991), eq. 2-26) to elaborate models based on molecular theories which take into account the effects of numerous parameters (for example, eq. 2-31). All of the static models are so called because they can be applied only under steady-state conditions, or at least they can model the steady-state slip behaviour of molten polymers.

To see this more clearly, let us consider a constitutive equation to predict the shear stress growth as a function of time in a steady simple shear experiment. For example, one may employ Wagner model (a special form of BKZ equation, described in Appendix C) to accomplish this. For simple shear Wagner model can be written as follows:

$$\sigma(t) = \int_{-\infty}^{t} \frac{G_i}{\lambda_i} e^{-\frac{t-t'}{\lambda_i}} \frac{\gamma(t,t')}{1+\alpha\gamma^{\beta}(t,t')} dt' \qquad \text{eq. 7-1}$$

where $\sigma(t)$ is the stress response as a function of time, $\gamma(t, t')$ is the shear deformation between times t and t', α and β are the parameters of the damping function, and G_i and λ_i comprise the relaxation spectrum determined from linear viscoelastic measurements (see section 5.4.1 on the procedure used to determine G_i and λ_i). All parameters of the model are listed in Table 7-2 below. Wagner model was used to predict the shear stress response of Dowlex 2049 as a function of time at different shear rates, and two examples are shown in Figure 7-1 for $\dot{\gamma}$ =18 s^{-1} and in Figure 7-2 for $\dot{\gamma}$ =110 s^{-1}.

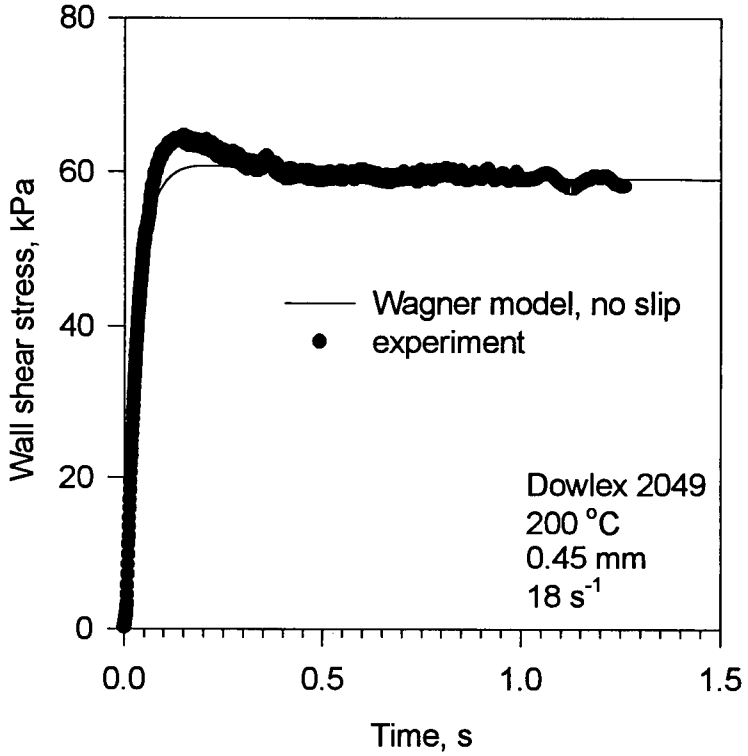

Figure 7-1. Start-up of steady shear experiment at a shear rate of 18 s^{-1} and comparison with the Wagner model predictions under no-slip conditions.

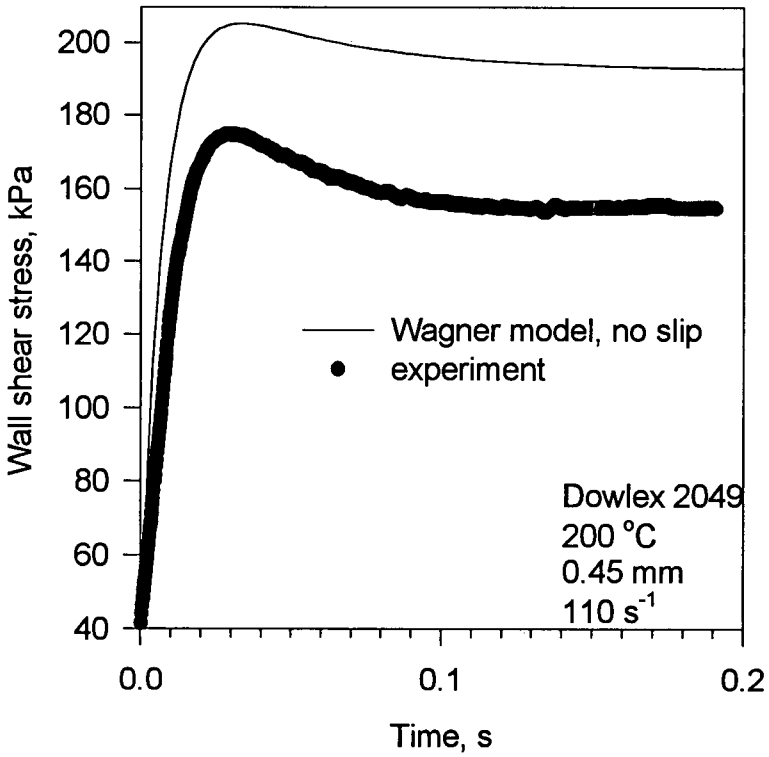

Figure 7-2. Start-up of steady shear experiment at a shear rate of 110 s^{-1} and comparison with the Wagner model predictions under no-slip conditions.

It can be seen that at the lower shear rate the steady-state experimental data and the model prediction agree, but there is no agreement at the higher shear rate. This is due to the fact that the polymer slips and as a result a reduction in the steady-state stress is obtained.

To improve the prediction of the model, the steady-state slip should be taken into account. A power-law static slip model (eq. 2-26) was coupled with the Wagner model, which resulted in an improved shear stress response. As Figure 7-3 shows, the predicted final steady-state value exactly matches the experimental shear stress. This is to be expected, since the parameters of the power-law slip model (a and m, eq. 2-26) were determined based on this type of experiment. However, the model fails to predict the overshoot that occurs during the start-up. The "static" slip model suppresses all the important dynamics of the flow. Therefore, a dynamic slip velocity model is needed to preserve the overshoot.

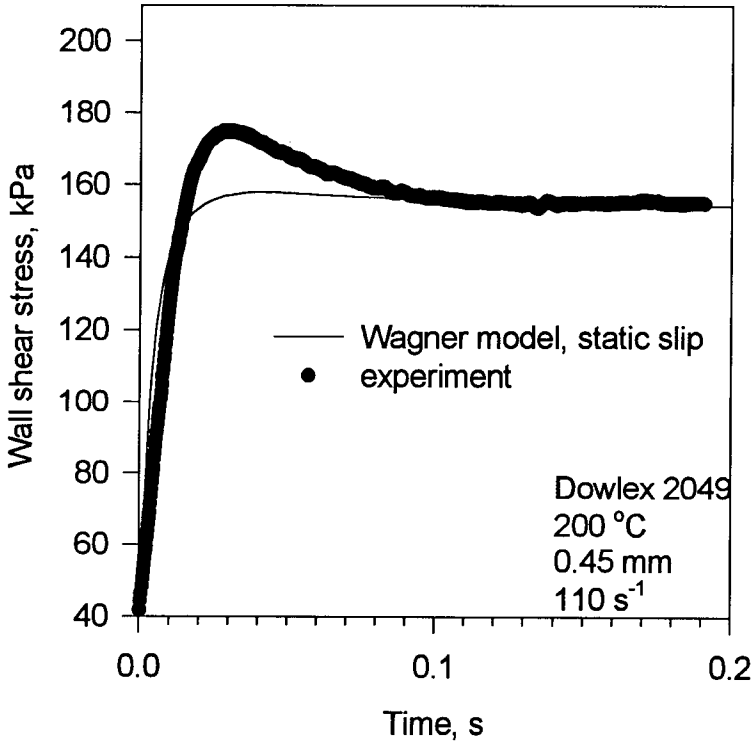

Figure 7-3. Start-up of steady shear experiment at 200 °C and comparison with predictions of the Wagner model coupled with a static slip model.

7.2.2 Dynamic Slip Model

Pearson and Petri (1968) first proposed a "memory" slip velocity model or a "retarded" slip boundary condition as they called it:

$$u_s + \lambda_s \frac{du_s}{dt} = \varphi(\sigma_w) \qquad \text{eq. 7-2}$$

where u_s is the slip velocity, λ_s is the slip relaxation time and σ_w is the wall shear stress. The choice of $\varphi(\sigma_w)$ depends on the considered "static" slip model. If λ_s is set to zero, the static slip model is recovered.

When the same power-law slip model is used [Hatzikiriakos and Dealy, 1991], eq. 7-2 becomes

$$u_s + \lambda_s \frac{du_s}{dt} = a\sigma_w^m \qquad \text{eq. 7-3}$$

were a is a slip coefficient and m is the power law exponent usually of the order of three. In order to examine its capabilities in predicting the transient behaviour of a molten polymer in start-up of steady shear experiments, eq. 7-3 was coupled with the Wagner model. The result is shown in Figure 7-4. It can be seen that the improvement in the prediction over the static model (Figure 7-3) is dramatic: not only does it yield the correct steady-state value of the shear stress, but also it predicts the presence of overshoot at small times. However, the position of the predicted overshoot does not match the experimental one; if an attempt is made to adjust it by changing λ_s in eq. 7-3, the predicted maximum in the shear stress would no longer agree with the experimental value.

These findings clearly call for a more versatile slip model, capable of predicting various non-linear phenomena with greater accuracy. The next section is devoted to the development of such a model.

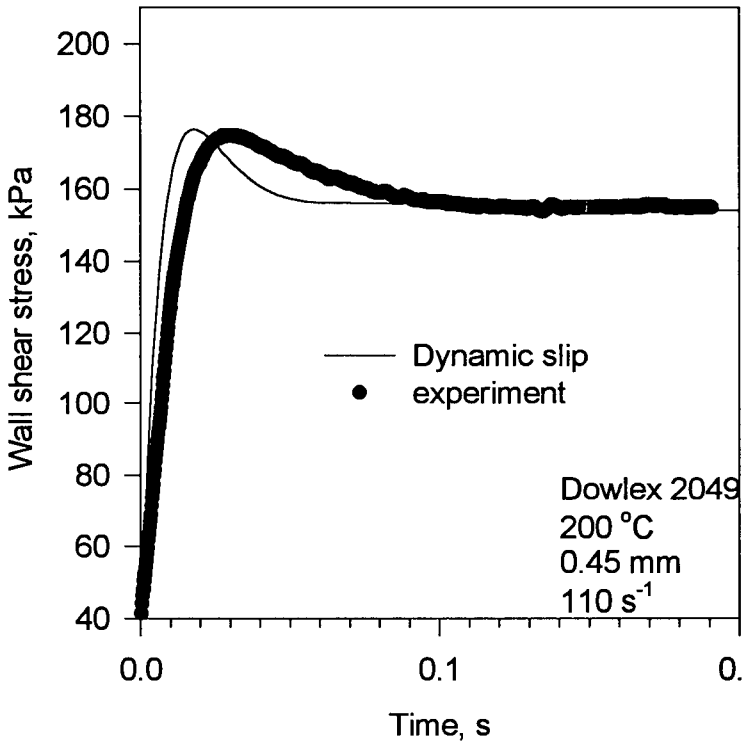

Figure 7-4. Start-up of steady shear experiment at 200 °C and comparison with predictions of the Wagner model coupled with a single-mode dynamic slip model.

7.3 Multimode Dynamic Slip Velocity Model

Taking a closer look at the dynamic slip model, eq. 7-3, one may notice its striking resemblance to the Maxwell mechanical model for viscoelasticity,

$$\sigma + \lambda \frac{d\sigma}{dt} = \eta_0 \dot{\gamma} , \qquad \text{eq. 7-4}$$

which approximates the behaviour of a linear viscoelastic material using a simple mechanical analogue, a Maxwell element consisting of a linear spring (Hookean solid) in series with a dashpot (Newtonian fluid). However, the actual behaviour of polymer melts is more complex and cannot be represented using a single set of parameters λ and η_0. The following generalised Maxwell model (see Appendix B for more details) was found to perform better:

$$\sigma_i + \lambda_i \frac{d\sigma_i}{dt} = \eta_{0,i}\dot{\gamma} \quad \text{and} \quad \sigma = \sum_i \sigma_i \qquad \text{eq. 7-5}$$

The total stress value, σ, is the sum of individual contributions, σ_i, and its accuracy depends on the number of the $\{\lambda_i, \eta_{0,i}\}$ pairs.

By analogy to the derivation of the generalised (or "multimode") Maxwell model from its single-mode counterpart, the single-mode dynamic slip model (eq. 7-3) can be extended to a multimode one, which can be written as follows:

$$u_{s,i} + \lambda_{s,i} \frac{du_{s,i}}{dt} = a_i \sigma_w^m \quad \text{and} \quad u_s = \sum_i u_{s,i} \qquad \text{eq. 7-6}$$

One constraint resulting from consideration of the steady-state slip velocity data, is that the sum of all the slip coefficients a_i must equal the static slip coefficient, a (eq. 2-26):

$$\sum_i a_i = a \qquad \text{eq. 7-7}$$

A question of great interest at this point is, how one can determine the parameters of eq. 7-6. In order to determine the parameters of the multimode slip model ($\{a_i, \lambda_{s,i}\}$ pairs) together with Wagner model, the following data are necessary:

Table 7-1. The input parameters needed to solve eq. 7-1, eq. 7-6 and eq. 7-7.

Parameters	How to determine
Relaxation spectrum, $\{G_i, \lambda_i\}$	Linear viscoelastic experiments
Static slip coefficient, a	Steady shear experiments with Mooney technique
Damping function, α and β	Step-strain experiments

In addition to these parameters, one must also choose a non-linear dynamic shear experiment for the purpose of comparison with the dynamic slip model predictions. Such an experiment should involve large enough deformations and shear stresses that exceed the critical shear stress

for the onset of slip. Once the experimental data under slip conditions is available, the next step is to find such a set of $\{a_i, \lambda_{s,i}\}$ parameters, that minimises the difference between the predicted and experimental data.

7.4 Determination of Model Parameters

Experiments were carried out with Dowlex 2049 (a linear low density polyethylene resin) at 200 °C using a sliding plate rheometer. The flow curve was determined for two different gap spacings by performing steady shear experiments. The dynamic moduli, G' and G'', were determined by using a parallel plate rheometer, and are plotted in Figure 7-5. These data are the same as those obtained with a different rheometer and plotted in Figure 6-4. The parameters (G_i, λ_i) of the memory function were calculated by using a non-linear optimisation technique from the linear viscoelastic data G' and G'' (the procedure is described in detail in section 5.4.1).

The values of α and β of the damping function were determined by measuring the stress relaxation after imposition of step strains by means of a sliding plate rheometer. The procedure involved the following steps. A sudden shear strain, γ, was imposed on a sample initially at rest and the value of resulting shear stress, $\sigma(t)$, was monitored as a function of time. After allowing the sample to rest, another step deformation was imposed using a different value of γ. This was repeated until the various values of γ covered a desired range, i.e. from 0.1 to 20. The relaxation moduli for these step strains are then calculated as follows:

$$G(t,\gamma) = \frac{\sigma(t)}{\gamma} \qquad \text{eq. 7-8}$$

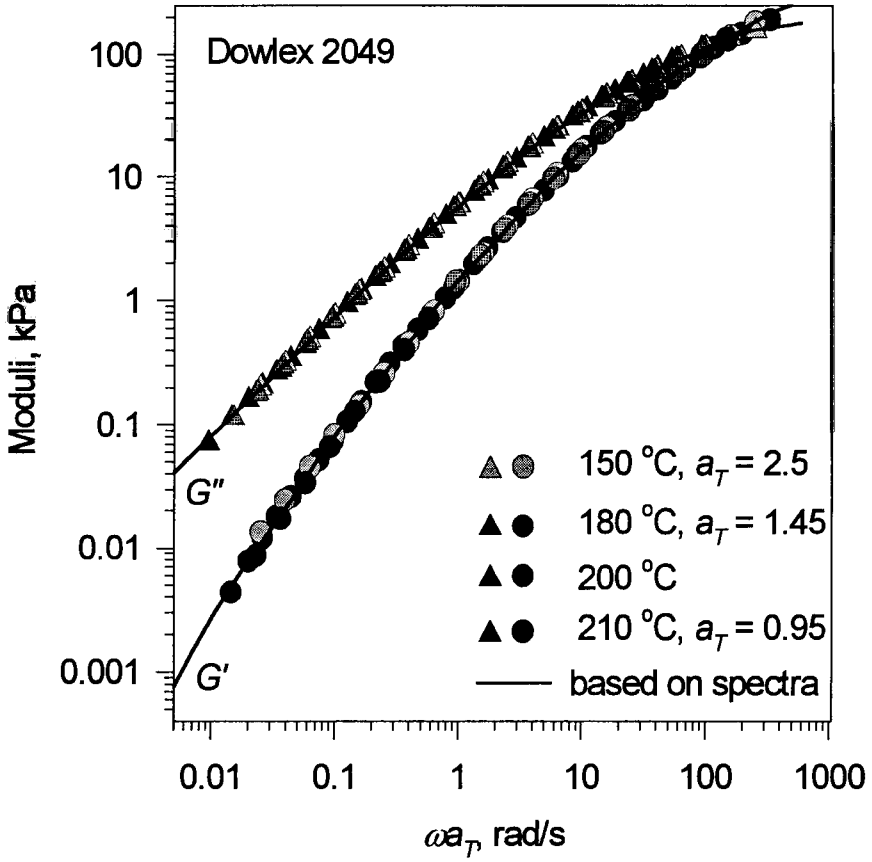

Figure 7-5. Storage and loss moduli of Dowlex 2049 at T_{ref} = 200 °C: experimental data (symbols) and values calculated from spectra (lines, using eq. 5-1).

These results are plotted in Figure 7-6. The upper curve, obtained for γ=0.1, is considered to represent the linear relaxation modulus, $G(t)$. Curves for all other strains are below it, which manifests the "dampening" of the linear response. The damping function is determined by finding the coefficient $h(\gamma)$, defined as:

$$h(\gamma) = \frac{G(\gamma, t)}{G(t)} \qquad \text{eq. 7-9}$$

that would cause all of the curves to superpose with the linear $G(t)$, as shown in Figure 7-7.

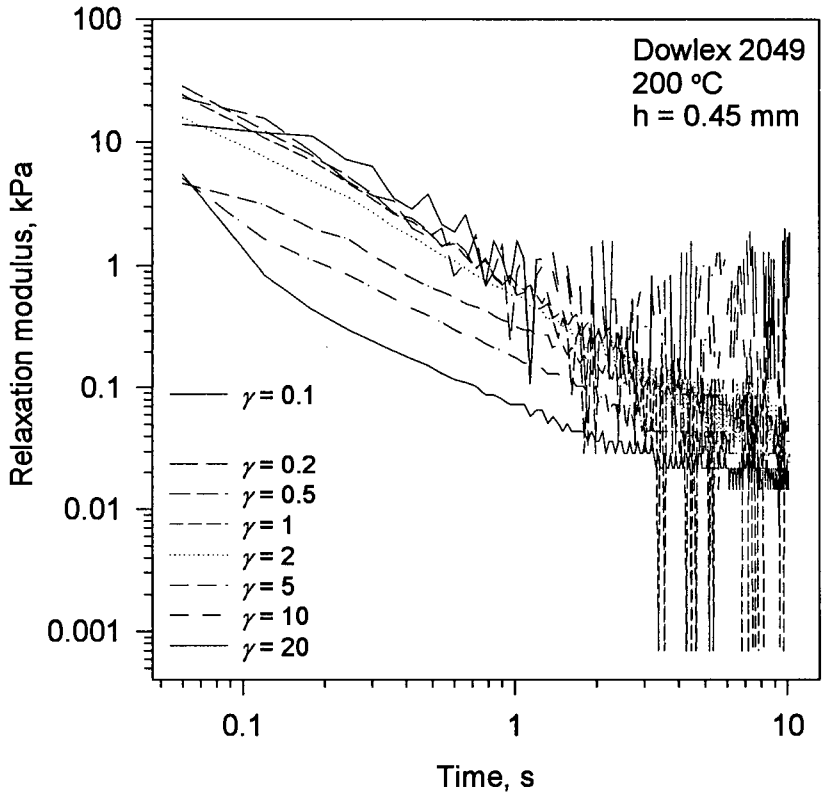

Figure 7-6. The relaxation modulus of Dowlex 2049 obtained at different values of step strain.

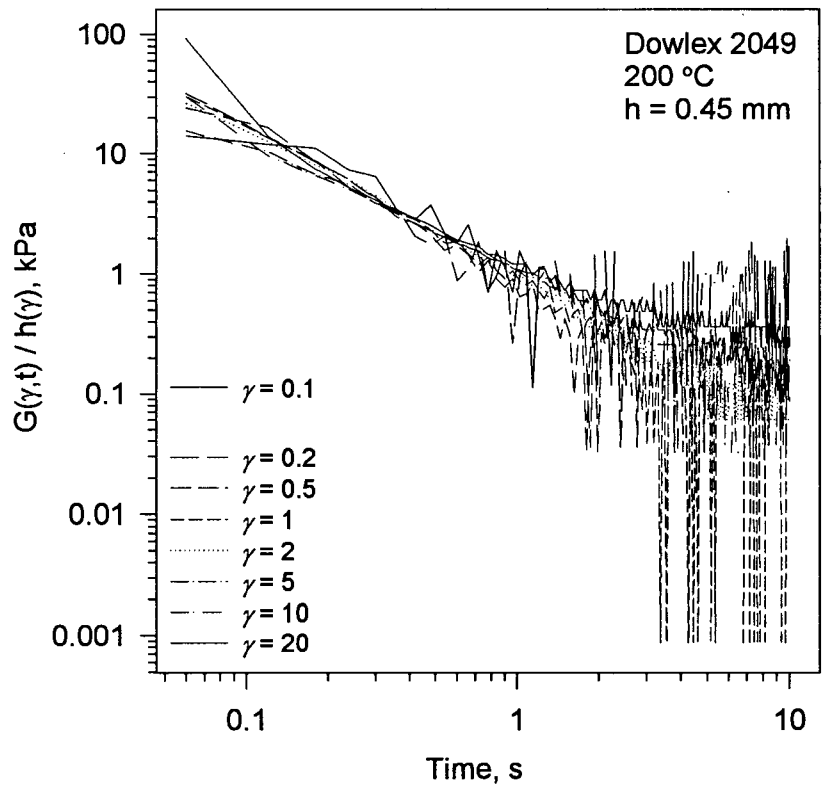

Figure 7-7. The superposition of the relaxation curves of Figure 7-6 to determine the damping function.

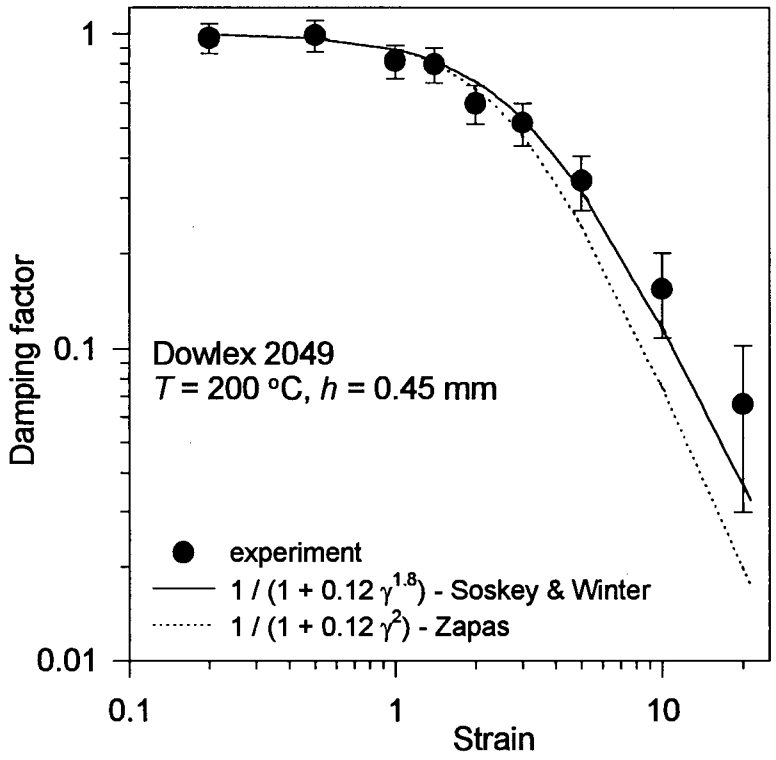

Figure 7-8. Damping function of Dowlex 2049 at 200 °C. The fits are to the equation proposed by Zapas (1966) and Soskey and Winter (1984).

The determined damping function, $h(\gamma)$, is plotted in Figure 7-8 together with two fitted equations. The best fit to the experimental data is attained by using the form proposed by Soskey and Winter (1984), with $\alpha = 0.12$ and $\beta = 1.8$.

Using the Wagner model (eq. 7-1), the flow curves were calculated under the assumption of no slip. Figure 7-9 shows the experimental flow curve for Dowlex 2049 plotted together with the Wagner model prediction. The 95% confidence interval was calculated to accurately determine the point of deviation from no-slip conditions. Deviations from the experimental results were interpreted as the effect of slip. The accuracy of this approach was confirmed by comparing the slip velocity thus obtained with the slip data resulting from the Mooney technique. Figure

7-10 demonstrates an example of the gap dependence of the shear stress from which the slip velocity data can be calculated using the Mooney technique (described in Appendix A).

As Figure 7-11 indicates, the two methods are in good agreement. The slip velocity was then used to determine the slip coefficient, a, and the exponent, m, of eq. 7-3 (setting λ_s to zero for the steady-state conditions). The critical shear stress for the onset of slip was also determined, and was found to be 90 kPa. The fitted parameters are listed in Table 7-2 below.

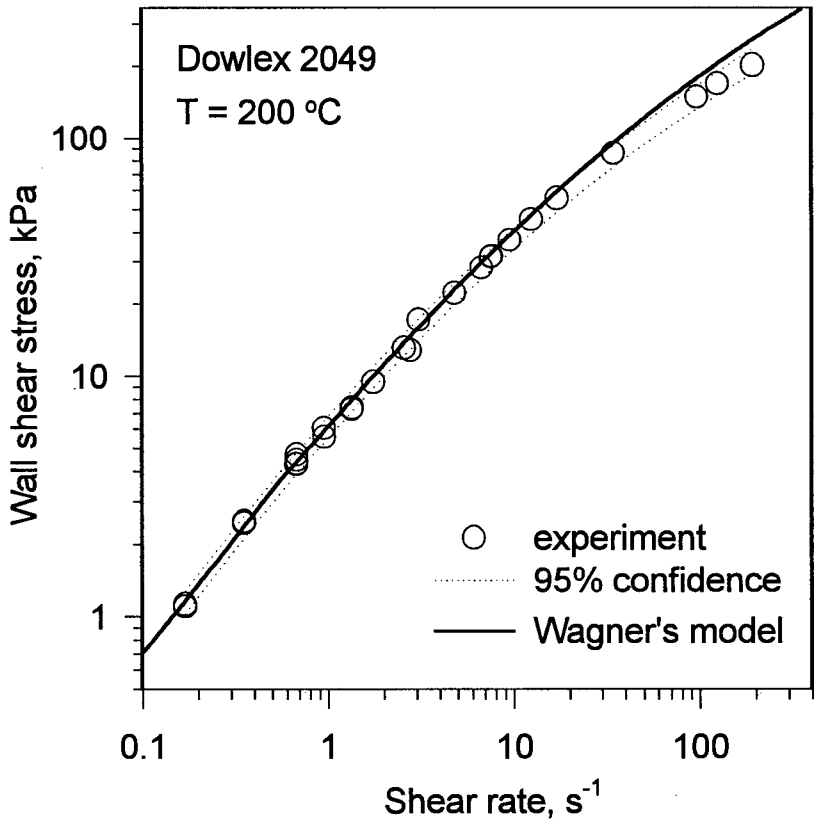

Figure 7-9. Flow curves of Dowlex 2049 at 200 °C obtained using sliding plate rheometer and from the Wagner model.

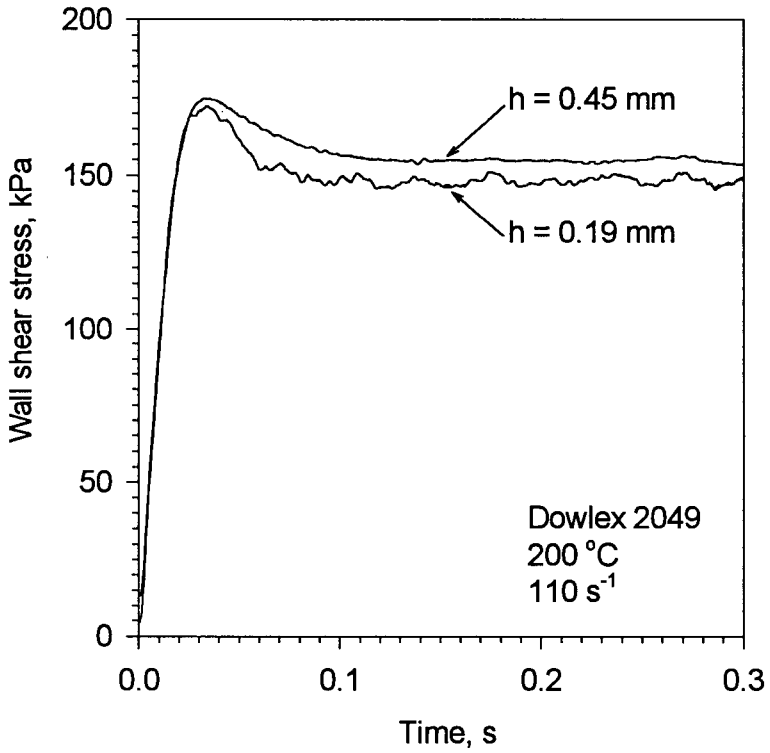

Figure 7-10. Flow curves of Dowlex 2049 at 200 °C obtained using sliding plate rheometer at two different gaps.

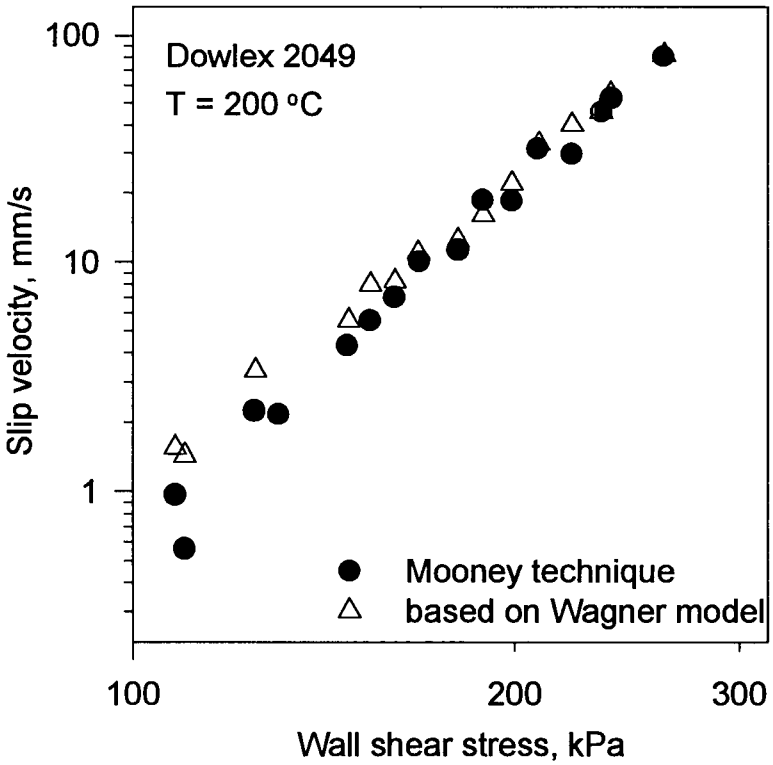

Figure 7-11. Slip velocity of Dowlex 2049 determined using the Mooney technique and based on deviations of the Wagner model from the flow curve.

Table 7-2. Parameters used to solve the equations in the multimode dynamic slip model.

G_i (kPa)	λ_i (s)	Others
422.8	$9.30 \cdot 10^{-4}$	$a = 1.7 \cdot 10^{-6}$ mm·kPa$^{-3.06}$
137.6	$6.97 \cdot 10^{-3}$	$m = 3.06$
46.78	0.03713	$\alpha = 0.12$
10.16	0.1992	$\beta = 1.80$
1.439	1.127	
0.155	7.527	

Large-amplitude oscillatory shear was chosen as a basis for fitting the additional parameters of the dynamic slip model. The LAOS experiments allow one to independently control the frequency, ω, and the strain amplitude, γ_0. By varying these two parameters, one can obtain a wide range of different shear stress responses at various time scales, as well as ensure that the stress exceeds the required threshold for the onset of slip. The following combinations of frequency and strain amplitude were used:

Table 7-3. LAOS test parameters.

Frequency, Hz	Strain amplitude	Shear rate amplitude ($=2\pi\omega\gamma_0$)
1	16	100.5
2	8	100.5
4	4	100.5
8	2	100.5
16	1	100.5

7.5 Results and Discussion

Table 7-4 summarises the parameters obtained for the three different slip models. The slip exponent, m, was kept constant for all of the simulations since it was determined from steady-state experiments. The steady-state slip model has only two parameters which are easily obtained by a linear regression between logarithms of the slip velocity and wall shear stress.

The single-mode dynamic slip model adds one more parameter, the slip relaxation time (λ_s). It is interesting to note that the determined value of λ_s, 17 milliseconds, is about 2.5 times higher than the characteristic relaxation time for this resin (7 ms, determined as a reciprocal of the crossover frequency in Figure 7-5).

Table 7-4. Parameter values for static, single-mode dynamic and multimode dynamic slip models.

Slip Model	Parameters	Methods
Steady-state $u_s = a\sigma_w^m$	a = 6.5·10^{-6} mm s^{-1} kPa^{-m} m = 2.8	Steady shear test, linear fit
Single-mode dynamic $u_s + \lambda_s \frac{du_s}{dt} = a\sigma_w^m$	a = 6.5·10^{-6} mm s^{-1} kPa^{-m} λ_s = 0.017 s m = 2.8	Frequency sweep
Multimode dynamic $u_{s,i} + \lambda_{s,i} \frac{du_{s,i}}{dt} = a_i\sigma_w^m$	a_1 = 5.1·10^{-6} mm s^{-1} kPa^{-m} $\lambda_{s,1}$ = 0.011 s a_2 = 1.4·10^{-6} mm s^{-1} kPa^{-m} $\lambda_{s,2}$ = 0.86 s m = 2.8	Frequency sweep, multi-parameter estimation

Finally, the multimode dynamic slip model adds two more parameters to the list. An iterative parameter estimation procedure was used to find the number of the $\{a_i, \lambda_{s,i}\}$ pairs and their values. It was found that, for the conditions tested, two pairs were sufficient to adequately simulate the shear stress response. It can also be noted that the values of a_i satisfy the condition imposed by eq. 7-7. Furthermore, the values of the slip relaxation time, $\lambda_{s,i}$, exhibit the following behaviour: $\lambda_{s,1}$ = 11 ms, which is not far from its single-mode counterpart. That value corresponds to the strongest slip coefficient a_1. The other slip relaxation time, $\lambda_{s,2}$, is much longer, but its contribution is significantly lower, as the a_2 value is only 27% of a_1.

The predictions of the three slip models, steady-state, single-mode and multimode (two-mode in this case) are shown in Figure 7-12 for two cases. It can be seen that the steady-state model underestimates the prediction, since it acts instantaneously to reduce the shear stress to its steady-state value. The single-mode model provides a better prediction, but fails when the stress value exceeds the critical stress for the onset of slip for prolonged periods of time. For example, in the upper graph in Figure 7-12 (ω=2 Hz, γ_0=8) the predictions of the single-mode and two-mode models coincide until 0.96 seconds (marked with an arrow). At this point, 0.96 s, the shear stress has already reached 130 kPa, i.e. well above the critical level (90 kPa). This means that a single-mode slip model is capable of accurate predictions only at very short time scales. The addition of a second set of parameters $\{a_i, \lambda_{s,i}\}$ has greatly improved the accuracy of the prediction. Note that $\lambda_{s,2}$ (which is greater than $\lambda_{s,1}$) is responsible for that improvement and allows accurate predictions at longer time scales.

The performance of the multimode dynamic slip model was further tested in an experiment which involved different deformation history compared to the one used for the parameter determination. Figure 7-13 shows the model prediction for start-up of steady shear. Comparing it to the prediction of a single-mode dynamic slip model (see Figure 7-3), one can see that a significant improvement in the accuracy of prediction is achieved.

As a final concluding remark, it is noted that the procedure described above for the parameter determination of the proposed slip model is only the first step. Many more experiments are required to fully comprehend the relationships between these parameters and other properties of polymeric melts, such as their molecular structure, characteristic relaxation time, and interfacial behaviour. In particular, it would be desirable to see how the proposed model does in predicting stress response for other deformation histories.

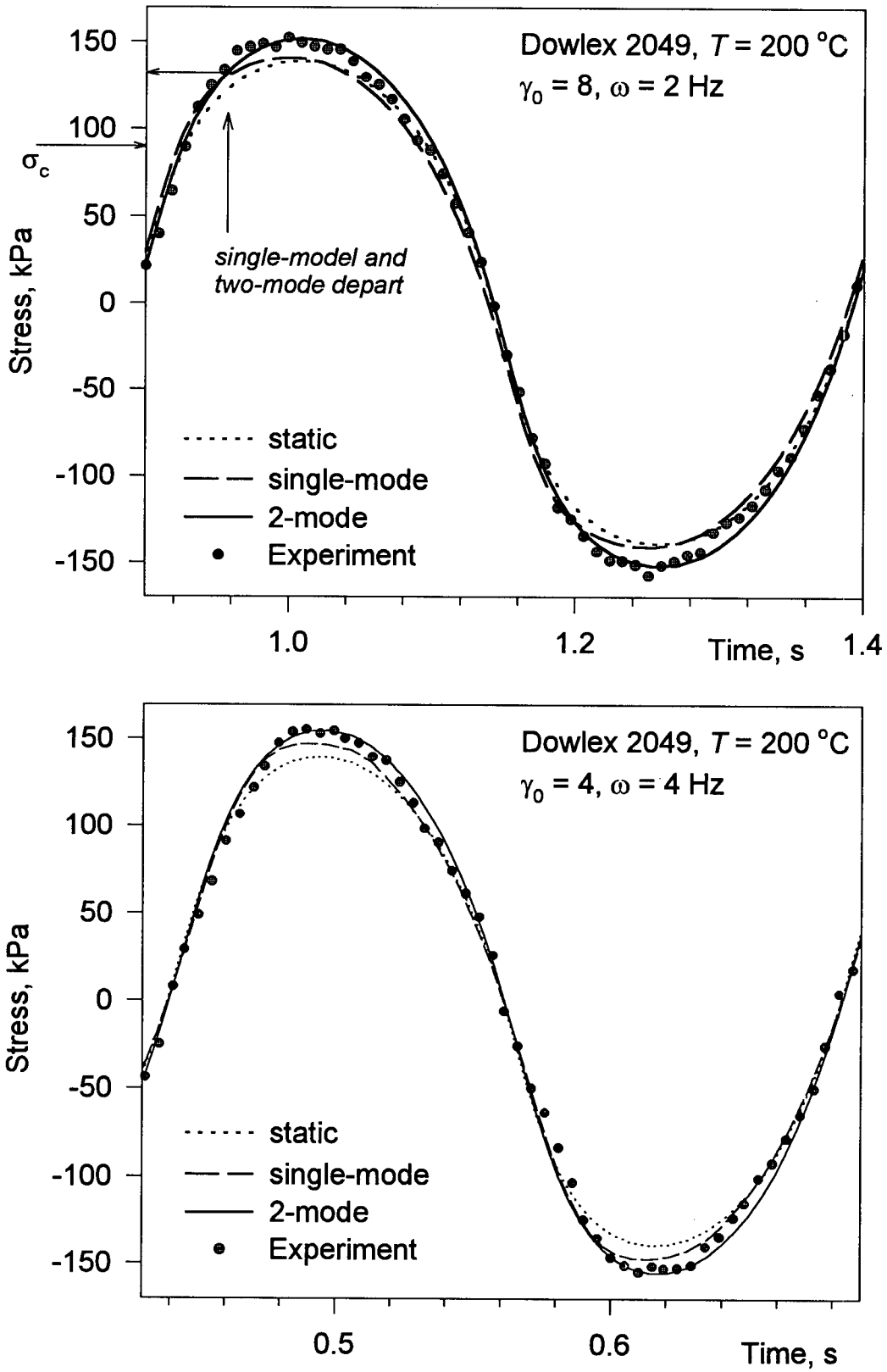

Figure 7-12. Comparisons of the multimode, single-mode, and static (steady-state) slip model predictions with experimental LAOS data for Dowlex 2049 at 200 °C.

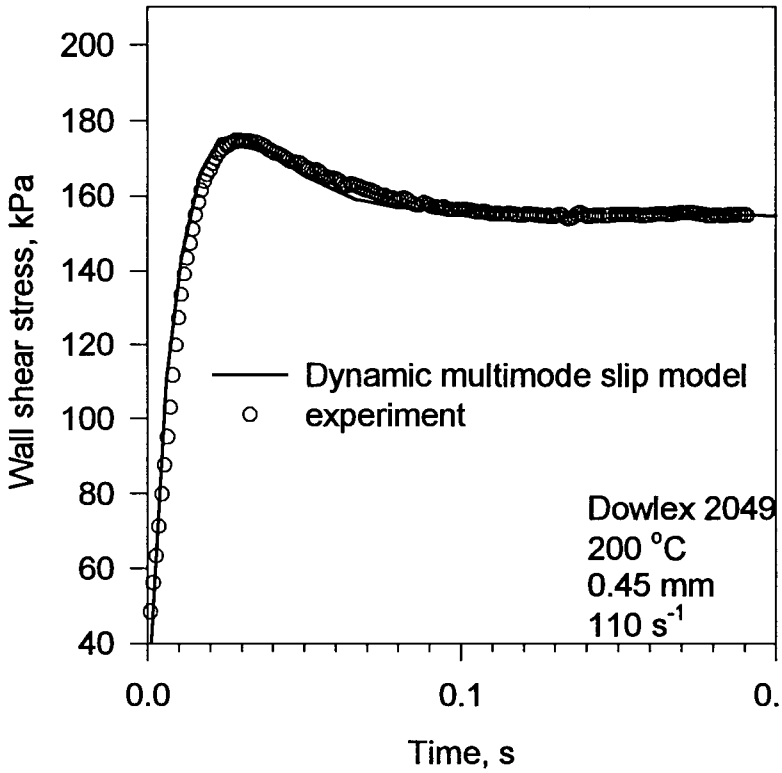

Figure 7-13. Start-up of steady shear experiment at 200 °C and comparison with predictions of the Wagner model coupled with a multimode dynamic slip model.

7.6 Conclusions

The slip behaviour of linear polymers may involve dynamics which are complicated by the viscoelastic nature of these materials. As discussed above, experimental evidence indicated that the assumption of a slip relaxation time is necessary to explain the transient response of linear polymers under slip conditions. Furthermore, while a single relaxation time can explain the experimental results qualitatively, it may be necessary to take into account multimode effects for a quantitative description.

In order to investigate these effects, steady shear experiments were performed for Dowlex 2049 in a sliding plate rheometer using two different gap spacings. A gap dependence of the

flow curves was obtained. Using the Mooney technique, the slip velocity was calculated as a function of shear stress, and fitted to a steady-state slip velocity model. A constitutive equation, Wagner's model was then used together with the steady-state slip model and a dynamic slip model to predict the shear stress response in start-up of steady shear experiments. Although the steady-state predictions were in good agreement with the experimental data, both models failed to accurately describe the dynamic behaviour. By the analogy to the derivation of a generalised Maxwell model from a simple mechanical two-element model, a multimode slip velocity model was formulated to take into account multiple slip relaxation times. A general procedure for the determination of its parameters based on comparisons with the LAOS data was described. The new multimode dynamic slip model was found to provide considerably better predictions of the shear stress in dynamic flow conditions, such as LAOS.

8. FLOW VISUALISATION

– EXECUTIVE SUMMARY –

■

Very few reports exist in literature on direct measurement of the velocity profile of molten polyethylene

■

A new experimental apparatus involving a fused quartz capillary has been developed. It allows observation of the flow at shear stresses of up to 0.2 MPa and temperatures up to 300 °C

■

The effect of Teflon and boron nitride on the flow of a molten polypropylene was studied by means of the flow visualisation technique. Boron nitride was found to be a better processing aid

8.1 Introduction

Most of the previous studies of slip employed techniques in which the slip velocity was obtained indirectly by interpreting various macroscopic measurements (e.g. heat transfer coefficient, divergence of flow curves). To the author's knowledge, direct measurements of wall slip of molten polymers in close vicinity to the wall have not been reported in the literature, with the exception of the studies of Galt and Maxwell (1964) and Migler (1993). However, their studies were confined only to low shear rates which are not of great importance in polymer processing.

In this chapter a new experimental apparatus designed to overcome those limitations, is described in detail. The experiments were performed using a polypropylene resin, and the effects of two processing aids on its flow curve and velocity profiles were determined. Measurements of the velocity fields both upstream and downstream of the sudden contraction were carried out using a photographic technique.

8.2 Experimental

8.2.1 Apparatus design

The flow visualisation apparatus developed during the course of this work is shown in Figure 8-1. It consists of the following parts:

Mounted on an optical bench:

- Helium-Neon laser having output power 10 mW, with a spatial filter and collimator with a focal length of 200 mm;
- Laser beam chopper, a DC motor with a plastic disc having 5 segments;

- Cylindrical lens, focal length 150 mm;
- Spherical focusing lens, focal length 600 mm.

Mounted on the capillary rheometer:

- Quartz capillary, 1.5 mm diameter, encased in a steel holder, surrounded by 4 radiation heaters;
- Microscope (Nikon SMZ-2T) and a 35 mm photographic camera.

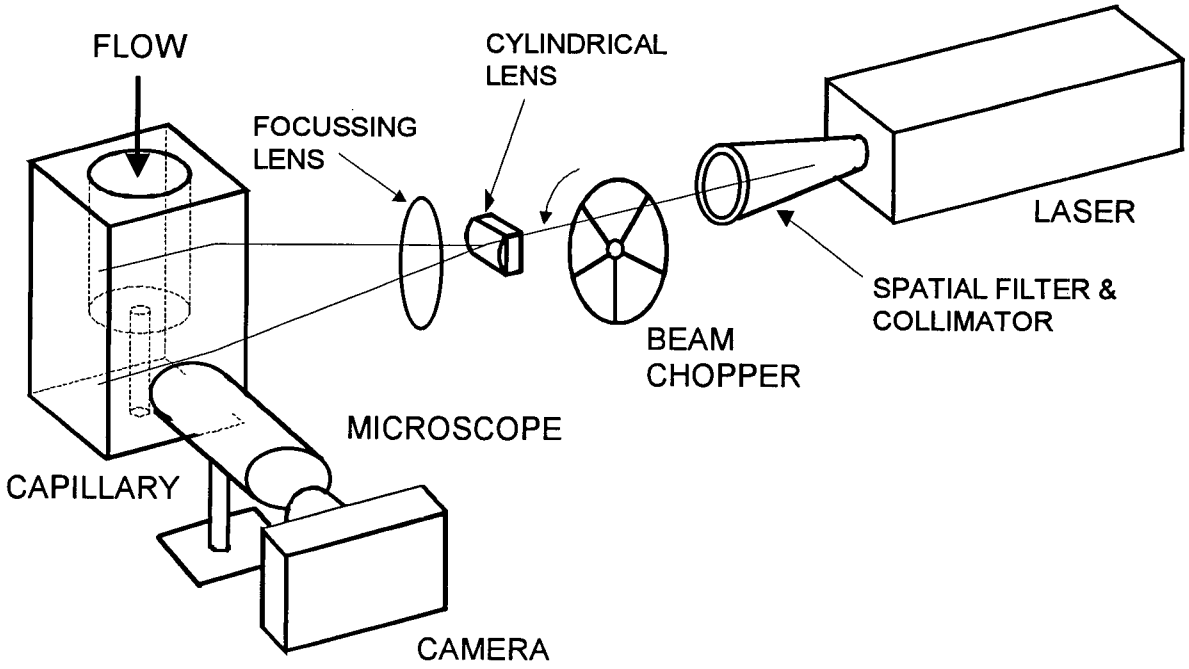

Figure 8-1. Schematic diagram of the flow visualisation experiments.

Figure 8-2 is a photograph of the beam forming system (extraneous elements have been edited out for the sake of clarity). The total length of the optical support rail is 2 metres, and the distance between the last focusing lens and the capillary is about 55 cm. The collimated laser beam is spread into a plane by means of a cylindrical lens and subsequently focused by a

spherical lens onto the centre axis of the capillary. The resulting thickness of the laser sheet crossing the capillary did not exceed 0.1 mm.

Figure 8-3 is a photo of the quartz capillary surrounded by four ceramic fibre heaters. The heaters are insulated on all sides except the side facing the capillary and provide enough radiation heat from a distance of 3 to 5 cm. The total electrical power was 240 W, controlled by a separate temperature controller. The thermocouple was attached to the lower part of the capillary holder.

Figure 8-4 shows the set-up from another side, where the microscope and the camera were placed. The distance between the capillary and the front lens of the microscope was about 15 cm.

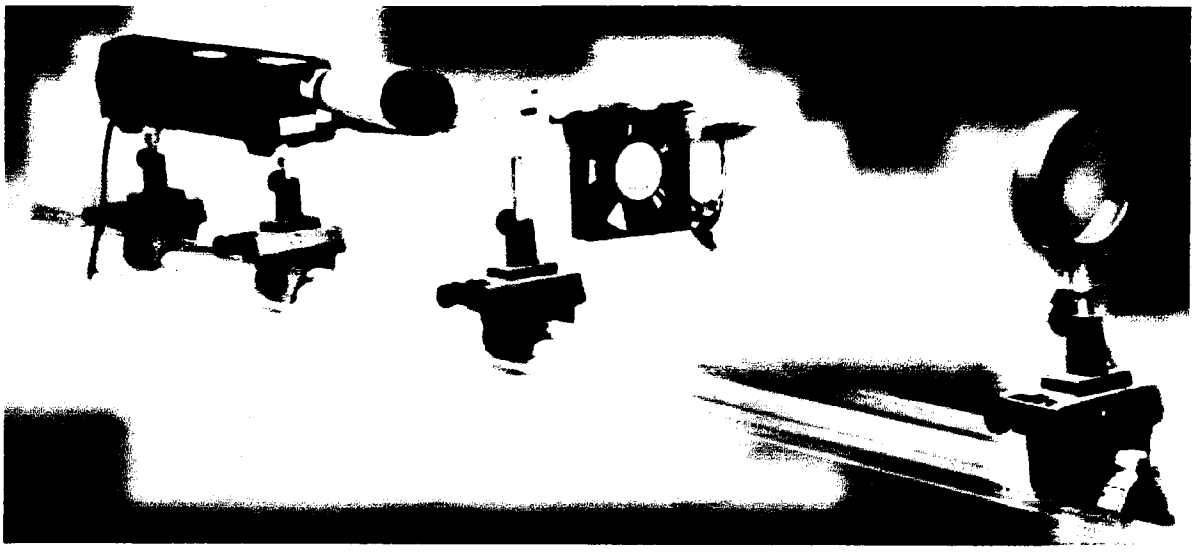

Figure 8-2. Photograph showing the laser and a beam forming system.

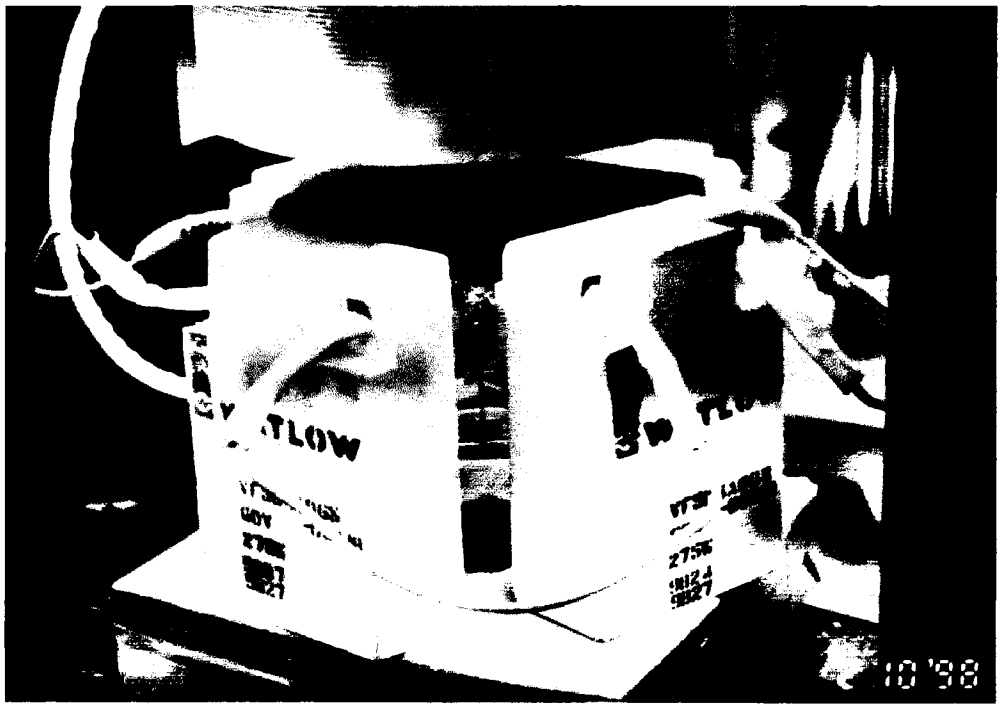

Figure 8-3. Photograph of the quartz capillary and radiation heaters.

Figure 8-4. Photograph of the lower part of the rheometer, microscope and camera.

The quartz capillary was designed to withstand pressures of up to 30 MPa. Its schematic drawing is shown in Figure 8-5. The capillary die was made by Precision Glass Products (USA). All vertical walls including the inside of the capillary are polished.

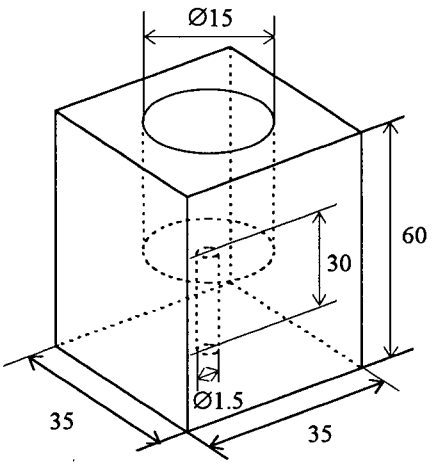

Figure 8-5. Schematic of the quartz capillary (dimensions in millimetres).

8.2.2 Flow curves

Figure 8-6 plots the apparent flow curve of polypropylene determined by using the quartz capillary die and that determined by using tungsten carbide dies [Kazatchkov, 1994]. It can be seen that the one corresponding to a fused quartz capillary is significantly lower. This can be due to two main factors: (1) occurrence of slip and (2) errors in temperature control. For example, the difference between the flow curves at $\dot{\gamma}_A$=30 s^{-1} can result from overheating of the quartz die by 23–24 °C (calculated using eq. 2-36, with E_a / R = 5900 K and T_{ref} = 473 K).

The addition of 0.1% of Teflon®, which is a widely used processing aid [Hatzikiriakos *et al.*, 1995], did not cause a further shear stress reduction: the corresponding shear stress is actually somewhat higher compared to that for pure polypropylene in the quartz die. This suggests that

Teflon cannot promote further slippage on a quartz die wall. The addition of 0.1% boron nitride (BN), which is a recently introduced processing aid [Buckmaster *et al.*, 1997], did result in a small stress reduction.

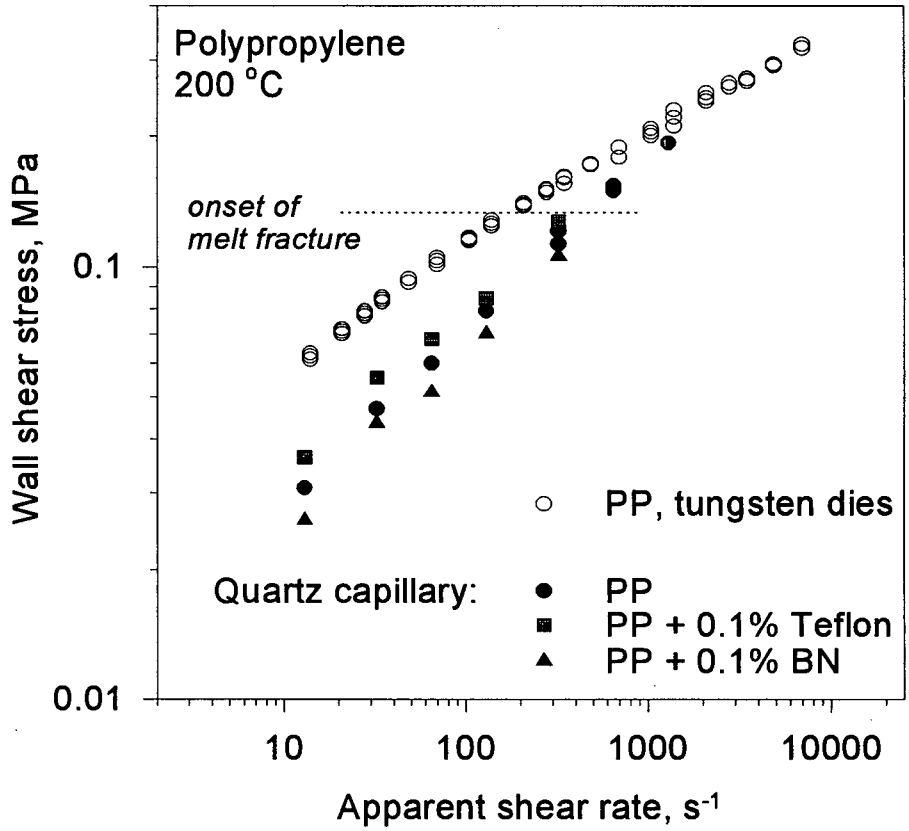

Figure 8-6. Apparent flow curves of polypropylene at 200 °C determined using capillaries made of quartz and tungsten.

8.2.3 Velocity Measurements

Figure 8-7 is a photograph of the lower section of the capillary (D = 1.5 mm) at three different shear rates. The interrupted streamlines are produced by fine chromium particles illuminated by flashes of laser light. The beam chopper provided flash frequencies ranging from 25 to 85 Hz. The frequency was adjusted depending on the shear rate to ensure a sufficient number of flashes during exposure. This was accomplished by calculating the average residence time

(based on known volumetric flow rate and capillary length). The number of flashes is the product of the residence time and the frequency used. Each exposure lasted 15 seconds and was recorded on a 400 ASA black-and-white film. The particles ranged from 50 to 100 μm in size and were added in a concentration of 0.1% by weight.

Measuring the distance between traces (l), and knowing the capillary diameter (D) and the frequency of laser flashes (f), one can calculate the stream velocity:

$$v = lf\frac{D}{D_{ph}} \qquad \text{eq. 8-1}$$

where D_{ph} is the capillary diameter measured in the photograph.

The flow velocity at various positions across the capillary was thus measured, and the results are plotted in Figure 8-8. Calculated velocity profiles (using eq. 2-9) based on the power-law index of 0.33 are also plotted. Apparent disagreement of the measured and calculated profiles may be due to several factors, such as wall slip, errors in the determination of the flash frequency and that the material does not obey the power law relationship at high shear rates. Based on these data, it is not possible to accurately measure the slip velocity. On some occasions, for example, at the shear rates of 32.4 and 324, the measured velocity values in the near vicinity to the wall are clearly non-zero, 1.5 and 2.4 mm/s respectively.

Figure 8-9 compares velocity profiles for virgin polypropylene and for polypropylene with addition of 0.1% of Teflon and boron nitride. At the lower shear rate, 32.4 s^{-1}, the velocity profiles are essentially the same. Although there are no data points for polypropylene with additives, the curves seem to indicate non-zero velocity values. At the higher shear rate, 324 s^{-1}, the difference between the velocity profiles becomes apparent: the shear stress for the melt with added BN is lower than with Teflon.

Figure 8-7. Photographs of the flow of polypropylene at 200 °C in a quartz capillary. White lines are traces of chromium particles in laser light. Shear rates: 32.4, 65, 130 s^{-1}, laser flash frequencies: 52.2, 52.2, 63.8 Hz.

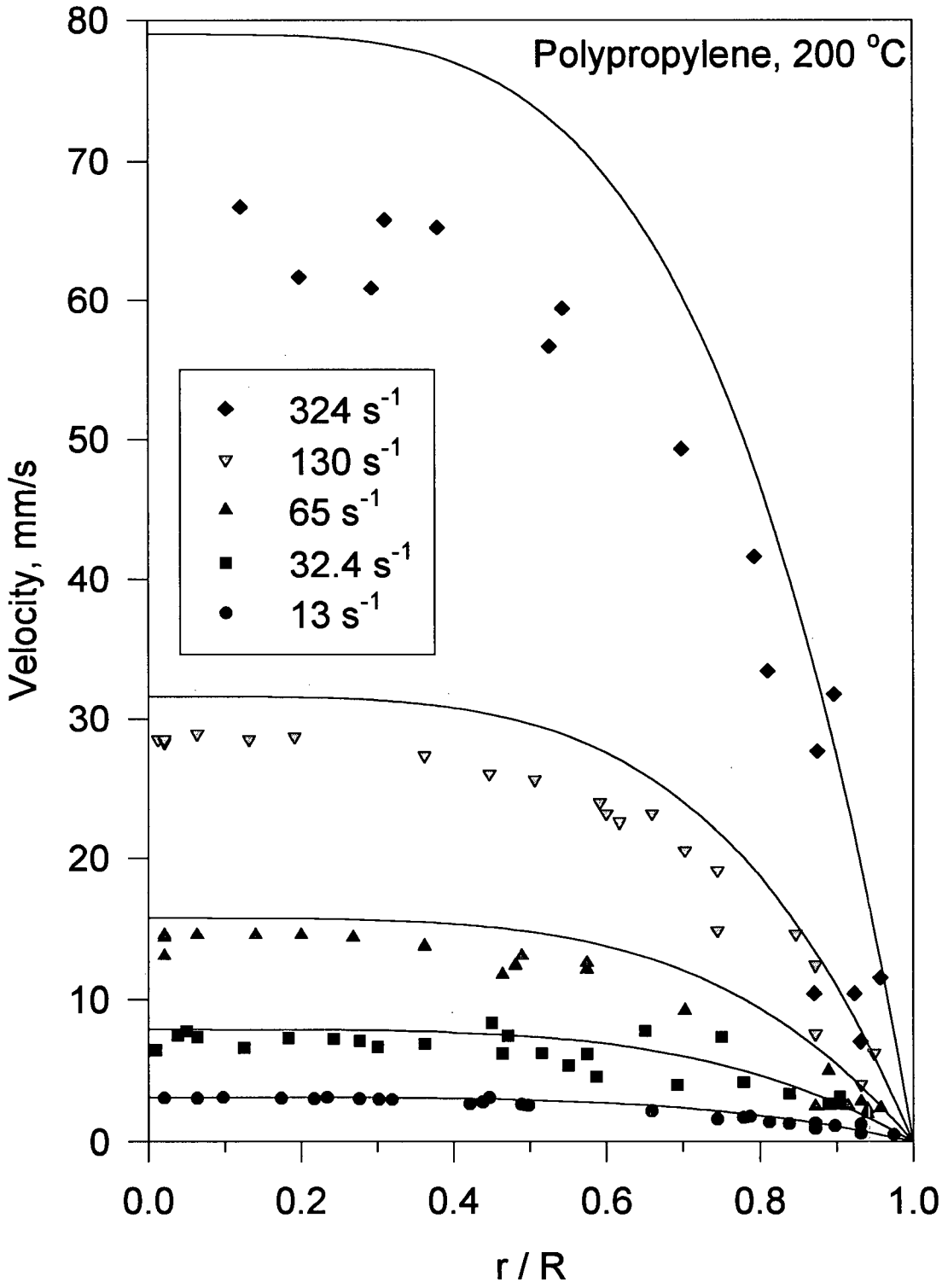

Figure 8-8. Velocity profile obtained in a quartz capillary for polypropylene at 200 °C as a function of radial position.

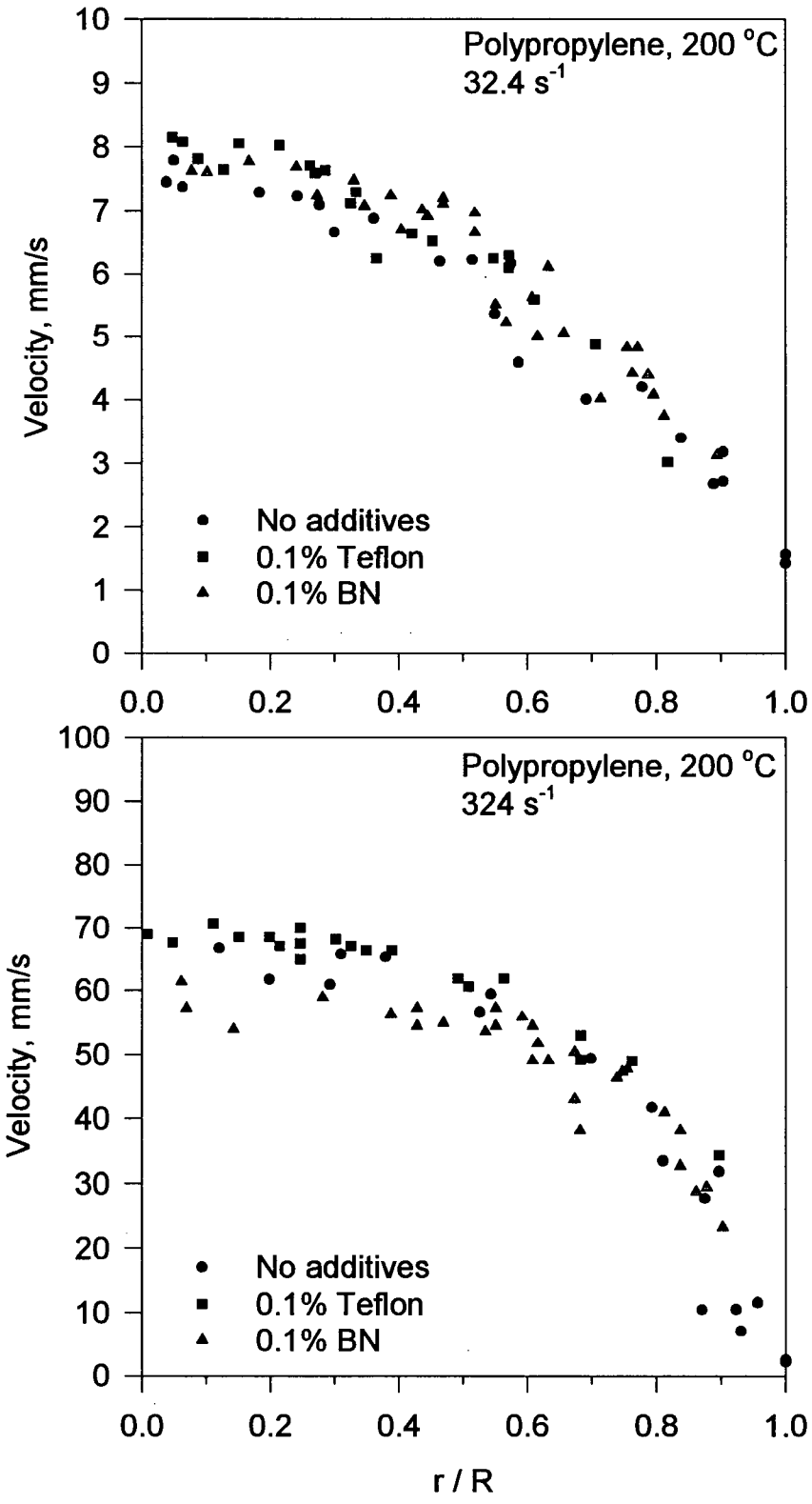

Figure 8-9. Effect of processing aids on the velocity profile of polypropylene at two different shear rates.

8.2.4 Flow near the Capillary Entrance

Several photographs of the capillary entry region were taken at different shear rates and melt composition in order to investigate the effect of processing aids on the development of flow patterns at the entry of the capillary. Gross melt fracture is known to originate from the entrance [Bergem, 1976] and such flow pattern observations may provide additional insight as to the action of processing aids in polymer processing.

Figure 8-10 shows the streamlines obtained at four different shear rates for polypropylene without addition of processing aids. The key points can be summarised as follows. At low shear rates the flow enters the capillary at higher angle, and the vortex in the corner of the reservoir is larger. As the shear rate increases, the streamlines bend more near the entrance to the capillary. Note that the vortex becomes smaller in size because it is pushed by the flow towards the corner. At higher shear rates, gross melt fracture is observed, and the streamlines are no longer smooth. It is not obvious from the photo, but it is clearly visible in the viewfinder that these zigzag lines are caused by discontinuous motion of parts of the bulk material. A schematic in Figure 8-11 is drawn to explain this flow pattern development. The flow in the entry region appears to be broken into several layers, and each layer moves with its own velocity. At regular time intervals, different in each layer, the motion stops for a brief period. The closer the layer is to the centre of the stream, the larger and more frequent are the jumps inside it.

An enlarged segment of Figure 8-10 (marked by a rectangle) is shown in Figure 8-12. It can be seen that the series of dots produced by illuminated (at a frequency of 85 Hz) tracer particles are interspaced by larger, brighter spots. These brighter spots are the result of the above described intermittent stops. This flow pattern closely resembles the stick-slip observed in the capillary flow of some polymers, with the difference that the former occurs at a polymer–polymer interface, as opposed to the latter that occurs at the polymer–wall interface.

Figure 8-13 is a photograph of the entry region with the flow produced by polypropylene with the addition of 0.1% Teflon, and Figure 8-14 – with the addition of 0.1% boron nitride. The shear rates are the same as in Figure 8-10. The addition of these processing aids resulted in a reduction of the corner vortices, especially at higher shear rates. However, the most important difference is that the presence of the processing aids, which are designed to promote slip at polymer–wall interface, affected the bulk flow. The addition of Teflon significantly reduced the amplitude of jumps which were observed for pure polypropylene at 650 s^{-1}. The presence of boron nitride resulted in their complete elimination. In the case of boron nitride the streamlines are smooth, and the flow seems to be more organised, with a lower number of inflexion points along the path. This suggests that boron nitride is a better processing aid than Teflon. To the author's knowledge, there have been no reports in the literature describing these findings. In polymer processing, boron nitride is used as a foam nucleating agent, and when added to the polymer melt acts as a very effective processing aid. BN, unlike fluoropolymers in the extrusion of polyethylene, can eliminate not only surface and stick-slip melt fracture but also significantly delay the onset of gross melt fracture to much higher shear rates [Buckmaster *et al.*, 1997; Rosenbaum *et al.*, 1998]. The mechanism by which the bulk flow is affected by addition of boron nitride remains to be explained.

8.3 Conclusions

A flow visualisation apparatus consisting of a low-power He-Ne laser, optical system and a heated quartz capillary was developed. Using a laser speckle photographic technique, velocity profiles for molten polypropylene were measured at high shear rates. The effects of two processing aids, Teflon and boron nitride, on its flow curve and velocity profiles were studied.

It was found that, although the addition of either of the two aids did not significantly change the velocity profiles in the quartz capillary, the presence of 0.1% boron nitride essentially eliminated the upstream flow instabilities and reduced the severity of melt fracture.

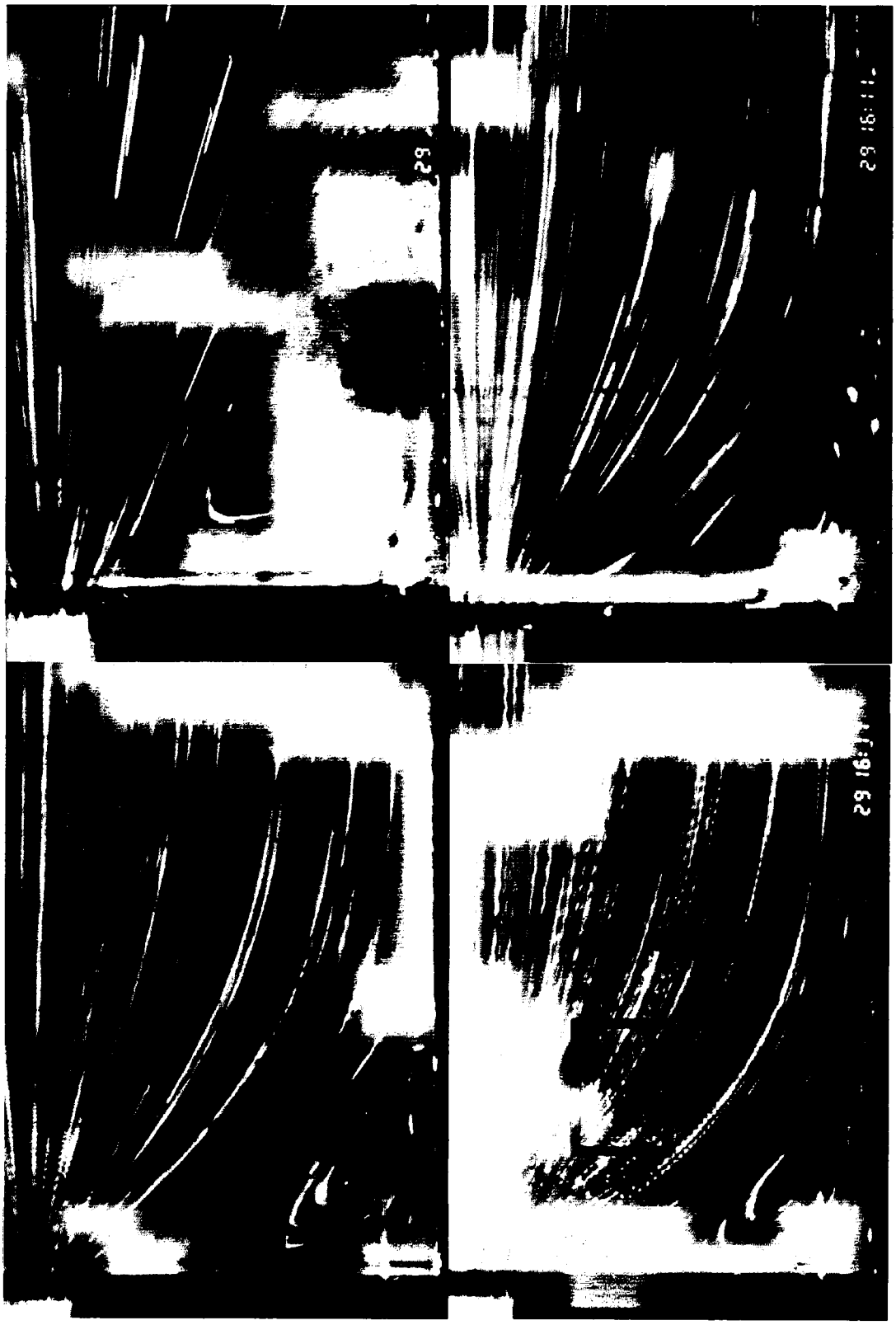

Figure 8-10. Flow of polypropylene at 200 °C near capillary entry region. Shear rates (left to right, top to bottom): 32.4, 130, 324 and 650 s^{-1}.

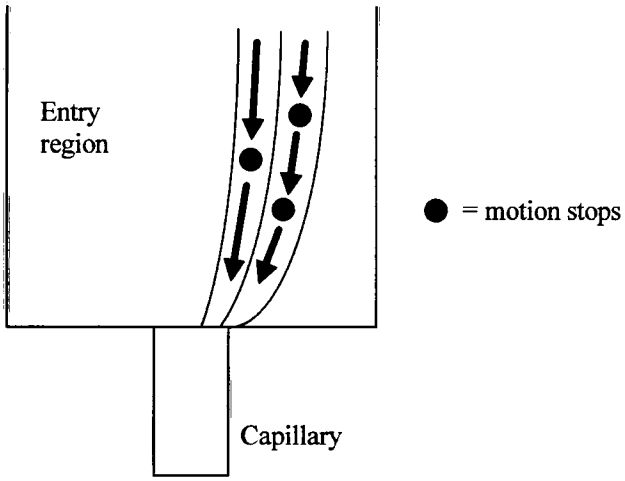

Figure 8-11. Observed flow patterns at the shear rate of 650 s^{-1} (schematic).

Figure 8-12. Enlarged segment of Figure 8-10: entry region of the capillary showing the flow instabilities in the bulk flow of polypropylene.

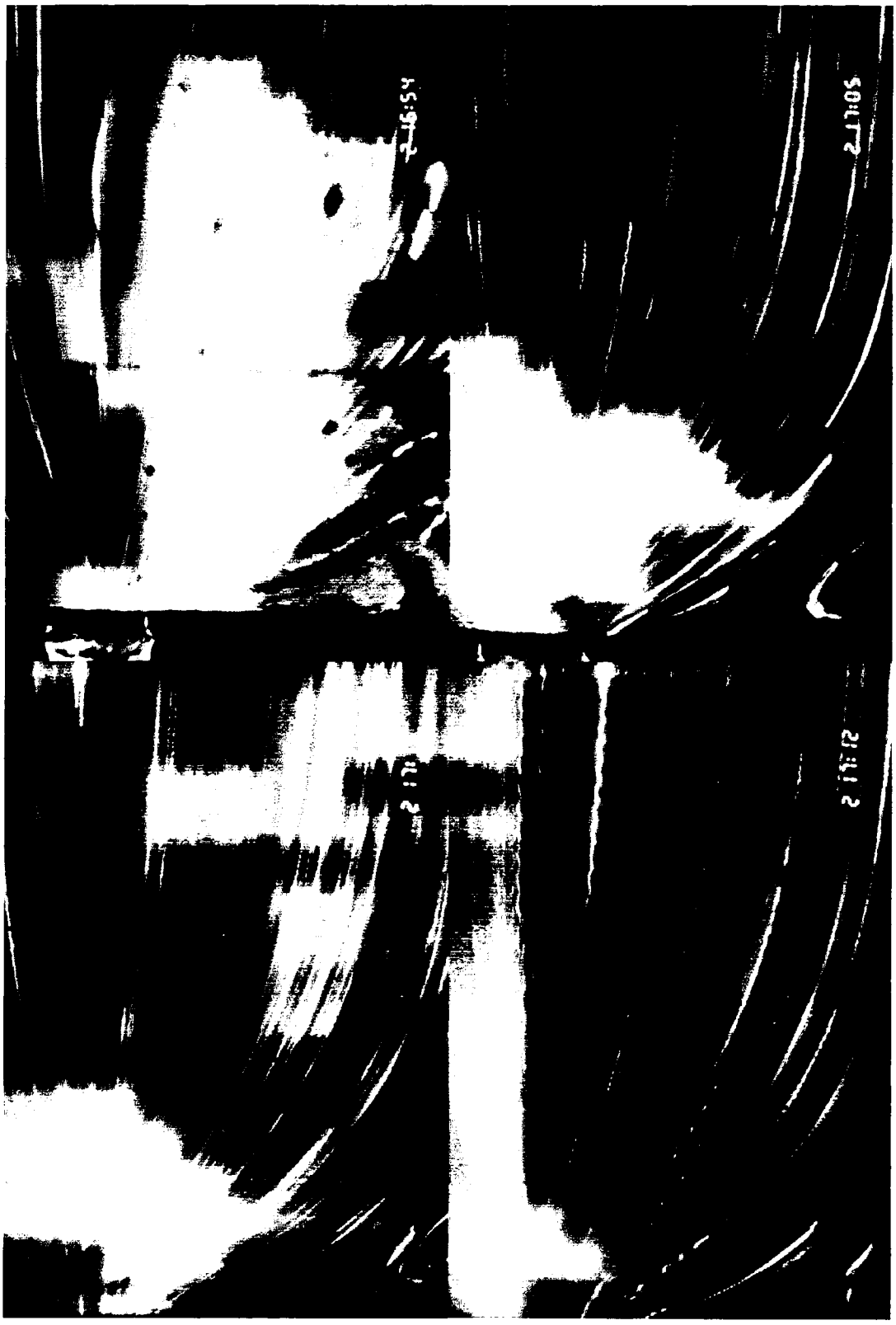

Figure 8-13. Flow of polypropylene with 0.1% Teflon at 200 °C near capillary entry region. Shear rates (left to right, top to bottom): 32.4, 130, 324 and 650 s^{-1}.

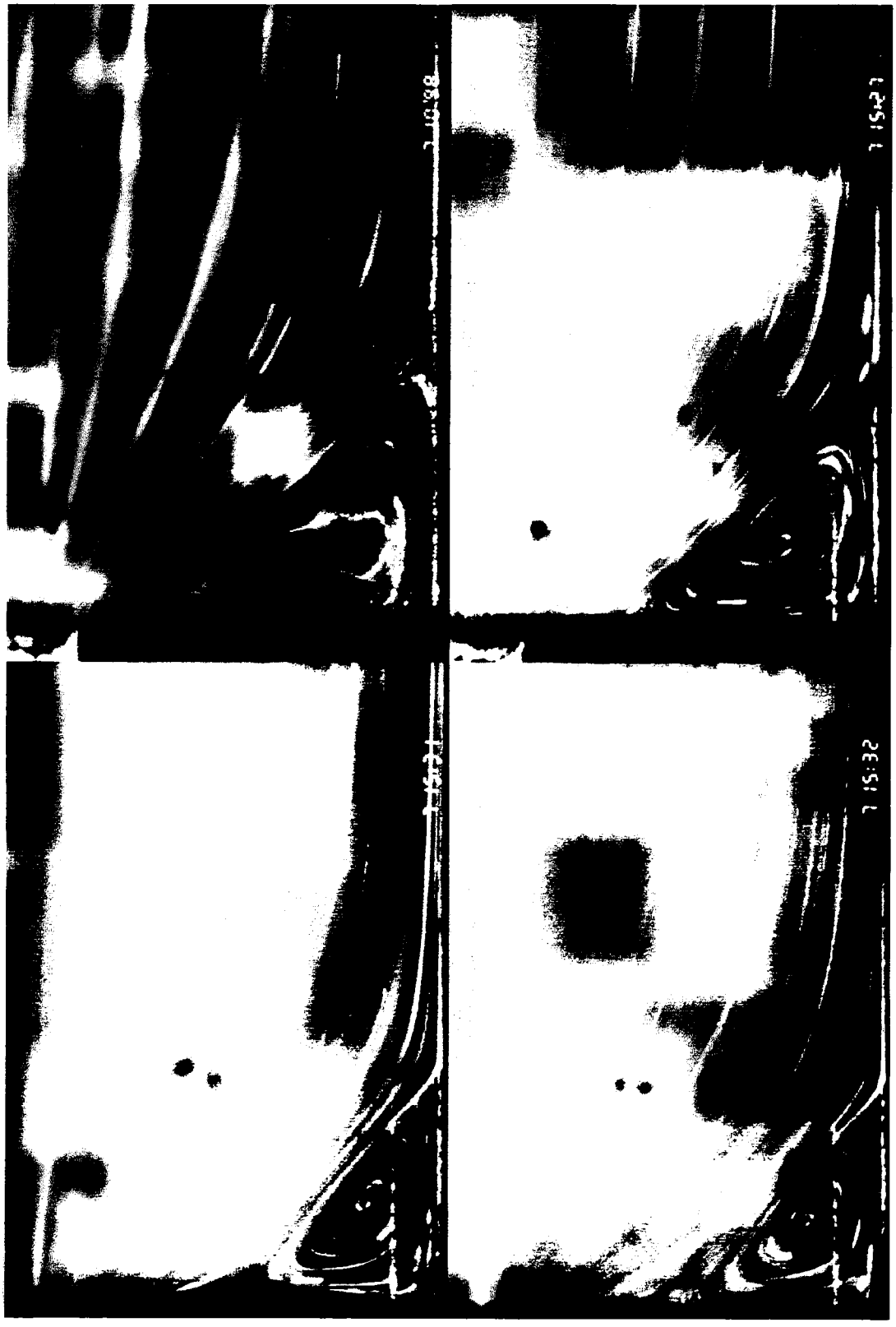

Figure 8-14. Flow of polypropylene with 0.1% BN at 200 °C near capillary entry region. Shear rates (left to right, top to bottom): 32.4, 130, 324 and 650 s^{-1}.

9. CONTRIBUTIONS TO KNOWLEDGE AND RECOMMENDATIONS

9.1 CONTRIBUTIONS TO KNOWLEDGE

This work resulted in a number of discoveries and novel developments that are outlined below.

1. By careful selection of polyethylene resins, the effects of the weight average molecular weight and the molecular weight distribution on the rheological and processing behaviour have been studied *separately*. A criterion for the best melt fracture performance has been identified and found to be related to a characteristic time of polymers that is defined as the ratio of the relaxation modulus to viscosity at the onset of melt fracture.

2. A novel technique of polymer characterisation based on determination of non-linear dynamic moduli in large-amplitude oscillatory shear experiments has been developed. A new method of determining the damping function based on LAOS experiments was proposed.

3. Unusually long start-up transients during the capillary extrusion of metallocene polyethylenes have been discovered. They have been found to result from a specific interaction of calcium stearate with the small degree of long chain branching of metallocene polyethylenes.

4. A qualitative molecular model based on flow-induced chain detachment and disentanglement has been proposed. The slip phenomena in the flow of polymers was explained from the perspective of a competition between chain detachment from the wall and sudden disentanglement. The mechanisms leading to wall slip are described and their relation to the molecular structure of the polymeric chains is identified.

5. A new multimode dynamic slip model has been developed. The model has been found to provide better predictions for the flow of molten polymers in transient experiments under slip conditions.

6. A flow visualisation apparatus allowing measurements of velocity profiles at high temperatures and shear stresses has been developed. The effect of processing aids on the flow curve of polypropylene and on the flow patterns near the capillary entrance was studied.

9.2 RECOMMENDATIONS FOR FUTURE WORK

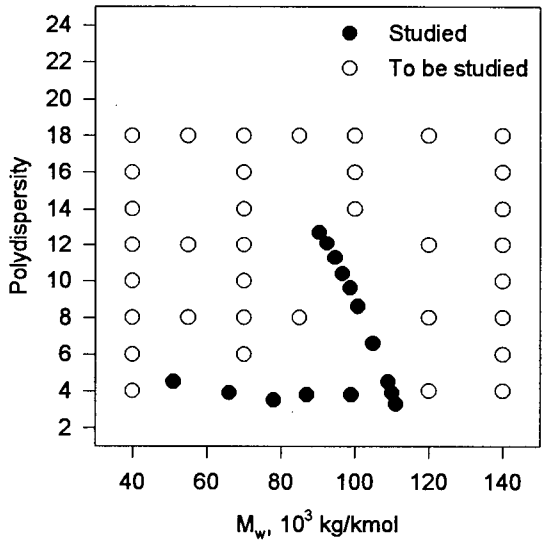

Figure 9-1. Ranges of the molecular characteristics studied and proposed for studying.

On the effect of molecular characteristics of polyethylene resins on their rheological and processing behaviour: expand the range of resins with different weight average molecular weights and molecular weight distributions to cover all possible combination of these two molecular characteristics, as shown in Figure 9-1.

On the qualitative molecular model for slip of entangled melts: obtain more experimental evidence using a wider range of resins and materials of die construction.

On the multimode dynamic slip model: test the model performance using different polymers and types of deformation. Incorporate a more sophisticated optimisation technique to assess the model parameters.

On flow visualisation: use resins from different groups of polymers (polyethylene, polyisobutylene, Teflon) in conjunction with various processing aids in order to identify mechanisms by which the bulk flow is affected by addition of the processing aids. Improve the optical system (alignment, focusing, magnification) in order to improve the resolution of the obtained images.

NOMENCLATURE

A	strain scale factor (exponential test)
a	parameter in the slip velocity equation (eq. 2-26), $MPa^{-m} \cdot m/s$
a_T	shift factor
B_L	extrudate swell ratio
b	Rabinowitsch correction
b	slip extrapolation length (eq. 2-27), m
c_p	heat capacity, $J/(kg \cdot K)$
D	capillary diameter, m
D	parameter in eq. 2-25, $Pa \cdot m/s$
E_a	flow activation energy, J/mol
f	flash frequency, Hz
G	shear modulus, Pa
G_i	modulus of i-element of Maxwell spectrum, Pa
$G'(\omega)$	storage modulus, Pa
$G''(\omega)$	loss modulus, Pa
G'_n, G''_n	n-th harmonics of the storage and loss moduli
G_d	stress to strain amplitude ratio, Pa
H	slit height, m
h	gap between plates, m
$h(\gamma)$	damping function
I	polydispersity
K	power-law consistency index, $MPa \cdot s^n$
k	heat conductivity, $W/(m \cdot K)$
l	distance between traces, m
L	capillary or slit length, m
M	torque, $N \cdot m$

M_e	molecular weight between entanglements, kg/kmol
M_n	number-average molecular weight, kg/kmol
M_s	viscosity molecular weight, kg/kmol
M_w	weight-average molecular weight, kg/kmol
m	parameter in the slip velocity equation (eq. 2-26)
n	power-law exponent
N_1	first normal stress difference
N_{MF}	melt fracture number, MPa
P	pressure, Pa
P_d	driving pressure, Pa
P_{end}	Bagley correction, Pa
Q	volumetric flow rate, m^3/s
R	capillary radius, m; gas constant, J/(mol · K)
T	absolute temperature, K
T_g	glass transition temperature, K
t	time, s
u	melt velocity, m/s
u_s	slip velocity, m/s
W	slit width, m
W_{adh}	work of adhesion, N/m

Greek Letters

α	pressure coefficient of viscosity (eq. 2-34), Pa^{-1}
α	exponential rate constant (exponential test), s^{-1}
α, β	parameters of the damping function (eq. C-8)
β	constant in eq. 2-27, Pa · s/m
β	pressure coefficient of viscosity, Pa^{-1}
γ	shear strain

γ_0	strain amplitude
γ_r	elastic recoil
γ_∞	recoverable shear strain
$\dot{\gamma}$	true shear rate, s^{-1}
$\dot{\gamma}_A$	apparent shear rate, s^{-1}
$\dot{\gamma}_{A,s}$	apparent shear rate, corrected for slip, s^{-1}
$\dot{\gamma}_n$	nominal shear rate, s^{-1}
$\dot{\gamma}_w$	wall shear rate, s^{-1}
δ	phase shift, rad
η	viscosity, Pa · s
η^e	exponential viscosity, Pa · s
η_0	zero-shear viscosity, Pa · s
η^0	viscosity at ambient pressure, Pa · s
η^-	shear stress decay coefficient, Pa · s
η^+	shear stress growth coefficient, Pa · s
λ	relaxation time, s
λ_i	relaxation time of i-element of Maxwell spectrum, s
λ_s	slip relaxation time, s
μ	Newtonian viscosity, Pa · s
ρ	density, kg/m^3
σ_c	critical shear stress for the onset of melt fracture, Pa
σ_{rz}, σ_{11}, σ_{22}	components of the shear stress tensor, Pa
σ_w	wall shear stress, Pa
$\sigma_{w,T}$	wall shear stress with viscous heating, Pa
ω	frequency, rad/s

BIBLIOGRAPHY

Adrian, D. W., Giacomin, A. J., *The transition to quasi-periodicity for molten plastics in large amplitude oscillatory shear.* Trans. ASME, 116, 446-450 (1994).

Anastasiadis, S. H., Hatzikiriakos, S. G., *The work of adhesion of polymer/wall interfaces and its association with the onset of wall slip.* J. Rheol., 42 (4), 795-812 (1998).

Archer L. A., Larson, R. G., Chen, Y. L., *Direct Measurements of slip in sheared polymer solutions.* J. Fluid Mech., 301, 133-151 (1995).

Athey, R. J., Thamm, R. C., Souffie, R. D., Chapman, G. R., *The processing behavior of polyolefins containing a fluoroelastomer additive.* SPE ANTEC '86 Tech. Papers, 1149-1153 (1986).

Atwood, B. T., Schowalter, W. R., *Measurements of slip at the wall during flow of high-density polyethylene through a rectangular conduit.* Rheol. Acta, 28, 134-146 (1989).

Bagley, E. B., Cabott, I. M., West, D. C., *Discontinuity in the flow curve of polyethylene.* J. Appl. Phys., 29, 109-110 (1958).

Bartos, O., *Fracture of polymer melts at high shear stress.* J. Appl. Phys., 35 (9), 2767 (1964).

Baumgaertel, M., Winter, H. H., *Determination of the discrete relaxation and retardation time spectra from dynamic mechanical data.* Rheol. Acta, 28, 511-519 (1989).

Benbow, J. J., Lamb, P., *New aspects of melt fracture.* SPE Trans., 3, 7 (1963).

Bergem, N., *Visualization studies of polymer melt flow anomalies in extrusion.* Proc. 8th Int. Congr. Rheol., Gothenberg, p. 50 (1976).

Berret J. F., Roux, D. C., Porte, G., Lindner, P., *Shear-induced isotropic-to-nematic phase transition in equilibrium polymers.* Europhys. Lett., 25, 521-526 (1994).

Bersted, B. H., *Model relating elastic properties of high-density polyethylene melts to molecular-weight distribution.* J. Appl. Polym. Sci., 20 (10), 2705-2714 (1976).

Bick D. K., McLeish, T. C. B., *Topological contributions to nonlinear elasticity in branched polymers.* Phys. Rev. Lett., 76, 2587-2590 (1996).

Bird, R. B., Armstrong, R. C., Hassager, O., *Dynamics of polymeric liquids, vol. 1: Fluid mechanics.* John Wiley, NY, 1987.

Bird, R. B., Armstrong, R. C., Hassager, O., *Dynamic of polymeric liquids, vol. 2: Kinetic theory*, Wiley, NY, 1987.

Blyler, L. L. Jr., Hart, A. C., *Capillary flow instability of ethylene polymer melts*. Polym. Eng. Sci., 10 (4), 193-203 (1970).

Boudreaux Jr., E., Cuculo, J. A., *Polymer flow instability: A review and analysis*. J. Macromol. Sci. - Rev. Macromol. Chem., C 16 (1), 39-77 (1977).

Brochard, F., de Gennes, P.-G., *Shear-dependent slippage at a polymer/solid interface*. Langmuir, 8, 3033-3037 (1992).

Buckmaster, M. D., Henry, D. L., Randa, S. K., *High speed extrusion*. U.S. Pat. No. 5,688,457 (1997).

Burton, R. H., Folkes, M. J., Narh, K. A., Keller, A., *Spatial variation in viscosity in shear of polymer melts*. J. Mater. Sci., 18, 315-320 (1983).

Carella J. M., Gotro, J. T., Graessley, W. W., *Thermorheological effects of long-chain branching in entangled polymer melts*. Macromolecules, 19, 659-667 (1986).

Chauffoureaux, J. C., Dehennau, C., Van Rijckevorsel, J., *Flow and thermal stability of rigid PVC*. J. Rheol., 23 (1), 1-24 (1979).

Chopra, D., Vlassopoulos, D., Hatzikiriakos, S. G., *Shear-induced mixing and demixing in SMA/PMMA blends*. J. Rheol., 42, 1227-1248 (1997).

Chopra, D., Private communication (1998).

Cogswell, F. N., *Stretching flow instabilities at the exits of extrusion dies*. J. Non-Newtonian Fluid Mech., 2, 37-47 (1977).

Cogswell, F. N., *Polymer Melt Rheology: A Guide to Industrial Practice*, Wiley, NY, 1981.

Cohen, Y., Metzner, A. B., *Apparent slip flow of polymer solutions*. J. Rheol., 29, 67 (1985).

Cox, H. W., Macosko, C. W., *Viscous dissipation in die flows*. AIChE J., 20 (4), 785-795 (1974).

de Gennes, P.-G., *Scaling concepts in polymer physics*. Cornell Univ. Press, Ithaca, 1979.

Dealy, J. M., *On the significance of pressure relaxations in capillary or slit flow*. Rheol. Acta, 34, 115-116 (1995).

Dealy, J. M., Wissbrun, K. F., *Melt rheology and its role in plastics processing: theory and applications.* Van Nostrand Reinhold, NY, 1990.

Denn, M. M., *Issues in viscoelastic fluid mechanics.* Annu. Rev. Fluid Mech., 22, 13-34 (1990).

Doi, M. and Edwards, S. F., *The theory of polymer dynamics.* Oxford Univ. Press, Oxford, 1986.

Drda P. A., Wang, S.-Q., *Stick-slip transition at polymer melt/ solid interfaces.* Phys. Rev. Lett., 75, 2698-2701 (1995).

El Kissi, N., Piau, J. M., *Ecoulement de fluides polymères enchevêtrés dans un capillaire. Modélisation du glissement macroscopique à la paroi.* C. R. Acad. Sci. Paris, II 309, 7-9 (1989).

Ferry J. D., *Viscoelastic properties of polymers.* 3rd ed., John Wiley, NY 1980.

Fowkes, F. M., *Attractive forces at interfaces.* Ind. Eng. Chem., 56, 40-52 (1964).

Galt, J., Maxwell, B., *Velocity profiles for polymer melts.* Mod. Plastics, December, 115-132 (1964).

Garvey, B. S., Whitlock, M. H., Freese, J. A., *Ind. Eng. Chem.*, 34, 1309 (1942).

Giacomin, A. J., Samurkas, T., Dealy, J. M., *A novel sliding plate rheometer for molten plastics.* Polym. Eng. Sci., 29, 499-504 (1989).

Giacomin, A. J., Oakley, J. G., *Obtaining Fourier series graphically from large amplitude oscillatory shear loops.* Rheol. Acta, 32, 328-332 (1993).

Goyal, S. K., Bohnet, N., Chow, M., Proc. XIIth Int. Congr. on Rheology, 441 (1996).

Graessley, W. W., *Effect of long chain branches on the temperature dependence of viscoelastic properties of polymer melts.* Macromolecules 15, 1164-1167 (1982).

Graham, M. D., *Wall slip and the nonlinear dynamics of large amplitude oscillatory shear flows.* J. Rheol., 39 (4), 697-712 (1995).

Han, J. M., Chin, C.-F., Li, D.-J., *Effect of flow geometry on the rheology of dispersed two-phase blends of polystyrene and poly(methyl) methacrylate.* Polymer, 36, 2451-2462 (1995)

Han, C. D., Villamizar, C. A., *Effects of molecular-weight distribution and long-chain branching on viscoelastic properties of high-density and low-density polyethylene melts.* J. Appl. Polym. Sci., 22 (6), 1677-1700 (1978).

Hatzikiriakos, S. G., *Wall Slip of Linear Polymers and its Role in Melt Fracture*, Ph.D. Thesis, McGill University (1991).

Hatzikiriakos, S. G., *A slip model for linear polymers based on adhesive failure.* Intern. Polymer Processing, VIII 2, 135-142 (1993).

Hatzikiriakos, S. G., *The onset of wall slip and sharkskin melt fracture in capillary flow.* Polym. Eng. Sci., 34 (19), 1441-1449 (1994).

Hatzikiriakos, S. G., *A multimode interfacial constitutive equation for molten polymers.* J. Rheol., 39 (1), 61-71 (1995).

Hatzikiriakos, S. G., Dealy, J. M., *Wall slip of molten high density polyethylene. I. Sliding plate rheometer studies.* J. Rheol., 35 (4), 497-523 (1991).

Hatzikiriakos, S. G., Dealy, J. M., *Wall slip of molten high density polyethylene. II. Capillary rheometer studies.* J. Rheol., 36, 703-741 (1992a).

Hatzikiriakos, S. G., Dealy, J. M., *Role of slip and fracture in the oscillating flow of HDPE in a capillary.* J. Rheol., 36 (5), 845-884 (1992b).

Hatzikiriakos, S. G., Dealy, J. M., *Start-up pressure transients in capillary rheometer.* Polym. Eng. Sci., 34, 493-499 (1994).

Hatzikiriakos, S. G., Kalogerakis, N., *A dynamic slip velocity model for molten polymers based on a network kinetic theory.* Rheol. Acta, 33, 38-47 (1994).

Hatzikiriakos, S. G., Hong, P., Ho, W., Stewart, C. W., *The effect of Teflon® coatings in polyethylene capillary extrusion.* J. Appl. Polym. Sci., 55, 595-603 (1995).

Henson, D. J., Mackay, M. E., *Effect of gap on the viscosity of monodisperse polystyrene melts: slip effects.* J. Rheol., 39 (2), 359-373 (1995).

Hill, D. A., Hasegawa, T., Denn, M. M., *On the apparent relation between adhesive failure and melt fracture.* J. Rheol., 34, 891-918 (1990).

Howells, E. R., Benbow, J. J., *Flow defects in polymer melts.* Trans. Plast. Inst., 30, 240-253 (1962).

Ishida, N., Shiga, I., Sakamoto, K., Kobunshi Kagaku, 28, 834 (1971).

Jeyaseelan, R. S., Giacomin, A. J., *Predicting polymer melt behavior near the inception of wall slip in oscillatory shear.* J. Non-Newtonian Fluid Mech., 53, 99-111 (1994).

Kalika, D. S., Denn, M. M., *Wall slip and extrudate distortion in linear low-density polyethylene.* J. Rheol., 31 (8), 815-834 (1987).

Kazatchkov, I. B., M.A.Sc. Thesis, *Extrudate distortion in the capillary/slit extrusion of a molten polypropylene.* University of British Columbia, Vancouver (1994).

Knappe, W., Krumböck, E., *Slip flow of non-plasticized PVC compounds.* Rheol. Acta, 25, 296-307 (1986).

Knight G. W., Lai, S., *Dow constrained geometry catalyst technology: new rules for ethylene-olefins interpolymers-unique structure and property relationships.* VIII International Polyolefins Conference SPE RETEC Conference Proceedings, 226-241 (1993).

Kraynik, A. M., Schowalter, W. R., *Slip at the wall and extrudate roughness with aqueous solutions of polyvinyl alcohol and sodium borate.* J. Rheol., 25, 95 (1981).

Kurath S. F., Yin, T. P., Berge, J. W., Ferry, J. D., *Dynamic mechanical properties and creep of poly-n-dodecyl methacrylate.* J. Colloid Sci., 14, 147-160 (1959).

Kurtz, S. J., *Die geometry solutions to sharkskin melt fracture.* Advances in Rheology, ed. B. Mena, A. Garcia-Rejon and C. Rangel Nafaile, UNAM, Mexico City, Vol. 3, 399 (1984).

Kurtz, S. J., *The Dynamics of sharkskin melt fracture: effect of die geometry.* Proc. XIth Int. Congr. on Rheology, Bruxelles, Belgium. In: Moldenaers P., Keunings R. (eds.) Theretical and applied rheology. Elsevier Science Publishers, 377-379, (1992).

Landel R. F., Ferry, J. D., *Dynamic mechanical properties of the system cellulose tributyrate-dimethyl phthalate.* J. Phys. Chem., 60, 294-301 (1956).

Larson, R. G., *Constitutive equations for polymer melts and solutions.* Butterworths, N.Y., 364 p., 1988.

Lau, H. C., Schowalter, W. R., *A model for adhesive failure of viscoelastic fluids during flow.* J. Rheol., 30 (1), 193-206 (1986).

Laun, H. M., *Orientation of macromolecules and elastic deformations in polymer melts. Influence of molecular architecture on the reptation of molecules.* Prog. Colloid Polym. Sci., 75, 111-139 (1987).

Leonov, A. I., *On the dependence of friction force on sliding velocity in the theory of adhesive friction of elastomers.* Wear, 141 (1), 137-145 (1990).

Lim, F. J., Schowalter, W. R., *Wall slip of narrow molecular weight distribution polybutadienes.* J. Rheol., 33 (8), 1359-1382 (1989).

Lin, Y.-H., *Explanation for slip-stick melt fracture in terms of molecular dynamics in polymer melts.* J. Rheol., 29 (6), 605-637 (1985)

Lupton, J. M., Regester, J. W., *Melt flow of polyethylene at high rates.* Polym. Eng. Sci., 5, 235-245 (1965)

Mavridis, H., Shroff, R. N., *Temperature dependence of polyolefin melt rheology.* Polym. Eng. Sci., 32, 1778-1791 (1992).

Mendelson, R. A., Finger, F. L., *High-density polyethylene melt elasticity - some anomalous observations on effects of molecular-structure.* J. Appl. Polym. Sci., 19 (4), 1061-1078 (1975).

Migler, K. B., Hervet, H., Léger, L., *Slip transition of a polymer melt under shear stress.* Phys. Review Letters, 70 (3), 287-290 (1993).

Migler, K. B., Massey, G., Hervet, H., *The slip transition at the polymer-solid interface.* J. Phys. Condens. Matter, 6, A301-A304 (1994).

Mooney, M., *Explicit formulas for slip and fluidity.* J. Rheol., 2, 210 (1931).

Mooney, M., Black, S. A., *A generalized fluidity power law and law of extrusion.* J. Colloid Sci., 7, 204 (1952).

Moynihan, R. H., Baird, D. G., Ramanathan, R., *Additional observations on the surface melt fracture behavior of LLDPE.* J. Non-Newtonian Fluid Mech., 36, 255-263 (1990).

Myerholtz R. W., *Oscillating flow behaviour of high-density polyethylene melts.* J. Appl. Polym. Sci., 11, 687-698 (1967).

Müller-Mohnssen, H., Löbl, H. P., Schauerte, W., *Direct determination of apparent slip for a ducted flow of polyacrylamide solutions.* J. Rheol., 31 (4), 323-336 (1987).

Pearson J. R. A., *Mechanics of polymer processing.* Elsevier, London 1985.

Pearson, J. R. A., Petrie, C. J. S., *On melt flow instability of extruded polymers.* in Polymer Systems: Deformation and Flow, ed. R. E. Wetton and R. H. Whorlow. Macmillan, London, 1968, p. 163-187.

Pearson, T. J., Denn, M. M., *The effect of die materials and pressure-dependent slip on the extrusion of linear low-density polyethylene.* J. Rheol., 41, 249-266 (1997).

Petrie, C. J. S., Denn, M. M., *Instabilities in polymer processing.* AIChE J., 22, 209 (1976).

Piau, J. M., El Kissi, N., Trenblay, B., *Low Reynolds number flow visualization of linear and branched silicones upstream of orifice dies.* J. Non-Newtonian Fluid Mech., 30, 197-232 (1988).

Piau, J. M., El Kissi, N., Trenblay, B., *Influence of upstream instabilities and wall slip on melt fracture and sharkskin phenomena during silicone extrusion through orifice dies.* J. Non-Newtonian Fluid Mech., 34, 145-180 (1990).

Piau, J. M., El Kissi, N., *The influence of interface and volume properties of polymer melts on their die flow stability.* Proc. XIth Int.Congr.on Rheology, Brussels, Belgium. In: Moldenaers P., Keunings R. (eds.) Theretical and applied rheology. Elsevier Science Publishers, 70-74, 1992.

Piau, J. M., El Kissi, N., *Measurement and modelling of friction in polymer melts during macroscopic slip at the wall.* J. Non-Newtonian Fluid Mech., 54, 121-142 (1994).

Plazek D. J., 1995 *Bingham medal address: oh, thermorheological simplicity, where art thou?* J. Rheol., 40, 987-1014 (1996).

Porter D., *Group interaction modelling of polymer properties,* Marcel Dekker, NY 1995.

Pudjijanto, S., Denn, M. M., *A stable "island" in the slip-stick region of linear low-density polyethylene.* J. Rheol., 38 (6), 1735-1744 (1994).

Ramamurthy, A. V., *Wall slip in viscous fluids and influence of materials of construction.* J. Rheol., 30 (2), 337-357 (1986).

Ramirez, R. W., *The FFT fundamentals and concepts.* Prentice-Hall, NJ (1985).

Rauwendaal, C., Fernandez, F., *Experimental study and analysis of a slit die viscometer.* Polym. Eng. Sci., 25 (12), 765-771 (1985).

Rosenbaum, E. E., Hatzikiriakos, S. G., Stewart, C. W., *Flow implications in the processing of Teflon® resins.* Intern. Polym. Proc., X, 204-212 (1995).

Rosenbaum, E. E., Hatzikiriakos, S. G., *Wall slip in the capillary Flow of molten polymers subject to viscous heating.* AIChE J., 43 (3), 598-608 (1997).

Rosenbaum, E. E., Randa, S. K., Hatzikiriakos, S. G., Stewart, C. W., Henry, D. L., Buckmaster, M. D., *A new processing additive eliminating surface and gross melt fracture in the extrusion of polyolefins and fluoropolymers.* SPE ANTEC '98 Tech. Papers, 44 (1998).

Rudin, A., Worm, A. T., Blacklock, J. E., *Fluorocarbon elastomer processing aid for LLDPE, HDPE and PP resins.* Processing and Property Enhancement Utilizing Modifiers and Additives in Polymers: First Intl. Conf., p.71-81 (1985).

Schreiber, H. P., *A study of time dependence of polyethylene flow in capillary viscometry.* J. Appl. Polym. Sci. IV, 38-44 (1960).

Shidara, H., Denn, M. M., *Polymer melt flow in very thin slits.* J. Non-Newtonian Fluid Mech., 48, 101-110 (1993).

Shroff, R. N., Mitsuzo, S., Soc. Plast. Eng., Tech. Pap., 23, 285 (1977).

Soskey, P. R., Winter, H. H., *Large step strain experiments with parallel-disk rotational rheometers.* J. Rheol. 28, 625-645 (1984).

Stewart, C. W., *Wall slip in the extrusion of linear polyolefins.* J. Rheol., 37 (3), 499-513 (1993).

Sukhadia, A. M., *Sharkskin melt fracture behavior of medium and high molecular weight polyethylenes in film blowing.* Soc. Plastics Eng., ANTEC '97 Tech. Papers, 43, 1059-1066 (1997).

Swogger, K. W., Lancaster, G. M., Lai, S. Y., Butler, T. I., *Improving polymer processability utilizing constrained geometry single site catalyst technology.* J. Plastic Film and Sheeting, 11, 102-108 (1995).

Tobolsky, A. V., McLoughlin, J. R., *Viscoelastic properties of crystalline polymers: polytrifluorochloroethylene.* J. Phys. Chem., 59, 989-990 (1955).

Tordella, J. P., *Fracture in the extrusion of amorphous polymers through capillaries.* J. Appl. Phys., 27, 454 (1956).

Tordella, J. P., *An unusual mechanism of extrusion of polytetrafluoroethylene at high temperature and pressure.* J. Appl. Polym. Sci., 7, 215-229 (1963).

Tordella, J. P., *Unstable flow of molten polymers.* In Rheology, Vol. 5, F. R. Eirich, ed., Academic Press, NY, 1969, p. 57.

Tsang, W. K. W., Dealy, J. M., *The use of large transient deformations to evaluate rheological models for molten polymers.* J. Non-Newt. Fluid. Mech., 9, 203-222 (1981).

Tzoganakis, C., *Rheological evaluation of linear and branched controlled-rheology polypropylenes.* Can. J. Chem. Eng., 72, 749-754 (1994).

Van Krevelen, D. W., *Properties of polymers: their correlation with chemical structure; their numerical estimation, and prediction from additive group contributions.* Elsevier, NY, 1991.

Vinogradov, G. V., Insarova, N. I., Boiko, B. B., Borisenkova, E. K., *Critical regimes of shear in linear polymers.* Polym. Eng. Sci., 12, 5 (1972).

Vinogradov, G. V., Ivanova, L. I., *Wall slippage and elastic turbulence of polymers in the rubbery state.* Rheol. Acta, 7, 243-254 (1968).

Vinogradov, G. V., *Ultimate regimes of deformation of linear flexible chain fluid polymers.* Polymer, 18, 1275 (1977).

Vinodradov, G. V., Malkin, A. Ya., *Rheology of polymers.* Mir, Moscow, Springer, Berlin, 1980.

Waddon, A. J., Keller, A., *A temperature window of extrudability and reduced flow resistance in high-molecular weight polyethylene: Interpretation in terms of flow-induced mobile hexagonal phase.* J. Polym. Sci., B 28, 1063-1073 (1990).

Wang S.-Q., Drda, P. A., Inn, Y.-W., *Exploring molecular origins of sharkskin, partial slip, and slope change in flow curves of linear low density polyethylene.* J. Rheol., 40, 875-916 (1996).

Wang, J., Porter, R. S., *On the viscosity-temperature behaviour of polymer melts.* Rheol. Acta, 34, 496-503 (1995).

Wasserman, S. H., *Characterizing the melt relaxation behavior of metallocene polyethylenes.* Soc. Plastics Eng., ANTEC '97 Tech. Papers, 43, 1129-1133 (1997).

Weill, A., *Capillary flow of linear polyethylene melt: sudden increase of flow rate.* J. Non-Newt. Fluid Mech., 7 (4), 303-314 (1980).

White, J. L., *Critique of flow patterns in polymer fluids at the entrance of a die and instabilities leading to extrudate distortion.* Appl. Polym. Symp., 20, 155-174 (1973).

White, J. L., Han, M. H., Nakajima, M., Brzoskowski, R., *The influence of materials of construction on biconical rotor, and capillary measurements of shear viscosity of rubber and its compounds and considerations of slippage.* J. Rheol., 35 (1), 167-189 (1991).

Winter, H. H., Baumgaertel, M., Soskey, P. R., *A parsimonious model for viscoelastic liquids and solids.* in Techniques in Rheological Measurement, Ed. Collyer, A.A., Chapman & Hall, London, 1993.

Winter, H. H., *Analysis of dynamic mechanical data: inversion into a relaxation time spectrum and consistency check.* J. Non-Newtonian Fluid Mech., 68, 225-239 (1997).

Worth, R. A., Parnaby, J., Helmey, H. A. A., *Wall slip and its implications in the design of single screw melt-fed extruders.* Polym. Eng. Sci., 17 (4), 257-265 (1977).

Yoshimura, A. S., Prud'homme, R. K., *Response of an elastic Bingham fluid to oscillatory shear.* Rheol. Acta, 26, 428-436 (1987).

Yoshimura, A. S., Prud'homme, R. K., *Wall slip effects on dynamic oscillatory measurements.* J. Rheol., 32 (6), 575-584 (1988).

Zeichner, G. R., Patel, P. D., *The influence of molecular-weight distribution on melt rheology of polypropylene.* J. Rheol., 26 (1), 93-93 (1982).

APPENDIX A – Mooney technique

Mooney (1931) used capillaries of different radii to determine the flow curve of raw rubbers. He found that the flow curves depended on the radius of the capillary, once the shear stress exceeded a critical value (see Figure A-1). He derived an explicit relation for determining the slip velocity as a function of wall shear stress by assuming that the wall shear stress, slip velocity and pressure gradient are all constant along the entire length of the capillary. This expression for the case of circular channels is as follows:

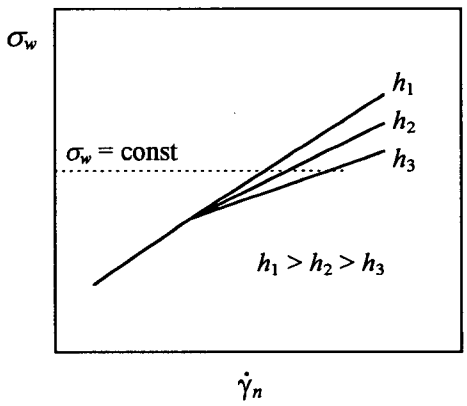

Figure A-1. Divergence of the flow curves for different gap spacings (or different capillary diameters).

$$\dot{\gamma}_A = \dot{\gamma}_{A,s} + 8\frac{u_s}{D} \qquad \text{eq. A-1}$$

where $\dot{\gamma}_A$ is the apparent shear rate, which for capillary flow is defined as $32Q/\pi D^3$; $\dot{\gamma}_{A,s}$ is the apparent shear rate corrected for the effects of slip, u_s is the slip velocity, Q is the volumetric flow rate, and D is the diameter of the capillary. For a constant wall shear stress, and thus a constant $\dot{\gamma}_{A,s}$, a plot of $\dot{\gamma}_A$ versus $1/D$ should result in a straight line with a slope equal to $8u_s$, if the slip velocity is solely a function of the wall shear stress.

If it is known that a material follows power-law behaviour, then the slip velocity can be calculated from a single apparent flow curve. For a power-law fluid $\dot{\gamma}_A$ can be replaced by $\dot{\gamma}_{A,s}$ in eq. 2-10, and by solving for the slip velocity the following equation can be obtained:

$$8\frac{u_s}{D} = \dot{\gamma}_A - \frac{4n}{3n+1}\left(\frac{\sigma_w}{K}\right)^{\frac{1}{n}} \qquad \text{eq. A-2}$$

Thus, if the power-law constants have been determined in experiments in which slip did not occur (e.g. at low shear rates), they can be used to calculate the slip velocity from a measured value of σ_w for any given value of $\dot{\gamma}_A$.

APPENDIX B – Generalised Maxwell model

A very simple model of a linear viscoelastic material, a Maxwell element, consists of a spring representing a Hookean solid in series with a dashpot representing a Newtonian fluid. If the spring constant is taken to be analogous to the modulus of the Hookean solid, then the Maxwell model is [Bird *et al.*, 1987]:

$$\tau + \lambda \frac{d\tau}{dt} = \eta_0 \dot{\gamma} \qquad \text{eq. B-1}$$

where τ is the stress tensor, λ is a time constant (the relaxation time), η_0 is the zero-shear viscosity of the linear viscoelastic material, and $\dot{\gamma}$ is the rate-of-deformation tensor. This equation can be solved for the stress tensor to give:

$$\tau = \int_{-\infty}^{t} \frac{\eta_0}{\lambda} e^{-\frac{t-t'}{\lambda}} \dot{\gamma}(t') dt' \qquad \text{eq. B-2}$$

When written in this form, the model states that the stress at the present time t depends on the rate of strain at all past times t' ($-\infty < t' \leq t$), with a weighting factor that decays exponentially.

Actual relaxation processes cannot be described by a single exponential function. More flexibility can be obtained by use of the generalised Maxwell model, which is achieved by connecting a number of Maxwell elements in parallel. Then the total stress is a superposition of the partial contributions of each element:

$$\tau_i + \lambda_i \frac{d\tau_i}{dt} = \eta_{0,i} \dot{\gamma} \quad \text{and} \quad \tau = \sum_{i=1}^{N} \tau_i \qquad \text{eq. B-3}$$

or

$$\tau = \int_{-\infty}^{t} \sum_{i=1}^{N} \frac{\eta_{0,i}}{\lambda_i} e^{-\frac{t-t'}{\lambda_i}} \dot{\gamma}(t') dt' \qquad \text{eq. B-4}$$

where N is the number of Maxwell elements.

APPENDIX C – BKZ model

Based on concepts of the theory of rubber viscoelasticity, Bernstein, Kearsley and Zapas proposed the following constitutive equation for a non-linear viscoelasticity:

$$\sigma_{ij}(t) = \int_{-\infty}^{t} \left[2\frac{\partial u}{\partial I_1} C_{ij}(t,t') - 2\frac{\partial u}{\partial I_2} B_{ij}(t,t') \right] dt' \qquad \text{eq. C-1}$$

where u is a time-dependent elastic energy potential function, C_{ij} and B_{ij} are the Cauchy and the Finger tensors, respectively, and I_1 and I_2 are the scalar invariants of the Finger tensor. For simple shear, the components of the Cauchy andFinger tensors are shown below:

$$C_{ij}(t,t') = \begin{bmatrix} 1 & [\gamma(t')-\gamma(t)] & 0 \\ [\gamma(t')-\gamma(t)] & \{1+[\gamma(t')-\gamma(t)]^2\} & 0 \\ 0 & 0 & 1 \end{bmatrix} \qquad \text{eq. C-2}$$

and

$$B_{ij}(t,t') = \begin{bmatrix} \{1+[\gamma(t)-\gamma(t')]^2\} & [\gamma(t)-\gamma(t')] & 0 \\ [\gamma(t)-\gamma(t')] & 1 & 0 \\ 0 & 0 & 1 \end{bmatrix} \qquad \text{eq. C-3}$$

A more useful form of the BKZ equation was formulated to incorporate the observation that the stress relaxation data could often be described as a product of a time-dependent and a strain dependent terms. Based on this experimental observation, Wagner proposed the following formulation:

$$\sigma_{ij}(t) = \int_{-\infty}^{t} m(t-t')h(I_1,I_2)B_{ij}(t,t')dt' \qquad \text{eq. C-4}$$

The term involving the Cauchy tensor has been omitted, which simplifies the use of the model, and the energy potential is replaced by the separable memory function, consisting of the time-dependent part, $m(t-t')$, and a strain dependent damping function, $h(I_1, I_2)$.

The shear component of the Finger tensor, B_{ij}, for simple shear becomes

$$\gamma(t,t') = \int_{t}^{t'} \dot{\gamma}(t'')dt'' \qquad \text{eq. C-5}$$

Using a form of the damping function proposed by Zapas,

$$h(\gamma) = \frac{1}{1+\alpha\gamma^2}, \qquad \text{eq. C-6}$$

and writing the constitutive equation for the shear stress component in terms of the relaxation spectrum (G_i, λ_i), the Wagner equation takes the following form:

$$\sigma(t) = \int_{-\infty}^{t} \frac{G_i}{\lambda_i} e^{-\frac{t-t'}{\lambda_i}} \frac{\gamma(t,t')}{1+\alpha\gamma^2(t,t')} dt' \qquad \text{eq. C-7}$$

The Wagner equation is used in this form in the present work; if necessary, the power of two in the damping function may be replaced by β, which gives a more general expression for the damping function [Soskey and Winter, 1984]. In that case, the damping function can be written as

$$h(\gamma) = \frac{1}{1+\alpha\gamma^{\beta}} \qquad \text{eq. C-8}$$

The parameters α and β are determined experimentally from step-strain experiments.